Transient and heterogeneous YAP1 activity drives self-organization in intestinal organoid development

Inauguraldissertation

zur

Erlangung der Würde eines Doktors der Philosophie

vorgelegt der

Philosophisch-Naturwissenschaftlichen Fakultät

der Universität Basel

von

Urs Mayr

2020

Genehmigt von der Philosophisch-Naturwissenschaftlichen Fakultät

auf Antrag von

Prof. Dr. Prisca Liberali

Prof. Dr. Susan Gasser

Prof. Dr. Darren Gilmour

Basel, den 17.12.2019

Prof. Dr. Martin Spiess

Dekan

Summary

Recent years have seen an explosion in the ability to grow organoids which phenocopy diverse organs ranging from intestinal epithelium to complex cerebral structures. All organoid models emerge from the potential of individual cells to self-organize into higher order structures under homogenous conditions. They can be established by extracting adult stem cells from healthy or diseased tissue or by directed differentiation of pluripotent stem cells. Protocols have been established to culture them in well-defined conditions and use them for any standard biological or molecular technology. In addition, they are more amenable to imaging approaches, allowing researchers to gain access to early development processes. Despite the exciting promises of organoid technologies and the hope that they will result in new human therapies, little is known about self-organization into complex organ like structures. This type of basic knowledge about the underlying process is required for applied breakthrough to occur.

In this work, we used the enormous regenerative capacity of the small intestine to study how cells with stem and non-stem cell identity self-organize into organoids. A quantitative study identified a YAP1 driven transient dedifferentiation, occurring independently of the starting population, into proliferative, homogenous cysts able to reconstitutes all cell types of the mature tissue. In contrast to the prevalent view of organoid development, this intermediate state exhibits not intestinal stem cell but fetal-like characteristics. By addressing how asymmetries emerge within homogenous cysts to specify Paneth cells, the first symmetry breaking event in this system, we identified large degrees of cell-to-cell variability in YAP1 activity preceding symmetry breaking. This YAP1 cell-to-cell variability in its subcellular localization is essential to drive a Notch-Delta lateral inhibition event that specifies Paneth cell fate.

In conclusion, this works shows how combining live and 4i multiplexed imaging, sequencing and perturbation approaches can bridge decision making at the single cell level, by lateral-inhibition driven cell-fate decision, to different phenotypic outcomes on the tissue level, the occurrence of budding organoids or because of failed symmetry breaking, enterocsyts. This study gives a first glance into the complex interaction networks endowing individual cells with the capacity to self-organize into organoids.

Table of contents

List of figures

Chapter 1: Introduction

One of the defining features of tissues is organization into specialized cell types with distinct functionality and defined spatial arrangements. During embryonic development, tissue homeostasis and regeneration, populations of cells have to undergo complex temporal and spatial coordinated processes to build, maintain or rebuild three-dimensional tissue structures[1]. Each transformational step emerges through collective behavior of interacting cells that encode, and decode, signaling and transcriptional networks[2]. To this end, each cell is equipped with a sophisticated sensing and sending machinery, which allows to probe the cellular microenvironment, react to and instruct neighboring cells and dynamically adapt cellular states to changing microenvironmental demands[1]. While each adaptation can cause multiple behavioral change on the single cell level including, proliferation, migration, and differentiation, ultimately the organization into multicellular tissues only emerges through coordinated interactions between cells[3,4].

Surprisingly little is known about underlying mechanisms orchestrating single cell behaviors during tissue patterning[3,5]. The search for conserved design principles underlying pattern-forming systems is a longstanding problem in biology[6]. Earlier schools of thought viewed patterning at a coarse-grained tissue level and introduced the concept of an organizing center[7,8], a localized region from which molecule spreads to induce changes in the surrounding tissue. Over time, the focus moved from the whole tissue to individual cells, genes and genetic networks[7,8]. This cell-centric view paved the way to understanding how early formed positional cues can translate into distinct cellular fates based on positional information[9,10]. However, the question of how initial asymmetries required to form positional cues in a collective of cells could arise remained elusive.

In 1952 Alan Turing presented an elegant conceptual framework to biologists explaining how asymmetries arises by non-linear interactions between individual cells from homogenous conditions[11,12]. In the simplest form of Turing's reaction-diffusion system, a short-range positive feedback coupled to a long-range negative feedback suffice to generate various patterns such as stable periodic patterns, travelling waves and oscillations[13]. Although the real-world relevance of strict Turing-Reactions in biology is debated[14], his theoretical analysis based on the diffusion of chemical molecules exemplifies a fundamental design principle in biology; self-organization. Whereas pre-patterned gradients of molecules can activate cell-intrinsic fate programs, by adding non-linear interactions between cells into the system, self-organizing patterns can emerge from homogenous conditions without a fixed reference[15]. Although Turing's ideas preceded many theories regarding pattern formation, interest in self-organization as a core patterning mechanism in biological systems is quite recent.

Self-organization

In a self-organizing system, entities interact with each other to spontaneously form higher order structures through collective behavior without the requirement of external positional guidance[16,17]. Self-organization is pervasive in biology, chemistry, and physics[17]. A framework of self-organization has proved helpful in explaining diverse biological phenomena ranging across different scales. Examples include the emergence of protein patterns in bacteria [18], oscillations in the presometic mesoderm[19], the recreation of entire organism[20] and the behavior of schools of fish and flocks of birds[11]. This thesis focuses on self-organization at the tissue level, in particular on self-organized tissue patterning starting from a single isolated cell and subsequent spontaneous occurrence of cell fate specification within a population of dividing cells.

Symmetry breaking

A crucial step during self-organization is symmetry breaking, where symmetry means uniformity[21]. Symmetry breaking therefore refers to the process by which such uniformity is broken to bring the system from a homogenous in a more structured and improbable state[21]. Similar to self-organization, symmetry breaking comprises multiple biological scales and depending on the context can refer to a variety of biological outcomes including the acquisition of cell polarity[22], asymmetric cell division[23], or embryonic body axis formation[24]. In mammalian systems, symmetry breaking often refers to cell fate determination. The event by which a uniform population of cells, a population where each cell has an identical potential to differentiate into prospective fates[1,25], breaks uniformity to realize a distinct cellular fate in a subset of these cells. Examples include Paneth cell specification during organoid development[26], the differentiation of progenitor cells into erythroid and myeloid fates[27], the differentiation of the totipotent embryo[28] and cell fate determination in the inner cell mass of the embryo[29]. This particular definition of symmetry breaking is the one this thesis focuses on, if not explicitly stated otherwise. Although the term symmetry breaking usually describes the outcome (the fate specification), the mechanism leading to this event can be comprised of multiple implicit symmetry breaking event on smaller scales.

Intrinsic noise and deterministic cell-to-cell variability in symmetry breaking

Since Turing's theory of chemical reaction and diffusion, various additional theoretical modeling frameworks have emerged which allow to model self-organizing processes[1]. Although rules and rationales differ between those modelling frameworks, they all share the idea that small initial perturbations within the homogenous system are mandatory to initiate symmetry breaking[1]. These initial heterogeneities allow then to be amplified and consolidated

to generate stable patterns[1]. Corroborating results comes from experimental evidence both *in vitro*[30] and *in vivo*[25,31,32] where extensive cellular heterogeneity on the gene and protein level precedes emergence of lineage segregation[25,31,32]. In two-dimensional cultures of embryonic stem cells (ESCs) grown under uniform conditions, cell-to-cell variability in NANOG and GATA6 expression emerges spontaneously[33]. The observed variability in NANOG levels between individual cells translate into distinct differentiation propensities of these cells. NANOG⁺ cell generate preferentially undifferentiated cell colonies, whereas NANOG⁻ cells show a higher propensity for differentiation[30]. Similar observations have been made during symmetry breaking in mouse pre-implantation development where OCT4 and SOX2 targets such as SOX21 are highly heterogeneously expressed to initiate cell-fate decision at the 4-cell stage[34].

Although cell-to-cell variability is omnipresent in populations of clonogenic cells[35], little is known about the source of this observable variability. The dogma has long been that such variability is just a random consequence of inherent stochasticity of biological processes called intrinsic noise. Nowadays, an increasing amount of studies suggest that these cell-to-cell variabilities arise through active sensing and adapting mechanism of individual cells to respond to their changing microenvironment (here referred to as deterministic cell-to-cell variability)[35].

Intrinsic noise

Biological processes which involve low copy numbers or infrequent interactions are inherently stochastic[36]. This is best understood in gene expression where the low copy numbers of one to two genes per cell lead to expression bursts which results in variability in protein and mRNA levels between cells[37]. Variability in a system is not only required for symmetry breaking in cell fate determination but also to allow other emergent phenomena as cell polarization or migration[38]. Although variability in biological systems may allow for flexibility and adaptability[36], it also raises the question of how a random process can cause robust and reproducible patterns[39]. At least to a certain degree, cells achieve robustness by using active and passive mechanism to filter molecular noise[40]. Active noise filters include feedback or feed-forward motifs for transcriptional regulation or regulator loops by microRNA expression[39] and nuclear compartmentalization makes up a powerful mechanism to buffer stochastic fluctuations of gene expression passively[41,42]. Cross-talks between distinct signaling pathways may also act to buffer noise[43]. Of note, even assuming an optimal noise-reducing feedback circuit, molecular noise has a fundamental limit in its controllability[44] which will display at least a minimal stochasticity as described by a single Poisson process[45]. In early studies of cellular noise, the sole measurement used was gene expression which lead to the conclusion that the observed fluctuations are of non-deterministic nature[37]. By separating the contribution of these

heterogeneities into intrinsic noise and extrinsic factors by aid of multivariate measurements[46,47], however, large parts of the observed variability can often be attributed to extrinsic factors while intrinsic noise in biological systems approaches minimal stochasticity[42,48-51].

Deterministic cell-to-cell variability

Extrinsic factors include cellular states such as the cell cycle stage but also the microenvironment of each cell. During division cells undergo extensive cellular reorganization on the chromatin, organelles and cytoskeletal levels[52]. As cells approach mitosis, cells attaching to the extracellular matrix disassemble focal adhesion[53] or change cell-to-cell contact mediated adhesion within a tissue context to reshape into a spherical geometry[53]. These cell cycle dependent changes in adhesion facilitate heart progenitor induction[54] and differentiation in mouse embryos[55]. Oscillations of the cell-cycle regulators cyclin D1-3 control differentiation signals including the TGF-β-SMAD2/3 pathway and different cell cycle stages directly affect activation of various signaling molecules[56,57]. YAP1 activity increases during G1[57], PKB (also known as AKT) activity fluctuates across the cell cycle[56] to show highest phosphorylation in G2[58] and Wnt signaling peaks in the G2/M phase of the cell cycle[59]. Cells continuously adapt their cellular state while progressing through the cell cycle. Moreover, by changing cell-to-cell contacts and reducing the available space, cellular division reshapes the microenvironment of neighboring cells.

The microenvironment of a cell is defined by its position within a population, the crowdedness of such a population and the amount of physical forces each cell exerts on its neighboring cell[58,60,61]. Even in populations of isogenic adherent cells, under homogenous growth conditions, divisions combined with cell motility result in a continuously changing local microenvironment[35]. As sparsely populated regions become denser, the available space for each cell becomes less, resulting in smaller cellular size and confined shape. In this dynamic environment of ever changing local cell densities, each cell has to constantly probe and translate the current state through multiple signaling pathways into population context dependent cellular adaptations including growth[60], proliferation[62], polarization[63], lipid composition[63,64] and gene expression[42]. Driven by asynchronous cell cycles and single cell adaptations to the local microenvironment, on the population level large degrees of cell-to-cell variability in cell shapes and cellular states emerge. For example, cell spreading allows cells in sparse region to activate focal adhesion kinases to adapt lipid composition differently than cells grown in dense region[63,64]. These differences in lipid composition translate into distinct signaling states within each single cell[64] and change within a population the propensity of each individual cell for viral infection[63]. Although each of these observations appears random when only considering one phenotypic read out such as phosphorylation of PKB[58,65] or efficiency of

virus infection[63], uncovering and measuring the hidden variables underlying these processes (cell cycle and population context) renders responses to the same stimulus predictable.

Particularly in the context of symmetry breaking, many fate decisions considered to be fully stochastic could have similar determining variables. In clonal populations of haematopoietic progenitor cell cellular heterogeneity in the stem cell marker Sca-1 is believed to occur stochastically. Sca-1 high cells show distinct transcriptomes and differentiation propensities compared to Sca-1 low cells[66]. Although, cell-cycle-dependent cell size variation contribute to only 1% of the observed variability of Sca-1 levels per cell, the observation that clear bimodal distributions only occur after more than one week where cells are grown form a single cell into colonies of cells may indicate a role of population context in the occurring heterogeneity. Similarly, cell programming of somatic cells into induced pluripotent stem (iPS) cells mediated by overexpression of OCT4, SOX2, KLF4 and MYC is believed to be a stochastic process. However, differentiation occurs in dense population of adherent cells[67,68] as does the occurrence of NANOG heterogeneity[69]. Indeed, by following single pancreatic progenitors in clusters of cells, Mamidi et al.[70], recently demonstrated that the ability to spread out for cells determines the propensity to break symmetry and express the fate-determining transcription factor PDX1. Dense cells in the center maintain high PDX1 expression, whereas spread cells at the periphery downregulate PDX1 expression. Expanding on the observation that in isolated cells manipulation of the local microenvironment directly links biophysical cues to cell fate determination[61,71]. Here the authors demonstrate that within the pancreas, cells probe the local microenvironment by an Integrin-F-actin-YAP1-Notch mechanosignaling axis to regulate cellular fate.

In conclusion, self-organization is now recognized as a core principle in pattern formation for multicellular systems[72]. The generation of complex three-dimensional topologies is not directly encoded within the genetic code but emerges by interconnected layers of interactions comprising physical as well as genetic mechanism[73]. A crucial aspect of symmetry breaking is heterogeneity of molecular key players involved in cell fate determination[74]. Although, heterogeneities comprise intrinsic noise, deterministic factors can often explain large degrees of the observed variability. Despite the importance of self-organization in biology, little is known on how individual cells have the intrinsic capability to self-organize, create heterogeneity, break symmetry and pattern into higher order structures.

Model systems to study self-organization

Unraveling the underlying mechanisms of multicellular interactions ranging over various temporal and spatial dimensions is a daunting task. Many *in vivo* model systems

including social amoeba[75], zebrafish[76] and fly[77], have been used to explain dynamics of pattern formation by using tools including conditional knock-outs, cellular ablation, lineage tracing and live imaging[78]. However, the study of self-organization *in vivo* is often hampered by confounding factors such as limited accessibility, low throughput or ethical considerations in case of human embryonic development[79].

Complementary to the *in vivo* model systems, over the last years' robust *in vitro* model systems recapitulating many processes of *in vivo* patterning have been developed. Improvements in culture conditions of pluripotent stem cells and adult stem cells have unraveled the potential of individual cells to self-organize into higher order structures resembling processes *in vivo*. Dissociated cells can recapitulate early embryonic spatial patterning in two-dimensional cultures[80] and generate various three-dimensional organoid structures when cultured in appropriate conditions[2,81]. Organoids provide a unique experimental system to study defined aspects of spatiotemporal dynamics of cells interacting in three-dimensions under defined conditions. Organoids are tractable, easily expandable and amendable to fast genetic manipulations[82].

The growing field of organoid research

The groundbreaking work of Yoshiki Sasai's laboratory showing that stem cells can organize into optical cups[83] and of Hans Clever's laboratory in the gut paved the way of today's booming organoid research[84]. The current definition of an organoid is ""a collection of organ-specific cell types that develops from stem or organ progenitors and self-organizes through cell sorting and spatially restricted lineage commitment in a manner similar to *in vivo*"[85]. Various organoid systems have been developed, including small intestine[84], stomach[86], pancreas[87], liver [88], optic cups [83] and cerebral structures[85] which are either initiated from single cells[84] or from aggregated cells[83]. Two main types of stem cells can induce organoid formation, pluripotent stem cells (PSC), including pluripotent embryonic stem (ES) cells and synthetic induced pluripotent stem (iPS) cells, and stem cells origin from the adult tissue (adult stem cells, ASCs)[89]. Although cells are self-organizing in the sense that the final structure emerges under homogenous conditions, each organoid type requires timed addition of growth factors and suitable mechanical support from the surrounding matrix[90]. Culture conditions are distinct for each organoid type and guide the culture towards the desired fate[90].

Pioneering discoveries paving the way for nowadays three dimensional cultures can be traced back to the 1970s[91]. Of fundamental importance to establish three dimensional cultures have been observations that the extracellular matrix (ECM) regulates gene expression[92], contributes to cell differentiation and promotes growth of tissue-like structures [93]. Such extracellular matrix with characteristics of the basement membrane can be extracted

from mouse sarcoma cells and used for organoid cultures. Nowadays, the most commonly used is a laminin-rich Engelbreth, Holm and Swarm (EHS) matrix also known as Matrigel[91]. It provides structural support for cellular attachment as well as growth promoting factors. By using this laminin-rich matrix, Bissel and colleagues showed for the first time that breast epithelial cells could recapitulate steps of mammary gland morphogenesis to organize into three dimensional ducts and ductules[91].

Small intestinal organoids

These early findings combined with an extensive knowledge about signaling requirements to maintain the stem cell niche of the small intestine later lead the group of Hans Clevers to generate self-organizing structures resembling cell type composition and morphology of the small intestine from adult intestinal stem cells[84]. This structures, termed mouse small intestinal organoids, are today one of the best-established and often used three-dimensional culture systems. They recapitulate many patterning processes observed *in vivo* and reconstitute all cell types of the epithelium as well as the crypt–villus architecture of the small intestine[84]. Compared to other three-dimensional systems that often require hundreds of starting cells to aggregate, small intestinal organoids grow from individual single cells into clonal organoids. This gives a unique advantage to study self-organization without the confounding factor of initial heterogeneities within each organoid and enables the tracking of individual cells within each organoid.

Of note, small intestinal organoids can also be derived from PSCs[94,95] of either mouse or human origin or from mouse fetal precursor cells[96]. Similar to small intestinal organoids with adult stem cell origin, these organoids contain all major epithelial cell types patterned into villus-like structures and crypt-like proliferative zones. However, while the final structures appear the same, culture conditions, tissue maturation and the underlying mechanisms governing self-organization may be distinct. Indeed, organoids derived from adult intestinal stem cells are believed to recapitulate mechanism resembling tissue regeneration or homeostasis[89] while pluripotent stem cells derived organoid development likely is closer to fetal development[89]. Within this thesis, if not specified otherwise, small intestinal organoids will refer to small intestinal organoids derived from adult stem cells of the mouse.

Intestinal organoid development

Small intestinal organoids grow from LGR5+ intestinal stem cells (CBC, ISC or LGR5^{+}) when placed in Matrigel and supplemented with three necessary growth factors (signaling pathways, structure and cell types of the small intestine are discussed in the next section: **The small intestine**): R-Spondin (RSPO), epidermal growth factor (EGF) and bone morphogenetic

protein (BMP) antagonist Noggin[84]. LGR5+ cells can develop into organoids without exogenous addition of the Wnt ligand WNT3A, however, the supplement of WNT3A leads to a significant increase in organoid forming efficiency[97,98]. Furthermore, by short pulses of WNT3A not only stem cells but also adult[99,100] and fetal progenitors[101,102] as well as differentiated cell types[103] can be coerced to develop into organoids (for more details see: **Development of the small intestine** and **Regeneration of the small intestine**).
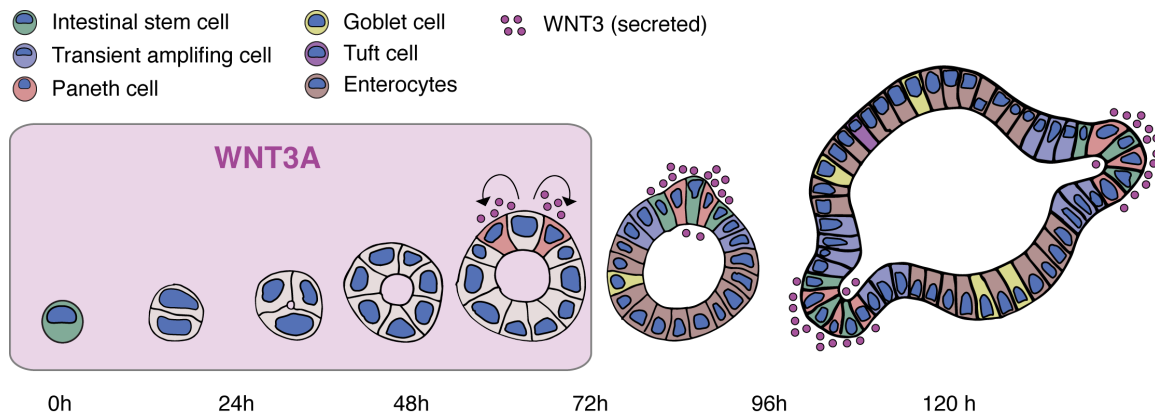
Fig. 1 | Stereotypic organoid development. Organoids develop from a single cell into a budding organoid within five days. Organoids reconstitute crypt-villus morphology and cell-type composition of the small intestine. In a uniform WNT3A environment, symmetry is broken and the first WNT3 secreting Paneth cells appear between day 2 and day 3. After the emergence of Paneth cells, WNT3A can be removed from the medium.

Under standard growth conditions supplemented with WNT3A, small intestinal organoids develop over five days highly stereotypically from a single cell into a budding organoid (that is an organoid with the crypt and villus structure and cell type composition observed *in vivo*) with hundreds of cells **(Fig. 1).** Between day 2 and 3 the first Paneth cells emerge within larger homogenous cysts. Appearing Paneth cells are the first and most crucial symmetry breaking event in intestinal organoid development. Differentiated Paneth cells show active Wnt signaling and secrete WNT3. This allows organoids to create self-sustaining Wnt gradients, which are believed to determine the future crypt sides and lead to budding after exogenous WNT3A is removed from the medium[104]. After five days, organoids have cell type composition and crypt-villus morphology reconstituted. Although genetic and chemical perturbation experiments have shed light on the signaling pathways involved in Paneth cell differentiation *in vivo*[105,106], little is known about what underlying self-organizing mechanisms result in Paneth cell specification. The common view is that it arises from a stochastic process[26].

When investigating such questions in intestinal organoid, one can start by studying the broad knowledge already available on cell types and signaling pathways involved in development, homeostasis and regeneration of the small intestinal epithelium.

The small intestine

The single-layered epithelium of the intestine is the most important barrier against the external environment. It maintains body homeostasis by up taking nutrients, electrolytes and water while preventing passage of intraluminal pathogens, toxins and antigens[107]. To withstand permanent abrasion from the luminal content while sustaining absorptive capabilities, the epithelium comprises a specialized folded structure of villi and intestinal crypts that undergoes constant self-renewal[108] **(Fig. 2)**. Villi are finger-like protrusions extending into the intestinal lumen mostly build by enterocytes responsible for nutrient uptake. Each villus protrusion is surrounded by multiple crypt invaginations, called crypts of Lieberkuehn, which harbors the stem cell niche[108].

Legend:
- Intestinal stem cell (LGR5+)
- Transient amplifying cell
- Paneth cell
- Goblet cell
- Tuft cell
- Enterocyte
- Enteroendrocine cell
- +4 cell
- Mesenchymal cell
- WNT3 (secreted)
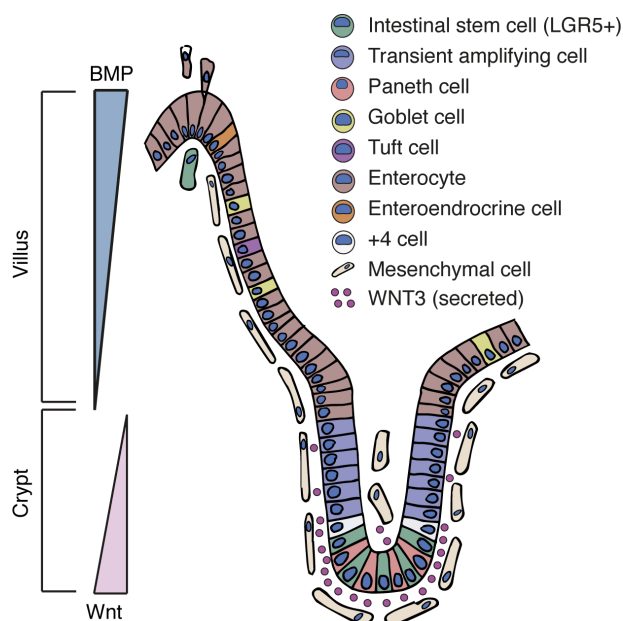
Fig. 2 | Structure of the adult small intestine. The epithelium of the small intestine is organized into crypts and villi. LGR5+ intestinal stem cells, interspersed by Paneth cells, at the crypt bottom generate a continuous flow of cells. Newly generated cells undergo lineage segregation and mature as they migrate upwards. After four to five days, differentiated cells reach the villus tip to become shed into the lumen. Stem cell maintenance and lineage specification require distinct gradients of signaling molecules provided by epithelium cells together with surrounding mesenchymal cells.

The intestinal stem cell niche and tissue homeostasis

To fuel the enormous demand of dividing cells required for constant self-renewal during homeostasis, crypts of Lieberkuehn house dedicated populations of stem cells and progenitor cells **(Fig. 2)**[109]. Intestinal stem cells residue at the crypt bottom interspersed by Paneth cells and marked by LGR5, a target gene of the Wnt signaling pathway. Intestinal stem cells are fast dividing cells which divide roughly every day symmetrically[110] to adapt stem cell fate or the fate of a highly proliferative transient amplifying cell stochastically[111]. TA cells further divide 4-5 times and gradually commit to either the secretory or the absorptive lineage while

they move upward and out of the crypt[112]. During the time cells exit the crypt, proliferation of differentiated cells stops[112]. Four to five days after birth, cells reach the tip of the villus where they undergo apoptosis before being shed into the lumen[113].

Despite the high turnover rates of the tissue, tissue composition and structure of the intestinal is remarkable robust. Each crypt harbors around 14 LGR5+ intestinal stem cells which give rise to a steady fraction of secretory and absorptive cell types[111].

The secretory lineage

The small intestine harbors four main types of secretory cells; Mucus secreting goblet cells, important to provide a defense barrier against invading pathogens; multiple hormone secreting enteroendocrine cells; chemosensing tuft cells; and Paneth cells[114].

Paneth cells

Committed secretory and absorptive cells normally migrate upwards along the villus and shed of at the villus tip within a week after birth. This behavior stands in contrast to Paneth cells where dedicated secretory progenitors mature into long-lived differentiated Paneth cells while migrating downward from the base of the TA compartment toward the crypt bottom[112]. At the crypt bottom, Paneth cells can live for up to 60 days[115] interspersed between intestinal stem cells. Each intestinal stem cell is in contact with at least one Paneth cell. This direct cell-to-cell contacts allows Paneth cells to support stem cell maintenance by cell contact facilitated Notch signaling, mediated by the expressing of DLL1 and DLL4, and by providing the secreted ligands WNT3, TNF and EGF[116]. Paneth cells further support intestinal stem cells metabolically by providing them with the essential nutrient lactate. Besides their role in stem cell maintenance, they also secrete antimicrobial products such as lysozyme, α-defensins and phospholipase A2[117], thus playing an important role in protecting the stem cell niche from pathogens and contributing to mucosal-immunity along the whole epithelium[118]. Consequently, Paneth cells play a role in gut-related diseases where aberration in Paneth cell functionality contributes to the onset and progression of inflammatory bowel disease[119].

The absorptive lineage

Enterocytes

In contrast to secretory precursor cells which give rise to various functional distinct secretory cells types[100], absorptive precursors predominantly give rise to enterocytes[108]. Enterocytes represent the vast majority of cells in the epithelial layer and play important roles absorbing nutrients such as ions, water, sugar, peptides, and lipids and secreting immunoglobulins[108]. After emergence from crypts, enterocytes continuously migrate along the

villus axis. During this maturation along the crypt axis each enterocyte traverses a series of cellular states linked to various functional specializations which results in a broad spatial zonation of enterocyte functionality along the villus axis[120]. Enterocytes at the bottom of the villi are specialized to express inflammasome components while enterocytes in the middle of the villus are compartmentalized into distinct nutrient absorbing zones[120].

Development of the mouse intestine

The mouse small intestine emerges from the definitive endoderm-derived primitive gut tube. Formation of the primitive gut tube is initiated at embryonic day 6 (E6.0), by the onset of gastrulation, and is fully formed around E9.0. Molecular cues including SOX2 in the anterior part and the CDX family of transcription factors in the posterior part regionalize the gut tube into primitive foregut, mid-gut, from which the small intestine emerges, and hindgut. Posterior fate via expression of CDX is mediated by upstream signaling of four major signaling pathways Wnt, FGF, RA and BMP[121]. After a non-canonical Wnt signaling mediated elongation and polarization period between E9.5 and E14.5[122], villus morphogenesis starts around E14.5 driven by aggregation of subepithelial mesenchymal clusters[123]. Compartmentalization of signals including SHH and BMP4 instruct the reorganized epithelium into non-proliferative villus and proliferative intervillus regions during villus morphogenesis[121,123]. Notable, LGR5+ progenitors with a characteristic intestinal stem cell signature emerge at E13.5[124]. From E16.5 to birth, proliferative intervillus progenitor cells give rise to absorptive enterocyte cells on the villi. Crypts of Lieberkuehn are formed during the first 2 postnatal weeks from distinct parts of the intervillus region (**Fig. 3**). Although embryonic tissue contains LGR5+ cells, at this stage of crypt formation and crypt expansion by fission, all cells of the epithelium can contribute to the stem cell pool of the final crypts[125]. Crypt morphogenesis is accompanied with a shift in lineage specification where the first secretory cells, goblet and enteroendocrine cells, arise. Of note, Paneth cells only emerge after crypt morphogenesis is completed at around postnatal day 14[126].
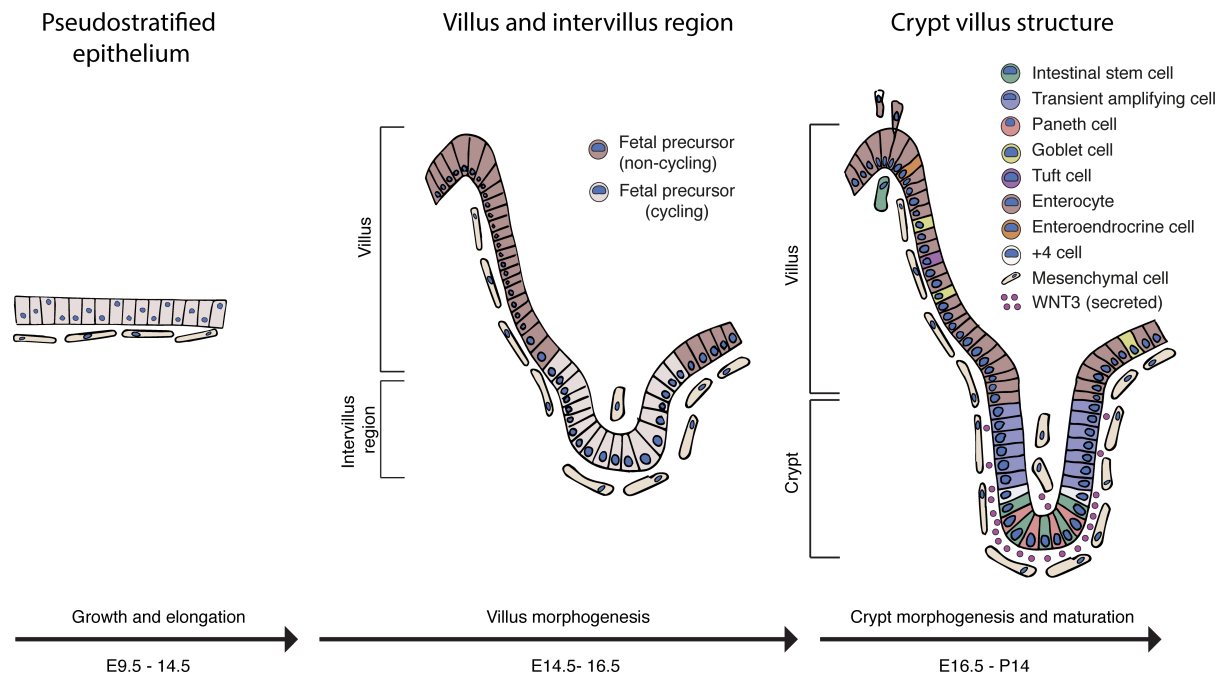
Fig. 3 | Development of the mouse small intestine. After a period of growth and elongation, the pseudostratified epithelium becomes restructured into a simple columnar epithelium. Villus morphogenesis starts around E14.5 and results into folding of non-proliferative villus and proliferative intervillus regions. After villification, proliferative intervillus progenitor cells give rise to absorptive enterocyte cells on the villi. Crypts of Lieberkuehn emerge 2 weeks after birth from distinct parts of the intervillus region. After crypt morphogenesis is completed, Paneth cells emerge at around postnatal day 14.

Fetal spheroids/enterospheres

Organoid-like structures called fetal spheroids can be grown from single cells extracted from the fetal intestinal tissue by supplementing the medium with Noggin, EGF and RSPO (similar to *ex-vivo* small intestinal organoids[84])[102], although RSPO is dispensable for spheroids[101]. Whereas organoids bud, show cell type differentiation and restricted proliferation to crypts[84], spheroids remain as thin polarized cysts with cycling progenitor cells across the whole surface[102]. Furthermore, spheroids transcriptomes are distinct from small intestinal organoids as well as from intestinal stem cells[102]. Compared to organoids, spheroids lack differentiation markers of the adult intestine and show strong downregulation of adult intestinal stem cell markers (*Lgr5, Axin2, Olfm4, Tert*)[102]. In contrast, markers associated with progenitor cells (*Cnx43, Trop2, and Ly6a/Sca1*) and tissue regeneration/development (*Ctgf and Clusterin*)[102] are upregulated. Notable, pulses of WNT3A can transit fetal organoids to mature budding organoids. This transition involves upregulation of canonical Wnt genes (*Lgr5, Axin2*) and secretory lineage markers[101].

Regeneration of the small intestine

The intestinal epithelium has not only an enormous intestinal stem cell driven capacity for self-renewing during homeostasis but can also flexibly adapt to different damage causing stressors including irradiation, toxins, chemotherapy, surgical resection, nutritional deprivation or acute inflammation[127]. Often regenerative responses are facilitated by intestinal stem cells. Indeed, inflammation and nutritional deprivation increases the proliferative potential of intestinal stem cells either directly[128] or mediated by Paneth cells[129]. However, cycling intestinal stem cells are susceptible to other types of damage including irradiation and therefore lost after injury[130]. Nevertheless, the intestinal epithelium regenerates[131]. Besides the cycling stem cells at the crypt bottom, a 'reserve' pool of quiescent, non-cycling cells, resides four cell diameters above the base of the crypt[127] **(Fig. 2)**. These so called +4 cells, marked by expression of BMI1, LRIG1, HOPX and TERT, are insensitive to injury and become activated when active stem cells at the crypt bottom are challenged[132]. Although lineage-tracing experiments have shown the regenerative potential of these rare +4 cells[133], the concept of a dedicated 'reserve' stem pool is disputed[127]. Initially believed to be mutual exclusive markers for reserve stem cells, theses markers show broad distribution on the transcriptional level[134,135]. Furthermore, findings that also cells above the +4 position including secretory[99] and absorptive progenitors[100] can reverse and repopulate the niche *in vivo* and generate organoids *in vitro*, challenges the concept of a dedicated 'reserve' stem cell pool. More recent lineage tracing studies indicate that the +4 cells likely are secretory progenitors that regain stem cell potential upon injury[136] (**Fig. 4**). In particular, GFP+ cells from a BMI1-GFP reporter mouse have been shown to be preterminal enteroendocrine cells able to reconstitute the niche[137].

Fig. 4 | Model of cellular plasticity in the intestine. Progenitors and mature intestinal cells retain stem cell potential and can revert to the stem cell state in response to an injury. Stem cell properties are not hardwired but can be regained during injury response.

Nonetheless, recently a novel extreme rare type of 'revival stem cell', which arises following injury, has been described. This rare cell marked by the expression of *Clusterin* is induced by YAP1-dependent signaling (see below) in response to injury. Activated cells then undergo fast expansion to repopulate the niche[138]. It is not yet entirely clear how this novel population differs from classically proposed 'reserve' stem cells[139] and whether the intestine may utilize different mechanism including general cell plasticity or dedicated 'reserve' or 'revival' stem cells for different regenerative responses.

Signaling pathways controlling the intestinal epithelium

Stem cells maintenances, robust lineage segregation and injury responses involve a sophisticated network of signaling molecules derived from the epithelium cells and from mesenchymal cells surrounding the epithelial layer[127]. Despite of the complexity of the processes involved, the set of signaling pathways with a well-described function in the intestine is small. These pathways include Wnt signaling; Notch signaling, TGF-β / BMP signaling, EGF signaling and YAP1-dependent signaling. The next section briefly summarizes theses pathways. A particular focus is set on YAP1-dependent signaling and its regulation.

Wnt signaling

Wnt signaling is one of the fundamental growth controlling pathways and is indispensable in most if not all stem cell types including embryonic and adult stem cells[140]. The Wnt signaling network is complex, containing many components and being subject to various cascades of finely controlled signal transduction steps as well as cross-talk mechanisms[141]. In mammals, there are 19 Wnt ligands[142]. Distinct ligands couple to different receptors and co-receptors and activate distinct downstream signaling cascades. Theses cascades are broadly classified into a canonical (β-catenin dependent) and non-canonical (β-catenin independent) Wnt signaling[141].

In canonical Wnt signaling, Wnt activity regulates the cytoplasmic pool of the key mediator β-catenin via a destruction complex. A multi protein complex comprising kinases: GSK3 and CKIα, and scaffolding proteins: DVL, APC and AXIN[142]. The core machinery of canonical Wnt signaling is triggered when secreted and palmitoylated proteins of the Wnt protein family bind to the FZD-LRP5/6 receptor complex. Without receptor bound ligands, GSK3 and CKIα phosphorylate β-catenin to mark it for degradation. Activation of the FZD-LRP5/6 complex leads to deactivation of the destruction complex, cytoplasmic β-catenin stabilized and enters the nucleus where it displaces the transcriptional repressor Groucho[143] to associate with transcription factors of the TCF and LEF family to regulate the transcription of target genes involved in cell fate, proliferation and self-renewal[141,144] **(Fig. 5).**

Non-canonical Wnt signaling is a loosely defined umbrella term for β-catenin independent Wnt pathways. These pathways work independently of LRP5/6 and are transduced either through Rho-associated kinase (ROCK), in case of the planar cell polarity (PCP) pathway or through G-protein dependent calcium release (Wnt/Ca^{++} pathway)[145]. Although non-canonical Wnt signaling is active during intestinal development[146], its exact role

is little understood. I will therefore focus on the more extensive studied canonical Wnt signaling pathway in the intestine.
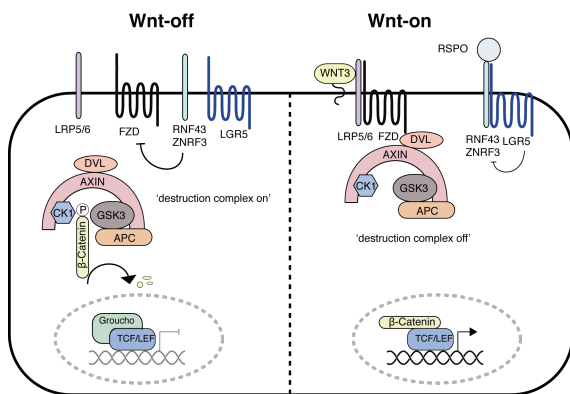

Fig. 5 | Canonical Wnt signaling in the small intestine. Without Wnt ligands, the destruction complex constitutively phosphorylates b-catenin and marks it for proteasomal degradation. When FZD/LRP receptors are engaged by ligands, the destruction complex becomes inactivated and β-catenin enters the nucleus to displace Groucho and initiates gene expression. Without RSPO, the free pool of FZD receptors is reduced by RNF43/ZNRF3. Binding of RSPO to its cognate LGR5-receptor leads to inhibition of RNF43/ZNRF3 and allows sustained Wnt activity.

In the small intestine, tight control of canonical Wnt signaling is essential to maintain proliferation and identity of intestinal stem cells[108]. Wnt ligands, predominately WNT3 and WNT2B, are redundantly expressed in epithelial Paneth cells[97] (WNT3) and in mesenchymal cells surrounding the lower crypt (WNT2B/3)[147,148] to form a Wnt signaling gradient along the crypt axis[104] (**Fig. 2**). Consequently, perturbations of Wnt signaling have severe consequences for intestinal stem cells maintenance. Knockout of the main effector of canonical Wnt signaling, TCF4, extinguishes intestinal stem cells in the developing embryo[149] and in homeostatic self-renewal[150]. A similar phenotype is observed by overexpression of the Wnt antagonist DKK1[151]. In contrast, hyperactive Wnt signaling caused by the deletion of the destruction complex scaffold APC leads to excessive growth of the intestine tissue and adenomas formation[109].

Even though Wnt ligands are abundant at the crypt bottom, intestinal stem cell maintenance requires enhanced Wnt pathway activity mediated by members of the R-Spondin (RSPO) protein family[152,153]. R-Spondins are secreted proteins which bind to their cognate LGR4 or 5 receptors on intestinal stem cells to control the length of the Wnt gradient along the crypt[104] (**Fig. 5**). Furthermore, β-catenin mediated Wnt signaling plays a role in Paneth cell differentiation[105,106] and inhibition of canonical Wnt signaling results in complete loss of all secretory cells[151]. Although the exact mechanism is not yet understood, these effects seem mediated via the canonical Wnt signaling target gene SOX9[154,155].

Notch signaling

In contrast to Wnt signaling, which relies on the secretion of signaling proteins to trigger a receptor response, Notch signaling is mediated by direct interactions between adjacent cells[156]. Interaction of a ligand from the Delta-like or Jagged family with a receptor of the Notch family triggers a series of catalytic steps which leads to the release of the transcriptional active Notch intracellular domain (NICD)[156]. The cleaved NICD translocates to the nucleus where it interacts with various proteins such as RBDJ (also known as CSL) to induce expression of multiple target genes, including members of the HES family of transcription factors[157].
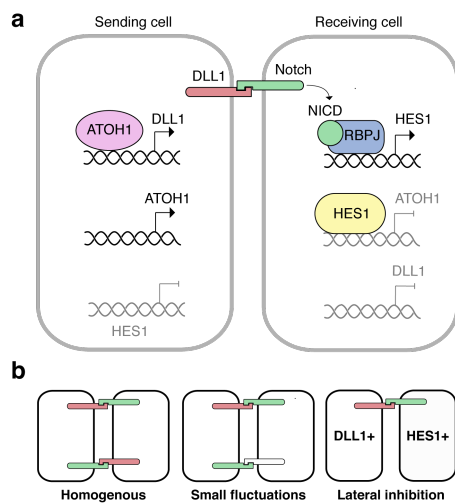
Fig. 6 | Notch signaling in the small intestine. a) Notch signaling cascade. In the receiving cell, interactions between DLL1 and Notch receptors lead to cleavage and nuclear translocation of NICD. Nuclear NICD binds to RBPJ to induce gene expression of HES1 which in turn represses ATOH1. In the sending cell, without the suppressing effect of HES1, ATOH1 is expressed constitutive to drive the expression of DLL1. b) Lateral inhibition. In a homogenous starting condition, sending and receiving cells express the same amount of ligand and receptor. Small fluctuations in ligand or receptor expression are sufficient to become amplified and break this balance. Thus, leading to a stable binary switch caused by competition between the two cells. The occurrence of this initial heterogeneitis are often believed to be random.

In the intestine, expression of HES1 in the receiving cell leads to repression of the transcription factor ATOH1. Without ATOH1 activity, expression of Notch ligands including DLL1 are repressed **(Fig. 6a)**. By this mechanism of lateral inhibition[158], initial small differences in Notch pathway activity are amplified and consolidated to establish a stable binary Notch 'on' or 'off' state between adjacent sending and receiving cells (**Fig. 6b**)[157].

Lateral inhibition is a powerful mechanism to induce alternative cell fates in a spatially precise manner. Examples include the definition of anchor cells in *C.elegans*[159], the sensory organ precursor development in *Drosophila*[160], specification of mechanosensing hair in the auditory sensory organ in mice[161] and the secretory lineage in the small intestine[157].

Notch signaling acts as the master regulator for secretory and absorptive lineage differentiation in the upper crypt where secretory progenitors express DLL1[114]. At the crypt bottom, a combination of Wnt and Notch signals is required for maintenance of the stem cell pool[114]. Paneth cells within the stem cell niche express DLL4 and transiently DLL1 to provide constant Notch signaling input to the adjacent stem cells[108]. Similar to inhibition of the Wnt pathway, inhibition of the Notch pathway results in loss of all intestinal stem cells[162,163]. Chemical and genetic perturbations of Notch signaling lead to conversion of proliferating crypt

progenitors into postmitotic secretory cells[162]. In contrast, loss of ATOH1, expressed in the progenitors of all secretory cells, leads to depletion of all secretory cells without affecting the absorptive enterocytes[164].

EGF signaling

EGF signaling controls the intestinal epithelium turnover by controlling stem cell proliferation[165,166]. Paneth cells within the epithelium and cells of the underlying mesenchyme secrete EGF ligands to the crypt region[108]. Intestinal stem cells respond to EGF ligands via the highly expressed EGFR receptor and MAPK pathway activation mediated by its downstream effector ERK1/2[167,168]. Hyper activation of the EGF pathway by KRAS mutants results in increased stem cell proliferation[165] while inhibition of EGF in presence of Wnt leads to reduced proliferation and cell cycle exit[168]. Although EGF inhibition reduces intestinal stem cell proliferation, it does not abolish expression of DTR-GFP in LGR5::DTR-GFP reporter mice[168], showing that EGF signaling is required to drive cell proliferation but not to sustain stem cell identity[168].

BMP signaling

BMP ligands of the TGF-β superfamily of ligands and their downstream effectors from the SMAD protein family play an important role in counteracting niche proliferation signals and promoting cell differentiation in the small intestine[169]. To protect the niche region from an inhibitory effect of BMP ligands, BMP inhibitors including Gremlin 1 and 2, Chordin-like 1 and Noggin are secreted in a tightly controlled fashion around the crypt region[108]. In contrast to EGF and Wnt, which are partially provided to the crypt from within the epithelium, BMP agonist are solely secreted by stromal mesenchymal cells[170] and BMP antagonists are mostly secreted by myofibroblasts and smooth muscle cells underlying the crypts[148,169,171].

YAP1-dependent signaling

As outlined under **Self-Organization** (see page **2)**, many emergent properties of populations of cells are not genetically encoded but emergent properties of interacting cells[172]. YAP1-dependent signaling is mediated by pathway components involved in many biological processes underlying or affected by these interactions such as cell-cell-adhesion, cell polarity, cell morphology but also by nutrient availability and general stresses[172]. This places YAP1-dependent signaling as a sensor of tissue and cellular integrity rather than responding to dedicated extracellular signaling inputs[173]. Indeed, in contrast to Wnt, Notch, BMP and EGF signaling, no dedicated receptors or ligands for YAP1-dependent signaling have been identified[173]. Rather, by mechanotransduction, the transcriptional co-activator YAP1 integrates

a diverse set of biomechanical signals, including cell shape[60], cell-extracellular matrix and cell-cell contacts, extracellular matrix stiffness and topology[174], tension forces as well as sheer stresses and transduce them into transcriptional output.

Two major steps control YAP1 activation, cytoplasmic phosphorylation and nuclear translocation of YAP1[175] **(Fig. 7)**. The best-known regulator of YAP1-dependent signaling is the Hippo pathway. The Hippo pathway is a conserved serine/threonine kinase signaling cascade with the core components MST1 and MST2, SAV1, LATS1 and LATS2, MOB1A/B[173]. When Hippo signaling is active, the MST1/2 kinases phosphorylate the LATS1/2 kinases, which phosphorylate YAP1. Phosphorylation of YAP1 prevents nuclear entry by cytoplasmic retention by 14-3-3 family proteins[176] or by ubiquitin-mediated protein degradation[177]. Thus, the Hippo kinases block YAP1 activity and suppress the transcriptional output of the Hippo pathway **(Fig. 7b)**.

Various upstream regulators mediate the Hippo pathway. Extracellular signaling molecules including hormones regulate the Hippo pathway via G-protein-coupled receptors[178], TAO1/2/3 kinases activate Hippo signaling by phosphorylating MST1/2 and cellular energy stress induces YAP1 phosphorylation via AMPK. Furthermore, cellular polarization and cell-cell junctions serves as strong inhibitors of YAP1 activity [172].

Cell polarity is associated with the asymmetric distribution of membrane proteins. The polarity determinant Scribble inhibits YAP1 activity by serving as a scaffold for the MST-LATS complex[179] and the apical crumbs complex (CRB) binds YAP1 to favor cytoplasmic localization [180]. At cell-cell junctions, the tumor suppressor and f-actin binding protein NF2 promotes plasma membrane association of LATS through direct binding to promote Hippo activity[181]. Although Hippo signaling sometimes is synonymous to YAP1 dependent signaling mechanotransduction can be independent of LATS signaling[172]. Indeed, NF2 also regulates YAP1 in a cell-cell adherent tension dependent manner independent of Hippo signaling[182]. Mechanotransduction is mediated by conformation and tension changes of the actomyosin cytoskeleton[172]. Under conditions of low mechanics at adherens junctions, NF2 is localized at theses junctions. However, as actomyosin forces on adherens junctions increase, NF2 is released to facilitate nuclear export of YAP1[182].

The tension state of the cytoskeleton itself is further largely dependent on the substrate to which cells attach[172]. Cells adhere to the extracellular matrix by focal adhesions which links the extracellular matrix to the cellular cytoskeleton[175]. Cells actively sense stiffness off the extracellular matrix to adapt spreading and cortical tension[60]. These adaptions directly translate into YAP1 nuclear localization[183]. How changes in cellular tensions at focal adhesions turns YAP1 activity on or off is not completely understood yet. Integrin, focal adhesion kinase and SRC signaling shows a regulatory function on LATS1/2[184,185]. Furthermore, it has been proposed that the LINC complex connects the cytoskeleton to the

nuclear envelope and transmits contractile forces directly into flattening of the nucleus. This opens nuclear pores and facilitates YAP1 shuttling into the nucleus[186,187]. Based on the large overlap of both LATS dependent and independent mechanotransduction it seems likely that full activation of YAP1 requires a synergistically effect controlling YAP1 phosphorylation and nuclear pore opening[172,175] **(Fig. 7a, b).**
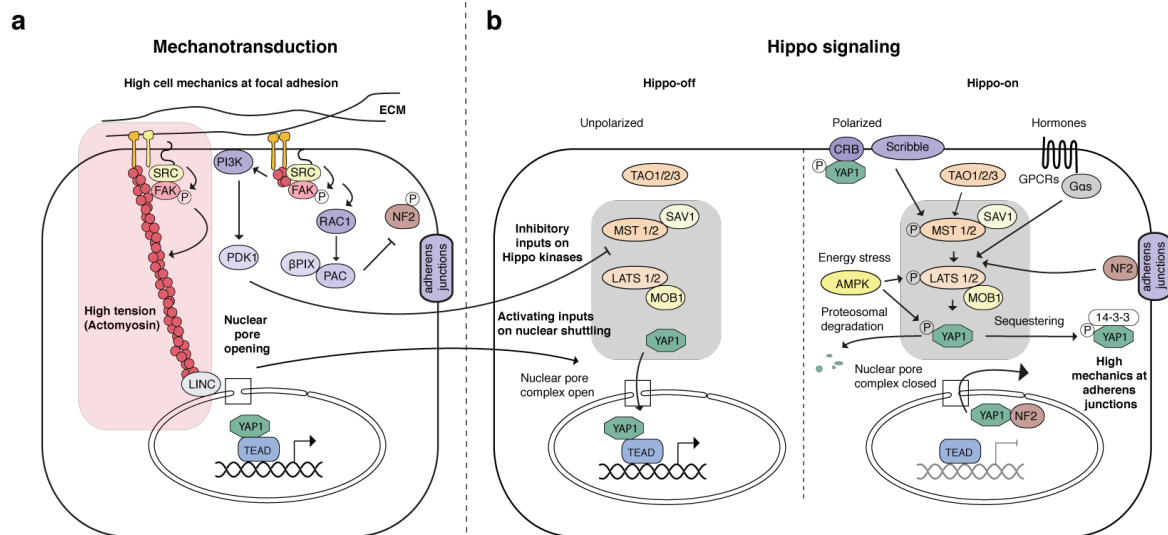

Fig. 7 | YAP1-dependent signaling. a) Biomechanical signal transduction to YAP1. Cells sense the state of the extracellular matrix through integrin signaling. Strong attachment to a stiff extracellular matrix leads to focal adhesion maturation and increased intracellular tension. Focal adhesion maturation involves activation of FAK–SRC signaling. FAK– SRC signaling disables Hippo activity via the FAK–SRC–PI3K–PDK1 or SRC–RAC1–PAK pathway and facilitates nuclear pore opening (red area). **b) Hippo signaling.** Active Hippo signaling prevents nuclear entry of YAP1 by phosphorylation and subsequent degradation or cytoplasmic retention. In contrast to focal adhesion mediated tensions, which promote YAP1 activation, adherens junctions and high tensional forces between adherens junctions favor YAP1 phosphorylation and nuclear export. In addition to mechanical inputs and cellular polarity, different kinases, energy stress, and hormones can modulate the activity of the Hippo core kinases (grey area).

Nuclear YAP1 binds to various DNA-bound cofactors, such as RUNX2 or TEAD proteins[172]. DNA bound YAP1-TEAD complexed further interact with numerous neighboring transcription factors to induce programs involved in survival, proliferation and differentiation[188].

Remarkably, given the well-established role of YAP1 in growth control in other tissues[189], depletion of YAP1 is reported to have no[190-192] or only a mild[193] adverse phenotype during normal intestinal homeostasis. Although, YAP1 is expressed throughout the intestinal crypts[192]. However, conditional knock-out of the negative upstream regulators MST1 and MST2 results in expansion of undifferentiated cells and leads to aberrant crypt-villus morphology[194], indicating that under homeostasis, YAP1 is dispensable and kept inactive by active Hippo signaling. This stands in clear contrast to injury response, where YAP1 activity is essential to drive tissue regeneration[138,195,196]. For instance, during the regenerative phase following dextran sodium sulfate induced colitis (DSS), YAP1 is dramatically upregulated[192] and leads to transient cell reprogramming required for regeneration[196]. Similar, upon injury

induction by irradiation, YAP1 induces a regenerative program, which results in reprogramming of LGR5+ intestinal stem cells, suppresses extensive Paneth cell differentiation and promotes proliferation[193]. Furthermore, various injury types including irradiation, targeted ablation of LGR5+ cells, or treatment with DSS trigger a YAP1 driven expansion of 'revival stem cells' which aids regeneration[138].

In summary, the intestinal tissue keeps a tight balance between proliferating and non-proliferating cells with distinct lineages during homeostasis and exhibits an enormous plasticity following injury. Fundamental for the functionality of each individual cell is the spatial and temporal localization of the cell within the collectivity. How each individual cell within a tissue responds to a changing environment depends on multiple, temporal and spatial factors that can influence the cellular state and behavior (see also **Chapter 2**). Location in the crypt is linked to stemness[197] and cellular age and position along villus axis determines function and maturity of enterocytes[120] and enteroendocrine cells[198]. Complex interfaced signaling pathways and genetic networks underlie and control these cellular changes during homeostasis and allow tightly controlled responses to injuries. *Ex vivo,* small intestinal organoid cultures can recapitulate many of the observed processes *in vivo*. However, insights about how individual cells integrate information and adapt to changing demands are still sparse. The next section briefly summarizes how recent advances in imaging technologies combined with multivariate data analysis methods can be used to follow individual cells within a tissue. It will focus on imaging organoids.

Imaging to study self-organization

The concomitant development of high-throughput single cells sequencing and imaging technologies has brought new and extremely powerful methods to acquire multiplexed measurements of mRNAs and proteins (for an in-depth overview over existing methods see **Chapter 2**). Multiplexed single cell approaches allow profiling of individual cells within populations. Whereas the high throughput of single cell sequencing allows covering of the full transcriptome, imaging technologies give insights into the influence of the cellular context.

Multiplexed iterative immunofluorescence imaging (4i)

Immunofluorescence (IF) imaging allows analyzing fixed cells within their cellular context by preserving their spatial information at multiple scales ranging from the tissue architecture to subcellular protein distribution. However, classical IF approaches are limited by the number of proteins that can be acquired simultaneous. Spectral overlap of fluorophores limits routine acquisition to four colors and species cross talk of the antibodies often limits

flexibility of antibody combinations. Multiplexed iterative immunofluorescence imaging (4i), the multiplexing method adapted for three dimensional organoid cultures in this thesis, allows to overcome these limitations by applying iterative sequential cycles of immunofluorescence followed by antibody elution[65]. This allowed the profiling of 40 distinct proteins in hundreds of attaching cells[65]. An alternative sequential multiplexed immunofluorescence method called MxIF[199], has successfully been used to image thin intestinal tissue slices[200], but has not yet been shown to work for three-dimensional structures such as organoids.

The combination of multiplexed imaging and sequencing has revealed an enormous degree of cellular heterogeneity in cell populations[201,202]. Although important to study underlying biological processes, cellular heterogeneity poses a challenge for data interpretation. Within one snap-shop experiment, multiple distinct phenotypes are covered. These distinctions are lost by simple average statistics over the population. In parallel to technical progresses for data acquisition, advances in bioinformatics have allowed for better and more efficient extraction of biological insights from the plethora of data acquired with multiplexed technologies. Novel clustering algorithm facilitate the characterization and grouping of different phenotypes based on multivariate feature sets[152] and trajectory inference algorithms can reconstruct dynamic events based on static population snap-shop measurements[153].

Trajectory inference

Grouping of subtypes by clustering approaches can disentangle individual groups and identify rare cell types[135,203] . However, particularly in development, these phenotypes emerge through a continuous process starting from a common progenitor through cell maturation and differentiation. With clustering, these cellular dynamics are lost. Trajectory inference allows ordering of each cell along a pseudotime trajectory governed by molecular progression. This allows studying marker dynamics, identifies the cellular states at which fate decisions are made and allows following delineated cell developmental lineages[204]. Mostly such computational frameworks are used to analyze single cell sequencing or mass cytometry data[205] to reconstruct diverse biological processes including human B and T cell development[205,206], early blood development in mice[207], early zebrafish embryogenesis[208] or developmental and regenerative biology in whole flatworms[209]. In contrast to early linear trajectories[205,210], more recent methods allow inferring branching trajectories[206]. Applied to 30 channel mass cytometry data of T-cell development, Wishbone, the trajectory inference method used within this thesis, was shown to successfully recover bifurcations of CD4+ helper

T cells and CD8+ cytotoxic T cells from lymphoid progenitors. This allowed following transcription factor dynamics along the inferred branches with high resolution.

In addition to single cell sequencing and mass cytometry, two recent studies showed that trajectory inferences can be used on imaging datasets. In the first study, Gut et al., presented how trajectories of cell cycle progression can be inferred from fixed snap-shot samples of hundreds of adherent cells[58]. In the second one, Herring et al., demonstrated how multiplexed imaging of parafilm embedded tissue slices can be used to infer cellular progression of intestinal cells from the stem cell niche to the villus tip[200].

Aim of this thesis

As outlined under **Self-organization** (page **2**), self-organization is a central principle in biology. Although still in its infancy, organoids provide an unprecedented tool to study complex spatial cellular organization at the cellular and tissue level. Despite extensive research in the intestinal tissue and the promises organoids hold for stem cell research and translational medicine[79], little is known about the intrinsic capacity of single cells to self-organize under homogenous conditions. This can partly be attributed to the fact that most of the organoid field focuses more on developing novel organoid models instead of trying to understand the developmental mechanisms of the established ones[3] but also because imaging approaches probing cellular complexity at different temporal and spatial scales only recently have started to gain traction in three-dimensional cell culture systems[211].

During my PhD, I set out to use the favorable properties of the small intestinal organoid system, their ease to manipulate and ability to grow in high throughput amenable plate formats under simple and controlled growth conditions, to apply multiplexed imaging approaches and high-dimensional data analysis methods such as trajectory inferences. My aim was to describe organoid development and symmetry breaking quantitatively to gain insight into the underling processes. In a shared project, together with Andrea Boni, a former postdoc, and Denise Serra, a PhD student, in the Liberali lab, we focused on the following main open questions concerning the self-organizing properties of intestinal organoids:

(1) Do distinct starting cells go through a common intermediate state?

Research shows that LGR5+ intestinal stem cells and various LGR5- cells can generate intestinal organoids when supplemented with WNT3A. However, whether stem cells and non-stem cells follow the same developmental paths to form organoids is not clear. We therefore tested whether distinct starting populations have similar growth patterns and signaling characteristics and whether organoid development goes through a common intermediate state where symmetry is broken.

(2) Which signaling pathways and gene networks underlie intestinal organoid development?

Intestinal homeostasis and regeneration relies on a tight balance of multiple signaling pathways including Notch, Wnt, BMP and YAP1-dependent signaling. Here we investigated signaling pathways and genetic networks that initiate organoid developments from single cells. Further, we compared whether the program driving self-organization in intestinal organoids

resembles homeostasis, normal intestine embryonic development or if it is more a regenerative process.

(3) What drives symmetry breaking?

Paneth cell differentiation is the first and most crucial symmetry breaking event in organoid formation. Wnt and Notch signaling are important to define the secretory lineage during development and homeostasis of the small intestine. Here we tried to determine when symmetry breaks and describe how signaling pathways and genetic networks interact to spontaneously form Paneth cells under homogenous condition.

Chapter 2: Review article

Exploring single cells in space and time during tissue development, homeostasis and regeneration

Exploring single cells in space and time during tissue development, homeostasis and regeneration

Urs Mayr*, Denise Serra*, Prisca Liberali

Development. 2019 Jun 15;146(12):

* These authors contributed equally

Summary

Complex three-dimensional tissues emerge from local interaction of individual cells. To decipher how collective behaviors arise, one has to understand what governs cellular behavior in time and space across multiple scales. This review discusses how spatial as well as temporal cues change cellular states in development, homeostasis and regeneration and provides a broad overview on current technologies that probe single cells in a quantitative manner across these scales.

My contribution

Denise wrote the introduction, which summarizes temporal as well as spatial cues that act on each individual cell. I wrote the overview over current spatial as well as temporal methods and parts of the conclusion and perspectives.

The Company of **Biologists**

REVIEW

Exploring single cells in space and time during tissue development, homeostasis and regeneration

Urs Mayr[1,2,*], Denise Serra[1,2,*] and Prisca Liberali[1,2,‡]

ABSTRACT

Complex 3D tissues arise during development following tightly organized events in space and time. In particular, gene regulatory networks and local interactions between single cells lead to emergent properties at the tissue and organism levels. To understand the design principles of tissue organization, we need to characterize individual cells at given times, but we also need to consider the collective behavior of multiple cells across different spatial and temporal scales. In recent years, powerful single cell methods have been developed to characterize cells in tissues and to address the challenging questions of how different tissues are formed throughout development, maintained in homeostasis, and repaired after injury and disease. These approaches have led to a massive increase in data pertaining to both mRNA and protein abundances in single cells. As we review here, these new technologies, in combination with *in toto* live imaging, now allow us to bridge spatial and temporal information quantitatively at the single cell level and generate a mechanistic understanding of tissue development.

KEY WORDS: Gene regulatory networks, Local interactions, Single cell, Multiplexed imaging, Cell-to-cell variability

Introduction

The cell is the smallest structural and functional unit of living organisms (Schwann, 1839). During development, populations of cells interact and coordinate their behaviors in space and time to generate, bottom up, tissues and organs without a pre-defined blueprint (Bryant and Mostov, 2008; Gilmour et al., 2017; O'Brien et al., 2002). In particular, cells integrate complex intracellular and extracellular cues, both chemical and mechanical, and make individual decisions with respect to cell proliferation, differentiation or migration that, at the population level, lead to emergent processes such as tissue morphogenesis, homeostasis and regeneration (Bryant and Mostov, 2008; Chau et al., 2012; Sasai, 2013; Xavier da Silveira Dos Santos and Liberali, 2018). To achieve this, single cells have evolved different molecular and cellular mechanisms to sense neighboring cells and their local environment, and to regulate numerous biological features such as the cell cycle, cell shape, gene expression and polarization (Bryant and Mostov, 2008; Kim et al., 2018; Snijder and Pelkmans, 2011). It is thus essential, in order to dissect the complexity of coordinated events such as development and regeneration in health and disease, to measure the multivariate phenotypic and genetic states of single

cells and to also place each single cell in its environmental context at a specific moment in time. A number of recently developed technologies now allow us to probe cells in this detailed manner. In this Review, we explore these approaches, highlighting how single cell methods that provide spatial and temporal resolution can be used to analyze tissue organization quantitatively and to ask fundamental questions about development, regeneration and disease.

Cell state changes during development, homeostasis and regeneration: integrating signals in time and space

During development, single cells become specified and cell lineages develop, thereby allowing tissues consisting of multiple functional cell types to form. Cell lineages are often described as discrete populations of cells undergoing progressive differentiation steps: stem cells, progenitors, transient amplifying cells, and differentiated cells; however, this hierarchy is not always linear and irreversible (Clevers, 2015; Clevers and Watt, 2018; Sánchez Alvarado and Yamanaka, 2014). During regeneration, for example, this hierarchy can be reverted and single differentiated cells can reprogram, often acquiring embryonic pluripotent states that confer extensive plasticity on the system. It is therefore often difficult to distinguish cell type from cell state. Currently, a 'cell type' is frequently defined by static and abundant cell features, such as functional molecular markers and landmark genes, whereas a 'cell state' is explained by temporary traits (Wagner et al., 2016; see also Morris, 2019, in this issue). As we briefly summarize below, these 'cell state' traits are often regulated rhythmically by the cell cycle and circadian rhythm, and may be spatially induced by local signaling, nutrients, mechanics and microenvironments, giving rise to fractions of cells with different probabilities of differentiating. Even in environmentally controlled cell culture conditions, cell-to-cell variability in cellular states is observed and can be accurately predicted by considering the local population context and cell cycle phases (Altschuler and Wu, 2010; Battich et al., 2013; 2015; Frechin et al., 2015; Gut et al., 2015; Snijder et al., 2009, 2012; Spencer et al., 2009).

Spatial regulation of cell states

Spatial regulation of cellular states has been observed during developmental processes but also during homeostasis and regeneration (Chacón-Martínez et al., 2018; Nowotschin et al., 2019; Page et al., 2013; Ritsma et al., 2014). One example of how cell position can influence cell state comes from the adult intestinal epithelium. In this context, tissue homeostasis is controlled by the whole intestinal stem cell compartment, but each cell contributes to tissue self-renewal to a different extent depending on its location in the stem cell niche (Ritsma et al., 2014). This also highlights the presence of variability within apparently uniform populations (Vermeulen and Snippert, 2014). Moreover, it has also been shown that differentiating progenitors in the intestinal epithelium can revert to a proliferative state and repopulate the stem cell niche

[1]Department of Quantitative Biology, Friedrich Miescher Institute for Biomedical Research (FMI), Maulbeerstrasse 66, 4058 Basel, Switzerland. [2]University of Basel, Petersplatz 1, 4001 Basel, Switzerland.
*These authors contributed equally to this work

‡Author for correspondence (prisca.liberali@fmi.ch)

P.L., 0000-0003-0695-6081

DEVELOPMENT

1

following injury (Buczacki et al., 2013; Tetteh et al., 2016; Tian et al., 2011; van Es et al., 2012). This suggests that 'stemness' is a cell state that can be reached by progenitors or more mature cells in specific environments or under certain conditions. Notably, this feature characterizes several tissues that display regeneration and a high degree of plasticity, such as the epidermis and liver, lung, kidney, intestine and stomach epithelia (Donati and Watt, 2015; Evans et al., 2013; Michalopoulos, 2011; Michalopoulos et al., 2005; Qiao et al., 2007; Stange et al., 2013; Tata et al., 2013; Tetteh et al., 2015; Vogetseder et al., 2007; Yan et al., 2017; Yanger et al., 2013).

Some of the factors that control the spatial regulation of cell state have been identified. Indeed, it is known that the stem cell niche, which consists of extracellular matrix, stem cells and their progeny, creates an environment that induces and maintains stemness. For instance, Paneth cells in the crypts of the intestine produce and release Wnt, express the Notch ligand Dll1 on their cell surface, and produce lactate, which sustains the stemness of neighboring Lgr5-positive cells (Clevers, 2013; Pellegrinet et al., 2011; Rodríguez-Colman et al., 2017; Sato and Clevers, 2013; Sato et al., 2011). Cells moving away from this location lose stem-like properties and start to differentiate (Chacón-Martínez et al., 2018; Sato et al., 2011). Progenitor cells in hair follicles similarly influence stem cell state, positively regulating stem cell proliferation by paracrine Sonic hedgehog (Shh) signaling (Hsu et al., 2014). The newly generated cells then compete with progenitor cells for space in the niche, thus separating the inducing progenitor cells further from the stem cells. By contrast, stem cells exposed to reduced Shh stimulation by distant progenitor cells divide less frequently and shift to a less proliferative state. It is therefore becoming clear that cell state is not hard-wired per se but is determined by the coordination of intracellular and extracellular inputs from neighboring cells and the environment (Chacón-Martínez et al., 2018; Hsu et al., 2014).

Spatial stimuli are not only chemical but can also be mechanical, arising for instance from changes in tissue architecture. Indeed, crowding in the basal layer of the embryonic epidermis regulates the state of progenitor cells and, accordingly, tissue homeostasis. In this context, crowded cells show reduced cortical tension and increased cell-to-cell adhesion and, thereby, exhibit reduced contact with the substrate, leading to differentiation and delamination of the crowded cells from the basal layer (Miroshnikova et al., 2018). In the adult epidermis, the mechanism monitoring cell state and the balance between proliferation and differentiation changes such that differentiating and delaminating cells trigger compensatory cell divisions in neighboring cells and exit from the G1 phase of the cell cycle (Mesa et al., 2018). These findings again highlight that cells sense their environment and change state depending on neighboring cells and spatial constraints.

Mechanical inputs also play a role in defining the spatial context and organization of cells and highlighting when this organization is perturbed. For example, cells flanking a wound after tissue injury are exposed to altered substrate stiffness, which induces reprogramming to a transitory progenitor-like state that restores the homeostatic condition. This phenomenon has been extensively studied in the epidermis but is also observed in heart repair (Evans et al., 2013; Morikawa et al., 2015). Important factors in this process are the cellular mechanosensors YAP/TAZ, which are co-transcriptional activators able to transduce changes in the spatial environment of a cell into different gene regulatory programs and cell behaviors (Dupont et al., 2011; Panciera et al., 2017). During homeostasis, YAP/TAZ are found in proliferating cells of the stem cell niche of the intestine, epidermis, mammary gland, and airway epithelia and

maintain their cellular state. More importantly, their activity is necessary during tissue regeneration *in vivo* and organoid formation *in vitro* (Dupont et al., 2011; Elbediwy et al., 2016; Evans et al., 2013; Gjorevski et al., 2016; Gregorieff et al., 2015; Gregorieff and Wrana, 2017; Morikawa et al., 2015; Panciera et al., 2017, 2016; Patel et al., 2017; Schlegelmilch et al., 2011; Serra et al., 2019; Tan et al., 2017; Tremblay and Camargo, 2012; Xin et al., 2013; Yui et al., 2018; Zhao et al., 2014). In the context of intestinal organoid development, which mimics intestinal regeneration, Yap1 acts as a sensor of tissue integrity and its transient and heterogeneous activation is essential for the regulation of cellular states and the induction of symmetry breaking (Serra et al., 2019).

In conclusion, these findings highlight the importance of the environment and neighboring cells in defining cell state. Different environments increase the propensity of a cell to transition towards a specific state and this transition can further influence the states of adjacent cells and eventually of the whole cell population, creating a feedback loop oriented towards a dynamic equilibrium.

Temporal regulation of cell states

Time is also an important cue that influences the state of a cell. In this regard, modulation of the cell cycle and the circadian clock are well-known mechanisms that temporally control cell states. For example, in several systems it has been argued that cells in the G1 phase of the cell cycle have a higher propensity to differentiate (Calegari and Huttner, 2003; Coronado et al., 2013; Lange and Calegari, 2010; Lange et al., 2009). During G1, cells integrate information from their spatial context, signaling pathways, metabolic and stress stimuli, among others, and decide whether to divide or stop proliferating and differentiate. It has been suggested that the longer the G1 phase is, the more time cells are exposed to factors that can accumulate and induce a cell-state conversion once they reach a specific threshold (Calegari and Huttner, 2003).

The role of time in regulating cell state has also been explored in human embryonic stem cells (hESCs), revealing that hESCs differentiate towards endoderm or neuroectoderm depending on whether they are in early G1 or late G1, respectively (Pauklin and Vallier, 2013). This effect is mediated by the transcriptional activity of Nodal/Activin signaling, which is high in early G1 and prompts the expression of endoderm-specific genes; by contrast, this activity is inhibited in late G1, when the concentration of cyclin D proteins is high and prevents nuclear localization of the Nodal/Activin downstream effectors Smad2/3, leading to neuroectoderm differentiation (Pauklin and Vallier, 2013).

Cellular states are also affected by the oscillatory activity of the circadian clock machinery. The circadian clock is connected to the cell cycle and regulates proliferation in several mammalian tissues and organs, such as the bone marrow, brain, skin, and oral mucosa (Bjarnason et al., 2001; Dickmeis and Foulkes, 2011; Granda et al., 2005). For example, quiescent neural progenitors (qNPs) of the mouse adult hippocampus exhibit oscillating proliferation events that peak during the night. Indeed, the Per2 and Bmal1 (Arntl) components of the clock machinery set a permissive time-frame in which qNPs can enter the cell cycle and divide (Bouchard-Cannon et al., 2013). These findings suggest that cells rhythmically experience varying cell states, based on the circadian clock, that affect their probability of transitioning to a differentiated state.

In summary, it is clear that individual cells within a tissue or organ are subjected to multiple factors, both spatially and temporally, that can influence their state, their probability to differentiate and hence their behavior (Fig. 1), ultimately affecting their form and function. Therefore, a single cell approach that
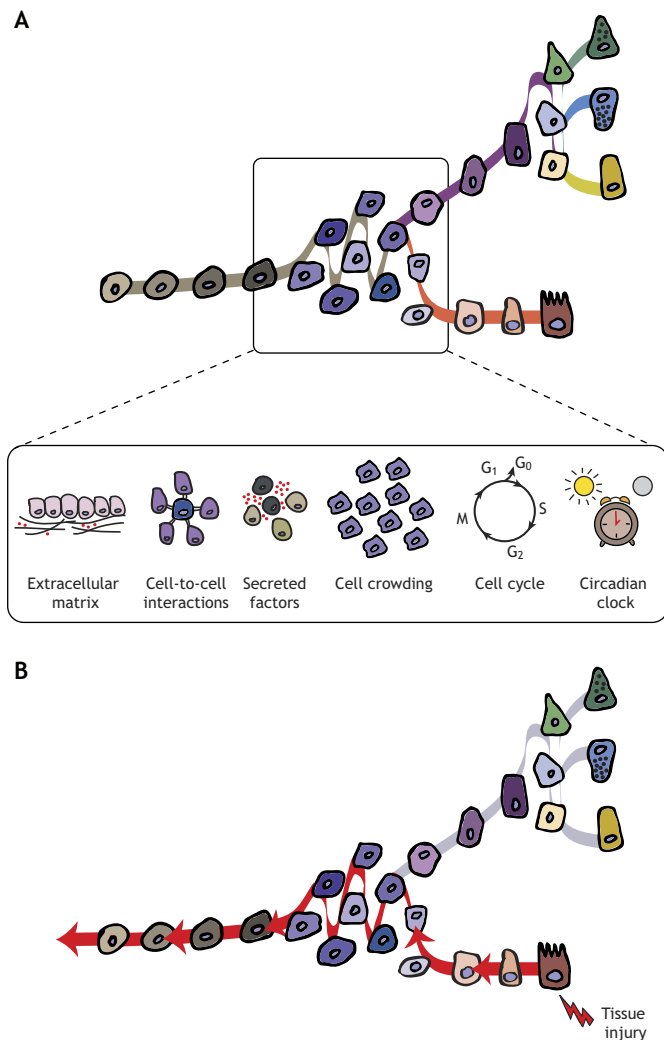
Fig. 1. Single cells in space and time. Single cells integrate multifactorial cues, both chemical and mechanical, to adapt their state in a timely manner and drive tissue morphogenesis, maintenance of homeostatic stem cell niches and repair of injured tissues. (A) Intestinal cells transition between diverse states and differentiate into distinct cell types, as visualized here on a pseudotime trajectory. Several factors can influence these cell states, especially at bifurcations and decision-making moments in the trajectory. These factors include the extracellular matrix, cell-to-cell interactions, secreted factors, cell crowding, the cell cycle and the circadian clock, among others. (B) After tissue injury, cells can revert their fate (indicated by red arrows), de-differentiate and adopt different cell states to re-establish tissue homeostasis.

(Hashimshony et al., 2016, 2012; Islam et al., 2014; Jaitin et al., 2014; Klein et al., 2015; Macosko et al., 2015; Picelli et al., 2013; Ramsköld et al., 2012; Rosenberg et al., 2018), allowing the quantification of cellular states as well as heterogeneity between individual cells (for recent reviews on the advantages and disadvantages of different methods, as well as the challenges of data analysis, see Papalexi and Satija, 2018; Stegle et al., 2015; and Tritschler et al., 2019, in this issue). Although accounting for complexity and noise in scRNAseq experiments remains an important technical hurdle (Tanay and Regev, 2017), we would argue that the major limitation of biological interpretation lies in the lack of spatial and temporal resolution provided by these techniques. Because these techniques require that tissues need to be first dissociated into single cells, the local microenvironment and social context of each cell is lost and, as we have highlighted above, it is this local context that is the key determinant of the cellular state and accounts for much of the observed heterogeneity between cells (Altschuler and Wu, 2010; Pelkmans, 2012; Snijder and Pelkmans, 2011). To understand the functional importance of cell-to-cell variability and to characterize processes that lead to cellular decision-making events, it is important to account for spatial information when analyzing single cell states. As we discuss below, this can be achieved either by mapping scRNAseq data onto spatial reference maps, or by directly visualizing transcriptomes and proteomes within intact cells, tissues and organs.

Mapping scRNAseq to spatial reference maps

An interesting approach to indirectly infer cell-to-cell interactions from scRNAseq data without explicit knowledge of spatial context is to map receptor expression in one cell to ligand expression in other cells (Camp et al., 2017; Kumar et al., 2018; Zepp et al., 2017). However, this only allows the identification of potential interactions and does not reveal whether pairs of cells are actually associated in space.

In parallel, different approaches have been developed to link single cell transcriptome information from scRNAseq data to the original spatial coordinates of the corresponding cell in its tissue context (Fig. 2A) (for reviews on single cell genomics expanding to spatial context, see Giladi and Amit, 2018; Lein et al., 2017; Moor and Itzkovitz, 2017; Tanay and Regev, 2017). This can be achieved by mapping cells computationally to known expression profiles of landmark genes (spatial reference maps) generated by *in situ* hybridization (Achim et al., 2015; Halpern et al., 2017; Satija et al., 2015). Such an approach has been applied successfully to study zebrafish embryos (with the aid of a computational approach called Seurat) (Satija et al., 2015), the brain of a marine annelid (Achim et al., 2015), *Drosophila* embryos (Karaiskos et al., 2017) and the mammalian liver (Halpern et al., 2017).

To allow mapping in the absence of pre-established landmark genes, scRNAseq has also been combined with laser capture microdissection (Moor et al., 2018). For example, analysis of the zonation of enterocytes along the villus axis of the small intestine has been performed by laser capture microdissection of equally spaced compartments of the villus to infer *de novo* landmark genes from bulk-RNAseq; the landmark genes were then used to map the positions of sequenced single cells onto the villus (Moor et al., 2018). Intriguingly, the extended heterogeneity measured between individual enterocytes could be explained by functional sub-specialization along the villi axis. Unfortunately, however, not all model systems are reproducible enough to show stereotypical spatial organization in order to assign landmark genes. This is often the case, for example, for *in vitro* organoid systems that show non-reproducible spatial variability (Huch et al., 2017).

considers these spatial and temporal localizations of a cell within a collectivity is important for understanding how tissue homeostasis is preserved and how development and regeneration are regulated. In the next section, we review recently developed single cell technologies that can provide us with such spatial and temporal resolution and discuss how their combination can bring us closer to an understanding of the key biological processes that govern development and regeneration.

Spatially resolved single cell methods

Current technologies that offer single cell resolution of transcriptomes and proteomes fall into two general categories: single cell RNA sequencing (scRNAseq) approaches and imaging-based approaches. Major progress in increasing the throughput and depth of scRNAseq has been achieved in recent years

3

A Mapping scRNAseq data

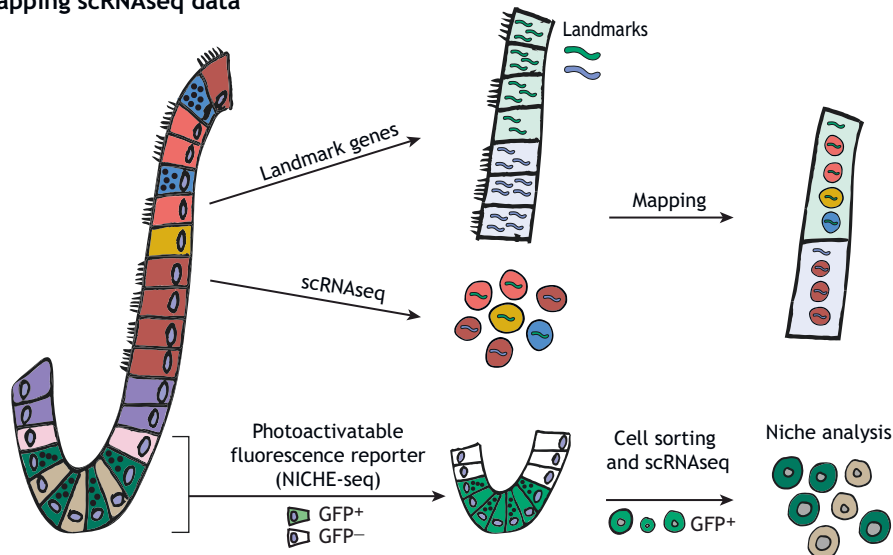## B Image-based transcriptome and proteome analysis

Fig. 2. Spatially resolved single cell methods. (A) Sequenced single cells (i.e. scRNAseq data) can be mapped to spatial coordinates within the tissue using known expression patterns of landmark genes. Landmark genes are often detected by *in situ* hybridization or can be identified by laser capture microdissection coupled to bulk sequencing. Alternatively, cells from a known and restricted spatial location can be analyzed with scRNAseq. In NICHE-seq, for example, cells within a precisely defined tissue location are fluorescently labeled and analyzed by scRNAseq. (B) Image-based methods allow the analysis of cells in their intact spatial context and microenvironment. Combining multiplexed read-outs with single cell segmentation allows the simultaneous quantification of protein and RNA expression together with information about localization, cell morphology and local environment (e.g. the number and identity of neighbors, local crowding, etc.).
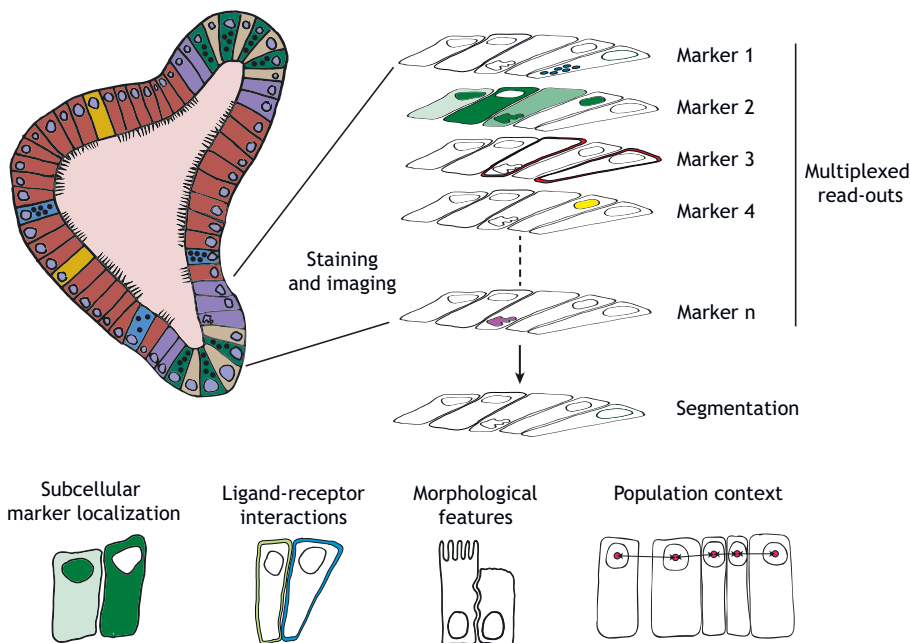
As an alternative to mapping cells to pre-established reference maps, an approach termed de novo spatial reconstruction (novoSpaRc) has been used to computationally infer positional information based on the underlying spatial organization of gene expression with or without knowledge about landmark genes (Nitzan et al., 2018). The scRNAseq-based analysis of cells in a known area of origin has also been used to preserve spatial information (Chen et al., 2017; Medaglia et al., 2017; Nichterwitz et al., 2016). For example, in an approach named NICHE-seq (Medaglia et al., 2017), cells expressing photoactivatable green fluorescent proteins were labeled within the lymph nodes and spleens of mice using two-photon microscopy; the subsequent analysis of labeled cells by scRNAseq allowed the characterization of T and B cell-specific niches after viral infection.

Although already very powerful, current methods for spatial mapping have their limitations. Landmark genes extracted from small regions of tissue [e.g. via laser capture microdissection or non-single cell fluorescence *in situ* hybridization (FISH)] are still relatively coarse, often representing an average of gene expression over a population of cells. At the moment, this prevents mapping with high spatial resolution to a single cell and does not allow the inference of direct cell-to-cell interactions. It will be interesting to see how reference maps with higher resolution, for example acquired with multiplexed single cell approaches, in combination with new computational frameworks (Nitzan et al., 2018) can be used to further alleviate this limitation. The power of mapping based on multiplexed landmark genes inferred from sequential single-molecule *in situ* hybridization data has recently been demonstrated by dissecting the contribution of cell type and spatial factors to variations in cell state within heterogeneous cellular populations (Zhu et al., 2018).

Image-based transcriptome and proteome analysis

As an alternative to relating scRNAseq-generated information to positional information, it is possible to use image-based approaches to analyze cells directly in their native context. Ideally, understanding how individual cells within the same spatial region communicate and interact requires the simultaneous assessment of cellular state, local environment, and cell-to-cell contacts (Fig. 2B). An intuitive approach to combined analysis of cell morphology, gene expression and protein localization is the fluorescence imaging of fixed samples combined with computer vision-based cell segmentation (Battich et al., 2015; Liberali et al., 2014; Snijder et al., 2009). This allows extraction of a large number of quantitative features describing multiple molecular factors and their subcellular localization, as well as providing information about cell morphology and population context. Single molecule *in situ* hybridization (smFISH) (Raj et al., 2008) and immunohistochemistry/immunofluorescence are widely used standard methods that allow the quantification of RNA and protein expression and localization with subcellular resolution, without destroying the local context of the cells. In a series of interesting publications, it has been demonstrated that the combined analysis of phenotypic states (as indicated by the cell cycle or marker expression) and the microenvironment (as indicated by local cell density) can predict cell-to-cell variability in mRNA or protein expression levels (Battich et al., 2015; Sero et al., 2015; Snijder et al., 2009).

Classically, these approaches allow the simultaneous quantification of only a small number of markers, because spectral overlap of the available fluorophores limits the number of simultaneously resolvable colors to between two and five. Various approaches have therefore been developed to increase the number of simultaneously resolvable colors. For example, the number was increased up to six using quantum dots (Han et al., 2001), up to seven with Fourier spectroscopy and singular value decomposition (Tsurui et al., 2000), up to nine using spectrally resolved fluorescence lifetime imaging microscopy (Niehorster et al., 2016), and even up to 32 by combining combinatorial labeling and super-resolution imaging (Lubeck and Cai, 2012). The downsides of these techniques, however, include the need for specialized and expensive equipment, a high sensitivity to signal-to-noise ratio (which can confound computational convolution), and limited scalability for higher throughput. As an alternative, methods using sequential read-out of colors have been developed for detecting multiple RNAs and proteins. As we move on to discuss below, these 'multiplexing' techniques have provided a marked increase in throughput using the standard color spectra of available fluorophores and therefore represent promising approaches.

Multiplexing transcriptomes
In situ sequencing

A very powerful approach, which is closely related to RNAseq of isolated cells, is *in situ* sequencing. In RNAseq, RNAs are extracted from the tissue for amplification and detection, whereas with *in situ* sequencing, enzymatic reactions are conducted directly within the original tissue (Ke et al., 2013; Lee et al., 2015, 2014) (for an overview of existing methods and limitations, see Crosetto et al., 2015; Lein et al., 2017; Moor and Itzkovitz, 2017). During this process, each of the four bases of DNA is encoded by one fluorescence color and bases of multiple target sequences are then read out sequentially, directly within the original tissue with subcellular resolution. For certain methods, such as fluorescence *in situ* sequencing (FISSEQ), this potentially allows scaling up to whole genome coverage with single-nucleotide resolution (Lee et al., 2014). However, implementation within complex cellular environments has so far proved difficult. This is especially true of

deep tissues in which auto-fluorescence masks fluorescently labeled molecules, and light scattering hampers reliable signal read-out, resulting in low efficiency and accuracy (Lein et al., 2017). In a recently developed method called spatially resolved transcript amplicon read-out mapping (STARmap; Wang et al., 2018b), Wang et al. combined hydrogel-tissue chemistry (Gradinaru et al., 2018) with *in situ* sequencing to facilitate sequencing of targeted sequences within intact 3D-tissues. In this approach, the cross-linking of selected intracellular biomolecules to a network of polymer allowed the preservation of three-dimensional tissue-structural relationships whilst also improving optical properties by clearing lipids and proteins. STARMap was shown to map up to 1000 genes in sections of the mouse brain at single cell resolution, revealing the spatial arrangement and self-clustering organization of different neuronal subtypes. As an alternative to reading out DNA bases directly within the tissue, spatial transcriptomics (Stahl et al., 2016) and Slide-seq (Rodrigues et al., 2019) involve transferring mRNAs from the tissue to either spatially barcoded oligonucleotides (Stahl et al., 2016) or DNA-barcoded microparticles (beads) encoding spatial information (Rodrigues et al., 2019). Sequencing is then performed outside of the tissue context and spatial information is reconstructed based on the spatial barcodes.

Multiplexed smFISH

Complementary to *in situ* sequencing, multiplexed smFISH methods have been established that allow quantification of the abundance of RNA molecules with high sensitivity and accuracy at subcellular resolution. Compared with normal smFISH, most multiplexed smFISH methods achieve a massive increase in throughput by applying multiple rounds of sequential hybridization and imaging. Similar to normal smFISH, these methods rely on detecting RNA molecules by hybridizing multiple fluorescent probes to transcripts in cells. This results in a single diffraction-limited fluorescence spot per transcript, which can then be resolved by conventional microscopy and accurately quantified. In seqFISH (Lubeck et al., 2014) (Fig. 3A), the identity of each targeted transcript is encoded as a unique color sequence (a barcode) that is sequentially read out over multiple rounds of imaging. However, because each color of each round needs to be identified correctly, and because images between subsequent rounds need to be aligned precisely to allow decoding of the transcript, this leads to the drawback that encoding becomes more prone to misidentification with increasing number of rounds. To overcome this, different error-correction schemes, such as Hamming distance-based error correction in MERFISH (Chen et al., 2015; Moffitt et al., 2016b) (Fig. 3A), have been introduced.

Similar to *in situ* sequencing, multiplexed smFISH is limited by factors such as auto-fluorescence and spatial crowding within cells, when transcripts are too close for simultaneous optical resolution. To overcome this, clearing (Moffitt et al., 2016a) and signal amplification (Choi et al., 2014; Shah et al., 2016a; Kishi et al., 2019) approaches have been developed. In HCR-seqFISH, for example, seqFISH is combined with single-molecule hybridization chain reaction (smHCR) to achieve signal amplification (Shah et al., 2016a); this approach was applied successfully to quantify single cell transcription profiles within the mouse hippocampus (Shah et al., 2016b). To increase the density of RNAs profiled, expansion microscopy (Chen et al., 2016a; Wang et al., 2018a) or a coding schema combining pseudocolors with barcoding (Eng et al., 2017) have been used. Indeed, using the latter method, the profiling of 10,421 nascent transcripts (Shah et al., 2018) as well as the imaging of RNAs for 10,000 genes in single cells has been demonstrated (Eng et al., 2019). As alternatives to sequential barcoding, other methods have used
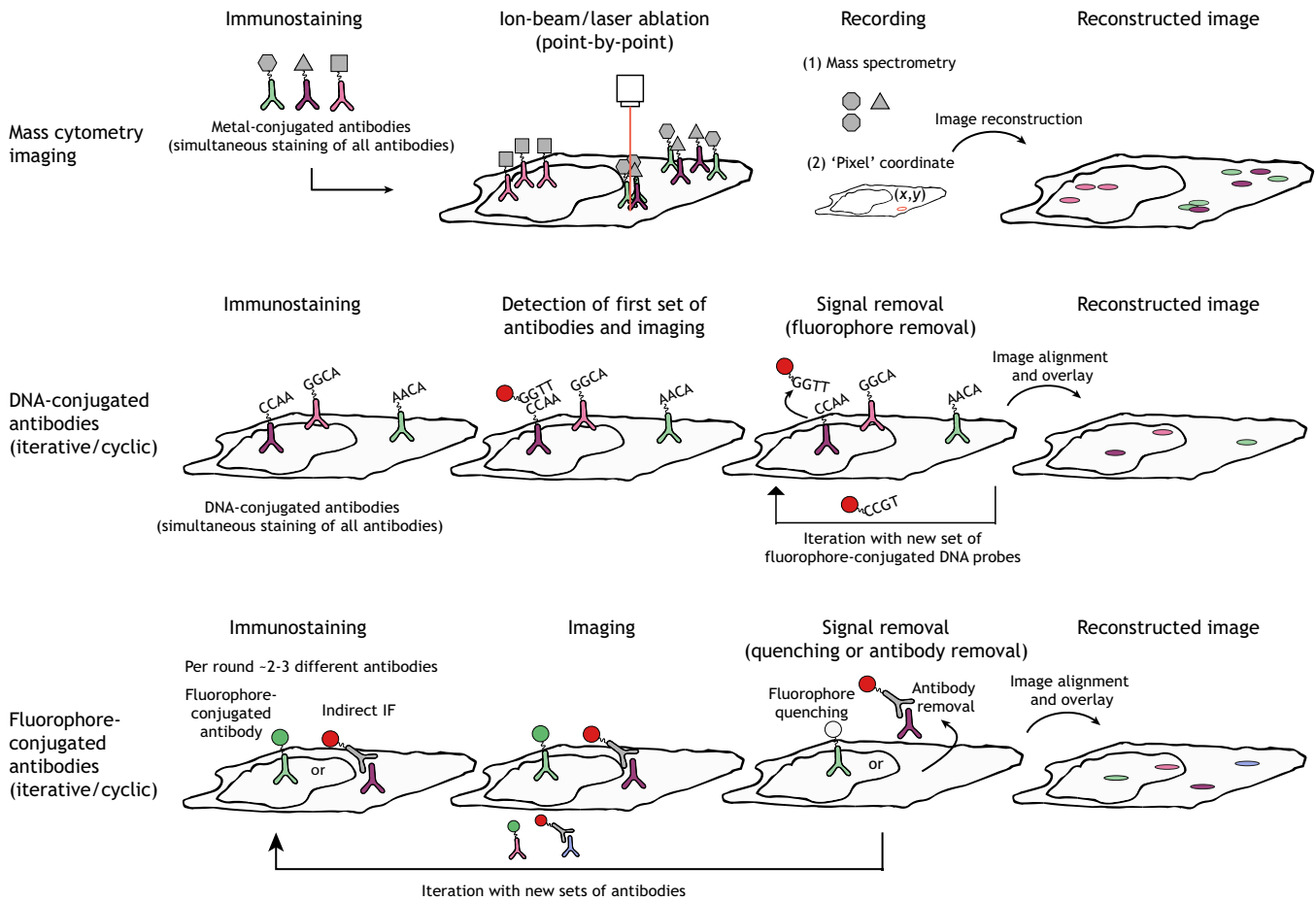
DEVELOPMENT

5
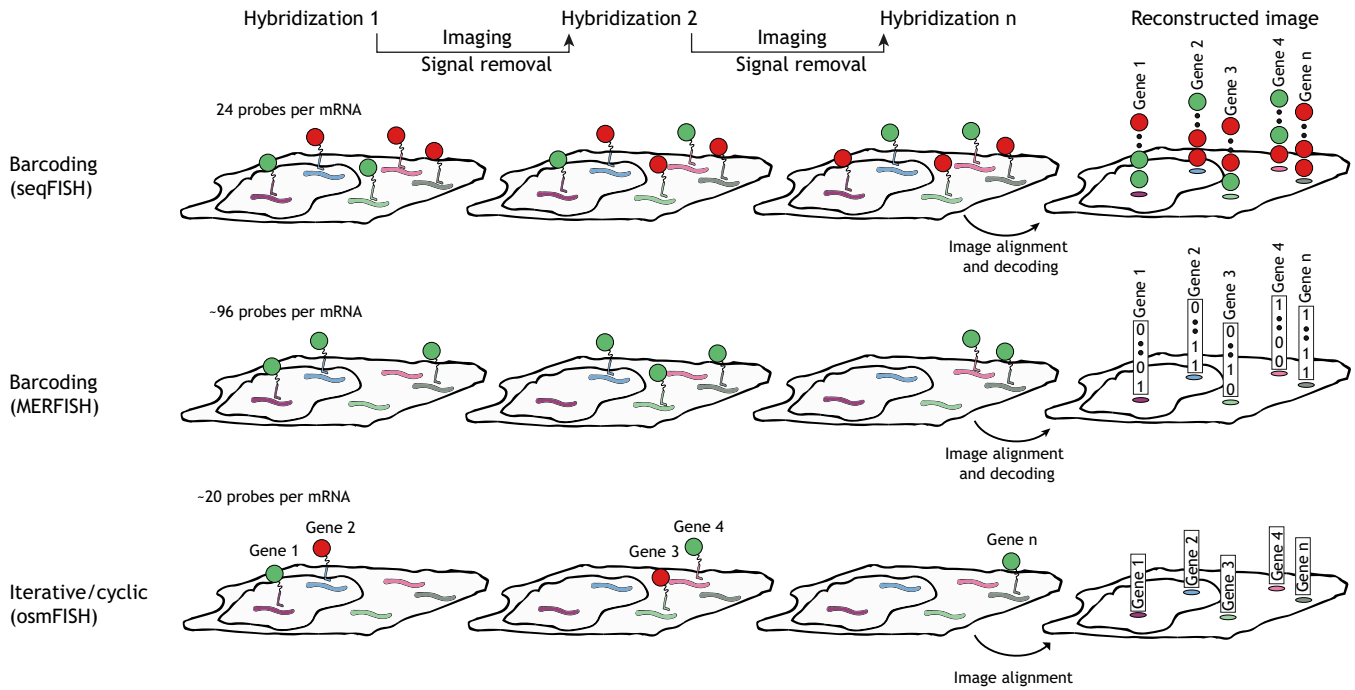
Fig. 3. See next page for legend.

Fig. 3. Schematics outlining multiplexed RNA and protein detection methods. (A) Multiplexing transcriptomes. In barcoding-based methods (e.g. seqFISH and MERFISH), RNA identity is encoded over sequential hybridization rounds. In seqFISH, RNA identity is barcoded as a color sequence. In MERFISH, RNA identity is barcoded as a binary string that allows error correction based on a modified Hamming code. In iterative/cycle multiplexing (e.g. osmFISH), RNA identity is distinguished by a unique color within each hybridization round. (B) Multiplexing proteomes. Mass cytometry imaging allows the labeling of all target proteins with heavy-metal-conjugated antibodies in one incubation step. Protein abundance is quantified by point-by-point ablation of the sample coupled to mass spectrometry. An image is reconstructed based on the ablation coordinates and mass data. In protein multiplexing with DNA-conjugated antibodies, all target proteins are labeled simultaneously and antibody identity is revealed by iterative exchange of fluorophore-conjugated DNA strands or with *in situ* incorporation of fluorophore-labeled nucleotides (not shown in the schematics). For fluorophore-conjugated antibodies, multiplexing is achieved by iterative rounds of staining, imaging and signal removal.

sequential hybridization whereby each RNA molecule is directly encoded by a unique color in each round, and multiplexing is achieved by multiple rounds of hybridization (Codeluppi et al., 2018; Kishi et al., 2019; Shah et al., 2016b) (Fig. 3A).

Multiplexing proteomes
Although the analysis of mRNA content and localization can provide significant insight, it alone is not sufficient to fully characterize cellular states and microenvironments, and therefore cellular decision making is, as most cellular functions are, ultimately, executed by proteins. Although mRNA often serves as a good estimator of protein abundance, the correlation may not always hold true (Edfors et al., 2016) and the ratio between mRNA and protein is itself dependent on the context of a cell (Popovic et al., 2018). Moreover, many signaling pathways involved in fate decisions or mechanosensing rely on direct protein interactions with membranes, or on the subcellular localization and post-transcriptional modifications of proteins. The same is true for many transcription factors involved in fate decisions, where nuclear or cytoplasmic localization often determines functionality. Thus, the detection and analysis of specific proteins within cells is key for understanding cell states. Compared with RNA detection in cells, however, multiplexed detection of proteins poses additional challenges. Protein detection relies on high-affinity reagents (most often antibodies), which, compared with nucleotide detection of RNAs, impairs flexibility of probe design (Baker, 2015). In addition, proteins, in contrast to RNA molecules, which are sparse, often occur in highly crowded intracellular environments and have dynamic ranges of molecule abundances several orders of magnitude higher than those of mRNA (Liu et al., 2016). Two general type of approaches have been used to achieve multiplexed detection of proteins within cells: mass cytometry imaging and multiplexed fluorescence imaging. As we highlight below, these methods now allow for a marked increase in throughput and predictability of cellular states.

Mass cytometry imaging
In mass cytometry imaging (Bodenmiller, 2016), antibodies are conjugated to heavy-metal isotopes and quantified by mass spectrometry (Fig. 3B). As these heavy-metal isotopes each have a unique atomic mass, mass spectrometry is used to discriminate isotopes with high accuracy and high multiplicity over a large dynamic range of molecule abundance. Two main mass cytometry imaging approaches exist, coupling either ion beam imaging [multiplexed ion beam imaging (MIBI); Angelo et al., 2014] or laser ablation [imaging mass cytometry (IMC); Giesen et al., 2014] to

mass cytometry. In contrast to regular mass cytometry (e.g. CyTof) (Spitzer and Nolan, 2016), in which suspension samples are analyzed, mass cytometry imaging involves point-by-point ablation of the sample out of its natural context. Computer reconstruction then allows the generation of images of protein expression, with spatial information, based on mass data. For instance, MIBI (Angelo et al., 2014) currently allows simultaneous measurement of the spatial expression of up to 36 proteins with subcellular resolution (Keren et al., 2018). Interestingly, using MIBI to study the tumor-immune microenvironment in triple-negative breast cancer patients, Keren et al. (2018) found that some cells from different lineages but with similar expression profiles tended to be enriched in spatial proximity. This suggests, again, that some phenotypic features of cells may be driven more by their microenvironment rather than being an intrinsic property of cell type. IMC allows the measurement of up to 32 proteins with a resolution of ∼1 μm (Giesen et al., 2014) and can be used for the simultaneous measurement of mRNA and protein levels (Schulz et al., 2018). Overall, these mass cytometry imaging techniques allow quantification of antibody abundance without the confounding factor of autofluorescence observed in fluorescence imaging and allow simultaneous staining of all antibodies in a single experimental step. However, the latter comes with the limitation that high-abundance antibodies may mask epitopes of low-abundance proteins. In addition, antibodies need to be labeled using costly and labor intense methods, and the technique generally involves low throughput by slow point-by-point scanning.

Multiplexed fluorescence imaging
Similar to multiplexed smFISH, various technologies have applied sequential fluorescence imaging to detect multiple proteins using standard fluorescence microscopy equipment. Promising methods, such as co-detection by indexing (CODEX) (Goltsev et al., 2018), DNA exchange imaging (DEI) (Wang et al., 2017) and Immuno-SABER (Saka et al., 2018 preprint), rely on DNA-barcoded antibodies (Fig. 3B). Similar to mass cytometry imaging, these methods involve a single round of immunostaining. The identity of each antibody is then revealed via sequential read-out of antibodies, either with *in situ* incorporation of fluorophore-dye-labeled nucleotides (CODEX) or by exchange of short fluorophore-conjugated DNA strands (for DEI and Immuno-SABER). Immuno-SABER also allows additional signal amplification steps.

Alternative methods, based on iterative antibody labeling, can increase the number of proteins that can be detected via the iteration of staining, signal removal, and re-staining with a new set of antibodies (Gerdes et al., 2013; Gut et al., 2018; Lin et al., 2015, 2018) (Fig. 3B). This allows direct use of a large palette of commercially available antibodies but has the disadvantage that many slow primary antibody incubation steps are required. These methods have had to overcome several previously encountered limitations such as incomplete antibody elution (Gendusa et al., 2014) or marked sample degradation due to harsh antibody elution protocols. Signal removal is usually achieved by chemical inactivation of fluorophore dyes (Gerdes et al., 2013; Lin et al., 2015, 2018) or by complete elution of primary and secondary antibodies (Gut et al., 2018). In CycIF (Lin et al., 2015, 2018), primary antibodies that are directly conjugated to fluorophore dyes are inactivated by hydrogen peroxide oxidation at high pH. This allows the quantification of up to 60 proteins (Lin et al., 2018) and has been demonstrated to work in high-throughput plate formats (Lin et al., 2015) as well as for formalin-fixed, paraffin-embedded (FFPE) samples (Lin et al., 2018). However, primary antibodies

that are already conjugated to the dye are often not commercially available or are dim. Using indirect immunofluorescence overcomes this limitation but has the drawback that primary antibodies produced in identical host species need to be removed after each imaging round (to avoid cross-labeling). In a variant of the CycIF protocol, this removal is achieved by enzymatically digesting the antibodies (Lin et al., 2015). An alternative indirect immunofluorescence approach, termed iterative indirect immunofluorescence imaging (4i) (Gut et al., 2018), has been optimized to work with standard unconjugated primary antibodies in combination with fluorophore dye-conjugated secondary antibodies. Building on previous antibody elution approaches (Pirici et al., 2009; Schubert et al., 2006; Toth and Mezey, 2007) and in particular by introducing an essential step to prevent photo-induced cross-linking of antibodies to the sample, this method allows efficient elution of primary and secondary antibodies. Indeed, by combining multiplexed imaging of more than 40 proteins in ~20,000 single cells with a data-driven computer vision approach, Gut et al. explored subcellular protein distributions in different cellular states (Gut et al., 2018). More recently, 4i multiplexing has been applied to study the 3D mouse intestinal organoid system. By combining multiplexed imaging time-course experiments with time-resolved scRNAseq data, the molecular mechanism underlying symmetry-breaking events during organoid development was characterized (Serra et al., 2019). This example demonstrates how the combination of single cell technologies with spatial and temporal resolution can quantitatively bridge single cell behavior to collective properties of a developing tissue.

Temporally resolved single cell methods
Another inherent component of biological systems is their dynamics. However, studying tissue dynamics in relation to single cells is a daunting task. Biological processes occur over timescales ranging from seconds to hours or even years. The challenge, therefore, is to plan appropriate time points for sampling at sufficient resolution to collect enough information to reconstruct the process under investigation. Currently, no single technology allows the plotting and capture of complex processes spanning several temporal and spatial scales with sufficient resolution in terms of time-point sampling and cellular state read-outs. However, the combination of multiple technologies is now paving the way for a more comprehensive –in terms of both time and space – understanding of tissue development.

It is clear that highly multiplexed spatially resolved single cell methods can provide snapshots of cell and microenvironment states with an unprecedented depth of information, allowing the study of spectrums of cell types and their spatial organization within tissues (Wang et al., 2018b). Such methods also allow correlation of cellular states and microenvironmental factors (Goltsev et al., 2018; Keren et al., 2018). Importantly, however, information about cell state transitions, the history of a cell, and how temporal events regulate cellular transitions is lost or hidden. Nonetheless, powerful computational inference frameworks have emerged that support the move from descriptive studies of cellular states to models of dynamic events (Bendall et al., 2014; Chen et al., 2016b; Guo et al., 2017; Haghverdi et al., 2016; Herring et al., 2018; Qiu et al., 2017; Setty et al., 2019; Setty et al., 2016; Shin et al., 2015; Trapnell et al., 2014; Weinreb et al., 2018; Wolf et al., 2019). These methods assume that single cells transit from one cellular state to another in a continuous fashion, and that all necessary cellular states for the process under investigation are sampled with sufficient depth, allowing the ordering of cells along a pseudotime trajectory of cellular progression. This process of 'trajectory inference' has been

applied successfully to various imaging (Gut et al., 2015; Herring et al., 2018; Serra et al., 2019), CyTof (Bendall et al., 2014; Setty et al., 2016) and sequencing (Chen et al., 2016b; Guo et al., 2017; Haghverdi et al., 2016; Qiu et al., 2017; Setty et al., 2019; Shin et al., 2015; Trapnell et al., 2014; Weinreb et al., 2018; Wolf et al., 2019) datasets. However, trajectory inference solely on cellular states has its limitations, as reviewed recently elsewhere (Kester and van Oudenaarden, 2018; Wagner et al., 2016; and, also in this issue, Tritschler et al., 2019).

As an alternative approach to studying cell state transitions, the clonal history of single cells (Alemany et al., 2018; Biddy et al., 2018; Frieda et al., 2017; Raj et al., 2018; Rodríguez-Fraticelli et al., 2018; Spanjaard et al., 2018; Wagner et al., 2018; Yao et al., 2017) or the history of dynamic molecular events (Frieda et al., 2017; Perli et al., 2016) can be recorded in the genome of each cell. Various methods allow cellular states and cellular history to be monitored simultaneously by using multiplexed end-point measurement. For example, Spanjaard et al. used CRISPR/Cas9-induced genetic scars to devise a genetic barcoding system that allows cell-lineage reconstruction based on recorded clonal history and cellular states extracted by scRNAseq (Spanjaard et al., 2018). In another approach, named MEMOIR (Frieda et al., 2017), barcoded recording elements called scratchpads are introduced into mouse ESCs and, by using CRISPR/Cas9-based targeted mutagenesis, the state of those scratchpads is altered in a stochastic fashion as cells proliferate, thus creating a heritable barcode. At an endpoint measurement, scratchpad states, cellular states and spatial information can then be read out by multiplexed smFISH. By using additional independent scratchpads targeted with orthogonal gRNAs expressed in response to specific signals, this system could, in principle, allow the storage of not only clonal history into the genome of each cell but also of dynamic and stimulus-triggered events.

As an alternative to storing events for later read-out, the combination of high temporal resolution time-lapse imaging (to record dynamic events in real time) with cellular endpoint measurements is a powerful tool to study biological processes on different scales. Recent studies have begun to exploit this possibility. Although live imaging may not always be possible because of physical inaccessibility or sample opaqueness, technological improvements in high-throughput confocal microscopy, and especially the introduction of light-sheet microscopy (Huisken et al., 2004; Reynaud et al., 2015), open up major possibilities for live imaging cell populations. Light-sheet microscopy combines high-speed acquisition with low phototoxicity and good optical sectioning at subcellular resolution. Tracking evolving biological processes over a long-term timescale (in days) and using high-speed recordings (seconds or minutes) can bridge different spatial and temporal scales (de Medeiros et al., 2016; Höckendorf et al., 2012). Indeed, light-sheet imaging has been applied to the study of calcium dynamics in plants (Costa et al., 2013), clathrin dynamics, organelle reorganization and cell migration in zebrafish (Liu et al., 2018), division dynamics in tumor spheroids (Lorenzo et al., 2011), mouse intestinal organoid development (Serra et al., 2019) and mouse embryo development, both from pre-implantation embryos (Strnad et al., 2016) and from gastrulation to organogenesis with single cell resolution (McDole et al., 2018). In combination with automated cell tracking, this method also opens up the intriguing possibility of constructing high-resolution fate maps for individual cells over the course of development (McDole et al., 2018; Strnad et al., 2016). However, high-resolution live-imaging data demands efficient ways to segment and visualize data, and major initiatives that tackle this challenge are under way. For example, the Allen Institute for Cell Science (Horwitz, 2016) is developing high-throughput

imaging approaches along with data visualization and integration tools to understand and predict cellular behavior (Chen et al., 2018 preprint; Ounkomol et al., 2018). Furthermore, although these imaging approaches can provide impressive insight into morphological changes, cell movements and cell divisions, the cellular-state read-outs for live imaging are limited to a maximum of six to seven colors (Cutrale et al., 2017; Valm et al., 2017). However, this limitation can be alleviated by combining live imaging with additional end-state measurements (Filipczyk et al., 2015; Hormoz et al., 2016; Takei et al., 2017). In a method called kin correlation analysis (KCA) (Hormoz et al., 2016), single cell tracking was combined with end-state measurements of three cell state markers measured by smFISH; this method was used to show that mouse ESCs traverse along a linear chain of metastable states in a stochastic and reversible fashion, in contrast with the prevailing view that ESC heterogeneity is mostly attributed to random noise. In a recent approach, Gehart et al. used a bi-fluorescent timer reporter to measure the time from the onset of enteroendocrine differentiation and combined it with end point scRNA-seq to build a time-resolved lineage tree of enteroendocrine differentiation in the small intestine (Gehart et al., 2019).

In addition to providing live dynamics for molecular markers, which can help unravel transitions between different cell states inferred from fixed samples, combining live imaging with inferred trajectories from multiplexed snapshots opens up a powerful opportunity to map events in pseudotime back to real time or vice versa. Pseudotime conveys stepwise progression of molecular markers along a trajectory. However, this may not necessarily represent dynamics in real time, which can make purposeful interpretation difficult. By simultaneously acquiring stereotypic features such as marker expression or morphological features from live-imaging and fixed samples, it is possible to infer the respective position of the observed state in both real time and pseudotime. This was recently demonstrated for intestinal organoids where a trajectory inferred from fixed imaging samples was mapped with growth dynamics extracted by light-sheet microscopy data (Serra et al., 2019).

Conclusions and perspectives
Thousands of RNAs and hundreds of proteins can now be quantified in single cells in their spatial context. Combined with powerful computational frameworks and live-imaging technologies, this now allows the mapping of cellular states and the inference of dynamic transitions between these states. Another important layer of information that will be essential to integrate with spatial information is the chromatin landscape (as reviewed in this issue by Ludwig and Bintu, 2019). Therefore, to understand how tissue organization and function emerges, we must continue to move forward from a view of single cells as isolated entities to one in which cellular functions are governed by the dynamic interactions between connected cells within a changing environment. The combination of multiscale spatial and temporal technologies is now enabling the quantitative morphological and molecular description of cells in their natural context and the study of their interactions over time. This will pave the way for fundamental discoveries in cell and developmental biology. For example, we will hopefully be able to obtain predictive models on how cell-to-cell variability emerges, and its functional implications in an evolving biological system. Moreover, these approaches will no doubt provide insights into how probabilistic and metastable cellular states transition to more stable cell fates and how these states are reversed during regeneration and diseases.

Combining datasets spanning multiple spatial and temporal scales will be a formidable task and will require new computational and experimental frameworks. Whereas in the past the limiting

number of biological read-outs often hampered interpretation of biological results or prevented study of the full complexity of the process, we now face the challenge of identifying and extracting meaningful conclusions from the plethora of data generated by new technologies. It will, therefore, be important to fit experimental design closely to the biological question of interest and to develop ways to quantitatively reduce data dimensionality and make data interpretation amiable. Moreover, computational frameworks will be required to efficiently handle, normalize, visualize and connect large datasets spanning different scales, with the ultimate aim of understanding decision making at single cell resolution and revealing the design principles of tissue organization during development, regeneration and disease.

References
Achim, K., Pettit, J. B., Saraiva, L. R., Gavriouchkina, D., Larsson, T., Arendt, D. and Marioni, J. C. (2015). High-throughput spatial mapping of single-cell RNA-seq data to tissue of origin. *Nat. Biotechnol.* **33**, 503-509. doi:10.1038/nbt.3209

Alemany, A., Florescu, M., Baron, C. S., Peterson-Maduro, J. and van Oudenaarden, A. (2018). Whole-organism clone tracing using single-cell sequencing. *Nature* **556**, 108-112. doi:10.1038/nature25969

Altschuler, S. J. and Wu, L. F. (2010). Cellular heterogeneity: do differences make a difference? *Cell* **141**, 559-563. doi:10.1016/j.cell.2010.04.033

Angelo, M., Bendall, S. C., Finck, R., Hale, M. B., Hitzman, C., Borowsky, A. D., Levenson, R. M., Lowe, J. B., Liu, S. D., Zhao, S. et al. (2014). Multiplexed ion beam imaging of human breast tumors. *Nat. Med.* **20**, 436-442. doi:10.1038/nm.3488

Baker, M. (2015). Reproducibility crisis: blame it on the antibodies. *Nature* **521**, 274-276. doi:10.1038/521274a

Battich, N., Stoeger, T. and Pelkmans, L. (2013). Image-based transcriptomics in thousands of single human cells at single-molecule resolution. *Nat. Methods* **10**, 1127-1133. doi:10.1038/nmeth.2657

Battich, N., Stoeger, T. and Pelkmans, L. (2015). Control of transcript variability in single mammalian cells. *Cell* **163**, 1596-1610. doi:10.1016/j.cell.2015.11.018

Bendall, S. C., Davis, K. L., Amir el, A. D., Tadmor, M. D., Simonds, E. F., Chen, T. J., Shenfeld, D. K., Nolan, G. P. and Pe'er, D. (2014). Single-cell trajectory detection uncovers progression and regulatory coordination in human B cell development. *Cell* **157**, 714-725. doi:10.1016/j.cell.2014.04.005

Biddy, B. A., Kong, W., Kamimoto, K., Guo, C., Waye, S. E., Sun, T. and Morris, S. A. (2018). Single-cell mapping of lineage and identity in direct reprogramming. *Nature* **564**, 219-224. doi:10.1038/s41586-018-0744-4

Bjarnason, G. A., Jordan, R. C., Wood, P. A., Li, Q., Lincoln, D. W., Sothern, R. B., Hrushesky, W. J. and Ben-David, Y. (2001). Circadian expression of clock genes in human oral mucosa and skin: association with specific cell-cycle phases. *Am. J. Pathol.* **158**, 1793-1801. doi:10.1016/S0002-9440(10)64135-1

Bodenmiller, B. (2016). Multiplexed epitope-based tissue imaging for discovery and healthcare applications. *Cell Syst.* **2**, 225-238. doi:10.1016/j.cels.2016.03.008

Bouchard-Cannon, P., Mendoza-Viveros, L., Yuen, A., Kaern, M. and Cheng, H. Y. (2013). The circadian molecular clock regulates adult hippocampal neurogenesis by controlling the timing of cell-cycle entry and exit. *Cell Rep.* **5**, 961-973. doi:10.1016/j.celrep.2013.10.037

Bryant, D. M. and Mostov, K. E. (2008). From cells to organs: building polarized tissue. *Nat. Rev. Mol. Cell Biol.* **9**, 887-901. doi:10.1038/nrm2523

Buczacki, S. J., Zecchini, H. I., Nicholson, A. M., Russell, R., Vermeulen, L., Kemp, R. and Winton, D. J. (2013). Intestinal label-retaining cells are secretory precursors expressing Lgr5. *Nature* **495**, 65-69. doi:10.1038/nature11965

Calegari, F. and Huttner, W. B. (2003). An inhibition of cyclin-dependent kinases that lengthens, but does not arrest, neuroepithelial cell cycle induces premature neurogenesis. *J. Cell Sci.* **116**, 4947-4955. doi:10.1242/jcs.00825

Camp, J. G., Sekine, K., Gerber, T., Loeffler-Wirth, H., Binder, H., Gac, M., Kanton, S., Kageyama, J., Damm, G., Seehofer, D. et al. (2017). Multilineage

communication regulates human liver bud development from pluripotency. *Nature* **546**, 533-538. doi:10.1038/nature22796

Chacón-Martínez, C. A., Koester, J. and Wickström, S. A. (2018). Signaling in the stem cell niche: regulating cell fate, function and plasticity. *Development* **145**. doi:10.1242/dev.165399

Chau, A. H., Walter, J. M., Gerardin, J., Tang, C. and Lim, W. A. (2012). Designing synthetic regulatory networks capable of self-organizing cell polarization. *Cell* **151**, 320-332. doi:10.1016/j.cell.2012.08.040

Chen, K. H., Boettiger, A. N., Moffitt, J. R., Wang, S. and Zhuang, X. (2015). RNA imaging. Spatially resolved, highly multiplexed RNA profiling in single cells. *Science* **348**, aaa6090. doi:10.1126/science.aaa6090

Chen, F., Wassie, A. T., Cote, A. J., Sinha, A., Alon, S., Asano, S., Daugharthy, E. R., Chang, J. B., Marblestone, A., Church, G. M. et al. (2016a). Nanoscale imaging of RNA with expansion microscopy. *Nat. Methods* **13**, 679-684. doi:10.1038/nmeth.3899

Chen, J., Schlitzer, A., Chakarov, S., Ginhoux, F. and Poidinger, M. (2016b). Mpath maps multi-branching single-cell trajectories revealing progenitor cell progression during development. *Nat. Commun.* **7**, 11988. doi:10.1038/ncomms11988

Chen, J., Suo, S., Tam, P. P. L., Han, J.-D. J., Peng, G. and Jing, N. (2017). Spatial transcriptomic analysis of cryosectioned tissue samples with Geo-seq. *Nat. Protoc.* **12**, 566-580. doi:10.1038/nprot.2017.003

Chen, J., Ding, L., Viana, M. P., Hendershott, M. C., Yang, R., Mueller, I. A. and Rafelski, S. M. (2018). The Allen Cell Structure Segmenter: a new open source toolkit for segmenting 3D intracellular structures in fluorescence microscopy images. *bioRxiv* 491035. doi:10.1101/491035

Choi, H. M., Beck, V. A. and Pierce, N. A. (2014). Next-generation in situ hybridization chain reaction: higher gain, lower cost, greater durability. *ACS Nano* **8**, 4284-4294. doi:10.1021/nn405717p

Clevers, H. (2013). The intestinal crypt, a prototype stem cell compartment. *Cell* **154**, 274-284. doi:10.1016/j.cell.2013.07.004

Clevers, H. (2015). STEM CELLS. What is an adult stem cell? *Science* **350**, 1319-1320. doi:10.1126/science.aad7016

Clevers, H. and Watt, F. M. (2018). Defining adult stem cells by function, not by phenotype. *Annu. Rev. Biochem.* **87**, 1015-1027. doi:10.1146/annurev-biochem-062917-012341

Codeluppi, S., Borm, L. E., Zeisel, A., La Manno, G., van Lunteren, J. A., Svensson, C. I. and Linnarsson, S. (2018). Spatial organization of the somatosensory cortex revealed by osmFISH. *Nat. Methods* **15**, 932-935. doi:10.1038/s41592-018-0175-z

Coronado, D., Godet, M., Bourillot, P. Y., Tapponnier, Y., Bernat, A., Petit, M., Afanassieff, M., Markossian, S., Malashicheva, A., Iacone, R. et al. (2013). A short G1 phase is an intrinsic determinant of naive embryonic stem cell pluripotency. *Stem Cell Res.* **10**, 118-131. doi:10.1016/j.scr.2012.10.004

Costa, A., Candeo, A., Fieramonti, L., Valentini, G. and Bassi, A. (2013). Calcium dynamics in root cells of Arabidopsis thaliana visualized with selective plane illumination microscopy. *PLoS ONE* **8**, e75646. doi:10.1371/journal.pone.0075646

Crosetto, N., Bienko, M. and van Oudenaarden, A. (2015). Spatially resolved transcriptomics and beyond. *Nat. Rev. Genet.* **16**, 57-66. doi:10.1038/nrg3832

Cutrale, F., Trivedi, V., Trinh, L. A., Chiu, C.-L., Choi, J. M., Artiga, M. S. and Fraser, S. E. (2017). Hyperspectral phasor analysis enables multiplexed 5D in vivo imaging. *Nat. Methods* **14**, 149-152. doi:10.1038/nmeth.4134

de Medeiros, G., Balázs, B. and Hufnagel, L. (2016). Light-sheet imaging of mammalian development. *Semin. Cell Dev. Biol.* **55**, 148-155. doi:10.1016/j.semcdb.2015.11.001

Dickmeis, T. and Foulkes, N. S. (2011). Glucocorticoids and circadian clock control of cell proliferation: at the interface between three dynamic systems. *Mol. Cell. Endocrinol.* **331**, 11-22. doi:10.1016/j.mce.2010.09.001

Donati, G. and Watt, F. M. (2015). Stem cell heterogeneity and plasticity in epithelia. *Cell Stem Cell* **16**, 465-476. doi:10.1016/j.stem.2015.04.014

Dupont, S., Morsut, L., Aragona, M., Enzo, E., Giulitti, S., Cordenonsi, M., Zanconato, F., Le Digabel, J., Forcato, M., Bicciato, S. et al. (2011). Role of YAP/TAZ in mechanotransduction. *Nature* **474**, 179-183. doi:10.1038/nature10137

Edfors, F., Danielsson, F., Hallström, B. M., Käll, L., Lundberg, E., Pontén, F., Forsström, B. and Uhlén, M. (2016). Gene-specific correlation of RNA and protein levels in human cells and tissues. *Mol. Syst. Biol.* **12**, 883. doi:10.15252/msb.20167144

Elbediwy, A., Vincent-Mistiaen, Z. I., Spencer-Dene, B., Stone, R. K., Boeing, S., Wculek, S. K., Cordero, J., Tan, E. H., Ridgway, R., Brunton, V. G. et al. (2016). Integrin signalling regulates YAP and TAZ to control skin homeostasis. *Development* **143**, 1674-1687. doi:10.1242/dev.133728

Eng, C. L., Shah, S., Thomassie, J. and Cai, L. (2017). Profiling the transcriptome with RNA SPOTs. *Nat. Methods* **14**, 1153-1155. doi:10.1038/nmeth.4500

Eng, C. L., Lawson, M., Zhu, Q., Dries, R., Koulena, N., Takei, Y., Yun, J., Cronin, C., Karp, C., Yuan, G. C. et al. (2019). Transcriptome-scale super-resolved imaging in tissues by RNA seqFISH. *Nature* **568**, 235-239. doi:10.1038/s41586-019-1049-y

Evans, N. D., Oreffo, R. O. C., Healy, E., Thurner, P. J. and Man, Y. H. (2013). Epithelial mechanobiology, skin wound healing, and the stem cell niche. *J. Mech. Behav. Biomed. Mater.* **28**, 397-409. doi:10.1016/j.jmbbm.2013.04.023

Filipczyk, A., Marr, C., Hastreiter, S., Feigelman, J., Schwarzfischer, M., Hoppe, P. S., Loeffler, D., Kokkaliaris, K. D., Endele, M., Schauberger, B. et al. (2015). Network plasticity of pluripotency transcription factors in embryonic stem cells. *Nat. Cell Biol.* **17**, 1235-1246. doi:10.1038/ncb3237

Frechin, M., Stoeger, T., Daetwyler, S., Gehin, C., Battich, N., Damm, E. M., Stergiou, L., Riezman, H. and Pelkmans, L. (2015). Cell-intrinsic adaptation of lipid composition to local crowding drives social behaviour. *Nature* **523**, 88-91. doi:10.1038/nature14429

Frieda, K. L., Linton, J. M., Hormoz, S., Choi, J., Chow, K. K., Singer, Z. S., Budde, M. W., Elowitz, M. B. and Cai, L. (2017). Synthetic recording and in situ readout of lineage information in single cells. *Nature* **541**, 107-111. doi:10.1038/nature20777

Gehart, H., van Es, J. H., Hamer, K., Beumer, J., Kretzschmar, K., Dekkers, J. F., Rios, A. and Clevers, H. (2019). Identification of enteroendocrine regulators by real-time single-cell differentiation mapping. *Cell* **176**, 1158-1173.e16. doi:10.1016/j.cell.2018.12.029

Gendusa, R., Scalia, C. R., Buscone, S. and Cattoretti, G. (2014). Elution of high-affinity (>10-9 KD) antibodies from tissue sections: clues to the molecular mechanism and use in sequential immunostaining. *J. Histochem. Cytochem.* **62**, 519-531. doi:10.1369/0022155414536732

Gerdes, M. J., Sevinsky, C. J., Sood, A., Adak, S., Bello, M. O., Bordwell, A., Can, A., Corwin, A., Dinn, S., Filkins, R. J. et al. (2013). Highly multiplexed single-cell analysis of formalin-fixed, paraffin-embedded cancer tissue. *Proc. Natl. Acad. Sci. USA* **110**, 11982-11987. doi:10.1073/pnas.1300136110

Giesen, C., Wang, H. A., Schapiro, D., Zivanovic, N., Jacobs, A., Hattendorf, B., Schuffler, P. J., Grolimund, D., Buhmann, J. M., Brandt, S. et al. (2014). Highly multiplexed imaging of tumor tissues with subcellular resolution by mass cytometry. *Nat. Methods* **11**, 417-422. doi:10.1038/nmeth.2869

Giladi, A. and Amit, I. (2018). Single-cell genomics: a stepping stone for future immunology discoveries. *Cell* **172**, 14-21. doi:10.1016/j.cell.2017.11.011

Gilmour, D., Rembold, M. and Leptin, M. (2017). From morphogen to morphogenesis and back. *Nature* **541**, 311-320. doi:10.1038/nature21348

Gjorevski, N., Sachs, N., Manfrin, A., Giger, S., Bragina, M. E., Ordóñez-Morán, P., Clevers, H. and Lutolf, M. P. (2016). Designer matrices for intestinal stem cell and organoid culture. *Nature* **539**, 560-564. doi:10.1038/nature20168

Goltsev, Y., Samusik, N., Kennedy-Darling, J., Bhate, S., Hale, M., Vazquez, G., Black, S. and Nolan, G. P. (2018). Deep profiling of mouse splenic architecture with CODEX multiplexed imaging. *Cell* **174**, 968-981.e915. doi:10.1016/j.cell.2018.07.010

Gradinaru, V., Treweek, J., Overton, K. and Deisseroth, K. (2018). Hydrogel-tissue chemistry: principles and applications. *Annu. Rev. Biophys.* **47**, 355-376. doi:10.1146/annurev-biophys-070317-032905

Granda, T. G., Liu, X. H., Smaaland, R., Cermakian, N., Filipski, E., Sassone-Corsi, P. and Lévi, F. (2005). Circadian regulation of cell cycle and apoptosis proteins in mouse bone marrow and tumor. *FASEB J.* **19**, 304-306. doi:10.1096/fj.04-2665fje

Gregorieff, A., Liu, Y., Inanlou, M. R., Khomchuk, Y. and Wrana, J. L. (2015). Yap-dependent reprogramming of Lgr5(+) stem cells drives intestinal regeneration and cancer. *Nature* **526**, 715-718. doi:10.1038/nature15382

Gregorieff, A. and Wrana, J. L. (2017). Hippo signalling in intestinal regeneration and cancer. *Curr. Opin. Cell Biol.* **48**, 17-25. doi:10.1016/j.ceb.2017.04.005

Guo, M., Bao, E. L., Wagner, M., Whitsett, J. A. and Xu, Y. (2017). SLICE: determining cell differentiation and lineage based on single cell entropy. *Nucleic Acids Res.* **45**, e54. doi:10.1093/nar/gkw1061

Gut, G., Tadmor, M. D., Pe'er, D., Pelkmans, L. and Liberali, P. (2015). Trajectories of cell-cycle progression from fixed cell populations. *Nat. Methods* **12**, 951-954. doi:10.1038/nmeth.3545

Gut, G., Herrmann, M. D. and Pelkmans, L. (2018). Multiplexed protein maps link subcellular organization to cellular states. *Science* **361**, eaar7042. doi:10.1126/science.aar7042

Haghverdi, L., Buttner, M., Wolf, F. A., Buettner, F. and Theis, F. J. (2016). Diffusion pseudotime robustly reconstructs lineage branching. *Nat. Methods* **13**, 845-848. doi:10.1038/nmeth.3971

Halpern, K. B., Shenhav, R., Matcovitch-Natan, O., Toth, B., Lemze, D., Golan, M., Massasa, E. E., Baydatch, S., Landen, S., Moor, A. E. et al. (2017). Single-cell spatial reconstruction reveals global division of labour in the mammalian liver. *Nature* **542**, 352-356. doi:10.1038/nature21065

Han, M., Gao, X., Su, J. Z. and Nie, S. (2001). Quantum-dot-tagged microbeads for multiplexed optical coding of biomolecules. *Nat. Biotechnol.* **19**, 631-635. doi:10.1038/90228

Harris, H. (2000). *The Birth of the Cell.* Yale University Press.

Hashimshony, T., Wagner, F., Sher, N. and Yanai, I. (2012). CEL-Seq: single-cell RNA-Seq by multiplexed linear amplification. *Cell Rep.* **2**, 666-673. doi:10.1016/j.celrep.2012.08.003

Hashimshony, T., Senderovich, N., Avital, G., Klochendler, A., de Leeuw, Y., Anavy, L., Gennert, D., Li, S., Livak, K. J., Rozenblatt-Rosen, O. et al. (2016). CEL-Seq2: sensitive highly-multiplexed single-cell RNA-Seq. *Genome Biol.* **17**, 77. doi:10.1186/s13059-016-0938-8

Herring, C. A., Banerjee, A., McKinley, E. T., Simmons, A. J., Ping, J., Roland, J. T., Franklin, J. L., Liu, Q., Gerdes, M. J., Coffey, R. J. et al. (2018).

Unsupervised trajectory analysis of single-cell RNA-Seq and imaging data reveals alternative tuft cell origins in the gut. *Cell Syst.* **6**, 37-51.e39. doi:10.1016/j.cels.2017.10.012

Höckendorf, B., Thumberger, T. and Wittbrodt, J. (2012). Quantitative analysis of embryogenesis: a perspective for light sheet microscopy. *Dev. Cell* **23**, 1111-1120. doi:10.1016/j.devcel.2012.10.008

Hormoz, S., Singer, Z. S., Linton, J. M., Antebi, Y. E., Shraiman, B. I. and Elowitz, M. B. (2016). Inferring cell-state transition dynamics from lineage trees and endpoint single-cell measurements. *Cell Syst* **3**, 419-433.e418. doi:10.1016/j.cels.2016.10.015

Horwitz, R. (2016). Integrated, multi-scale, spatial-temporal cell biology–A next step in the post genomic era. *Methods* **96**, 3-5. doi:10.1016/j.ymeth.2015.09.007

Hsu, Y.-C., Li, L. and Fuchs, E. (2014). Transit-amplifying cells orchestrate stem cell activity and tissue regeneration. *Cell* **157**, 935-949. doi:10.1016/j.cell.2014.02.057

Huch, M., Knoblich, J. A., Lutolf, M. P. and Martinez-Arias, A. (2017). The hope and the hype of organoid research. *Development* **144**, 938-941. doi:10.1242/dev.150201

Huisken, J., Swoger, J., Del Bene, F., Wittbrodt, J. and Stelzer, E. H. (2004). Optical sectioning deep inside live embryos by selective plane illumination microscopy. *Science* **305**, 1007-1009. doi:10.1126/science.1100035

Islam, S., Zeisel, A., Joost, S., La Manno, G., Zajac, P., Kasper, M., Lonnerberg, P. and Linnarsson, S. (2014). Quantitative single-cell RNA-seq with unique molecular identifiers. *Nat. Methods* **11**, 163-166. doi:10.1038/nmeth.2772

Jaitin, D. A., Kenigsberg, E., Keren-Shaul, H., Elefant, N., Paul, F., Zaretsky, I., Mildner, A., Cohen, N., Jung, S., Tanay, A. et al. (2014). Massively parallel single-cell RNA-seq for marker-free decomposition of tissues into cell types. *Science* **343**, 776-779. doi:10.1126/science.1247651

Karaiskos, N., Wahle, P., Alles, J., Boltengagen, A., Ayoub, S., Kipar, C., Kocks, C., Rajewsky, N. and Zinzen, R. P. (2017). The Drosophila embryo at single-cell transcriptome resolution. *Science* **358**, 194-199. doi:10.1126/science.aan3235

Ke, R., Mignardi, M., Pacureanu, A., Svedlund, J., Botling, J., Wahlby, C. and Nilsson, M. (2013). In situ sequencing for RNA analysis in preserved tissue and cells. *Nat. Methods* **10**, 857-860. doi:10.1038/nmeth.2563

Keren, L., Bosse, M., Marquez, D., Angoshtari, R., Jain, S., Varma, S., Yang, S. R., Kurian, A., Van Valen, D., West, R. et al. (2018). A structured tumor-immune microenvironment in triple negative breast cancer revealed by multiplexed ion beam imaging. *Cell* **174**, 1373-1387.e1319. doi:10.1016/j.cell.2018.08.039

Kester, L. and van Oudenaarden, A. (2018). Single-cell transcriptomics meets lineage tracing. *Cell Stem Cell* **23**, 166-179. doi:10.1016/j.stem.2018.04.014

Kim, E. J. Y., Korotkevich, E. and Hiiragi, T. (2018). Coordination of cell polarity, mechanics and fate in tissue self-organization. *Trends Cell Biol.* **28**, 541-550. doi:10.1016/j.tcb.2018.02.008

Kishi, J. Y., Lapan, S. W., Beliveau, B. J., West, E. R., Zhu, A., Sasaki, H. M., Saka, S. K., Wang, Y., Cepko, C. L. and Yin, P. (2019). SABER amplifies FISH: enhanced multiplexed imaging of RNA and DNA in cells and tissues. *Nat. Methods* **16**, 533-544. doi:10.1038/s41592-019-0404-0

Klein, A. M., Mazutis, L., Akartuna, I., Tallapragada, N., Veres, A., Li, V., Peshkin, L., Weitz, D. A. and Kirschner, M. W. (2015). Droplet barcoding for single-cell transcriptomics applied to embryonic stem cells. *Cell* **161**, 1187-1201. doi:10.1016/j.cell.2015.04.044

Kumar, M. P., Du, J., Lagoudas, G., Jiao, Y., Sawyer, A., Drummond, D. C., Lauffenburger, D. A. and Raue, A. (2018). Analysis of single-cell RNA-Seq identifies cell-cell communication associated with tumor characteristics. *Cell Rep.* **25**, 1458-1468.e1454. doi:10.1016/j.celrep.2018.10.047

Lan, H. Y., Mu, W., Nikolic-Paterson, D. J. and Atkins, R. C. (1995). A novel, simple, reliable, and sensitive method for multiple immunoenzyme staining: use of microwave oven heating to block antibody crossreactivity and retrieve antigens. *J. Histochem. Cytochem.* **43**, 97-102. doi:10.1177/43.1.7822770

Lange, C. and Calegari, F. (2010). Cdks and cyclins link G1 length and differentiation of embryonic, neural and hematopoietic stem cells. *Cell Cycle* **9**, 1893-1900. doi:10.4161/cc.9.10.11598

Lange, C., Huttner, W. B. and Calegari, F. (2009). Cdk4/cyclinD1 overexpression in neural stem cells shortens G1, delays neurogenesis, and promotes the generation and expansion of basal progenitors. *Cell Stem Cell* **5**, 320-331. doi:10.1016/j.stem.2009.05.026

Lee, J. H., Daugharthy, E. R., Scheiman, J., Kalhor, R., Yang, J. L., Ferrante, T. C., Terry, R., Jeanty, S. S., Li, C., Amamoto, R. et al. (2014). Highly multiplexed subcellular RNA sequencing in situ. *Science* **343**, 1360-1363. doi:10.1126/science.1250212

Lee, J. H., Daugharthy, E. R., Scheiman, J., Kalhor, R., Ferrante, T. C., Terry, R., Turczyk, B. M., Yang, J. L., Lee, H. S., Aach, J. et al. (2015). Fluorescent in situ sequencing (FISSEQ) of RNA for gene expression profiling in intact cells and tissues. *Nat. Protoc.* **10**, 442-458. doi:10.1038/nprot.2014.191

Lein, E., Borm, L. E. and Linnarsson, S. (2017). The promise of spatial transcriptomics for neuroscience in the era of molecular cell typing. *Science* **358**, 64-69. doi:10.1126/science.aan6827

Liberali, P., Snijder, B. and Pelkmans, L. (2014). A hierarchical map of regulatory genetic interactions in membrane trafficking. *Cell* **157**, 1473-1487. doi:10.1016/j.cell.2014.04.029

Lin, J. R., Fallahi-Sichani, M. and Sorger, P. K. (2015). Highly multiplexed imaging of single cells using a high-throughput cyclic immunofluorescence method. *Nat. Commun.* **6**, 8390. doi:10.1038/ncomms9390

Lin, J. R., Izar, B., Wang, S., Yapp, C., Mei, S., Shah, P. M., Santagata, S. and Sorger, P. K. (2018). Highly multiplexed immunofluorescence imaging of human tissues and tumors using t-CyCIF and conventional optical microscopes. *Elife* **7**, e31657. doi:10.7554/eLife.31657

Liu, Y., Beyer, A. and Aebersold, R. (2016). On the dependency of cellular protein levels on mRNA abundance. *Cell* **165**, 535-550. doi:10.1016/j.cell.2016.03.014

Liu, T. L., Upadhyayula, S., Milkie, D. E., Singh, V., Wang, K., Swinburne, I. A., Mosaliganti, K. R., Collins, Z. M., Hiscock, T. W., Shea, J., (2018). Observing the cell in its native state: imaging subcellular dynamics in multicellular organisms. *Science* **360**, eaaq1392. doi: 10.1126/science.aaq1392

Lorenzo, C., Frongia, C., Jorand, R., Fehrenbach, J., Weiss, P., Maandhui, A., Gay, G., Ducommun, B. and Lobjois, V. (2011). Live cell division dynamics monitoring in 3D large spheroid tumor models using light sheet microscopy. *Cell Div.* **6**, 22. doi:10.1186/1747-1028-6-22

Lubeck, E. and Cai, L. (2012). Single-cell systems biology by super-resolution imaging and combinatorial labeling. *Nat. Methods* **9**, 743-748. doi:10.1038/nmeth.2069

Lubeck, E., Coskun, A. F., Zhiyentayev, T., Ahmad, M. and Cai, L. (2014). Single-cell in situ RNA profiling by sequential hybridization. *Nat. Methods* **11**, 360-361. doi:10.1038/nmeth.2892

Ludwig, C. H. and Bintu, L. (2019). Mapping chromatin modifications at the single cell level. *Development* **146**, dev170217. doi:10.1242/dev.170217

Macosko, E. Z., Basu, A., Satija, R., Nemesh, J., Shekhar, K., Goldman, M., Tirosh, I., Bialas, A. R., Kamitaki, N., Martersteck, E. M. et al. (2015). Highly parallel genome-wide expression profiling of individual cells using nanoliter Droplets. *Cell* **161**, 1202-1214. doi:10.1016/j.cell.2015.05.002

McDole, K., Guignard, L., Amat, F., Berger, A., Malandain, G., Royer, L. A., Turaga, S. C., Branson, K. and Keller, P. J. (2018). In toto imaging and reconstruction of post-implantation mouse development at the single-cell level. *Cell* **175**, 859-876.e833. doi:10.1016/j.cell.2018.09.031

Medaglia, C., Giladi, A., Stoler-Barak, L., De Giovanni, M., Salame, T. M., Biram, A., David, E., Li, H., Iannacone, M., Shulman, Z. et al. (2017). Spatial reconstruction of immune niches by combining photoactivatable reporters and scRNA-seq. *Science* **358**, 1622-1626. doi:10.1126/science.aao4277

Mesa, K. R., Kawaguchi, K., Cockburn, K., Gonzalez, D., Boucher, J., Xin, T., Klein, A. M. and Greco, V. (2018). Homeostatic epidermal stem cell self-renewal is driven by local differentiation. *Cell Stem Cell* **23**, 677-686.e674. doi:10.1016/j.stem.2018.09.005

Michalopoulos, G. K. (2011). Liver regeneration: alternative epithelial pathways. *Int. J. Biochem. Cell Biol.* **43**, 173-179. doi:10.1016/j.biocel.2009.09.014

Michalopoulos, G. K., Barua, L. and Bowen, W. C. (2005). Transdifferentiation of rat hepatocytes into biliary cells after bile duct ligation and toxic biliary injury. *Hepatology* **41**, 535-544. doi:10.1002/hep.20600

Miroshnikova, Y. A., Le, H. Q., Schneider, D., Thalheim, T., Rubsam, M., Bremicker, N., Polleux, J., Kamprad, N., Tarantola, M., Wang, I. et al. (2018). Adhesion forces and cortical tension couple cell proliferation and differentiation to drive epidermal stratification. *Nat. Cell Biol.* **20**, 69-80. doi:10.1038/s41556-017-0005-z

Moffitt, J. R., Hao, J., Bambah-Mukku, D., Lu, T., Dulac, C. and Zhuang, X. (2016a). High-performance multiplexed fluorescence in situ hybridization in culture and tissue with matrix imprinting and clearing. *Proc. Natl. Acad. Sci. USA* **113**, 14456-14461. doi:10.1073/pnas.1617699113

Moffitt, J. R., Hao, J., Wang, G., Chen, K. H., Babcock, H. P. and Zhuang, X. (2016b). High-throughput single-cell gene-expression profiling with multiplexed error-robust fluorescence in situ hybridization. *Proc. Natl. Acad. Sci. USA* **113**, 11046-11051. doi:10.1073/pnas.1612826113

Moor, A. E. and Itzkovitz, S. (2017). Spatial transcriptomics: paving the way for tissue-level systems biology. *Curr. Opin. Biotechnol.* **46**, 126-133. doi:10.1016/j.copbio.2017.02.004

Moor, A. E., Harnik, Y., Ben-Moshe, S., Massasa, E. E., Rozenberg, M., Eilam, R., Bahar Halpern, K. and Itzkovitz, S. (2018). Spatial reconstruction of single enterocytes uncovers broad zonation along the intestinal villus axis. *Cell* **175**, 1156-1167.e1115. doi:10.1016/j.cell.2018.08.063

Morikawa, Y., Zhang, M., Heallen, T., Leach, J., Tao, G., Xiao, Y., Bai, Y., Li, W., Willerson, J. T. and Martin, J. F. (2015). Actin cytoskeletal remodeling with protrusion formation is essential for heart regeneration in Hippo-deficient mice. *Sci. Signal.* **8**, ra41. doi:10.1126/scisignal.2005781

Morris, S. A. (2019). The evolving concept of cell identity in the single cell era. *Development* **146**, dev169748. doi:10.1242/dev.169748

Nichterwitz, S., Chen, G., Aguila Benitez, J., Yilmaz, M., Storvall, H., Cao, M., Sandberg, R., Deng, Q. and Hedlund, E. (2016). Laser capture microscopy coupled with Smart-seq2 for precise spatial transcriptomic profiling. *Nat. Commun.* **7**, 12139. doi:10.1038/ncomms12139

Niehorster, T., Loschberger, A., Gregor, I., Kramer, B., Rahn, H. J., Patting, M., Koberling, F., Enderlein, J. and Sauer, M. (2016). Multi-target spectrally resolved fluorescence lifetime imaging microscopy. *Nat. Methods* **13**, 257-262. doi:10.1038/nmeth.3740

Nitzan, M., Karaiskos, N., Friedman, N. and Rajewsky, N. (2018). Charting a tissue from single-cell transcriptomes. *bioRxiv* 456350. doi:10.1101/456350

DEVELOPMENT

Nowotschin, S., Setty, M., Kuo, Y.-Y., Liu, V., Garg, V., Sharma, R., Simon, C. S., Saiz, N., Gardner, R., Boutet, S. C. et al. (2019).The emergent landscape of the mouse gut endoderm at single-cell resolution. *Nature* **569**, 361-367. doi:10.1038/s41586-019-1127-1

O'Brien, L. E., Zegers, M. M. and Mostov, K. E. (2002). Opinion: Building epithelial architecture: insights from three-dimensional culture models. *Nat. Rev. Mol. Cell Biol.* **3**, 531-537. doi:10.1038/nrm859

Ounkomol, C., Seshamani, S., Maleckar, M. M., Collman, F. and Johnson, G. R. (2018). Label-free prediction of three-dimensional fluorescence images from transmitted-light microscopy. *Nat. Methods* **15**, 917-920. doi:10.1038/s41592-018-0111-2

Page, M. E., Lombard, P., Ng, F., Göttgens, B. and Jensen, K. B. (2013). The epidermis comprises autonomous compartments maintained by distinct stem cell populations. *Cell Stem Cell* **13**, 471-482. doi:10.1016/j.stem.2013.07.010

Panciera, T., Azzolin, L., Fujimura, A., Di Biagio, D., Frasson, C., Bresolin, S., Soligo, S., Basso, G., Bicciato, S., Rosato, A. et al. (2016). Induction of expandable tissue-specific stem/progenitor cells through transient expression of YAP/TAZ. *Cell Stem Cell* **19**, 725-737. doi:10.1016/j.stem.2016.08.009

Panciera, T., Azzolin, L., Cordenonsi, M. and Piccolo, S. (2017). Mechanobiology of YAP and TAZ in physiology and disease. *Nat. Rev. Mol. Cell Biol.* **18**, 758-770. doi:10.1038/nrm.2017.87

Papalexi, E. and Satija, R. (2018). Single-cell RNA sequencing to explore immune cell heterogeneity. *Nat. Rev. Immunol.* **18**, 35-45. doi:10.1038/nri.2017.76

Patel, S. H., Camargo, F. D. and Yimlamai, D. (2017). Hippo signaling in the liver regulates organ size, cell fate, and carcinogenesis. *Gastroenterology* **152**, 533-545. doi:10.1053/j.gastro.2016.10.047

Pauklin, S. and Vallier, L. (2013). The cell-cycle state of stem cells determines cell fate propensity. *Cell* **155**, 135-147. doi:10.1016/j.cell.2013.08.031

Pelkmans, L. (2012). Cell Biology. Using cell-to-cell variability–a new era in molecular biology. *Science* **336**, 425-426. doi:10.1126/science.1222161

Pellegrinet, L., Rodilla, V., Liu, Z., Chen, S., Koch, U., Espinosa, L., Kaestner, K. H., Kopan, R., Lewis, J. and Radtke, F. (2011). Dll1- and dll4-mediated notch signaling are required for homeostasis of intestinal stem cells. *Gastroenterology* **140**, 1230-1240, e1231-1237. doi:10.1053/j.gastro.2011.01.005

Perli, S. D., Cui, C. H. and Lu, T. K. (2016). Continuous genetic recording with self-targeting CRISPR-Cas in human cells. *Science* **353**, aag0511. doi:10.1126/science.aag0511

Picelli, S., Björklund, Å. K., Faridani, O. R., Sagasser, S., Winberg, G. and Sandberg, R. (2013). Smart-seq2 for sensitive full-length transcriptome profiling in single cells. *Nat. Methods* **10**, 1096-1098. doi:10.1038/nmeth.2639

Pirici, D., Mogoanta, L., Kumar-Singh, S., Pirici, I., Margaritescu, C., Simionescu, C. and Stanescu, R. (2009). Antibody elution method for multiple immunohistochemistry on primary antibodies raised in the same species and of the same subtype. *J. Histochem. Cytochem.* **57**, 567-575. doi:10.1369/jhc.2009.953240

Popovic, D., Koch, B., Kueblbeck, M., Ellenberg, J. and Pelkmans, L. (2018). Multivariate control of transcript to protein variability in single mammalian cells. *Cell Syst.* **7**, 398-411.e396. doi:10.1016/j.cels.2018.09.001

Qiao, X. T., Ziel, J. W., McKimpson, W., Madison, B. B., Todisco, A., Merchant, J. L., Samuelson, L. C. and Gumucio, D. L. (2007). Prospective identification of a multilineage progenitor in murine stomach epithelium. *Gastroenterology* **133**, 1989-1998. doi:10.1053/j.gastro.2007.09.031

Qiu, X., Mao, Q., Tang, Y., Wang, L., Chawla, R., Pliner, H. A. and Trapnell, C. (2017). Reversed graph embedding resolves complex single-cell trajectories. *Nat. Methods* **14**, 979-982. doi:10.1038/nmeth.4402

Raj, A., van den Bogaard, P., Rifkin, S. A., van Oudenaarden, A. and Tyagi, S. (2008). Imaging individual mRNA molecules using multiple singly labeled probes. *Nat. Methods* **5**, 877-879. doi:10.1038/nmeth.1253

Raj, B., Wagner, D. E., McKenna, A., Pandey, S., Klein, A. M., Shendure, J., Gagnon, J. A. and Schier, A. F. (2018). Simultaneous single-cell profiling of lineages and cell types in the vertebrate brain. *Nat. Biotechnol.* **36**, 442-450. doi:10.1038/nbt.4103

Ramsköld, D., Luo, S., Wang, Y.-C., Li, R., Deng, Q., Faridani, O. R., Daniels, G. A., Khrebtukova, I., Loring, J. F., Laurent, L. C. et al. (2012). Full-length mRNA-Seq from single-cell levels of RNA and individual circulating tumor cells. *Nat. Biotechnol.* **30**, 777-782. doi:10.1038/nbt.2282

Reynaud, E. G., Peychl, J., Huisken, J. and Tomancak, P. (2015). Guide to light-sheet microscopy for adventurous biologists. *Nat. Methods* **12**, 30-34. doi:10.1038/nmeth.3222

Ritsma, L., Ellenbroek, S. I. J., Zomer, A., Snippert, H. J., de Sauvage, F. J., Simons, B. D., Clevers, H. and van Rheenen, J. (2014). Intestinal crypt homeostasis revealed at single-stem-cell level by in vivo live imaging. *Nature* **507**, 362-365. doi:10.1038/nature12972

Rodríguez-Colman, M. J., Schewe, M., Meerlo, M., Stigter, E., Gerrits, J., Pras-Raves, M., Sacchetti, A., Hornsveld, M., Oost, K. C., Snippert, H. J. et al. (2017). Interplay between metabolic identities in the intestinal crypt supports stem cell function. *Nature* **543**, 424-427. doi:10.1038/nature21673

Rodriguez-Fraticelli, A. E., Wolock, S. L., Weinreb, C. S., Panero, R., Patel, S. H., Jankovic, M., Sun, J., Calogero, R. A., Klein, A. M. and Camargo, F. D. (2018). Clonal analysis of lineage fate in native haematopoiesis. *Nature* **553**, 212-216. doi:10.1038/nature25168

Rodriques, S. G., Stickels, R. R., Goeva, A., Martin, C. A., Murray, E., Vanderburg, C. R., Welch, J., Chen, L. M., Chen, F. and Macosko, E. Z. (2019). Slide-seq: A scalable technology for measuring genome-wide expression at high spatial resolution. *Science* **363**, 1463-1467. doi:10.1126/science.aaw1219

Rosenberg, A. B., Roco, C. M., Muscat, R. A., Kuchina, A., Sample, P., Yao, Z., Graybuck, L. T., Peeler, D. J., Mukherjee, S., Chen, W. et al. (2018). Single-cell profiling of the developing mouse brain and spinal cord with split-pool barcoding. *Science* **360**, 176-182. doi:10.1126/science.aam8999

Saka, S. K., Wang, Y., Kishi, J. Y., Zhu, A., Zeng, Y., Xie, W., Kirli, K., Yapp, C., Cicconet, M., Beliveau, B. J. et al. (2018). Highly multiplexed in situ protein imaging with signal amplification by Immuno-SABER. *bioRxiv* 507566. doi:10.1101/507566

Sánchez Alvarado, A. and Yamanaka, S. (2014). Rethinking differentiation: stem cells, regeneration, and plasticity. *Cell* **157**, 110-119. doi:10.1016/j.cell.2014.02.041

Sasai, Y. (2013). Cytosystems dynamics in self-organization of tissue architecture. *Nature* **493**, 318-326. doi:10.1038/nature11859

Satija, R., Farrell, J. A., Gennert, D., Schier, A. F. and Regev, A. (2015). Spatial reconstruction of single-cell gene expression data. *Nat. Biotechnol.* **33**, 495-502. doi:10.1038/nbt.3192

Sato, T. and Clevers, H. (2013). Growing self-organizing mini-guts from a single intestinal stem cell: mechanism and applications. *Science* **340**, 1190-1194. doi:10.1126/science.1234852

Sato, T., van Es, J. H., Snippert, H. J., Stange, D. E., Vries, R. G., van den Born, M., Barker, N., Shroyer, N. F., van de Wetering, M. and Clevers, H. (2011). Paneth cells constitute the niche for Lgr5 stem cells in intestinal crypts. *Nature* **469**, 415-418. doi:10.1038/nature09637

Schlegelmilch, K., Mohseni, M., Kirak, O., Pruszak, J., Rodriguez, J. R., Zhou, D., Kreger, B. T., Vasioukhin, V., Avruch, J., Brummelkamp, T. R. et al. (2011). Yap1 acts downstream of alpha-catenin to control epidermal proliferation. *Cell* **144**, 782-795. doi:10.1016/j.cell.2011.02.031

Schubert, W., Bonnekoh, B., Pommer, A. J., Philipsen, L., Böckelmann, R., Malykh, Y., Gollnick, H., Friedenberger, M., Bode, M. and Dress, A. W. (2006). Analyzing proteome topology and function by automated multidimensional fluorescence microscopy. *Nat. Biotechnol.* **24**, 1270-1278. doi:10.1038/nbt1250

Schulz, D., Zanotelli, V. R. T., Fischer, J. R., Schapiro, D., Engler, S., Lun, X. K., Jackson, H. W. and Bodenmiller, B. (2018). Simultaneous multiplexed imaging of mRNA and Proteins with subcellular resolution in breast cancer tissue samples by mass cytometry. *Cell Syst.* **6**, 531. doi:10.1016/j.cels.2018.04.004

Schwann, T. (1839). *Mikroskopische Untersuchungen über die Uebereinstimmung in der Strucktur und dem Wachsthum der Thiere und Pflanzen*. Berlin, Sander.

Sero, J. E., Sailem, H. Z., Ardy, R. C., Almuttaqi, H., Zhang, T. and Bakal, C. (2015). Cell shape and the microenvironment regulate nuclear translocation of NF-kappaB in breast epithelial and tumor cells. *Mol. Syst. Biol.* **11**, 790. doi:10.15252/msb.20145644

Serra, D., Mayr, U., Boni, A., Lukonin, I., Rempfler, M., Challet Meylan, L., Stadler, M. B., Strnad, P., Papasaikas, P., Vischi, D. et al. (2019). Self-organization and symmetry breaking in intestinal organoid development. *Nature* **569**, 66-72. doi:10.1038/s41586-019-1146-y

Setty, M., Tadmor, M. D., Reich-Zeliger, S., Angel, O., Salame, T. M., Kathail, P., Choi, K., Bendall, S., Friedman, N. and Pe'er, D. (2016). Wishbone identifies bifurcating developmental trajectories from single-cell data. *Nat. Biotechnol.* **34**, 637-645. doi:10.1038/nbt.3569

Setty, M., Kiseliovas, V., Levine, J., Gayoso, A., Mazutis, L. and Pe'er, D. (2019). Characterization of cell fate probabilities in single-cell data with Palantir. *Nat. Biotechnol.* **37**, 451-460. doi:10.1038/s41587-019-0068-4

Shah, S., Lubeck, E., Schwarzkopf, M., He, T. F., Greenbaum, A., Sohn, C. H., Lignell, A., Choi, H. M., Gradinaru, V., Pierce, N. A. et al. (2016a). Single-molecule RNA detection at depth by hybridization chain reaction and tissue hydrogel embedding and clearing. *Development* **143**, 2862-2867. doi:10.1242/dev.138560

Shah, S., Lubeck, E., Zhou, W. and Cai, L. (2016b). In situ transcription profiling of single cells reveals spatial organization of cells in the mouse hippocampus. *Neuron* **92**, 342-357. doi:10.1016/j.neuron.2016.10.001

Shah, S., Takei, Y., Zhou, W., Lubeck, E., Yun, J., Eng, C. L., Koulena, N., Cronin, C., Karp, C., Liaw, E. J. et al. (2018). Dynamics and spatial genomics of the nascent transcriptome by intron seqFISH. *Cell* **174**, 363-376.e316. doi:10.1016/j.cell.2018.05.035

Shin, J., Berg, D. A., Zhu, Y., Shin, J. Y., Song, J., Bonaguidi, M. A., Enikolopov, G., Nauen, D. W., Christian, K. M., Ming, G. L. et al. (2015). Single-cell RNA-Seq with waterfall reveals molecular cascades underlying adult neurogenesis. *Cell Stem Cell* **17**, 360-372. doi:10.1016/j.stem.2015.07.013

Snijder, B. and Pelkmans, L. (2011). Origins of regulated cell-to-cell variability. *Nat. Rev. Mol. Cell Biol.* **12**, 119-125. doi:10.1038/nrm3044

Snijder, B., Sacher, R., Rämö, P., Damm, E.-M., Liberali, P. and Pelkmans, L. (2009). Population context determines cell-to-cell variability in endocytosis and virus infection. *Nature* **461**, 520-523. doi:10.1038/nature08282

Snijder, B., Sacher, R., Ramo, P., Liberali, P., Mench, K., Wolfrum, N., Burleigh, L., Scott, C. C., Verheije, M. H., Mercer, J. et al. (2012). Single-cell analysis of population context advances RNAi screening at multiple levels. *Mol. Syst. Biol.* **8**, 579. doi:10.1038/msb.2012.9

Spanjaard, B., Hu, B., Mitic, N., Olivares-Chauvet, P., Janjuha, S., Ninov, N. and Junker, J. P. (2018). Simultaneous lineage tracing and cell-type identification using CRISPR-Cas9-induced genetic scars. *Nat. Biotechnol.* **36**, 469-473. doi:10.1038/nbt.4124

Spencer, S. L., Gaudet, S., Albeck, J. G., Burke, J. M. and Sorger, P. K. (2009). Non-genetic origins of cell-to-cell variability in TRAIL-induced apoptosis. *Nature* **459**, 428-432. doi:10.1038/nature08012

Spitzer, M. H. and Nolan, G. P. (2016). Mass cytometry: single cells, many features. *Cell* **165**, 780-791. doi:10.1016/j.cell.2016.04.019

Stahl, P. L., Salmen, F., Vickovic, S., Lundmark, A., Navarro, J. F., Magnusson, J., Giacomello, S., Asp, M., Westholm, J. O., Huss, M. et al. (2016). Visualization and analysis of gene expression in tissue sections by spatial transcriptomics. *Science* **353**, 78-82. doi:10.1126/science.aaf2403

Stange, D. E., Koo, B. K., Huch, M., Sibbel, G., Basak, O., Lyubimova, A., Kujala, P., Bartfeld, S., Koster, J., Geahlen, J. H. et al. (2013). Differentiated Troy+ chief cells act as reserve stem cells to generate all lineages of the stomach epithelium. *Cell* **155**, 357-368. doi:10.1016/j.cell.2013.09.008

Stegle, O., Teichmann, S. A. and Marioni, J. C. (2015). Computational and analytical challenges in single-cell transcriptomics. *Nat. Rev. Genet.* **16**, 133-145. doi:10.1038/nrg3833

Strnad, P., Gunther, S., Reichmann, J., Krzic, U., Balazs, B., de Medeiros, G., Norlin, N., Hiiragi, T., Hufnagel, L. and Ellenberg, J. (2016). Inverted light-sheet microscope for imaging mouse pre-implantation development. *Nat. Methods* **13**, 139-142. doi:10.1038/nmeth.3690

Takei, Y., Shah, S., Harvey, S., Qi, L. S. and Cai, L. (2017). Multiplexed Dynamic Imaging of Genomic Loci by Combined CRISPR Imaging and DNA Sequential FISH. *Biophys. J.* **112**, 1773-1776. doi:10.1016/j.bpj.2017.03.024

Tan, Q., Choi, K. M., Sicard, D. and Tschumperlin, D. J. (2017). Human airway organoid engineering as a step toward lung regeneration and disease modeling. *Biomaterials* **113**, 118-132. doi:10.1016/j.biomaterials.2016.10.046

Tanay, A. and Regev, A. (2017). Scaling single-cell genomics from phenomenology to mechanism. *Nature* **541**, 331-338. doi:10.1038/nature21350

Tata, P. R., Mou, H., Pardo-Saganta, A., Zhao, R., Prabhu, M., Law, B. M., Vinarsky, V., Cho, J. L., Breton, S., Sahay, A. et al. (2013). Dedifferentiation of committed epithelial cells into stem cells in vivo. *Nature* **503**, 218-223. doi:10.1038/nature12777

Tetteh, P. W., Farin, H. F. and Clevers, H. (2015). Plasticity within stem cell hierarchies in mammalian epithelia. *Trends Cell Biol.* **25**, 100-108. doi:10.1016/j.tcb.2014.09.003

Tetteh, P. W., Basak, O., Farin, H. F., Wiebrands, K., Kretzschmar, K., Begthel, H., van den Born, M., Korving, J., de Sauvage, F., van Es, J. H. et al. (2016). Replacement of lost Lgr5-positive stem cells through plasticity of their enterocyte-lineage daughters. *Cell Stem Cell* **18**, 203-213. doi:10.1016/j.stem.2016.01.001

Toth, Z. E. and Mezey, E. (2007). Simultaneous visualization of multiple antigens with tyramide signal amplification using antibodies from the same species. *J. Histochem. Cytochem.* **55**, 545-554. doi:10.1369/jhc.6A7134.2007

Trapnell, C., Cacchiarelli, D., Grimsby, J., Pokharel, P., Li, S., Morse, M., Lennon, N. J., Livak, K. J., Mikkelsen, T. S. and Rinn, J. L. (2014). The dynamics and regulators of cell fate decisions are revealed by pseudotemporal ordering of single cells. *Nat. Biotechnol.* **32**, 381-386. doi:10.1038/nbt.2859

Tremblay, A. M. and Camargo, F. D. (2012). Hippo signaling in mammalian stem cells. *Semin. Cell Dev. Biol.* **23**, 818-826. doi:10.1016/j.semcdb.2012.08.001

Tritschler, S., Büttner, M., Fischer, D. S., Lange, M., Bergen, V, Lickert, H. and Theis, F. J. (2019). Concepts and limitations for learning developmental trajectories from single cell genomics. *Development* **146**, dev170506. doi:10.1242/dev.170506

Tsurui, H., Nishimura, H., Hattori, S., Hirose, S., Okumura, K. and Shirai, T. (2000). Seven-color fluorescence imaging of tissue samples based on Fourier spectroscopy and singular value decomposition. *J. Histochem. Cytochem.* **48**, 653-662. doi:10.1177/002215540004800509

Valm, A. M., Cohen, S., Legant, W. R., Melunis, J., Hershberg, U., Wait, E., Cohen, A. R., Davidson, M. W., Betzig, E. and Lippincott-Schwartz, J. (2017). Applying systems-level spectral imaging and analysis to reveal the organelle interactome. *Nature* **546**, 162-167. doi:10.1038/nature22369

van Es, J. H., Sato, T., van de Wetering, M., Lyubimova, A., Yee Nee, A. N., Gregorieff, A., Sasaki, N., Zeinstra, L., van den Born, M., Korving, J. et al. (2012). Dll1+ secretory progenitor cells revert to stem cells upon crypt damage. *Nat. Cell Biol.* **14**, 1099-1104. doi:10.1038/ncb2581

Vermeulen, L. and Snippert, H. J. (2014). Stem cell dynamics in homeostasis and cancer of the intestine. *Nat. Rev. Cancer* **14**, 468-480. doi:10.1038/nrc3744

Vogetseder, A., Palan, T., Bacic, D., Kaissling, B. and Le Hir, M. (2007). Proximal tubular epithelial cells are generated by division of differentiated cells in the healthy kidney. *Am. J. Physiol. Cell Physiol.* **292**, C807-C813. doi:10.1152/ajpcell.00301.2006

Wagner, A., Regev, A. and Yosef, N. (2016). Revealing the vectors of cellular identity with single-cell genomics. *Nat. Biotechnol.* **34**, 1145-1160. doi:10.1038/nbt.3711

Wagner, D. E., Weinreb, C., Collins, Z. M., Briggs, J. A., Megason, S. G. and Klein, A. M. (2018). Single-cell mapping of gene expression landscapes and lineage in the zebrafish embryo. *Science* **360**, 981-987. doi:10.1126/science.aar4362

Wang, Y., Woehrstein, J. B., Donoghue, N., Dai, M., Avendano, M. S., Schackmann, R. C. J., Zoeller, J. J., Wang, S. S. H., Tillberg, P. W., Park, D. et al. (2017). Rapid sequential in situ multiplexing with DNA exchange imaging in neuronal cells and tissues. *Nano Lett.* **17**, 6131-6139. doi:10.1021/acs.nanolett.7b02716

Wang, G., Moffitt, J. R. and Zhuang, X. (2018a). Multiplexed imaging of high-density libraries of RNAs with MERFISH and expansion microscopy. *Sci. Rep.* **8**, 4847. doi:10.1038/s41598-018-22297-7

Wang, X., Allen, W. E., Wright, M. A., Sylwestrak, E. L., Samusik, N., Vesuna, S., Evans, K., Liu, C., Ramakrishnan, C., Liu, J. et al. (2018b). Three-dimensional intact-tissue sequencing of single-cell transcriptional states. *Science* **361**, eaat5691. doi:10.1126/science.aat5691

Weinreb, C., Wolock, S., Tusi, B. K., Socolovsky, M. and Klein, A. M. (2018). Fundamental limits on dynamic inference from single-cell snapshots. *Proc. Natl. Acad. Sci. USA* **115**, E2467-E2476. doi:10.1073/pnas.1714723115

Wolf, F. A., Hamey, F., Plass, M., Solana, J., Dahlin, J. S., Göttgens, B., Rajewsky, N., Simon, L. and Theis, F. J. (2019). PAGA: graph abstraction reconciles clustering with trajectory inference through a topology preserving map of single cells. *Genome Biol.* **20**, 59. doi:10.1186/s13059-019-1663-x

Xavier da Silveira Dos Santos, A. and Liberali, P. (2018). From single cells to tissue self-organization. *FEBS J.* **286**, 1495-1513. doi:10.1111/febs.14694

Xin, M., Kim, Y., Sutherland, L. B., Murakami, M., Qi, X., McAnally, J., Porrello, E. R., Mahmoud, A. I., Tan, W., Shelton, J. M. et al. (2013). Hippo pathway effector Yap promotes cardiac regeneration. *Proc. Natl. Acad. Sci. U.S.A.* **110**, 13839-13844. doi:10.1073/pnas.1313192110

Yan, K. S., Gevaert, O., Zheng, G. X. Y., Anchang, B., Probert, C. S., Larkin, K. A., Davies, P. S., Cheng, Z. F., Kaddis, J. S., Han, A. et al. (2017). Intestinal enteroendocrine lineage cells possess homeostatic and injury-inducible stem cell activity. *Cell Stem Cell* **21**, 78-90.e76. doi:10.1016/j.stem.2017.06.014

Yanger, K., Zong, Y., Maggs, L. R., Shapira, S. N., Maddipati, R., Aiello, N. M., Thung, S. N., Wells, R. G., Greenbaum, L. E. and Stanger, B. Z. (2013). Robust cellular reprogramming occurs spontaneously during liver regeneration. *Genes Dev.* **27**, 719-724. doi:10.1101/gad.207803.112

Yao, Z., Mich, J. K., Ku, S., Menon, V., Krostag, A. R., Martinez, R. A., Furchtgott, L., Mulholland, H., Bort, S., Fuqua, M. A. et al. (2017). A single-cell roadmap of lineage bifurcation in human ESC models of embryonic brain development. *Cell Stem Cell* **20**, 120-134. doi:10.1016/j.stem.2016.09.011

Yui, S., Azzolin, L., Maimets, M., Pedersen, M. T., Fordham, R. P., Hansen, S. L., Larsen, H. L., Guiu, J., Alves, M. R. P., Rundsten, C. F. et al. (2018). YAP/TAZ-dependent reprogramming of colonic epithelium links ECM remodeling to tissue regeneration. *Cell Stem Cell* **23**, 35-49.e37. doi:10.1016/j.stem.2017.11.001

Zepp, J. A., Zacharias, W. J., Frank, D. B., Cavanaugh, C. A., Zhou, S., Morley, M. P. and Morrisey, E. E. (2017). Distinct mesenchymal lineages and niches promote epithelial self-renewal and myofibrogenesis in the lung. *Cell* **170**, 1134-1148.e1110. doi:10.1016/j.cell.2017.07.034

Zhao, R., Fallon, T. R., Saladi, S. V., Pardo-Saganta, A., Villoria, J., Mou, H., Vinarsky, V., Gonzalez-Celeiro, M., Nunna, N., Hariri, L. P. et al. (2014). Yap tunes airway epithelial size and architecture by regulating the identity, maintenance, and self-renewal of stem cells. *Dev. Cell* **30**, 151-165. doi:10.1016/j.devcel.2014.06.004

Zhu, Q., Shah, S., Dries, R., Cai, L., Yuan, G. C. (2018). Identification of spatially associated subpopulations by combining scRNAseq and sequential fluorescence in situ hybridization data. *Nat. Biotechnol.* doi:10.1038/nbt.4260

Chapter 3: Research article

Self-organization and symmetry breaking in intestinal organoid development

Self-organization and symmetry breaking in intestinal organoid development

Denise Serra*, **Urs Mayr***, Andrea Boni*, Ilya Lukonin, Markus Rempfler, Ludivine Challet Meylan, Michael B. Stadler, Petr Strnad, Panagiotis Papasaikas, Dario Vischi, Annick Waldt, Guglielmo Roma & Prisca Liberali

Nature. 2019 Apr; 569, 66-72.

* These authors contributed equally

The supplementary information accompanying this article can be found in the appendix section.

Summary

Single cells with small intestinal origin can self-organize under homogenous conditions into organoids recapitulating morphology and cell type composition of the small intestine. A major step during organoid development is the occurrence of the first Paneth cells. Within homogenous cysts, symmetry is broken whereby a subset of cells differentiate into Paneth cells. These Paneth cells are believed to specify the future crypt site of the developing crypt-villus structure. Despite the importance of self-organization in organoid development, little is known on how individual cells interact with each other to generate asymmetries and build emergent higher order structures. In this study, we used imaging as well as sequencing approaches to quantitatively describe organoid development from single cells into budding organoids. We showed that organoid development resembles a regenerative process driven by transient activation of the transcriptional co-activator YAP1. We also show that symmetry is broken by cell-to-cell variability in YAP1 subcellular localization, which initiates Notch-Delta mediated lateral inhibition and subsequent Paneth cells formation. This study sheds light on signaling pathways and transcriptional network interactions that endows single intestinal cells with the capacity to self-organize into organoids.

My contribution

        This shared project (with Denise Serra and Andrea Boni) is the main work of my PhD. Denise did the sequencing and perturbation experiments and Andrea conducted most of the live imaging and did the data analysis for the live imaging experiments. My main contribution was the development of a 4i multiplexed imaging and analysis pipeline for three-dimensional organoid cultures. The development of this pipeline greatly benefited from collaborations with Markus Rempfler and Dario Vischi. Markus implemented the neural networks used for two and three-dimensional segmentation and helped with the analysis of single cell data. Dario developed the linking algorithm facilitating the analysis of multiplexed datasets. I designed the pipeline, wrote most of the code used for feature extraction and data analysis and conducted all the multiplexing experiments. This pipeline allowed me to infer trajectories of organoid growth and enabled the study of the different signaling pathways simultaneously and at the single cell level. The combination of our independent, complementary methods, which corroborated each other's results, made this study possible and successful. Furthermore, I generated most of the stable organoid lines used in this study by lentivirus transfection. Finally, I also contributed to the light sheet imaging experiments.

ARTICLE

Self-organization and symmetry breaking in intestinal organoid development

Denise Serra[1,2,6], Urs Mayr[1,2,6], Andrea Boni[1,5,6], Ilya Lukonin[1,2], Markus Rempfler[1], Ludivine Challet Meylan[1], Michael B. Stadler[1,3], Petr Strnad[1,5], Panagiotis Papasaikas[1,3], Dario Vischi[1], Annick Waldt[4], Guglielmo Roma[4] & Prisca Liberali[1,2]*

Intestinal organoids are complex three-dimensional structures that mimic the cell-type composition and tissue organization of the intestine by recapitulating the self-organizing ability of cell populations derived from a single intestinal stem cell. Crucial in this process is a first symmetry-breaking event, in which only a fraction of identical cells in a symmetrical sphere differentiate into Paneth cells, which generate the stem-cell niche and lead to asymmetric structures such as the crypts and villi. Here we combine single-cell quantitative genomic and imaging approaches to characterize the development of intestinal organoids from single cells. We show that their development follows a regeneration process that is driven by transient activation of the transcriptional regulator YAP1. Cell-to-cell variability in YAP1, emerging in symmetrical spheres, initiates Notch and DLL1 activation, and drives the symmetry-breaking event and formation of the first Paneth cell. Our findings reveal how single cells exposed to a uniform growth-promoting environment have the intrinsic ability to generate emergent, self-organized behaviour that results in the formation of complex multicellular asymmetric structures.

Genetically identical cells grown under the same conditions can display extensive variability in their potential to grow and differentiate[1–3]. This may be attributed to stochastic fluctuations in gene expression[4,5], or non-genetic variability emerging from collective cell behaviour[6–8]. The latter is generated by single cells that sense the 'population context', resulting in microenvironmental effects that can feed back on their physiological state and gene expression programs[9]. This enables single cells to break the symmetry of a population by changing their differentiation potential[10] with respect to other identical cells.

Organoids recapitulate the self-organizing potential of stem cells, creating three-dimensional structures in vitro. In particular, intestinal organoids recapitulate patterning processes and contain all cell types found in the adult intestine[11,12]. A characteristic of these intestinal organoids is that they develop from a single LGR5-positive (LGR5^{+}) stem cell[11]. Despite their extensive use, it is unclear how single intestinal stem cells give rise to cell populations with the capability of self-organization, and which transcriptional program it is that cells use. First, the stem cell generates a symmetrical sphere-like structure. Next, a secretory cell, named a Paneth cell, emerges and is believed to determine the future crypt site. Paneth cells create the niche environment and secrete WNT3A[13]. In vivo, these cells are not the only source of Wnt[14,15]. After this symmetry-breaking event, a gradient of WNT3A is formed around the Paneth cell, which induces the formation of a crypt[16]. The seemingly spontaneous emergence of a Paneth cell within a sphere—which is formed by genetically identical cells—represents the first and most crucial symmetry-breaking event in the formation of intestinal organoids, but how this occurs remains unknown.

Here we characterize the development of intestinal organoids using a combination of single-cell genomics and imaging approaches to show that generation of organoids is not limited to LGR5^{+} cells, and organoid formation is a regenerative process that relies on transient YAP1 activation. Finally, we show that for effective organoid development, YAP1 needs to display transient cell-to-cell variability in localization, which in turn initiates a Notch and DLL1 lateral inhibition

event that drives differentiation of Paneth cells and subsequent crypt formation.

Intestinal organoid development from single cells

Many intestinal cell types can de-differentiate in vivo during injury, and both LGR5^{+} and LGR5^{−} cells can generate organoids[17–19]. We characterized the growth of intestinal organoids from sorted single LGR5^{+} and LGR5^{−} cells derived from a LGR5::DTR-eGFP mouse[20] (Fig. 1a). Cells were seeded as multiple individual cells and cultured in ENR medium, containing WNT3A for the first three days only[13]. Organoids were fixed at different time points, stained with multiplexed immunofluorescence (4i)[21], imaged at high resolution and segmented using cellular computer vision algorithms (Fig. 1a, b, Extended Data Fig. 1a–c).

The efficiency of organoid formation was approximately 18%, for LGR5^{+} and 7.5% for LGR5^{−} (Fig. 1c). Both starting populations induce a similar, stereotyped pattern of organoid development: single cells at 24 h; small spheres with a lumen at 48 h; larger spheres of which most contain one Paneth cells at 72 h; asymmetric spheres with initial buds at 96 h; and organoids with crypts at 120 h (Fig. 1b). Organoids increase exponentially in size and cell number during the first 72 h (approximately 500 cells by 96 h, Fig. 1d, e). Notably, organoid eccentricity—a feature that measures object roundness—displayed bimodal distributions at 120 h (Extended Data Fig. 1d), which indicates that two morphologically distinct organoids developed (Fig. 1f). Markers of different intestinal cell types revealed the existence of spherical organoids that consist entirely of enterocytes, and are devoid of other cell types (Extended Data Fig. 1e, f). We refer to these organoids as 'enterocysts', as compared to budding organoids. Enterocysts appear after 60 h and, at 120 h, approximately 20% of multicellular structures are enterocysts, whereas around 80% are budding organoids (Fig. 1g). There is an increase in enterocysts from LGR5^{−} cells, which suggests that some progenitors have a higher probability to become enterocysts (Fig. 1g). In the absence of Wnt, enterocysts die
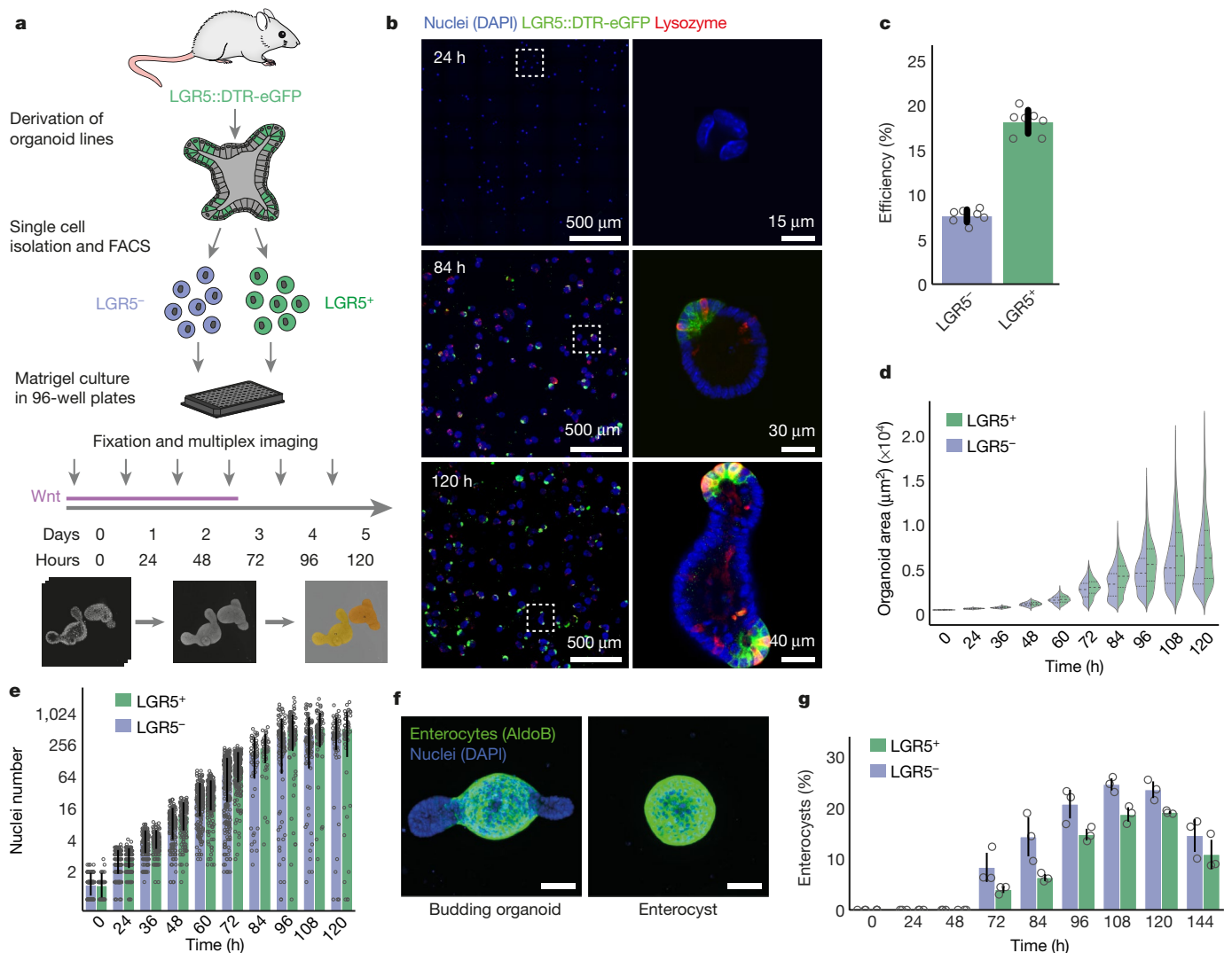
Fig. 1 | Intestinal organoids development from LGR5⁺ and LGR5⁻ single cells. a, Workflow of organoid-development time course from LGR5⁺ and LGR5⁻ single cells sorted by fluorescence-activated cell sorting (FACS) (LGR5::DTR-eGFP mice). **b**, Representative images of organoids (nuclei, DAPI), stem cells (LGR5::DTR-eGFP) and Paneth cells (lysozyme). Left, maximum intensity projections (MIP). Right, single-plane zoom-in. **c**, LGR5⁺ higher efficiency of organoid formation

($n = 7$ replicates for each condition). $P = 7.6 \times 10^{-10}$, two-sided t-test. **d**, Organoid area (LGR5⁺ $n = 9,798$ organoids; LGR5⁻ $n = 13,623$ organoids). Violin plot lines denote quartile for each group. **e**, Nuclei number ($n = 2,829$ organoids). **f**, Representative images of budding organoids and enterocysts. Scale bar, 50 μm. **g**, Relative amount of enterocysts over time ($n = 3$ replicates for each condition). $P = 0.019$, two-sided t-test at 120 h. Data in **c**, **e**, **g** are mean ± s.d.

after 120 h (Fig. 1g). We propose that enterocysts develop owing to an absence of symmetry breaking and no Paneth cell differentiation (and thus an absence of endogenously produced Wnt). To test this hypothesis, we modulated the rate of Paneth cell differentiation, resulting in changes in enterocyst formation that show a strong correlation between the absence of Paneth cells and enterocyst formation (Extended Data Fig. 1g). Thus, the successful formation of budding organoids requires a symmetry-breaking event, which results in the differentiation into a Paneth cell in the presence of exogenous Wnt.

Trajectory of LGR5 dynamics and organoid development

We next quantified the time progression of organoid development to pinpoint when symmetry breaks (Fig. 2a, b). The subsampling of temporal progression with fixed organoid time courses prohibits the determination of the exact morphological and phenotypic stages at which enterocysts emerge. We therefore inferred continuous single-organoid trajectories of development using the imaging multidimensional feature space[22,23] (Extended Data Fig. 2a–d). Notably, organoids grown from LGR5⁺ and LGR5⁻ cells display identical patterns of growth (Fig. 2c, d, Extended Data Fig. 2e, f). This revealed a single 'pseudotime' trajectory

up to approximately 0.3, after which it bifurcates into budding organoid and enterocyst branches (Fig. 2d, e). Both enterocysts and budding organoids are proliferative but only the budding organoids stay proliferative after removal of Wnt (Fig. 2e). Paneth cells appear only in budding organoids after pseudotime 0.3, and the timing is very similar for both starting populations (Fig. 2e, Extended Data Fig. 3). Mapping the cell number per organoid revealed that the bifurcation occurs when organoids have around 16–32 cells (Fig. 2f).

To map real time onto the trajectory, we performed time-lapse imaging from single cells using a custom-built light-sheet microscope suitable for organoids (Fig. 2g, Extended Data Fig. 4a–f). This revealed similar growth and proliferation dynamics for both budding organoids and enterocysts until 48 h (Fig. 2g, Extended Data Fig. 4g, Supplementary Videos 1–3). A sphere is created at the two-cell stage, with a subsequent fast rate of cell division of around 8 h. After 72 h, when exogenous Wnt is removed, budding organoids show localized cell proliferation, representing the site of crypt formation, whereas cells in enterocysts stop proliferating. Comparing organoid area over time with that of fixed organoids along the trajectory shows that pseudotime is slightly compressed in the beginning and stretched
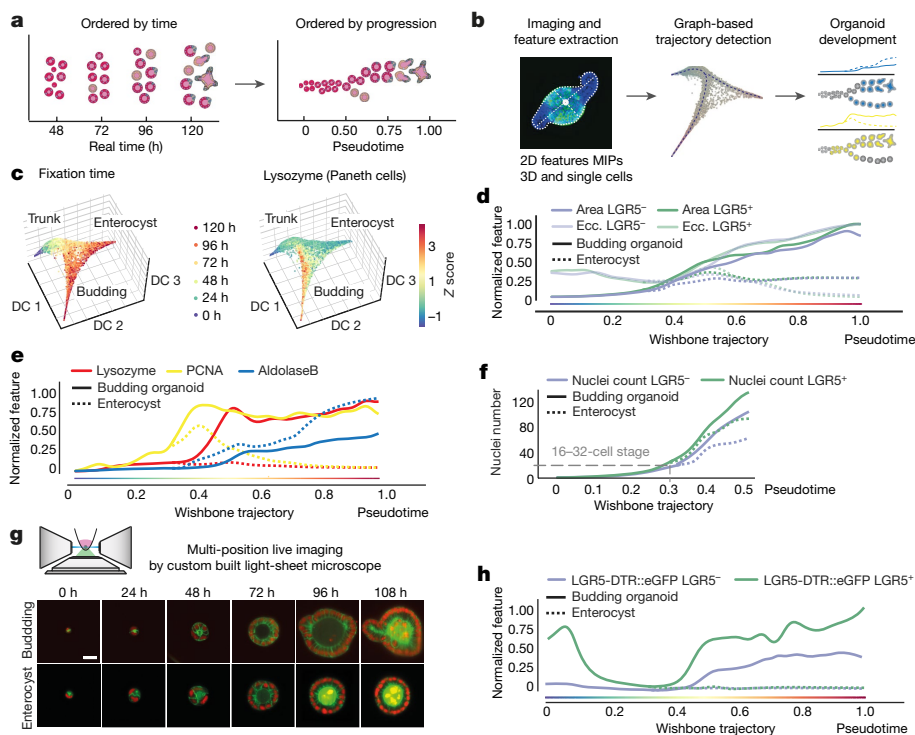
Fig. 2 | Trajectory of organoid development. a, b, Pseudotime ordering and trajectory inferences. **c**, Diffusion maps for pooled LGR5+ and LGR5− organoids ($n = 23{,}421$). Colour-coding denotes fixation time and lysozyme intensity (Paneth cells). **d**, Morphological features on pseudotime of LGR5+ ($n = 9{,}798$) and LGR5− ($n = 13{,}623$) organoids. Ecc., eccentricity. **e**, Cell types and proliferation markers on pseudotime ($n = 23{,}421$). **f**, Nuclei number on pseudotime for LGR5+ ($n = 4{,}104$),

LGR5− ($n = 5{,}593$) organoids. Dashed lines denote cell state around the branch point. **g**, Light-sheet imaging of single cells forming budding organoids or enterocysts (H2B–mCherry, red; MEM9–GFP, green). Single planes in the middle of organoids. Scale bar, 25 μm. **h**, LGR5::DTR-eGFP reporter signal on pseudotime of LGR5+ ($n = 9{,}798$) and LGR5− ($n = 13{,}623$) organoids.

towards the end (Extended Data Fig. 4h). Mapping real time onto pseudotime further revealed that the bifurcation at approximately 0.3 pseudotime corresponds to around 45 h. Thus, a trajectory of organoid progression—inferred from thousands of fixed organoids obtained with a time-course experiment—provides an accurate representation of organoid development dynamic. Moreover, it allows us to directly compare experiments performed in a time course with live-cell imaging.

Following the expression of LGR5 along the trajectory led to an unexpected discovery. LGR5+ cells strongly downregulate LGR5 expression during the first day and reacquire it only around 0.4 pseudotime (approximately 62 h) after the appearance of Paneth cells (Fig. 2h, Extended Data Fig. 5a, b). This loss of LGR5 expression also strongly correlates with the onset of fast proliferation and was confirmed with live-cell imaging of a single LGR5+ cell (Extended Data Fig. 5c, d, Supplementary Video 4). LGR5 was also upregulated at 62 h in organoids from LGR5− cells, although slightly delayed and dimmer (Fig. 2h). This shows that LGR5+ and LGR5− cells display similar patterns of organoid development through a transient proliferative sphere that consists of cells that do not express LGR5, after which LGR5 is expressed in stem cells in the newly formed crypts of budding organoids.

Transient YAP1 activation during organoid development

To determine the transcriptional programs modulated during the first days of organoid growth, RNA sequencing (RNA-seq) time-course analysis was performed and mapped onto pseudotime (Fig. 3a, Extended Data Fig. 6a, Supplementary Table 1). This shows that stem-cell markers are similarly downregulated at the transcriptional and protein level and, then, reacquired after Paneth cell differentiation (Fig. 3b, Extended Data Fig. 6b–d). Similar expression dynamics were also observed for all other cell-type-specific genes (Fig. 3b, Extended Data Fig. 6b–d). Notably, canonical Wnt targets are downregulated and

non-canonical targets are upregulated in the first days (Extended Data Fig. 6e). To gain an overview of transcriptional changes, we then clustered the temporal expression patterns (Fig. 3c). This revealed three major clusters: first, a red cluster that is enriched in stem-cell markers, other cell-type-specific genes and genes involved in secretion and cell migration. There is a re-programming of cells into an undifferentiated state, which is followed by the re-establishment of LGR5+ stem cells and acquisition of differentiation after Paneth cell formation (Extended Data Fig. 6f). Second, a blue cluster that is enriched in functions linked to mitochondria, actin cytoskeleton, cell cycle and extracellular matrix. These genes are probably required to supply the energetic demand of undergoing rapid cell divisions. Third, a green cluster that is enriched in functions related to metabolism and cell-type-related functions (Extended Data Fig. 6f).

To focus on the earliest phase of development, we quantified transcription-factor-binding motifs in the promoters of genes expressed at 24 h (Fig. 3d). The most important motifs were for FOSL1, TEAD1 and TEAD4, which all require YAP1 as transcriptional co-activator[24,25]. These transcription factors show an early increased expression, whereas the expression of *Yap1* mRNA stays constant (Fig. 3e, Extended Data Fig. 6g). YAP1 is a mechanosensing nuclear effector of the Hippo pathway and regulates organ growth, regeneration and tumorigenesis[26,27]. It is also an important effector of intestinal regeneration, in which it reprograms LGR5+ cells into LGR5− cells, thus inhibiting Paneth cell differentiation[28,29]. When we correlated the expression levels of the early expressed genes (24 h versus 0 h) in organoid development with the expression levels of YAP1-dependent gene expression[28], we observed a good correlation ($r = 0.45$) (Fig. 3f). These early genes include YAP1 target genes[30] and fetal genes involved in regeneration[31]. Thus, this provides support for a model in which organoid development follows a regenerative response with a transient activation of YAP1 target genes in a LGR5− sphere.
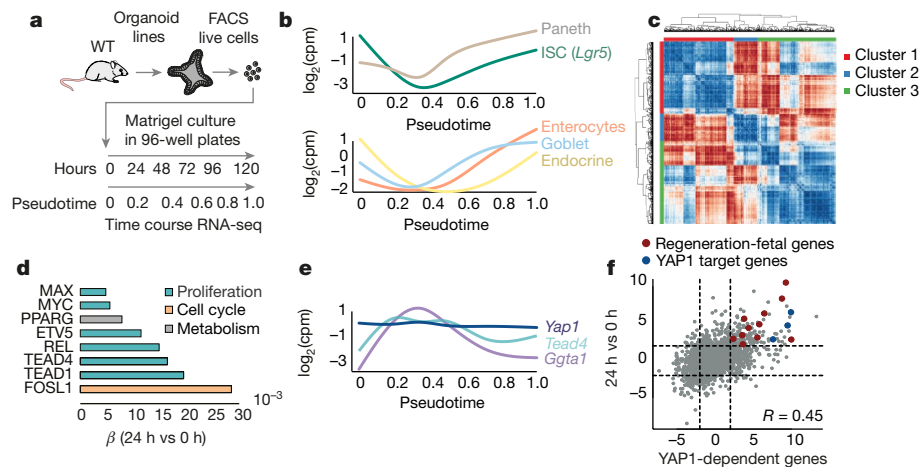
Fig. 3 | YAP1 target genes are transiently expressed during organoids development. a, Workflow for bulk RNA-seq time course. **b**, Expression profiles of cell-type markers mapped on pseudotime. Paneth cells (*Lyz1*), intestinal stem cells (ISCs; *Lgr5*), enterocytes (*Apoc3*), goblet cells (*Muc2*), endocrine cells (*Sst*). **c**, Hierarchical clustering of gene expression correlation profiles. **d**, Magnitude of contribution (β) of transcription factors to differential expression at 24 h versus 0 h. **e**, Gene expression profiles of *Yap1*, *Tead4* and *Ggta1* mapped on pseudotime. **f**, Pearson correlation between genes expressed at 24 h versus 0 h, and genes expressed in YAP1 overexpression versus knockdown. $n = 3$ organoid cultures from three independent mice.

Variable YAP1 activation determines symmetry breaking

YAP1 targets are transiently upregulated while *Yap1* mRNA is unchanged (Fig. 3e), which suggests post-transcriptional regulation. We therefore analysed YAP1 protein during organoid development. YAP1 protein abundance in organoids shows an initial increase until 48 h (Fig. 4a, b), whereas its subcellular localization starts to become variable between single cells after 24 h, increasing entropy in its ON and OFF state (Extended Data Fig. 7a, b). More precisely, in the four-cell stage, little cell-to-cell variability in the nuclear localization of YAP1 is observed whereas in the eight-cell and sixteen-cell stages—when cells are more crowded—YAP1 is translocated to the cytosol, and thus inactivated, in a subset of cells (Fig. 4a). After removal of Wnt, YAP1 protein levels strongly decreased (Fig. 4b), with YAP1 regionalizing only in the crypt area. YAP1 is absent in enterocysts. Removing Wnt earlier promotes relocalization of YAP1 to the cytosol, and decreased expression (Extended Data Fig. 7c).

When we generated organoids from single cells that, on average, have more YAP1 activity (all single cells extracted from 72-h-old organoids), we observed a strong increase in efficiency in organoid formation (Fig. 4c, Extended Data Fig. 7d). Inhibition of YAP1 and YAP1 knock-out result in reduced organoid efficiency (Fig. 4d, e, Extended Data Fig. 7e). Conversely, ectopic activation of YAP1 by YAP1 overexpression, or by activation of its downstream effector EREG[28], increases the efficiency of organoid formation (Fig. 4f). All these phenotypes require the presence of exogenous Wnt (Extended Data Fig. 7f).

Homogeneous inhibition of YAP1 after 48 h in all cells reduces Paneth cell differentiation, and increases the number of enterocysts. Notably, this phenotype is similar to YAP1-overexpression organoids (in which YAP1 is homogeneously active in all cells), and neither form Paneth cells nor display symmetry breaking (Fig. 4g, h, Extended Data Fig. 7g, h). Instead, they either develop into enterocysts or remain as undifferentiated symmetrical spheres when YAP1 expression is high (Extended Data Fig. 7i). In addition, organoids that lack the LATS1 and LATS2 tumour suppressors[28] remain symmetrical and contain no Paneth cells (Extended Data Fig. 7g, h). We then added EREG, which led to the heterogeneous activation of YAP1, resulting in decreased enterocyst formation (Fig. 4g). From these findings, we conclude that during the first 72 h of organoid development, YAP1 is transiently active in every cell and induces cell proliferation, after which it becomes inactive in only few cells. Both homogeneous inactivation and overactivation of YAP1 in spheres abolish symmetry breaking and organoid formation, which suggests that it is not the absolute level of YAP1 but rather its varying activation state between single cells that drives symmetry breaking.

A YAP1–Notch switch drives symmetry breaking

To understand how YAP1 variability drives symmetry breaking, we performed single-cell (sc) RNA-seq at different time points (Fig. 5a, Extended Data Figs. 8a, b, 9a). At 72 h, the population of cells is homogeneous, with only a few stem cells and Paneth cells, and no enterocytes (Extended Data Fig. 9b). At 120 h, most cell types are represented[32,33] (Extended Data Fig. 9b, c). A subset of cells from organoids at 72 h shows high expression of YAP1 target genes (Fig. 5b, Supplementary Table 1), the levels of which correlate with the expression level of Notch ligands such as DLL1 (Fig. 5b, c, Extended Data Fig. 9d). This suggests that the variability in YAP1 activation might generate variability in expression of Notch ligands. Interestingly, Notch signalling is a regulator of the intestinal stem-cell niche, specifying distinct cell fates[34,35]. In vivo and in mature organoids, it is known that inhibition of Notch increases the differentiation of secretory cells[36]. Nuclear localization of YAP1 is variable between cells after the 4-cell stage and precedes the expression of DLL1 in few cells between the 8-cell and 16-cell stages. DLL1 expression occurs in cells with high levels of nuclear YAP1 (Fig. 5d–f, Extended Data Fig. 10a). This is consistent with findings in other tissues that *DLL1* is a YAP1 target gene[28,37]. Moreover, HES1 is expressed in single cells that neighbour DLL1+ cells (Fig. 5d, Extended Data Fig. 10a). Between the 16-cell and the 32-cell stages, Paneth cells appear, which are all positive for DLL1 and start losing nuclear YAP1 (Fig. 5e, f, Extended Data Fig. 10a, b), as also seen in the loss of YAP1 target gene expression in Paneth cells from scRNA-seq (Fig. 5c). This indicates that variability in nuclear YAP1 is involved in the initiation of a Notch–DLL1 event, which, once established, maintains itself in the absence of YAP1[38,39]. We then homogeneously inactivated or activated YAP1, and in both conditions, no Notch–DLL1 event is observed (Extended Data Fig. 10c, d). By contrast, when we used EREG, Notch–DLL1 is activated (Extended Data Fig. 10c, d). Finally, to determine whether Notch–DLL1 activation is required for symmetry breaking, we used gamma-secretase inhibitors. All these inhibitors reduce symmetry breaking and Paneth cell differentiation, resulting in an increased fraction of enterocysts (Fig. 5g, Extended Data Fig. 10e), and strengthening the correlation between the absence of Paneth cells and enterocyst formation. Adding the Notch inhibitor *N*-[*N*-(3,5-difluorophenacetyl)-L-alanyl]-*S*-phenylglycine *t*-butyl ester (DAPT) after 120 h shows the expected increase in secretory cells (Extended Data Fig. 10f). Thus, although Notch lateral inhibition is required for
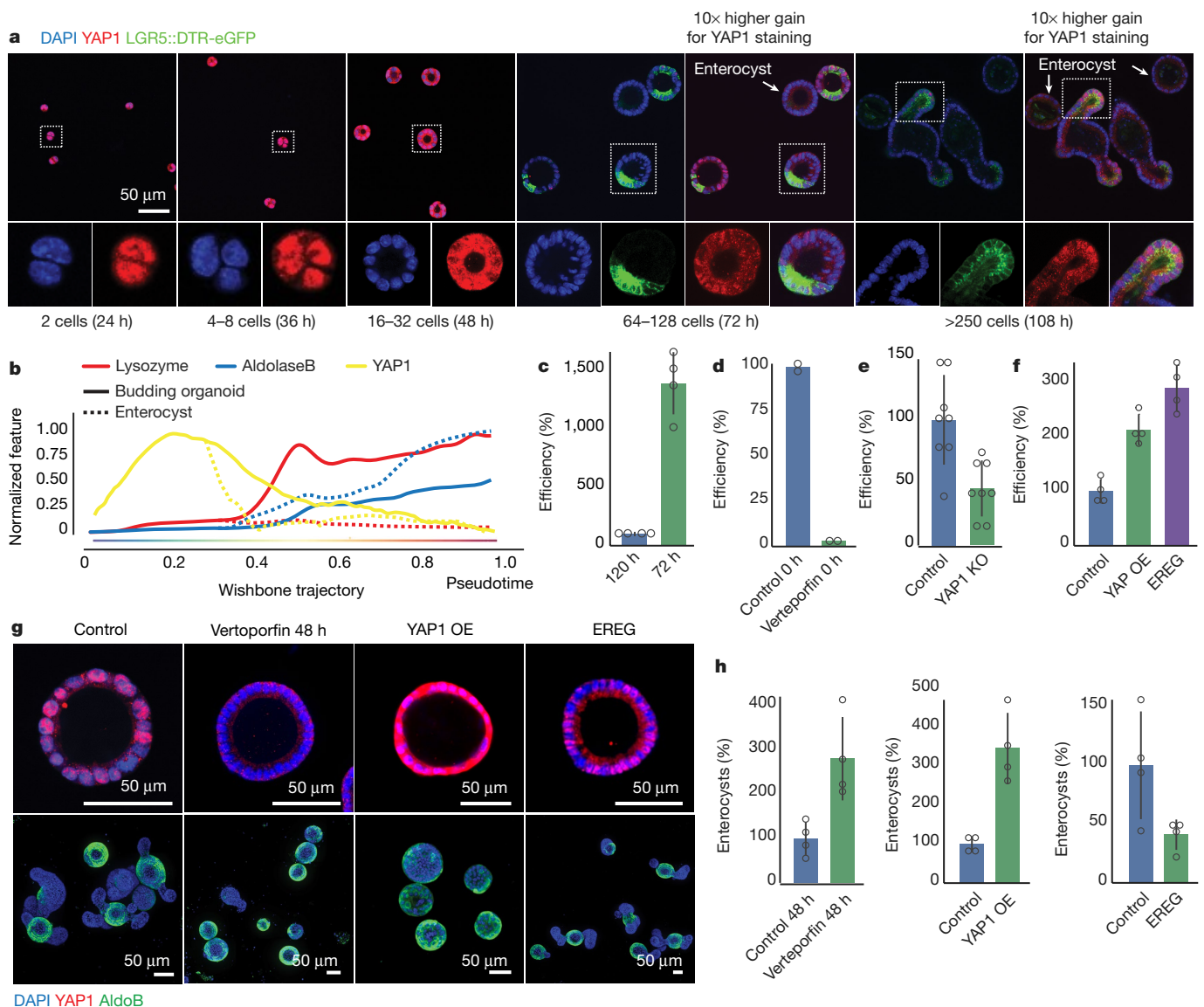
a DAPI YAP1 LGR5::DTR-eGFP

10× higher gain for YAP1 staining

10× higher gain for YAP1 staining

Enterocyst

Enterocyst

50 μm

2 cells (24 h)   4–8 cells (36 h)   16–32 cells (48 h)   64–128 cells (72 h)   >250 cells (108 h)

b
— Lysozyme — AldolaseB — YAP1
— Budding organoid
···· Enterocyst

Normalized feature

Wishbone trajectory   Pseudotime

c Efficiency (%)
120 h 72 h

d Efficiency (%)
Control 0 h Verteporfin 0 h

e Efficiency (%)
Control YAP1 KO

f Efficiency (%)
Control YAP OE EREG

g Control   Verteporfin 48 h   YAP1 OE   EREG

50 μm   50 μm   50 μm   50 μm

50 μm   50 μm   50 μm   50 μm

DAPI YAP1 AldoB

h Enterocysts (%)
Control 48 h Verteporfin 48 h

Enterocysts (%)
Control YAP1 OE

Enterocysts (%)
Control EREG

Fig. 4 | Transient YAP1 activation is necessary for symmetry breaking.
a, YAP1 localization (LGR5::DTR-eGFP). **b**, YAP1 protein abundance along pseudotime ($n = 6,892$ organoids). **c**, Efficiency of organoids formation from cells isolated from organoids at 72 h and at 120 h (normalization: 120 h). Fixed at 72 h ($n = 4$ replicates). $P = 0.00007$, two-sided t-test. **d**, Efficiency of organoid formation after verteporfin treatment (normalization: control). Fixed at 48 h ($n = 2$ replicates). **e**, Efficiency of organoid formation from YAP1 knockout (KO) (normalization: control). Fixed: 72 h ($n = 8$ replicates). $P = 0.002$, two-sided t-test.

f, Efficiency of organoid formation from YAP1 overexpression (OE) and EREG activation (normalization: control) ($n = 4$ replicates). $P = 0.001$ (YAP1 OE); $P = 0.0002$ (EREG), two-sided t-test. **g**, Images of organoids treated with verteporfin (at 48 h), YAP1-overexpression and EREG. Top, nuclei (blue) and YAP1 (red), fixed at 72 h. Bottom, nuclei (blue) and AldoB (green), fixed at 96 h (YAP1-overexpression) or 120 h (control, verteporfin, EREG). AldoB, aldolaseB. **h**, Quantification of enterocysts as in **g** (normalization: control) ($n = 4$ replicates). $P = 0.01$ (verteporfin); $P = 0.002$ (YAP1 OE); $P = 0.05$ (EREG), two-sided t-test. Data are mean ± s.d.

enterocyte differentiation in large organoids, it needs to be activated in small symmetrical spheres to drive symmetry breaking and the formation of the first secretory DLL1^{+} cell, the Paneth cell. Together, this shows that variability in nuclear YAP1 initiates a Notch–DLL1 event. Cells with high levels of nuclear YAP1 become DLL1^{+} cells and subsequently Paneth cells. Once having become a Paneth cell, the upstream regulation of YAP1 on DLL1 is then lost.

Discussion

Here we characterize the development of intestinal organoids from single cells, and show that it exploits the plasticity of the intestine and is driven by transient YAP1 activation, following a regeneration process. We then show that cell-to-cell variability in nuclear YAP1—emerging in symmetrical spheres—initiates a Notch–DLL1 lateral inhibition event between the 8- and 16-cell stage, which constitutes the first symmetry-breaking event in intestinal organoid growth and drives the formation of the first

Paneth cell (Fig. 5h). It is yet not clear what drives the variability in YAP1 subcellular localization but it may be determined by a combinatorial effect of local variation in cell crowding caused by asynchronous cell divisions[40] and extracellular matrix density[41] (Extended Data Fig. 10g). Subsequently, variability in YAP1 results in variability in DLL1 activation. Although fluctuations in DLL1 ligand can be amplified by negative feedback[42], we show here that it does not arise from intrinsic stochasticity, but can be determined by cell-to-cell variability in the mechanosensor YAP1. Thus, Notch signalling has a dual role in organoid development—first in symmetry breaking and then, after homeostasis has been reached, in maintaining enterocyte differentiation[36].

Together, our findings underscore the notion that YAP1 acts as a sensor of tissue integrity. After tissue dissociation, YAP1 is activated to drive tissue repair, but once it is repaired, local cell crowding increases and induces heterogeneous activation of YAP1 in organoids and possibly also in vivo, driving the heterogeneous expression of DLL1 and
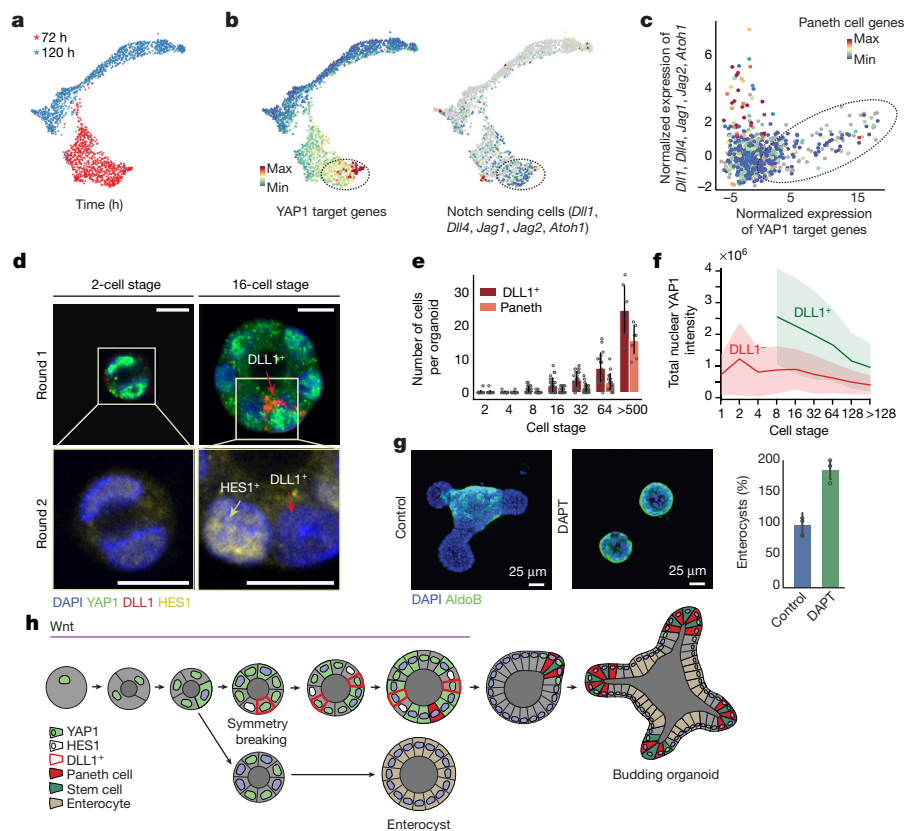
Fig. 5 | YAP1 cell-to-cell variability allows Notch–DLL1 activation and symmetry breaking. a, Griph (graph inference of population heterogeneity)-based visualization (72 h and 120 h) of single cells. **b**, Single-cell expression of YAP1 targets and Notch-sending cell marker genes. Dotted square denotes high YAP1 target-expressing cells. **c**, Spearman correlation between YAP1 target genes and expression of Notch-sending cell marker genes at 72 h ($n = 798$ cells). **d**, Multiplexed imaging of YAP1 variability and DLL1$^+$ cells. Top, nuclei (blue), YAP1 (green), DLL1 (red). Bottom, nuclei (blue) and HES1 (yellow). Arrows: red (DLL1$^+$ cells), yellow (HES1$^+$). Scale bar, 10 μm. **e**, Number of DLL1$^+$ and Paneth cells ($n = 170$ organoids). **f**, Nuclear YAP1 intensity in DLL1$^+$ (green) and DLL1$^-$ (red) cells ($n = 73,899$ cells). Shading denotes s.d. **g**, Left, images of organoids treated with DAPT. Fixed at 96 h. Right, quantification of fraction of enterocysts (normalization: control). Fixed at 96 h ($n = 3$ replicates). $P = 0.003$, two-sided t-test. **h**, Model of organoid development and symmetry breaking. Data in **e**, **g** are mean ± s.d.

formation of Paneth cells. Notably, cells that neighbour these Paneth cells show an increase in the canonical Wnt signalling response (TCF–GFP expression) (Extended Data Fig. 10h). Thus, Paneth cells might switch a general non-canonical/YAP1-dependent response in transient-amplifying-like cells to a locally induced canonical Wnt response in their neighbouring cells with the re-expression of LGR5 and the recreation of a stem-cell niche, bringing the system back to homeostasis. Indeed, YAP1 could be a general sensor for tissue injury and repair in many other tissues[43–45], by having a broad regulatory role at enhancers and distal regions of progenitor-specific genes[45,46]. This could shed light on the development of cancer[47], which may often reflect an inability to reacquire homeostasis upon tissue damage[28]. Finally, this work reveals how single cells have the intrinsic ability to generate emergent, self-organized behaviours that result in multicellular asymmetric structures.

Reporting summary

Further information on research design is available in the Nature Research Reporting Summary linked to this paper.

Data availability

RNA-seq data are available at the Gene Expression Omnibus (GEO) under accession codes GSE115955 (bulk) and GSE115956 (single cells).

Code availability

Code used for image analysis in this study was developed in the Liberali laboratory in Matlab and Python 3. For Python 3, multiple open source Python libraries for scientific computing and image analysis were used. The code for organoid 2D and 3D segmentation, feature extraction and organoid linkage is available under https://github.com/fmi-basel/glib-nature2018-materials. An R implementation of the Griph algorithm for scRNA-seq analysis is available as an R package at https://github.com/ppapasaikas/Griph.

Online content

Any methods, additional references, Nature Research reporting summaries, source data, statements of data availability and associated accession codes are available at https://doi.org/10.1038/s41586-019-1146-y.

1. Sasai, Y. Cytosystems dynamics in self-organization of tissue architecture. *Nature* **493**, 318–326 (2013).
2. Ohnishi, Y. et al. Cell-to-cell expression variability followed by signal reinforcement progressively segregates early mouse lineages. *Nat. Cell Biol.* **16**, 27–37 (2014).
3. Goolam, M. et al. Heterogeneity in Oct4 and Sox2 targets biases cell fate in 4-cell mouse embryos. *Cell* **165**, 61–74 (2016).
4. Hanna, J. et al. Direct cell reprogramming is a stochastic process amenable to acceleration. *Nature* **462**, 595–601 (2009).
5. Eldar, A. & Elowitz, M. B. Functional roles for noise in genetic circuits. *Nature* **467**, 167–173 (2010).
6. Snijder, B. et al. Population context determines cell-to-cell variability in endocytosis and virus infection. *Nature* **461**, 520–523 (2009).
7. Battich, N., Stoeger, T. & Pelkmans, L. Control of transcript variability in single mammalian cells. *Cell* **163**, 1596–1610 (2015).
8. Loewer, A. & Lahav, G. We are all individuals: causes and consequences of non-genetic heterogeneity in mammalian cells. *Curr. Opin. Genet. Dev.* **21**, 753–758 (2011).
9. Snijder, B. & Pelkmans, L. Origins of regulated cell-to-cell variability. *Nat. Rev. Mol. Cell Biol.* **12**, 119–125 (2011).

10. Wennekamp, S., Mesecke, S., Nédélec, F. & Hiiragi, T. A self-organization framework for symmetry breaking in the mammalian embryo. *Nat. Rev. Mol. Cell Biol.* **14**, 452–459 (2013).
11. Sato, T. et al. Single Lgr5 stem cells build crypt-villus structures *in vitro* without a mesenchymal niche. *Nature* **459**, 262–265 (2009).
12. Spence, J. R. et al. Directed differentiation of human pluripotent stem cells into intestinal tissue *in vitro*. *Nature* **470**, 105–109 (2011).
13. Sato, T. et al. Paneth cells constitute the niche for Lgr5 stem cells in intestinal crypts. *Nature* **469**, 415–418 (2011).
14. Shoshkes-Carmel, M. et al. Subepithelial telocytes are an important source of Wnts that supports intestinal crypts. *Nature* **557**, 242–246 (2018).
15. San Roman, A. K., Jayewickreme, C. D., Murtaugh, L. C. & Shivdasani, R. A. Wnt secretion from epithelial cells and subepithelial myofibroblasts is not required in the mouse intestinal stem cell niche *in vivo*. *Stem Cell Reports* **2**, 127–134 (2014).
16. Farin, H. F. et al. Visualization of a short-range Wnt gradient in the intestinal stem-cell niche. *Nature* **530**, 340–343 (2016).
17. van Es, J. H. et al. Dll1+ secretory progenitor cells revert to stem cells upon crypt damage. *Nat. Cell Biol.* **14**, 1099–1104 (2012).
18. Tetteh, P. W. et al. Replacement of lost Lgr5-positive stem cells through plasticity of their enterocyte-lineage daughters. *Cell Stem Cell* **18**, 203–213 (2016).
19. Yan, K.S. et al. intestinal enteroendocrine lineage cells possess homeostatic and injury-inducible stem cell activity. *Cell Stem Cell* **21**, 78–90.76 (2017).
20. Tian, H. et al. A reserve stem cell population in small intestine renders Lgr5-positive cells dispensable. *Nature* **478**, 255–259 (2011).
21. Gut, G., Herrmann, M. D. & Pelkmans, L. Multiplexed protein maps link subcellular organization to cellular states. *Science* **361**, eaar7042 (2018).
22. Setty, M. et al. Wishbone identifies bifurcating developmental trajectories from single-cell data. *Nat. Biotechnol.* **34**, 637–645 (2016).
23. Herring, C.A. et al. Unsupervised trajectory analysis of single-cell RNA-seq and imaging data reveals alternative tuft cell origins in the gut. *Cell Syst.* **6**, 37–51 e39 (2018).
24. Zanconato, F. et al. Genome-wide association between YAP/TAZ/TEAD and AP-1 at enhancers drives oncogenic growth. *Nat. Cell Biol.* **17**, 1218–1227 (2015).
25. Stein, C. et al. YAP1 exerts its transcriptional control via tead-mediated activation of enhancers. *PLoS Genet.* **11**, e1005465 (2015).
26. Dupont, S. et al. Role of YAP/TAZ in mechanotransduction. *Nature* **474**, 179–183 (2011).
27. Camargo, F. D. et al. YAP1 increases organ size and expands undifferentiated progenitor cells. *Curr. Biol.* **17**, 2054–2060 (2007).
28. Gregorieff, A., Liu, Y., Inanlou, M. R., Khomchuk, Y. & Wrana, J. L. Yap-dependent reprograming of Lgr5+ stem cells drives intestinal regeneration and cancer. *Nature* **526**, 715–718 (2015).
29. Barry, E. R. et al. Restriction of intestinal stem cell expansion and the regenerative response by YAP. *Nature* **493**, 106–110 (2013).
30. Azzolin, L. et al. YAP/TAZ incorporation in the β-catenin destruction complex orchestrates the Wnt response. *Cell* **158**, 157–170 (2014).
31. Yui, S. et al. YAP/TAZ-dependent reprogramming of colonic epithelium links ECM remodeling to tissue regeneration. *Cell Stem Cell* **22**, 35–49.e37 (2018).
32. Haber, A. L. et al. A single-cell survey of the small intestinal epithelium. *Nature* **551**, 333–339 (2017).
33. Moor, A.E. et al. Spatial reconstruction of single enterocytes uncovers broad zonation along the intestinal villus axis. *Cell* **175**, 1156–1167.e1115 (2018).
34. Fre, S. et al. Notch signals control the fate of immature progenitor cells in the intestine. *Nature* **435**, 964–968 (2005).
35. Noah, T. K. & Shroyer, N. F. Notch in the intestine: regulation of homeostasis and pathogenesis. *Annu. Rev. Physiol.* **75**, 263–288 (2013).
36. Yin, X. et al. Niche-independent high-purity cultures of Lgr5+ intestinal stem cells and their progeny. *Nat. Methods* **11**, 106–112 (2014).
37. Totaro, A. et al. YAP/TAZ link cell mechanics to Notch signalling to control epidermal stem cell fate. *Nat. Commun.* **8**, 15206 (2017).
38. Bray, S. J. Notch signalling in context. *Nat. Rev. Mol. Cell Biol.* **17**, 722–735 (2016).
39. Chen, K. Y. et al. A Notch positive feedback in the intestinal stem cell niche is essential for stem cell self-renewal. *Mol. Syst. Biol.* **13**, 927 (2017).
40. Carroll, T. D. et al. Interkinetic nuclear migration and basal tethering facilitates post-mitotic daughter separation in intestinal organoids. *J. Cell Sci.* **130**, 3862–3877 (2017).
41. Gjorevski, N. et al. Designer matrices for intestinal stem cell and organoid culture. *Nature* **539**, 560–564 (2016).
42. Sjoqvist, M. & Andersson, E. R. Do as I say, Not(ch) as I do: lateral control of cell fate. *Dev. Biol.* **447**, 58–70 (2017).
43. Zhang, H., Pasolli, H. A. & Fuchs, E. Yes-associated protein (YAP) transcriptional coactivator functions in balancing growth and differentiation in skin. *Proc. Natl Acad. Sci. USA* **108**, 2270–2275 (2011).
44. Xin, M. et al. Hippo pathway effector Yap promotes cardiac regeneration. *Proc. Natl Acad. Sci. USA* **110**, 13839–13844 (2013).
45. Yimlamai, D. et al. Hippo pathway activity influences liver cell fate. *Cell* **157**, 1324–1338 (2014).
46. Cebola, I. et al. TEAD and YAP regulate the enhancer network of human embryonic pancreatic progenitors. *Nat. Cell Biol.* **17**, 615–626 (2015).
47. Panciera, T., Azzolin, L., Cordenonsi, M. & Piccolo, S. Mechanobiology of YAP and TAZ in physiology and disease. *Nat. Rev. Mol. Cell Biol.* **18**, 758–770 (2017).

Author contributions P.L. conceived and supervised the study, P.L., D.S., U.M. and A.B. designed the experiments, D.S., U.M., L.C.M. and A.B. performed the time courses, I.L. performed the first YAP1 experiments, U.M. and A.B. designed the image analysis, M.R. and D.V. developed 3D and single-cell imaging, U.M. developed the trajectory inference, A.B. and P.S. built the light-sheet, A.B. and U.M. performed the light-sheet experiments, A.B. performed the light-sheet image analysis, D.S. performed all transcriptomics experiments, M.B.S. designed transcription factor motifs analysis, D.S. and M.B.S. performed the analysis of RNA-seq data, M.B.S. and P.P. developed Griph, A.W. and G.R. performed the scRNA-seq analysis, U.M. performed the multiplexing experiments, P.L., D.S., U.M. and A.B. wrote the paper.

Competing interests A.B. and P.S. are co-founders of Viventis Microscopy Sàrl that commercializes the light-sheet microscope used in this study.

Additional information
Extended data is available for this paper at https://doi.org/10.1038/s41586-019-1146-y.
Supplementary information is available for this paper at https://doi.org/10.1038/s41586-019-1146-y.
Reprints and permissions information is available at http://www.nature.com/reprints.
Correspondence and requests for materials should be addressed to P.L.
Publisher's note: Springer Nature remains neutral with regard to jurisdictional claims in published maps and institutional affiliations.
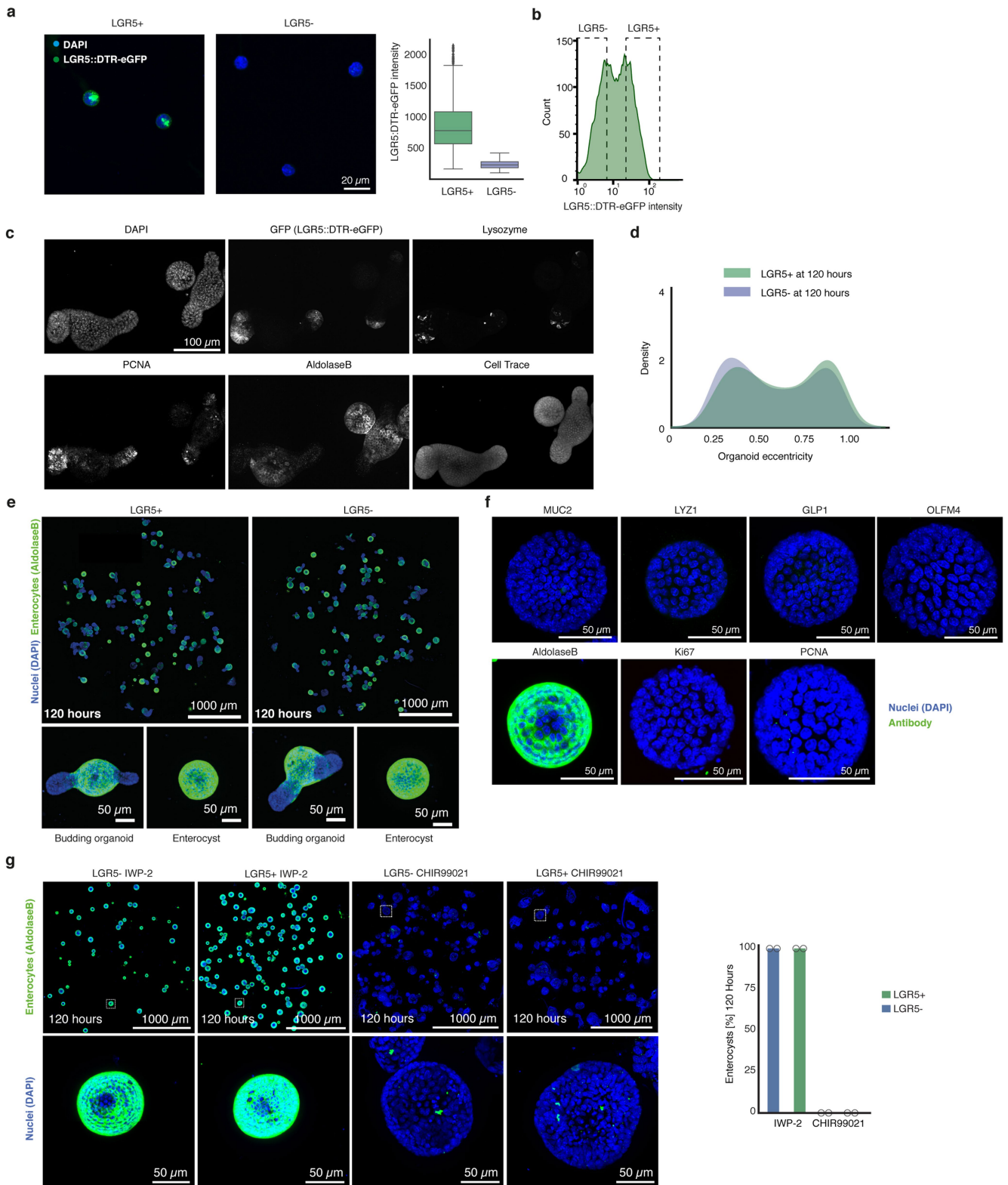
Extended Data Fig. 1 | See next page for caption.

Extended Data Fig. 1 | Intestinal development of LGR5$^+$ and LGR5$^-$ organoids. a, LGR5$^+$ and LGR5$^-$ single cells sorted from LGR5::DTR-eGFP reporter mouse 3 h after FACS (left), with box plot showing LGR5::DTR-eGFP intensity quantification (right) ($n = 602$ organoids for LGR5$^+$; $n = 576$ organoids for LGR5$^-$). Box plot elements show quartiles, and whiskers denote 1.5× the interquartile range. **b**, FACS histogram of GFP signal of LGR5::DTR-eGFP single cells. Dashed boxes depict gating. **c**, Representative images of 4i imaging showing the same organoids stained with DAPI, GFP, lysozyme, proliferating cell nuclear antigen (PCNA), aldolaseB and Cell Trace. **d**, Distribution of eccentricity at 120 h of development for LGR5$^+$ and LGR5$^-$ starting populations (LGR5$^+$ $n = 463$ organoids; LGR5$^-$ $n = 711$ organoids). **e**, Representative images of LGR5$^+$ and LGR5$^-$ cells at 120 h of development. Bottom, enlargements depict budding organoids and enterocysts. **f**, Representative images of enterocysts stained with DAPI, different cell-type and proliferation markers. **g**, Left, representative images of organoids grown from LGR5$^+$ and LGR5$^-$ single cells in the presence of Wnt signalling inhibition (IWP-2, 2 μM) or activation (CHIR99021, 5 μM). Organoids are fixed at 120 h and stained for nuclear marker (DAPI) and enterocyte marker (aldolaseB). Top row shows complete well overview; bottom row shows magnified examples of single organoid. Right, quantification of enterocysts at 120 h of organoid development after Wnt signalling inhibition (IWP-2, 2 μM) or activation (CHIR99021, 2 μM) ($n = 2$ replicates). Data are mean values.
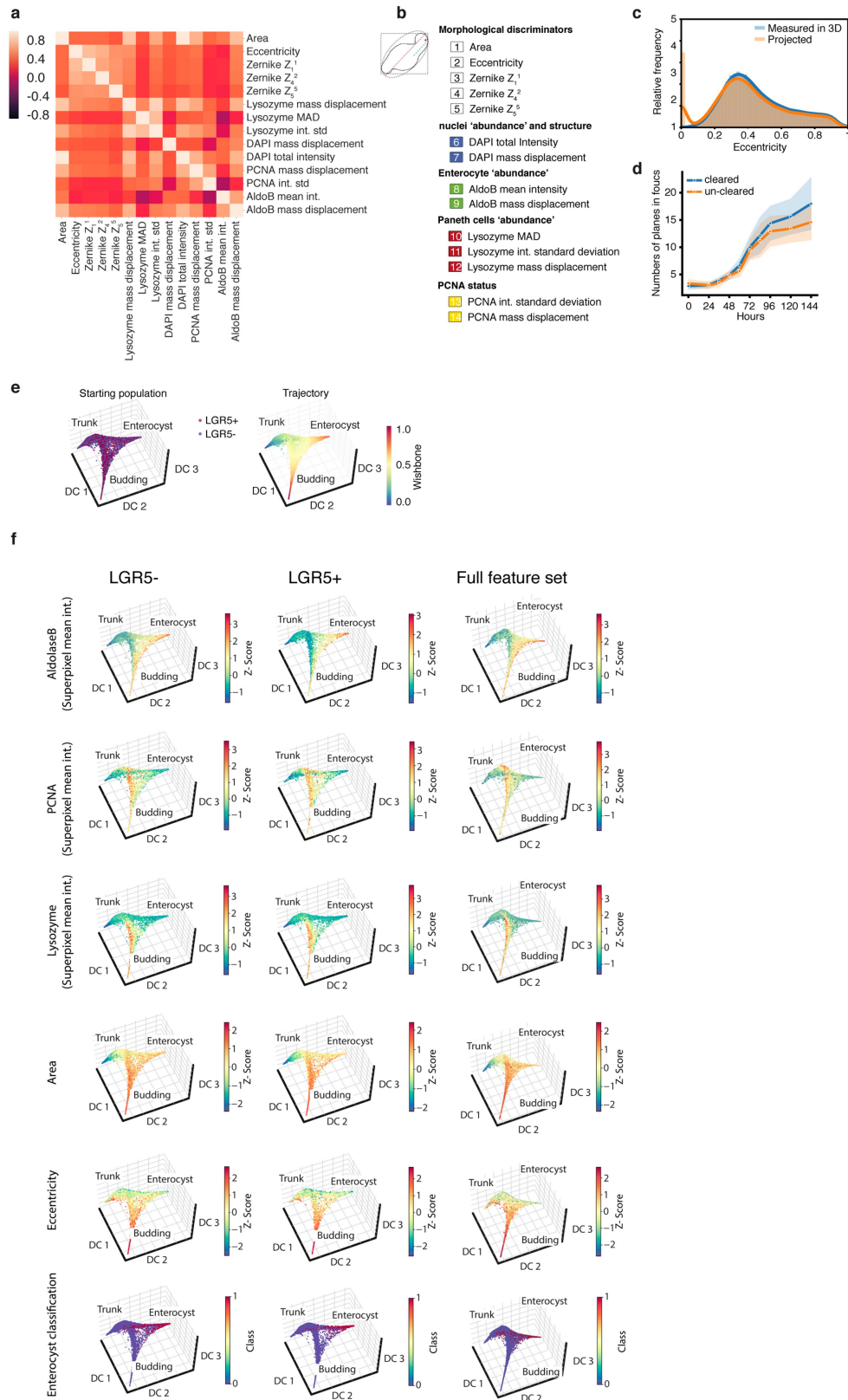
Extended Data Fig. 2 | Feature selection for organoid development.
a, Pearson correlation heat map of the 14 selected features used for trajectory inference ($n = 23,421$ organoids). **b**, Fourteen selected features are grouped based on the underlying information. **c**, Comparison between eccentricities calculated on projected images and on 3D volumes ($n = 16,175$ organoids). **d**, Number of in-focus planes at different time points in cleared and uncleared organoids ($n = 2,310$ organoids). Planes are classified as in-focus with a logistic regression using the ratio of maximum in-plane intensity to maximum intensity in the whole stack as feature. Shading denotes s.d. **e**, Diffusion maps for pooled LGR5^{+} and LGR5^{−} organoids (14 selected features, $n = 23,421$ organoids). Colour-coding denotes starting population and pseudotime. **f**, Diffusion maps for LGR5^{−} (first column, 14 selected features, $n = 13,623$) and LGR5^{+} (second column, 14 selected features, $n = 9,798$) organoids, and for the pooled dataset with the full feature set (third column, 66 features, $n = 23,421$). Colour-coding denotes enterocytes (aldolaseB), PCNA, Paneth cells (lysozyme), organoid area, eccentricity and enterocyst classification (in which class 1 denotes enterocysts).
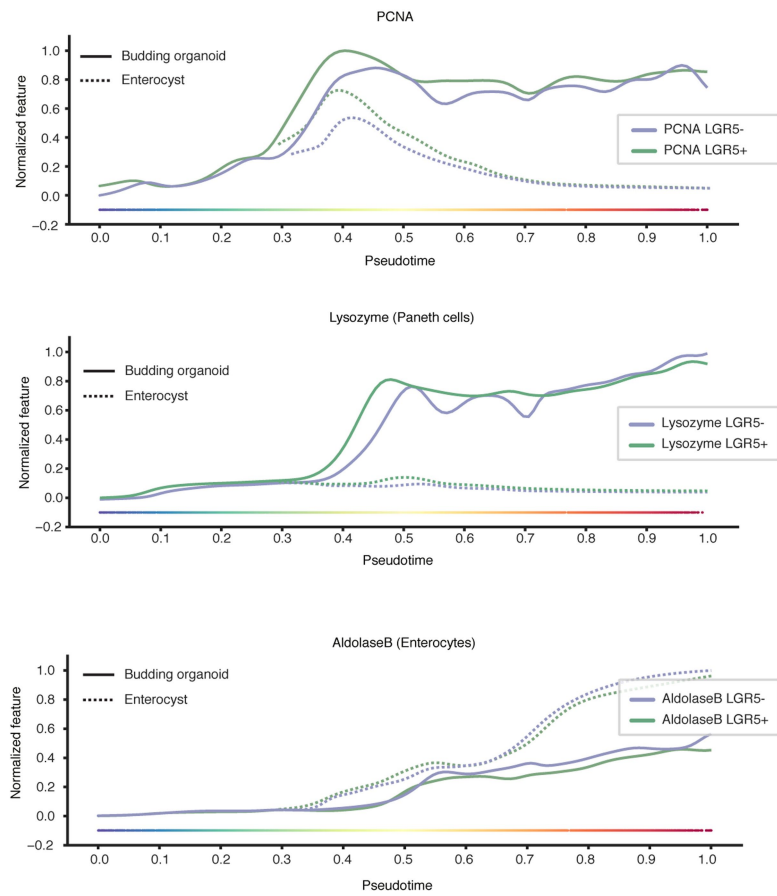
Extended Data Fig. 3 | Cell types and proliferation markers along organoid development trajectories. Proliferation (PCNA) and cell-type marker (lysozyme and aldolaseB) trends on pseudotime for LGR5^{+} ($n = 9,798$) and LGR5^{−} ($n = 13,623$) organoids.
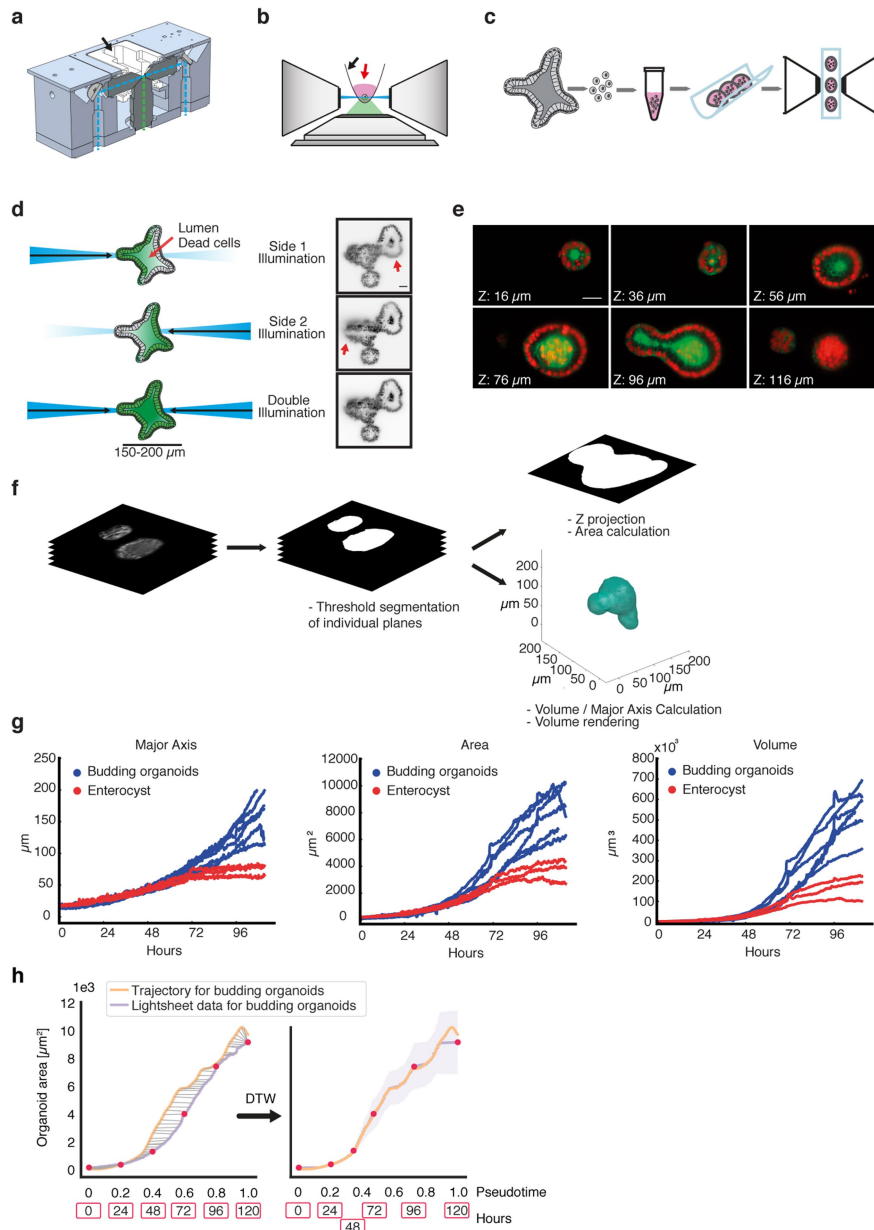
Extended Data Fig. 4 | Dual illumination inverted light-sheet imaging of organoids. a, Cross-sectional view of objective mounting block showing illumination paths (light blue dashed line) and imaging path (green dashed line). Illumination and imaging objective are solid mounted in the aluminium block and immersed in water contained in the reservoir (black arrow). **b**, Side view of microscope objectives arrangement: the sample embedded in Matrigel (red arrow) is held on the FEP membrane (black arrow) mounted in a sample holder and positioned between the two illumination objectives. **c**, Organoids handling procedure: grown organoids are dissociated and single cells are embedded in Matrigel. Several Matrigel drops can be transferred into the imaging chamber allowing imaging parallelization. **d**, Illustration of image improvement by double illumination. Scattering of single illumination beam by the

organoid prevents complete and homogenous illumination (red arrows). This problem is minimized by double illumination. Scale bar, 25 μm. **e**, Representative images of an organoid expressing H2b–mCherry (red) and membrane-bound GFP (green). Slices every 20 μm across the organoid volume are shown. Scale bar, 25 μm. **f**, Workflow of light-sheet data analysis. **g**, Morphological features (major axis, area and volume) derived from light-sheet imaging. Budding organoids $n = 6$, enterocysts $n = 3$. **h**, Dynamic time-warp mapping of light-sheet data onto the trajectory. Budding organoid branch for mean area progression inferred from the trajectory (orange line, $n = 23,421$) and mean area progression extracted from time-lapse light-sheet imaging (violet line, $n = 6$) before (left) and after (right) morphing. Red dots indicate positions of real time (h) relative to pseudotime. Shading denotes s.d.
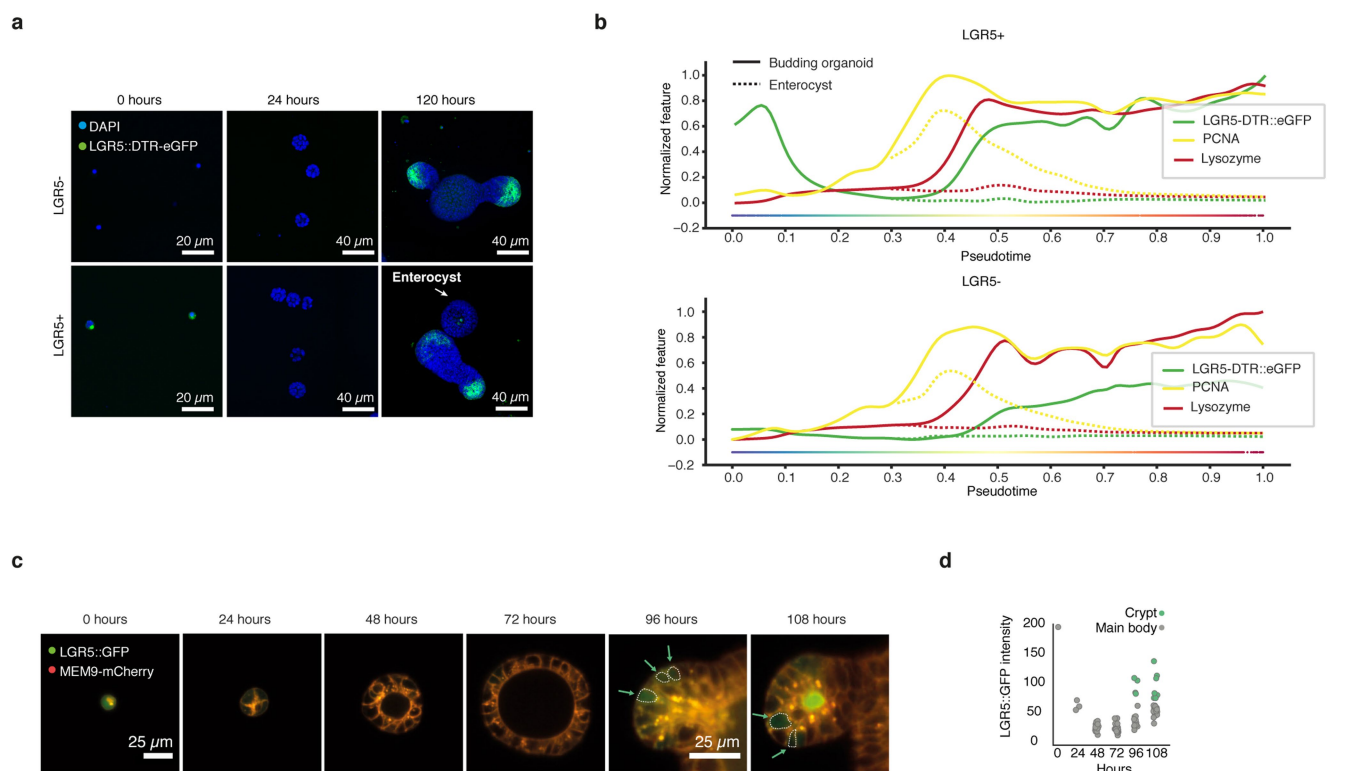
Extended Data Fig. 5 | LGR5 dynamics during organoid development.
a, Representative images of organoids grown from LGR5+ and LGR5−
starting populations at 0, 24 and 120 h of development. **b**, Cell types and
proliferation markers plotted on pseudotime for LGR5+ (top, $n = 9,798$)
and LGR5− (bottom, $n = 13,623$) starting populations. **c**, Light-sheet time-
lapse imaging of organoid formation starting from a single LGR5+ cell
(GFP signal) expressing membrane-bound mCherry (MEM9–mCherry).
Green arrows are pointing to cells re-acquiring GFP signal from LGR5
reporter in the organoid crypts. **d**, Quantification of GFP signal of LGR5
reporter from time lapse shown in **c**. Cells localized in the organoid crypt
are plotted in green, cells localized outside the crypt and on the main body
are plotted in grey ($n = 91$ cells).
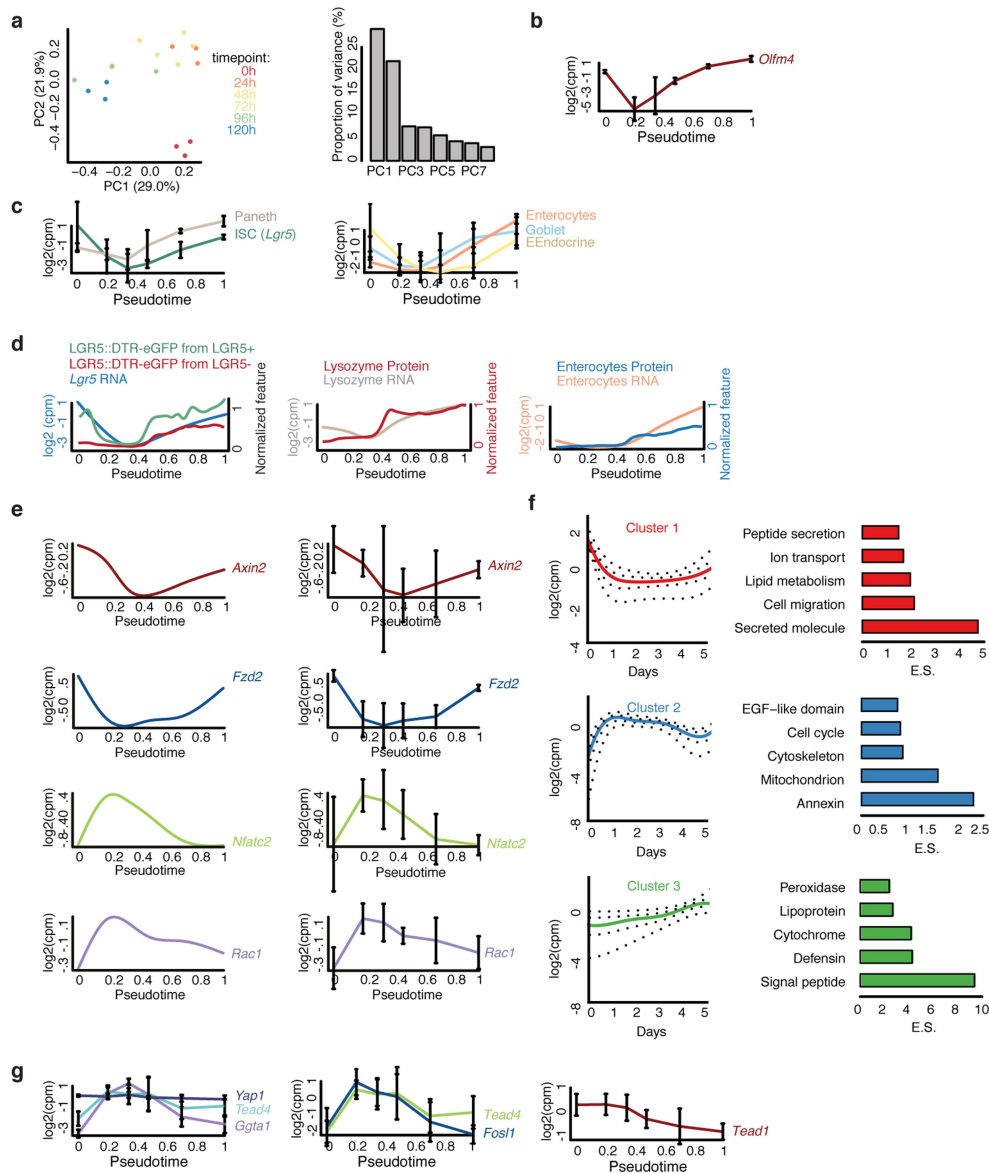
Extended Data Fig. 6 | Bulk RNA-seq analysis. a, Principal component analysis (PCA) analysis of time-course (0–120 h) bulk RNA-seq shows no mouse or batch effect ($n = 3$ biological replicates). **b**, Unsmoothed gene expression profile mapped on pseudotime trajectory of stem cell marker *Olfm4*. **c**, Unsmoothed gene expression profiles mapped on pseudotime trajectory of cell-type-specific genes. Paneth cell: *Lyz1*; ISC: *Lgr5*; enterocyte: *Apoc3*; goblet cell: *Muc2*; enteroendocrine cell: *Sst*. **d**, Left, protein abundance and gene expression profile of ISC marker *Lgr5* mapped on pseudotime trajectory. Middle, protein abundance and gene expression profile of Paneth cell marker *Lyz1* mapped on pseudotime trajectory. Right, protein abundance of enterocyte marker aldolaseB

and gene expression profile of enterocyte marker *Apoc3* mapped on pseudotime trajectory. **e**, Smoothed and unsmoothed gene expression profile of canonical Wnt target gene *Axin2*, *Fzd2* and non-canonical target genes *Nfatc2* and *Rac1*. **f**, Mean expression profile for each cluster and relative quantiles (0.05, 0.25, 0.50, 0.75 and 0.95). Annotation enrichments are shown on the right. E.S., enrichment score. **g**, Unsmoothed gene expression profile of *Yap1*, *Tead4* and *Ggta1* and top three transcription factors (*Tead1*, *Tead4* and *Fosl1*) contributing to differential gene expression between 24 h and 0 h. Data in **b**, **c**, **e**, **g** are mean and s.d. ($n = 3$ biological replicates).
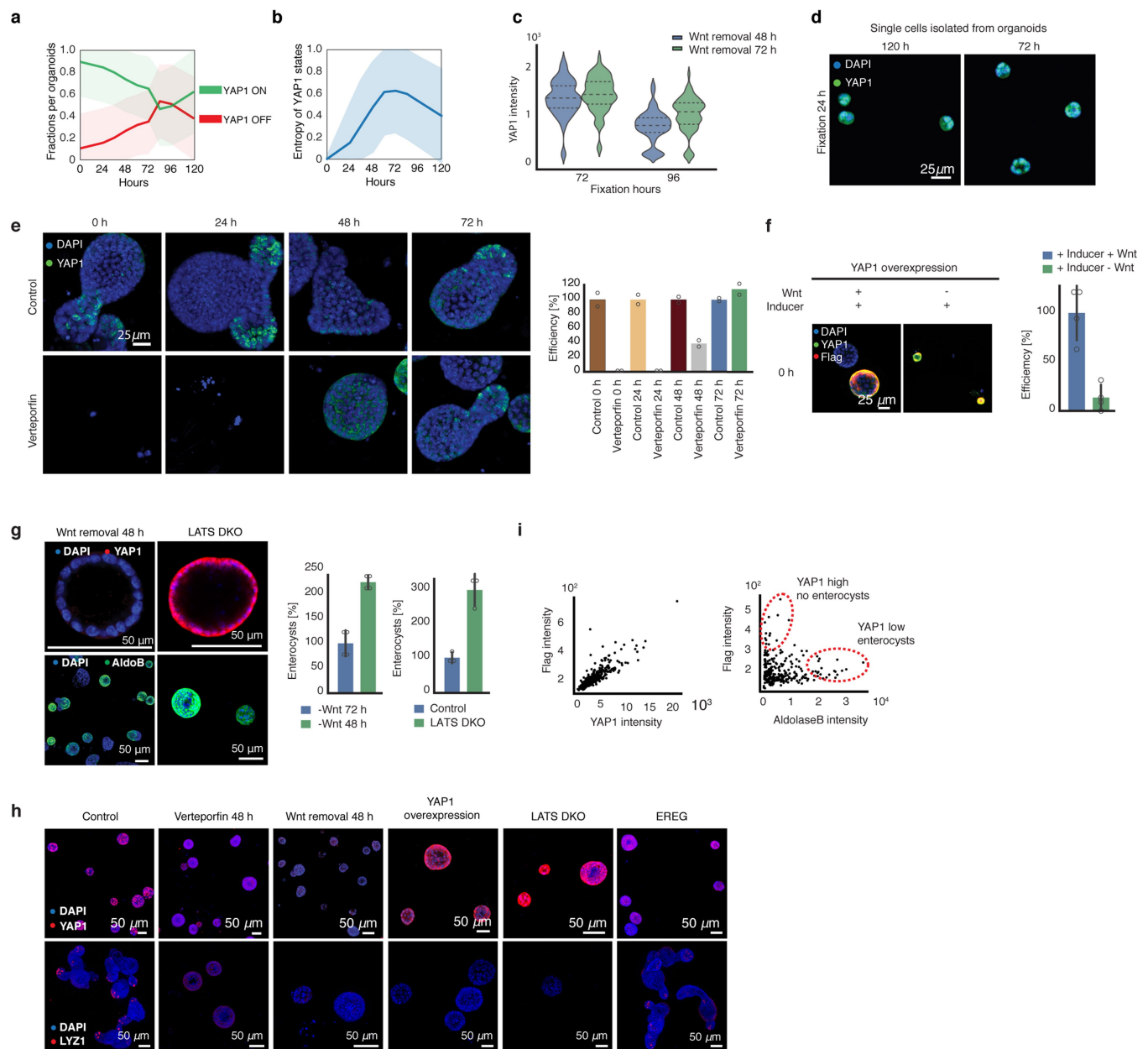
Extended Data Fig. 7 | YAP1 is necessary but not sufficient for organoid formation. a, Fraction of cells per organoid having YAP1 in the ON state (green, nuclear localization) or in the OFF state (red, cytoplasm localization) over time ($n = 1,074$ organoids). **b**, Entropy of YAP1 states (that is, variability in YAP1 activation in ON and OFF states) over time ($n = 1,074$ organoids). Shading denotes s.d. **c**, Quantification of YAP1 mean intensity after Wnt removal at 48 h or 72 h in organoids fixed at 72 h or 96 h ($n = 4$ replicates). Violin plot lines show quartiles. **d**, Images of organoids derived from single cells isolated from organoids at 72 h or at 120 h. **e**, Organoids treated at different time points with control or with verteporfin. Fixation at 96 h. Left, representative images; right, efficiency quantification (normalization: control, $n = 2$ replicates). Bar plots depict the mean. **f**, YAP1 overexpressing organoids with or without Wnt. Fixation at 96 h. Left, representative images; right, efficiency quantification (normalization: control, $n = 4$ replicates). $P = 0.001$,

two-sided t-test. **g**, Left, images of organoids with Wnt removal at 48 h, or after double knockout of LATS1 and LATS2 (LATS DKO). Top, fixation at 72 h. Bottom, fixation at 96 h (Wnt removal at 48 h) or 120 h (LATS DKO). Right, quantification of enterocysts as retrieved in the left panel ($n = 4$ replicates for Wnt removal at 48 h; $n = 3$ replicates for LATS DKO). $P = 0.0001$ (Wnt removal); $P = 0.002$ (LATS DKO), two-sided t-test. **h**, Representative images of control, verteporfin treatment at 48 h, Wnt removal at 48 h, YAP1 overexpression, LATS DKO or treatment with EREG at 0 h. Top, fixation at 72 h; bottom, fixation at 96 h (Wnt removal at 48 h, YAP1 overexpression, LATS DKO) or 120 (control, verteporfin 48 h, EREG). **i**, Scatter plot of Flag mean intensity signal and YAP1 mean intensity signal (left) and of Flag mean intensity and aldolaseB mean intensity (right) in YAP1-overexpressing organoids at 96 h. Data are mean ± s.d.
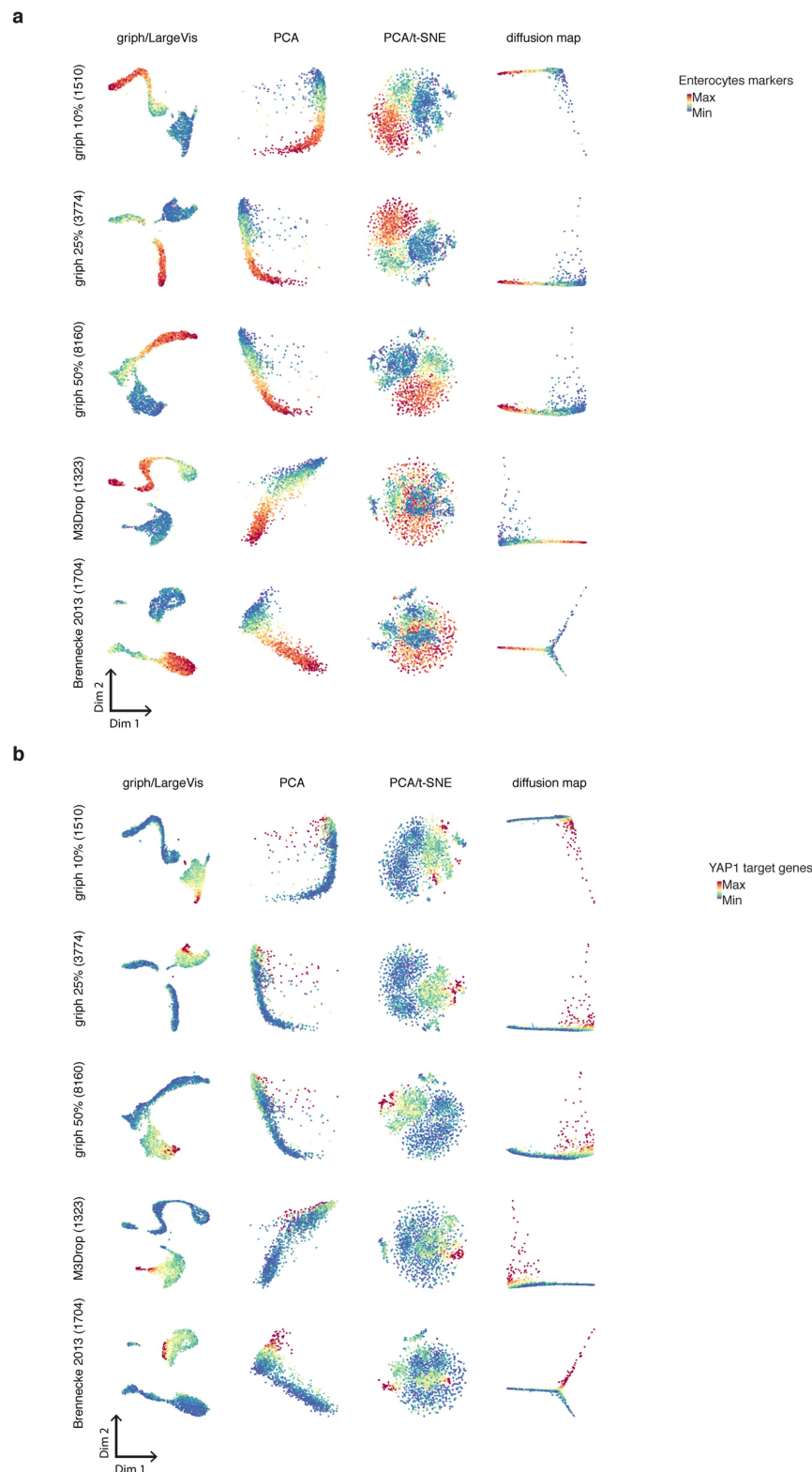
Extended Data Fig. 8 | Griph robustness analysis and comparison to other methods. Comparison of Griph lower dimensional embedding (Griph/LargeVis) to different embedding approaches (PCA, PCA combined with distributed stochastic neighbor embedding (*t*-SNE), diffusion maps) and analysis of method sensitivity for variable gene selection. Five different sets of variable genes have been selected (using Griph to retain 10%, 25% or 50% of genes per bin, by Michaelis–Menten fitting of the gene dropout rates as implemented in M3Drop, or by the previously described mean-variance fitting procedure[48]) and analysed. **a**, **b**, First and second dimension are shown and results are colour-coded for enterocyte marker genes (as in Extended Data Fig. 9b) (**a**) and YAP1 target genes (as in Fig. 5b) (**b**). *n* = 1,863 cells.

48. Brennecke, P. et al. Accounting for technical noise in single-cell RNA-seq experiments. *Nat. Methods* **10**, 1093–1095 (2013).
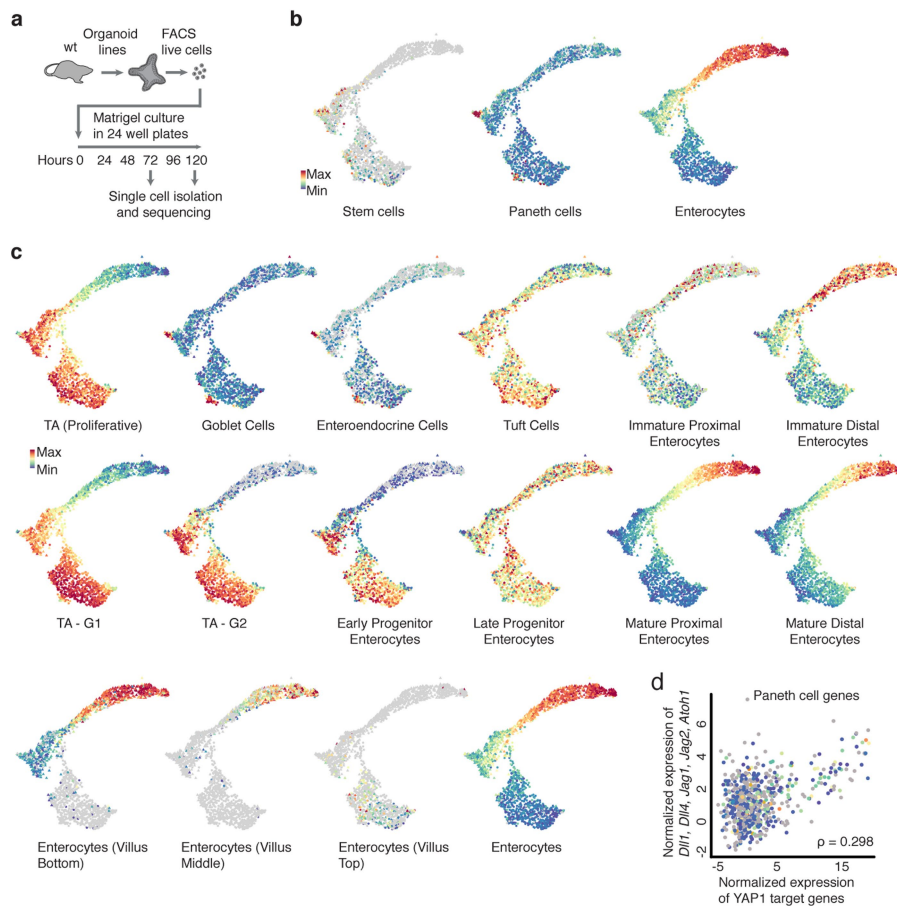
Extended Data Fig. 9 | scRNA analysis. a, Experimental workflow for scRNA-seq. **b**, Griph-based visualization of single-cell degree of expression of marker genes for stem cells, Paneth cells and enterocytes. **c**, Griph-based visualization of single-cell degree of expression of marker genes for transient-amplifying cells, goblet cells, enteroendocrine cells, tuft cells, immature proximal enterocytes, immature distal enterocytes, transient-amplifying cells G1-phase, transient amplifying cells G2-phase, early progenitor enterocytes, late progenitor enterocytes, mature proximal enterocytes, mature distal enterocytes, enterocytes (villus bottom), enterocytes (villus middle), enterocytes (villus top) and enterocytes. **d**, Spearman correlation between expression of YAP1 target genes and expression of *Dll1*, *Dll4*, *Jag1*, *Jag2* and *Atoh1* in single cells at 120 h not expressing Paneth, goblet, enteroendocrine, enterocyte and stem-cell markers ($n = 696$ cells).
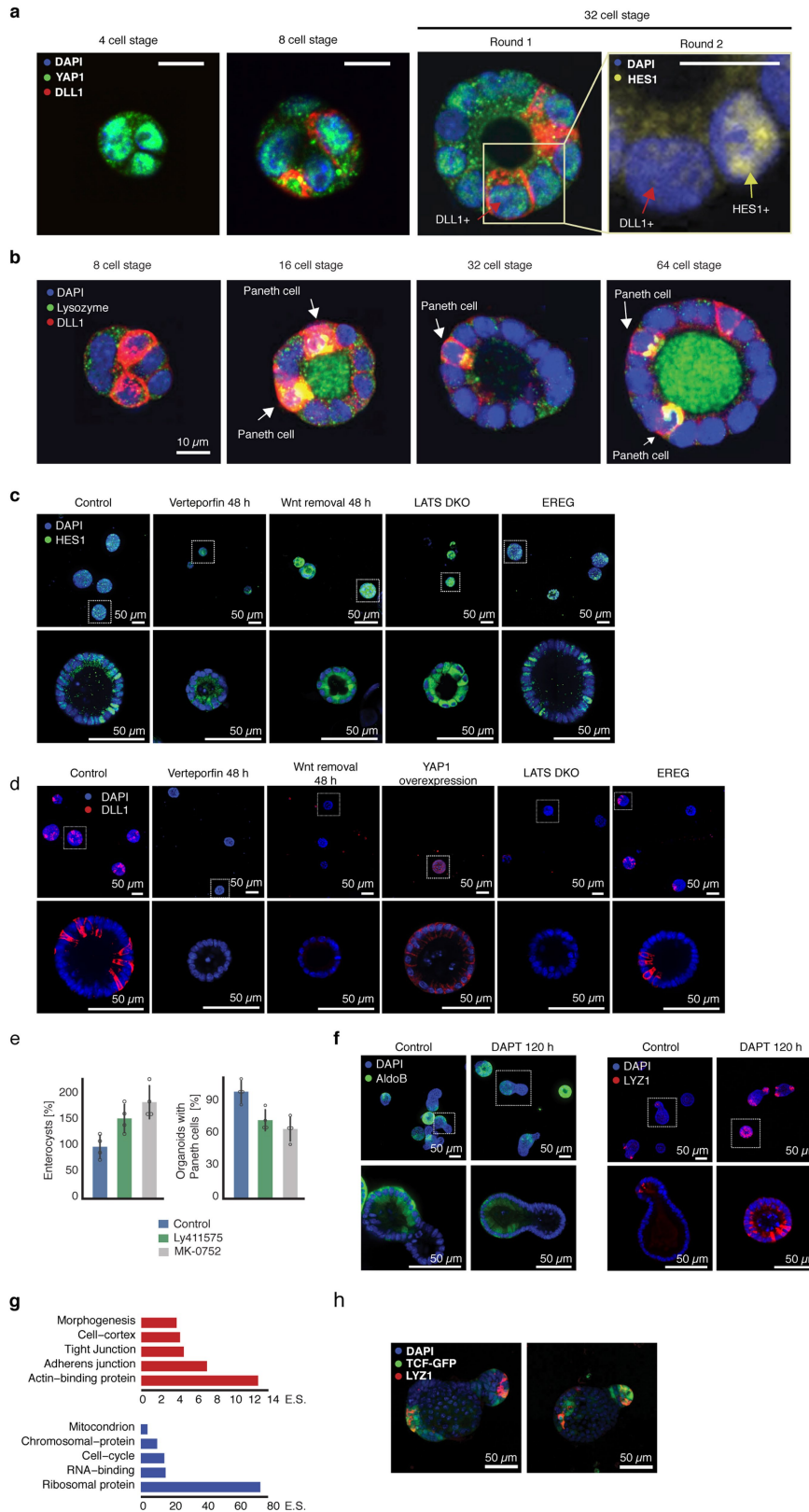
Extended Data Fig. 10 | See next page for caption.

Extended Data Fig. 10 | YAP1 cell-to-cell variability allows a Notch–DLL1 event and symmetry breaking. a, Images showing YAP1 variability and DLL1$^+$ cells. Magnified view denotes nuclear localization of HES1 in the same organoid. Arrows: red (DLL1$^+$ cells), yellow (HES1$^+$ cells). Scale bar, 10 μm. **b**, Images showing overlap of Paneth cells with DLL1$^+$ cells. **c**, MIP images (top) and magnified single plane images (bottom) of: control, verteporfin addition at 48 h, Wnt removal at 48 h, LATS double-knockout (DKO) and EREG treatment. Organoids are fixed at 72 h. **d**, MIP images (top) and magnified single plane images (bottom) of: control, verteporfin addition at 48 h, Wnt removal at 48 h, YAP1 overexpression, LATS DKO and EREG treatment. Organoids are fixed at 72 h. **e**, Fraction of enterocysts (left) and fraction of organoids with Paneth cells (right) for control and organoids treated with Ly411575 or MK-0752 at 0 h. Fixation at 120 h (normalization: control, $n = 4$ replicates). Ly411575 $P = 0.009$; MK-0752 $P = 0.003$, two-sided t-test. Data are mean $\pm$ s.d. **f**, MIP images (top) and magnified single plane images (bottom) of organoids treated with control or DAPT at 120 h and fixed at 144 h and stained for AldoB (left) or LYZ (right) **g**, Top, annotation enrichment of genes correlated with expression of YAP1 target genes in cells expressing YAP1 target genes and *Dll1*, *Dll4*, *Jag1*, *Jag2* and *Atoh1* genes. Bottom, annotation enrichment of genes anti-correlated with YAP1 target genes expression in cells expressing YAP1 target genes and *Dll1*, *Dll4*, *Jag1*, *Jag2* and *Atoh1* genes. E.S., enrichment score. **h**, MIP images of organoids at 120 h, showing the canonical Wnt signalling response (TCF–GFP) in cells neighbouring Paneth cells.

nature research

Corresponding author(s): Prisca Liberali

Last updated by author(s): Mar 6, 2019

Reporting Summary

Nature Research wishes to improve the reproducibility of the work that we publish. This form provides structure for consistency and transparency in reporting. For further information on Nature Research policies, see Authors & Referees and the Editorial Policy Checklist.

Statistics

For all statistical analyses, confirm that the following items are present in the figure legend, table legend, main text, or Methods section.

n/a	Confirmed	
☐	☒	The exact sample size (n) for each experimental group/condition, given as a discrete number and unit of measurement
☐	☒	A statement on whether measurements were taken from distinct samples or whether the same sample was measured repeatedly
☐	☒	The statistical test(s) used AND whether they are one- or two-sided *Only common tests should be described solely by name; describe more complex techniques in the Methods section.*
☐	☒	A description of all covariates tested
☐	☒	A description of any assumptions or corrections, such as tests of normality and adjustment for multiple comparisons
☐	☒	A full description of the statistical parameters including central tendency (e.g. means) or other basic estimates (e.g. regression coefficient) AND variation (e.g. standard deviation) or associated estimates of uncertainty (e.g. confidence intervals)
☐	☒	For null hypothesis testing, the test statistic (e.g. F, t, r) with confidence intervals, effect sizes, degrees of freedom and P value noted *Give P values as exact values whenever suitable.*
☒	☐	For Bayesian analysis, information on the choice of priors and Markov chain Monte Carlo settings
☒	☐	For hierarchical and complex designs, identification of the appropriate level for tests and full reporting of outcomes
☐	☒	Estimates of effect sizes (e.g. Cohen's d, Pearson's r), indicating how they were calculated

Our web collection on statistics for biologists contains articles on many of the points above.

Software and code

Policy information about availability of computer code

Data collection   To collect imaging data, custom written segmentation code was used. The code was written in the Liberali lab and implemented with MATLAB 2016b (MathWorks) or Python 3.6 (relying on multiple open source Python libraries for scientific computing and image analysis). To collect imaging data Wako Software Suite version 1 was used. CellRanger suite 1.3.0 was used to collect sequencing data.

Data analysis   To analyze imaging data, Fiji (version 1.0) as well as custom written code in MATLAB 2016b (MathWorks) and Python 3.6 ((relying on multiple open source Python libraries for scientific computing and image analysis) was used. To analyze RNA-seq data, custom written R code (exact packages and parameters are described in the methods), STAR (version 2.5.2b), Griph 0.1.1, DAVID Bioinformatics Resources 6.8, JASPAR2016 Bioconductor package (version 1.6) was used.

For manuscripts utilizing custom algorithms or software that are central to the research but not yet described in published literature, software must be made available to editors/reviewers. We strongly encourage code deposition in a community repository (e.g. GitHub). See the Nature Research guidelines for submitting code & software for further information.

Data

Policy information about availability of data

All manuscripts must include a data availability statement. This statement should provide the following information, where applicable:
- Accession codes, unique identifiers, or web links for publicly available datasets
- A list of figures that have associated raw data
- A description of any restrictions on data availability

All data are available in the manuscript or the supplementary materials. All the custom-code is available on GitHub. All genomic data of figure 4 are in Table 1 and all single cell-genomic data of figure 6

Field-specific reporting

Please select the one below that is the best fit for your research. If you are not sure, read the appropriate sections before making your selection.

☒ Life sciences   ☐ Behavioural & social sciences   ☐ Ecological, evolutionary & environmental sciences

For a reference copy of the document with all sections, see nature.com/documents/nr-reporting-summary-flat.pdf

Life sciences study design

All studies must disclose on these points even when the disclosure is negative.

Sample size	No sample size calculations were performed. In most cases, we assumed a minimum of around 100 organoids would be sufficient to recognize differences between control and perturbations based upon historical experiments in other contexts. In the time course experiments thousands of organoids were analyzed. Thousands of cells have been used for each time point of the single cell RNA sequencing
Data exclusions	Exclusion criteria for segmentation and RNA seq experiments were pre-defined. Parameters used to exclude datapoints were defined based on data distributions. Some organoids with segmentation artefact were excluded from the analysis with Z-score filtering. In the single cell RNA sequencing analysis high quality cells have been selected based on the maximum second derivative of the UMI count distribution, and genes with 0 counts or negligible variance (coefficient of variation, CV< 0.001) across all libraries were removed. In the bulk RNA sequencing analysis genes with less than two samples with at least one read per million reads were removed.
Replication	All experiments were replicated at least twice (if not indicated otherwise under Statistics and reproducibility) with similar finding. Multiplexing experiments and single cell RNAseq were only repeated once due to prohibitive costs.
Randomization	Samples were randomly assigned.
Blinding	The same investigators both performed experiments and data analyses therefore blinding was possible.

Reporting for specific materials, systems and methods

We require information from authors about some types of materials, experimental systems and methods used in many studies. Here, indicate whether each material, system or method listed is relevant to your study. If you are not sure if a list item applies to your research, read the appropriate section before selecting a response.

Materials & experimental systems

n/a	Involved in the study
☐	☒ Antibodies
☒	☐ Eukaryotic cell lines
☒	☐ Palaeontology
☐	☒ Animals and other organisms
☒	☐ Human research participants
☒	☐ Clinical data

Methods

n/a	Involved in the study
☒	☐ ChIP-seq
☐	☒ Flow cytometry
☒	☐ MRI-based neuroimaging

Antibodies

Antibodies used	anti-AldolaseB (Abcam ab75751, clone EPR3138Y, various lots for example GR121452-7, dilution 1:300), anti-Yap (Cell signaling technology mAB #14074, clone D8H1X, lot #4, dilution 1:200), anti-FLAG (Sigma-Aldrich F1804, clone M2, lot SLBT765, dilution 1:500), anti-Lysozyme (DAKO A0099, clone NA (Polyclonal), lot 20040597, dilution 1:400), anti-Dll1 (R&D Systems AF3970, clone NA (Polyclonal), various lots for example YXZ0114081, dilution 1:100), anti-Hes1 (Cell signaling technology mAB #11988, clone D6P2U, lot #3, dilution 1:100), anti-GFP (Abcam ab5450, clone NA (Polyclonal), lot GR3215617-1, dilution 1:500), anti-PCNA (Cell signaling technology mAb #2586, clone PC10, lot #5, dilution 1:600), anti-Muccin2 (Santa Cruz #SC-15334, clone NA (Polyclonal), lot K0315 no longer available, dilution 1:200), anti-Glp1 (Abcam ab111125, clone EPR4042-407, lot GR74272, dilution 1:200), anti-Olfm4 (Cell signaling technology mAB #39141, clone D6Y5A, lot #1, dilution 1:100), anti-Ki67 (Abcam ab16667, clone SP6, lot GR216200-1, dilution 1:200), Alexa Fluor 488 donkey anti rabbit IgG (Thermo fisher scientific A-21206, clone NA (Polyclonal), lot 1981155, dilution 1:500), Alexa Fluor 568 donkey anti rabbit IgG (Thermo fisher scientific A10042, clone NA (Polyclonal), lot 1964370, dilution 1:500), Alexa Fluor 488 donkey anti mouse IgG (Thermo fisher scientific A-21202, clone NA (Polyclonal), lot 1890861, dilution 1:500), Alexa Fluor 568 donkey anti mouse IgG (Thermo fisher scientific A10037, clone NA (Polyclonal), lot 1752099, dilution 1:500), Alexa Fluor 488 donkey anti goat IgG (Thermo fisher scientific A-11055, clone NA (Polyclonal), lot 1827671, dilution 1:500), Alexa Fluor 568 donkey anti goat IgG (Thermo fisher scientific A-11057, clone NA (Polyclonal), lot 1711491, dilution 1:500),

Alexa Fluor 488 donkey anti sheep IgG (Thermo fisher scientific A-11015, clone NA (Polyclonal), lot 1900213, dilution 1:500),
Alexa Fluor 568 donkey anti sheep IgG (Thermo fisher scientific A-21099, clone NA (Polyclonal), lot 1878508, dilution 1:500),
Alexa Fluor 647 donkey anti sheep IgG (Thermo fisher scientific A-21448, clone NA (Polyclonal), lot 1914541, dilution 1:500).

Validation

Validation statements available from manufacturers:
AldolaseB (https://www.abcam.com/aldolase-b-antibody-epr3138y-ab75751.html),
anti-Yap (https://www.cellsignal.com/products/primary-antibodies/yap-d8h1x-xp-rabbit-mab/14074),
anti-FLAG (https://www.sigmaaldrich.com/catalog/product/sigma/f1804?
lang=de&region=CH&gclid=EAIaIQobChMIyfGH3oXr3wIVC-aaCh3l3ALcEAAYASAAEgIdnfD_BwE),
anti-Lysozyme (https://www.agilent.com/en/product/immunohistochemistry/antibodies-controls/primary-antibodies/lysozyme-ec-3-2-1-17-(concentrate)-76124),
anti-Dll1 (https://www.rndsystems.com/products/mouse-rat-dll1-antibody_af3970,
additional validated in ref: "Distinct expression patterns of Notch ligands, Dll1 and Dll4, in normal and in inflamed mice intestine"),
anti-Hes1 (https://www.cellsignal.com/products/primary-antibodies/hes1-d6p2u-rabbit-mab/11988,
additional mouse intestinal crypt Immunohistochemistry shown in ref: "Paneth Cell Multipotency Induced by Notch Activation following Injury"),
anti-GFP (https://www.abcam.com/gfp-antibody-ab5450.html),
anti-PCNA (https://www.cellsignal.com/products/primary-antibodies/pcna-pc10-mouse-mab/2586),
anti-Muccin2 (Santa Cruz #SC-15334, No longer available from Santa Cruz),
anti-Glp1 (https://www.abcam.com/glp1-antibody-epr4042-407-ab111125.html),
anti-Olfm4 (https://www.cellsignal.com/products/primary-antibodies/olfm4-d6y5a-xp-rabbit-mab-mouse-specific/39141),
anti-Ki67 (https://www.abcam.com/ki67-antibody-sp6-ab16667.html),
Alexa Fluor 488 donkey anti rabbit IgG (https://www.thermofisher.com/antibody/product/Donkey-anti-Rabbit-IgG-H-L-Highly-Cross-Adsorbed-Secondary-Antibody-Polyclonal/A-21206),
Alexa Fluor 568 donkey anti rabbit IgG (https://www.thermofisher.com/antibody/product/Donkey-anti-Rabbit-IgG-H-L-Highly-Cross-Adsorbed-Secondary-Antibody-Polyclonal/A10042),
Alexa Fluor 488 donkey anti mouse IgG (https://www.thermofisher.com/antibody/product/Donkey-anti-Mouse-IgG-H-L-Highly-Cross-Adsorbed-Secondary-Antibody-Polyclonal/A-21202)
Alexa Fluor 568 donkey anti mouse IgG (https://www.thermofisher.com/antibody/product/Donkey-anti-Mouse-IgG-H-L-Highly-Cross-Adsorbed-Secondary-Antibody-Polyclonal/A10037),
Alexa Fluor 488 donkey anti goat IgG (https://www.thermofisher.com/antibody/product/Donkey-anti-Goat-IgG-H-L-Cross-Adsorbed-Secondary-Antibody-Polyclonal/A-11055),
Alexa Fluor 568 donkey anti goat IgG (https://www.thermofisher.com/antibody/product/Donkey-anti-Goat-IgG-H-L-Cross-Adsorbed-Secondary-Antibody-Polyclonal/A-11057),
Alexa Fluor 488 donkey anti sheep IgG (https://www.thermofisher.com/antibody/product/Donkey-anti-Sheep-IgG-H-L-Cross-Adsorbed-Secondary-Antibody-Polyclonal/A-11015),
Alexa Fluor 568 donkey anti sheep IgG (https://www.thermofisher.com/antibody/product/Donkey-anti-Sheep-IgG-H-L-Cross-Adsorbed-Secondary-Antibody-Polyclonal/A-21099)
Alexa Fluor 647 donkey anti sheep IgG (https://www.thermofisher.com/antibody/product/Donkey-anti-Sheep-IgG-H-L-Cross-Adsorbed-Secondary-Antibody-Polyclonal/A-21448).

Animals and other organisms

Policy information about studies involving animals; ARRIVE guidelines recommended for reporting animal research

Laboratory animals

Male and female outbred mice between 7 and 15 weeks old were used for all experiments. Mouse lines used: C57BL/6 wild type (Charles River Laboratories), Lgr5–EGFP–Ires–CreERT2 (kind gift from Momo Bentires-Alj, University Hospital in Basel), Lgr5::DTR-EGFP (Genentech, de Sauvage laboratory), H2B-mCherry C57BL/6 x C3H F1 females heterozygous for H2B-mCherry (kind gift from T. Hiragi lab, EMBL), Lats1/; Lats2/ (LATS DKO, kind gift from Jeff Wrana, Department of Molecular Genetics, University of Toronto, Canada)48, Yap1tm1.1Dupa/J (Yap1flox)49 from The Jackson Laboratory.

Wild animals

The study did not involve wild animals

Field-collected samples

The study did not involve samples collected from the field

Ethics oversight

All animal experiments were approved by the Basel Cantonal Veterinary Authorities and conducted in accordance with the Guide for Care and Use of Laboratory Animals.

Note that full information on the approval of the study protocol must also be provided in the manuscript.

Flow Cytometry

Plots

Confirm that:

☒ The axis labels state the marker and fluorochrome used (e.g. CD4-FITC).

☒ The axis scales are clearly visible. Include numbers along axes only for bottom left plot of group (a 'group' is an analysis of identical markers).

☒ All plots are contour plots with outliers or pseudocolor plots.

☒ A numerical value for number of cells or percentage (with statistics) is provided.

Methodology

Sample preparation	Murine organoids were collected 5-7 days after passaging and digested with TripLE (Invitrogen) for 20 min at 37 °C. Dissociated cells were passed through a cell strainer with a pore size of 20 μm.
Instrument	BD Influx cell sorter (Becton Dickinson) and BD FACS Aria III
Software	For collection the BD FACS Sortware 1.2.0.142 (for BD Influx cell sorter) or BD FACS Diva 8.0.1 (for BD FACS Aria III). To visualize the gating in Extended Data Figure 1b, FLOWJO (FLOWJO, LLC) in version 10.2 was used.
Cell population abundance	After final gating, for both Lgr5- and Lgr5+, the average abundance was around 10%. Purity of Lgr5+ and Lgr5- cells was determined by fixation of plated cells and quantification of the Lgr5:DTR-EGFP signal 3h after sorting (see Extended data figure 1a)
Gating strategy	To remove debris, dead cells and cell doublets SSC-A/FSC-A gating, SSC-H/SSC-W gating and FSC-H/FSC-W gating were used. Lgr5+ and Lgr5- populations were separated based on the Lgr5:DTR-EGFP intensity (Extended data figure 1b).

☒ Tick this box to confirm that a figure exemplifying the gating strategy is provided in the Supplementary Information.

Chapter 4: Discussion

The enduring question of how cellular systems become structured by their own internal processes is a long-standing conundrum in stem cell and developmental biology[212]. It has for long been hindered by the technical difficulties to address it[17]. During my PhD, I used small intestinal organoids as a framework for self-organization and symmetry breaking to gain first insights into the mechanisms underlying the self-organizing capacity of adult intestinal cells. My main achievement was developing a high-throughput multiplexed imaging and analysis pipeline for fixed organoid samples which allows inferring the quantitative features for thousands of organoids. These paved the way for the first quantitative in-depth image based analysis of intestinal organoid development from a single cell into budding organoids at the single cell and tissue level. Combining multiplexed imaging analysis with live imaging, sequencing and perturbation approaches, we show (in **Chapter 3**) that different starting populations dedifferentiate into a common fetal-like intermediate state. Thus, reinforcing the concept of cellular plasticity of the intestine. We demonstrate that this first step resembles regeneration *in vivo* and is driven by homogenous YAP1 activity. After the 4-cell stage YAP1 subcellular localization becomes heterogeneous between individual cells. We show that this heterogeneity is required for the appearance of Paneth cells, which is mediated by Notch-Delta lateral inhibition, and thus for symmetry breaking to occur.

In the first part of this discussion, I will briefly focus on multiplexed imaging and multivariate analysis and how this work contributes to the field of organoid research. In a second part, I will enlarge upon how our findings (presented in **Chapter 3**) aid to answer the questions posed in the introduction: Do distinct starting cells go through a common intermediate state? Which signaling pathways and gene networks underlie intestinal organoid development and what drives symmetry breaking? Finally, I will conclude with my perspective on the relevance of our finding in a broader context of organoid research and translational medicine. Throughout the discussion, I will propose future directions for subsequent research based on the findings of the current work.

High-throughput imaging to study organoid development

Compared to *in vivo* systems, organoids have the advantage that they are easy expandable and amendable for imaging. One major bottleneck of current organoid research is however low reproducibility in terms of morphological outcome and maturity of the final organoids[79]. In small intestinal organoids, a broad distribution of morphological traits emerges over the five days of organoid development. Individual organoids develop with different paces and only a subset of organoids breaks symmetry **(Chapter 3, Fig. 1d-g).** Likewise, although all budding organoids reconstitute the stereotypic crypt-villus morphology of the small intestine, the number of crypts per organoid, their spatial arrangement and cell type composition can be very diverse **(Chapter 3, Fig. 1b).** Although different phenotypes give insights into distinct molecular mechanism, size, shape and marker diversity within the culture is often largely ignored[213].

To cover most of the observed phenotypes and reconstruct the processes that lie at the root of the observed differences requires the sampling of hundreds of organoids. To distinguish different organoid phenotypes, each organoid need to be described with a set of multivariate features taking into account spatial cell arrangement and cell type diversity. High throughput imaging of fixed samples combined with computer vision approaches to segment and extract characteristic features for each object is well equipped to this task[214]. This combination allows following various complex processes in two-dimensional cell cultures including virus infection[63], control of transcript variability[42] or subcellular organization[65]. However, examples for its usage in three-dimension organoid cultures are sparse[215] and so far, often focused on drug screening applications. With few exceptions (Lukonin et al., under revision) one read-out such as cell viability[216] or organoid swelling[217] is used to characterize each organoid.

4i imaging in organoids

We show that multiplexed iterative indirect immunofluorescence imaging (4i)[65] combined with computer vision based segmentation and multivariate feature extraction (see also **Chapter 1, Imaging to study intestinal self-organization**) can be a powerful approach to study intestinal organoid development. 4i multiplexing allows with a simple and fast protocol to expand four color imaging to multiple rounds of antibody staining. Our current implementation of 4i for three-dimensional tissue cultures enables us to multiplex up to six rounds reliably **(Fig. 8)**. However multiple rounds of acquisition lead to sample degradation and epitope loss, rendering the use of certain antibodies in later rounds impossible. Both problems have already been observed for most elution based multiplexing approaches[65,218]. Because organoids are three-dimensional tissues embedded in a semi-stable matrix,

compared to flat layers of attaching cells, they require harsher elution conditions. This treatment leads to translational and rotational movements or even sometimes loss of organoids between individual imaging rounds. To circumvent such limitations and increase multiplexing capacity, one could improve sample stability by using intramolecular epoxide linkages[219] or crosslinking of a three-dimensional network of hydrophilic polymers[220] to better tether the organoids and the extracellular matrix. In addition, promising DNA-barcoded antibody based methods, which do not rely on antibody elution steps, have recently been reported and should be tested for three-dimensional organoid structures[221,222] (for advantages and disadvantages see **Chapter 2**).
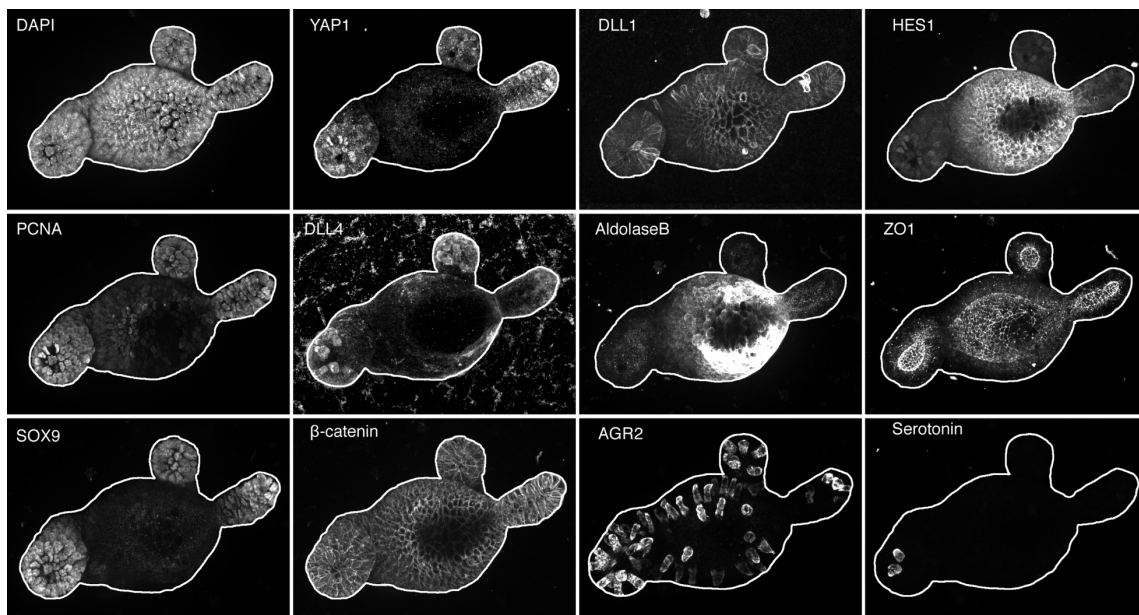
Fig. 8 | 4i applied to intestinal organoids. Maximum intensity projection images showing the same organoid imaged over six sequential multiplexing rounds. Round 1 (DAPI, YAP1, DLL1); Round 2 (HES1, PCNA), Round 3 (DLL4), Round 4 (AldolaseB, ZO1), Round 5 (SOX9, β-catenin), Round 6 (AGR2, Serotonin). White lines indicate organoid outlines. Experiment conducted as described in the appendix section.

Trajectories of stereotypic organoid growth

Our 4i imaging and feature extraction pipeline creates vast amounts of information to characterize thousands of heterogeneous organoids based on a characteristic set of multivariate features. These features include shape descriptors and intensity measurements to approximate protein expression and localization. In contrast to live imaging, fixation comes, however, with the flipside that each organoid is only measured at one specific time point of its development[204]. The dynamic information how molecular markers change along organoid development is lost.

I approached this limitation by using trajectory inference **(Chapter 3, Fig. 2a, b)**, which for the first time allowed the reconstruction of organoid development into distinct branches:

budding organoids and enterocsyts. With this method, we were able to follow dynamic changes of markers along organoid development **(Chapter 3, Fig. 2d, h, Extended Data Fig. 3 and Extended Data Fig. 5b**) and could show that the bifurcation occurs when cysts have between 16 to 32 cells **(Chapter 3, Fig. 2f).** Nonetheless, trajectory inference has strong underlying assumptions that can limit its applicability and need to be taken in account[204]. Sampling needs to be sufficiently high to cover infrequent phenotypes, in our particular case enterocsyts, and features need to be selected carefully that the process under investigation is robustly recapitulated (**Chapter 3, Extended Data Fig. 2a, b, f**). Both parameters rely on a given specific question and must be tested separately. Furthermore, the selection of a good markers set is essential to pinpoint the bifurcation point accurately. Our trajectory was designed to follow bifurcation from a progenitor state into budding organoids and enterocsyts. Since Paneth cells are a clear distinction between these states, the Paneth cell marker lysozyme proved essential for trajectory inference. Of note, since the publication of the Wishbone algorithm in 2016[206], various other inference algorithms able to resolve branching trajectories have been described[223-225]. These algorithms can improve the resolution of the inferred pseudo-time trajectories. Thus, I would suggest trying a probabilistic inference algorithm such as Palantir[225], the Wishbone successor, on our data set and compare its performance against Wishbone.

One drawback of trajectory inference is the non-intuitive nature of pseudotime, which can be difficult to align to real-time. However, one can reconcile both by combining trajectory information with landmark points obtained from real time imaging. In my work, I used a simple mapping between organoid areas of pseudotime and real-time (**Chapter 3, Extended Data Fig. 4h**). In future works, mapping accuracy can be improved by using multiple features and more robust mapping algorithm. For example, a live-reporter which corresponds to one of the stained markers in the fixed samples can be combined with morphological features for mapping.

Furthermore, mapping fixed datasets of perturbed organoid development against wild type organoid development trajectories can become a powerful approach to visualize effects of distinct perturbations, compare trends of markers between different conditions and pin point timings when different molecular mechanisms occur.

Do distinct starting cells go through a common intermediate state?

Recent studies have shed light on the enormous plasticity of the small intestinal tissue emphasized by the ability to grow intestinal organoids (see **Chapter 1, Intestinal organoid development**) from LGR5+ intestinal stem cells[84] but also from diverse LGR5- populations[136] including, secretory[99] and absorptive progenitors[100] as well as more mature enteroendorcine[226], Tuft[226], and Paneth cells[103] (see **Chapter 1, Regeneration of the small intestine**). However, whether single cells derived from distinct starting populations follow a similar path to the final organoid structures is still not known. Our findings show that both LGR5+ and LGR5- starting populations (**Chapter 3, Fig. 1a**) go through a similar fetal-like intermediate state and behave very similar in growth, timing of symmetry breaking and overall morphology during organoid development (**Chapter 3**, **Fig. 1c-g**). Noteworthy, enterocysts were present in organoids derived from both starting populations. This newly described subpopulation of organoids fails to break symmetry, never acquires Paneth cells, remain spherical and fully differentiate into enterocytes (**Chapter 3**, **Fig 1f** and **Extended Data Fig. 1e**, **f).**

Dedifferentiation into a fetal-like state after single cell dissociation

Despite being cultured with strong activators of the canonical Wnt pathway, LGR5+ intestinal stem cells lose their stem cell identity markers, many of which are canonical Wnt target genes, within the first ~24 hours of organoid development. Both on the protein level, where LGR5::DTR-GFP expression vanishes (**Chapter 3, Fig. 2h** and **Extended Data Fig. 5a, b**) and on the transcript level where stem cell identity genes including *Lgr5, Axin2 and Olfm4* are downregulated (**Chapter 3, Fig. 3b** and **Extended Data Fig. 6b, e**). Likewise, LGR5- starting cells lose expression of adult cell type markers (**Chapter 3, Fig. 3b**). In contrast, independent of the starting population, markers associated with fetal development (see **Chapter1: Development of the intestine**) including *Sca-1*, *Clusterin* and *Annexin-1* are strongly upregulated (**Fig. 9** and **Chapter 3, Fig. 3f**).
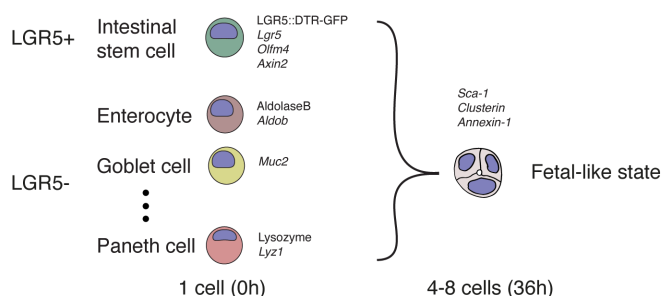
Fig. 9 | Distinct starting populations go through a common fetal-like intermediate state. Independent of the starting population, intestinal cells dedifferentiate into a homogenous fetal-like intermediate state where mature cell identities are lost. This multipotent state has the capacity to reconstitute all cell types of the small intestine.

Intriguingly, these behaviors are very similar to recent in vivo findings for injury response after parasite infection[227] or by dextran sulfate sodium (DSS) induced colitis[196]. In both studies, intestinal cells lost mature cell identity and increased expression of marker genes associated with fetal development[196,227]. Organoid development therefore mimics a regenerative response in which mature cell types lose adult identity to reverse into a more primitive multipotent and highly proliferative state.

It should however be noted that while recent comparison showed over 4'500 differently expressed genes between adult intestinal stem cells and fetal cells at E11.5[124], the assignment to a fetal-like state is based on only a small subset of marker genes which are distinct between fetal and adult tissue derived organoids[101,102]. This fetal-like state therefore may indicate that certain genes active in fetal development are repurposed in general stress response to enable fast proliferation and multipotency rather than cells fully converting back to a fetal intestinal cell. Indeed, among the strongest upregulated marker within fetal-like transcriptomes are *Sca-1* which acts as a transcription factor in many stem and progenitor cells[228] and *Clusterin*[229] and *Annexin-1*[230] that are known to be required in stress response in other contexts[230].

Cellular plasticity of distinct starting populations

Although single cells from both starting populations (LGR5+ and LGR5-) dedifferentiated into similar homogenous cysts with fetal-like characteristics, we noted subtitle differences in growth depending on the cell origin. Most salient, with ~18% compared to ~7.5%, LGR5+ cells form organoids at a higher efficiency (**Chapter 3**, **Fig. 1c**). Furthermore, LGR5+ cells develop slightly faster than organoids derived from LGR5- cells. After 24 hours, LGR5+ cells have reached higher number of nuclei and likely as a result are bigger (**Chapter 3**, **Fig. 1d, e**). This trend is consistent over the course of the five days. In contrast to the pure LGR5+ intestinal stem cell population, LGR5- cells consist of a pooled population of distinct cell types. Although recent findings indicate that almost all these cells can dedifferentiate given a strong enough stimulus[231], one still has to investigate if it is the case in our experimental setup and if all subpopulation of cells do it with comparable efficiencies. Compared to LGR5+ cells which are cycling and multipotent, LGR5- can also be non-proliferative and fully differentiated. The required more extensive re-modeling of the cellular make up to dedifferentiate and reinitiate the cell cycle could explain the longer lag phase and potentially lower efficiencies within this cell populations.

Moreover, LGR5- cells have a significant higher propensity to fail symmetry breaking (**Chapter 3**, **Fig. 1g**). Also, they re-acquire the signal of the stem cell marker LGR5::DTR-GFP later and weaker than LGR5+ derived cells (**Chapter 3, Fig. 2h**). This could indicate that

budding organoids derived from LGR5- cells contain less stem cells or that stem cells have lower Wnt signaling activity. Interestingly, a lower responsiveness to Wnt signaling has been implicated with slower regeneration in older mice after radiation-induced damage[232]. It will be important to carefully investigate where the observed differences stem from and test whether the observed reduction in LGR5+ expression affect the regeneration capacities of organoids over multiple passages. This would also have crucial consequences for *in vivo* regeneration where crypts reconstituted from non-stem cells may exhibit reduced regeneration abilities for subsequent injuries.

The underlying causes for the observed small differences are currently not clear. Differences in cellular components including proteins, membrane compartments, organelles or DNA modifications could all play a role[233]. Early studies showed few differences in the active histone marks H3K4me2 and H3K27ac at the same genome sites between intestinal stem cells, secretory progenitors and absorptive progenitors[137,234]. This lead to the conclusion that intestinal plasticity can be explained by a permissive open chromatin state which is maintained throughout differentiation[108]. Therefore, cell differentiation would be predominantly determined by the environment[108]. This view has recently shifted, by using ATAQ-seq experiments Jadhav et al., demonstrated that despite the similarity in histone modifications, strong differences in chromatin accessibility between different cell types exist[137]. During reprogramming, these chromatin barriers have to be overcome rapidly by dynamic rearrangements of open chromatin signatures[137]. However, whether all cell types can undergo this reversion and whether it is complete in all dedifferentiated cell types remains still to be determined.

In conclusion, our results show that single cells derived from both starting populations go through a similar multipotent fetal-like cyst from which all cell types of the small intestine can be reconstituted. Regeneration in the intestine is classically believed to be fueled by a designated pool of rare reserve stem cells[235,236] or by dedifferentiation of cells into an intestinal stem cell like state[99,100,136] (see **Chapter 1: Regeneration of the small intestine**) which occurs after cells fall back into the signaling environment of the crypt[127]. In the light of these new evidences, it is however likely that the first steps of regeneration are driven by reverting into a more primitive multipotent state. This dedifferentiation is fueled by a large pool of diverse cell types and not exclusively by few dedicated 'reserve' stem cells. Nonetheless, certain cells may have a higher propensity to dedifferentiate either due to crypt proximity or because of some favorable factors such as high levels of *Clusterin*[138] expression. This may explain the observation of 'dedicated' reserve stem cells that predominantly repopulate the niche in lineage tracing experiments after injury.

Further, different cell-type respond to different injuries[231] and it is currently not known whether some cell types acquire intestinal stem cell potential only for a short period or long term[237]. To decipher whether some cell types within the intestine retain some sort of "cellular memory" of their differentiated state and if so if it has any biological consequences one could make use of existing reporter mice and sort distinct subpopulation including, intestinal stem cells[238], 'reserve' stem cells[239], 'revival' stem cells[138], secretory progenitors[99], absorptive progenitors[100] and mature cell types[240] and systematically check whether all starting cells reconstitute the same organoid morphology and patterning. Time course experiments can be used to quantitatively compare growth, efficiency and final morphology between the different cell types and should be repeated over multiple passages of organoid growth. Furthermore, I would suggest doing ATAQ-seq time course experiments to compare open chromatin conformations and probe whether distinct cell types fully revert to a similar state before symmetry breaking. This data set could further be compared to fetal intestine samples to determine to which degree cells revert to the fetal state.

It is still not clear why intestinal stem cells which can give rise to all cell types of the intestine revert into a more primitive state during regeneration. One explanation could be that rapid cellular expansion is more important than maintaining genomic stability. Reversion to a fetal-like state that has a high proliferative potential (with a complete cell cycle of around 8 hours (**Chapter 3**) compared to 24 hours in stem cells[108]) but is likely less efficient in DNA damage repair[241,242] may allow for this expansion more efficient.

Which signaling pathways and gene networks underlie intestinal organoid development?

YAP1 driven dedifferentiation of adult intestinal cells

We show that this first dedifferentiation step of organoid development is driven by YAP1 activity. It correlates with the onset of proliferation and suppression of markers of cell type identity, the later corroborating similar findings in the intestinal tissue *in vivo*[195,196]. A similar YAP1 transient reprogramming of differentiated cells into multipotent proliferative cells has been described *in vivo* following colon injury[196] and *in vitro* for mammary, neural and pancreatic cells[243]. How YAP1 activation leads to various genome wide transcriptional changes is not fully understood yet. Recently Monroe et al.[244] showed that conditional overexpression of an active YAP1 mutant (YAP5SA) leads to reversion of adult cardiomyocytes into a proliferative state with fetal-like chromatin and transcriptional signatures [244]. Particularly chromatin accessibility at TEAD elements was increased. Instead of acting on a specific transcriptional side, YAP1 acts more as global genome remodeler[245]. The

transcriptional co-activator YAP1 preferentially interacts with DNA-binding proteins occupying enhancer regulatory regions to recruit chromatin remodeling complexes including p300, the SWI/SNF complex as well as the NuRD complexe[245]. Taken together, it seems that YAP1 is able to act at the same time as an activator and as a repressor of gene expression[245]. A similar YAP1 driven remodeling of chromatin accessibility may underlie the fetal-like reversion observed in organoids.

Specificity of YAP1 activity and the subsequent remodeling depends on temporal interactions with various transcription factors and signaling pathway components[245]. During organoid development, YAP1 shows extensive cross talk with multiple signaling pathways. YAP1 activation leads to activation of EGF signaling and is mediated by expression of the EGFR ligand and direct YAP1 target gene *Ereg*[195]. Increased cell proliferation is one of the best described effects of YAP1 activation[172]. Besides activation of genes directly involved in cell cycle progression and regulation (such as FOSL1, **Chapter 3, Fig. 3d**)[172], YAP1 driven EGF signaling likely contributes to the observed fast proliferation. Indeed, addition of purified EREG leads to increased organoid growth (own observations) and increases the efficiency of organoid formation (**Chapter 3, Fig. 4f**). Furthermore, YAP1 activity is intricately connected to Wnt signaling (discussed in the next paragraph) and cross-talks with Notch-signaling (see under **What drives symmetry breaking?**)

YAP1 interfaces with Wnt signaling to promote fetal like-cysts

YAP1 activation correlates with repression of canonical Wnt target genes including *Axin2*, and *Lgr5*[191,195] and increased expression of the non-canonical Wnt target genes *Nfatc2* and *Rac1* (**Chapter 3**, **Extended Data Fig. 6d, e**). Notably, in organoids only a subset of genes classically assigned to canonical Wnt signaling in the intestine is affected whereas other intestinal canonical Wnt target genes including *Cd44*[246]*, Ascl2* (a master regulator of intestinal stem cells[247]*), and Sox9*[248] increase during the first dedifferentiation steps of organoid development (**Fig. 10**). However, whether these genes are only activated by β-catenin remains to be determined.
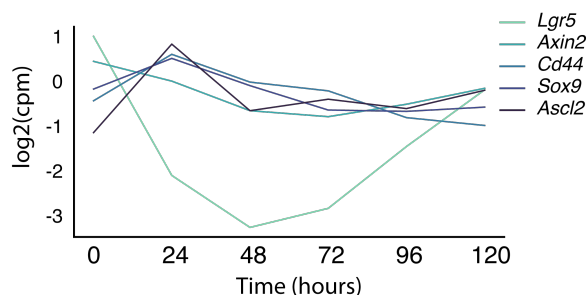
Fig. 10 | Dynamics of canonical Wnt signaling genes. Whereas *Lgr5* and *Axin2* show a downregulation during the first 48 hours of organoid development, other canonical Wnt target genes such as *Cd44, Sox9* and *Ascl2* show an increase in expression during the first 24 hours. Data from Chapter 3, Supplementary Table 1

In the embryonic small intestine until embryonic day 11.5, the non-canonical ligand WNT5A is the only source of Wnt[124] and Wnt/β-catenin-dependent signaling is actively repressed by the transcriptional regulator Id2[124]. Loss of Id2 results in precocious differentiation into adult LGR5+ cells[124]. Furthermore, fetal spheroids require the addition of WNT3A to transition from a fetal to a mature organoid state[102]. Taken together, dampening of canonical Wnt signaling is required to revert LGR5+ cells and retain fetal-like cysts. The early steps of organoid development may utilize non-canonical Wnt signaling. Nonetheless, the respective roles of canonical and non-canonical Wnt signaling requires further investigation.

How YAP1 mechanistically dampens Wnt transcriptional output is not clear yet. As mentioned above (**YAP1 driven dedifferentiation of adult intestinal cells**), repression at the chromatin level could play a role. Alternatively, direct prevention of nuclear translocation of Wnt pathway components by YAP1 have been described[190]. Interestingly, the reporter signal for TCF-GFP, a reporter that is only activated when nuclear β-catenin binds TCF to trigger target gene expression, is only detected after Paneth cells appear (**Chapter 3, Extended Data Fig. 10h**), indicating, that β-catenin does not enter the nucleus. However, this should be confirmed by immunofluorescence imaging using a β-catenin antibody.

YAP1 protein levels are dependent on WNT3A

Despite the suppressing effect of canonical Wnt signaling, the protein levels of YAP1 itself are dependent on WNT3A. Protein levels of YAP1 substantially drop after removal of exogenous WNT3A from the medium (**Chapter 3 Extended Data Fig. 7c**). Furthermore, in budding organoids and in the intestine *in vivo* YAP1 levels are highest around the Wnt gradient in the crypt regions (**Chapter 3, Fig. 4a)**[191]. Moreover, without supplemented WNT3A LGR5-derived organoids cannot form[84].

YAP1 mRNA levels stay constant during organoid development **(Chapter 3, Fig. 3e)**, indicating that WNT3A ligands are required to stabilize and amplify the free pool of YAP1, possibly by a positive feedback loop where activated and therefore nuclear YAP1 is protected from cytoplasmic degradation. Although disputed, YAP1 may act as an active part of the Wnt destruction complex. Without canonical Wnt ligands, the destruction complex is in its active state and acts as a cytoplasmic sink for YAP1[249]. Only when WNT3A is present, YAP1 is released from the destruction complex into the cytoplasm from where it can translocate to the nucleus

On the other hand, Park et al., proposed an 'alternative' Wnt-FZD/ ROR-Ga$_{12/13}$-Rho-LATS1/2-YAP1 signaling cascade where Wnt ligands (WNT3A and WNT5A/B) promote YAP1 activation[250]. It is independent of the canonical Wnt co-receptor LRP5/6 and blocks canonical Wnt signaling by secreted downstream targets of YAP1 including WNT5A/B, DKK1, BMP4,

IGFBP4, CTGF and CYR61. Interestingly, we see upregulation of CTGF and IGFBP4 during the first 24 hours of organoid growth (CTGF, fold change 4.8, p-value 0.0001; IGFBP4, fold change 1.2, p-value 0.07). If this pathway is also active in organoids, DKK1, a specific inhibitor for canonical Wnt signaling which interacts with LRP5/6 should not affect YAP1 signaling. Furthermore, WNT3A could be replaced with WNT5A/B. Alternatively, if WNT3A is required to turn-off the destruction complex, an APC mutant line (where the destruction complex is constitutively off) should render organoids independent of WNT3A and activate YAP1 during the first hours. Notably, LGR5+ derived organoids can grow without WNT3A in the medium. One should check the state of YAP1 in such organoids.

While both mechanisms could explain how the cytoplasmic pool of free YAP1 is stabilized it is probably a synergistic mechanism that causes the simultaneous YAP1 nuclear translocation (and therefore activation). Currently we do not know what triggers this activation, based on the role of YAP1 as sensor of tissue integrity (see **Chapter 1, YAP1 dependent signaling**), it is tempting to speculate that a change in extracellular environment, from a crowded tissue context to isolated single cells, promotes YAP1 activation[251,252].

YAP1 activation after single cell dissociation

Stiffness properties of the substrate translate into YAP1 nuclear translocation in intestinal stem cells grown in artificial matrices[253]. Furthermore, organoids with aberrant morphologies with flat, stretched nuclei caused by growth defects[254] or induced by prostaglandin 2 treatment (own observation), show high levels of nuclear YAP1 whereas cells in a packed tissue context show cytoplasmic localization **(Fig. 11a)**. These observations point to a role of cell geometry, tension forces and local cell crowding in YAP1 regulation also in intestinal organoids. Densely packed epithelial cells are often rich in actomyosin cables associated with adherent junctions, transmembrane E-cadherins and their associated catenins[255]. This dense packaging leads to suppression of nuclear localization of YAP1 in various contexts[182,256] (see **Chapter 1, YAP1-dependent signaling**). Single cell dissociation ruptures this connection and allows single cells to spread and attach more strongly to the extracellular matrix via focal adhesions **(Fig. 11b).**
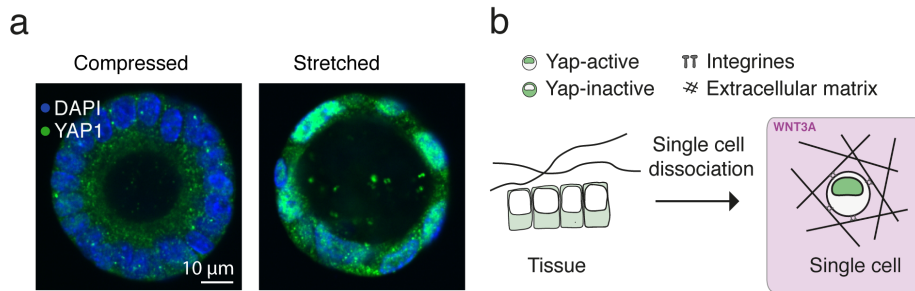
Fig. 11 | Mechanosensing by YAP1. a) Organoids with packed nuclei show deactivation of YAP1 whereas organoids with stretched nuclei show high levels of nuclear YAP1. Experimental conditions as described in the appendix section. **b)** Cartoon depicting a model for YAP1 activation. Single cell separation disrupts adherens junctions and allows cells to spread and attach to the extracellular matrix more firmly. This promotes the maturation of focal adhesions and YAP1 activation.

Binding to the extracellular matrix firmly by focal adhesions, particularly by β1-integrin, activates focal adhesion kinases and SRC signaling. This leads to inhibition of LATS1/2 activity (mediated by the FAK–SRC–PI3K–PDK1[257] pathway or the SRC–RAC1–PAK pathway[185]) and Hippo independent nuclear pore opening[186]. Both required for full activation of YAP1. Interestingly, following damage in the colon, YAP1 is activated by integrin, focal adhesion kinase and SRC signaling[196] to drive a regenerative response similar to the one observed in the small intestine. Furthermore, *in vitro* growth of single intestinal stem cells relies on integrin-based adhesion and cytoskeletal tension[253] . Noteworthy, β1-integrin (fold change 0,4, p-value 0.022), SRC (fold change 0.6, p-value 0.007) and RAC1 (fold change 0.6, p-value 0.001) show a small but significant increase in expression within the first 24 hours of organoid growth. Besides, data stemming from a compound screen done in the lab show that both inhibition of SRC and FAK abolish organoid growth. However, it is still not clear whether this is caused by the nuclear exclusion of YAP1 or by other growth impairing mechanisms.

Taken together, one should investigate whether single cells upregulate FAK and SRC signaling within the first 24 hours of organoid growth. Immunofluorescence using phospho-FAK antibodies can be used to stain for activated FAK. Furthermore, further pharmacological blocking of integrin, SRC and FAK signaling at different time points should be performed to probe whether inhibition of any of them affects nuclear localization of YAP1. In addition, YAP1 has other upstream regulators including cellular stress, cell cycle and apico-basal cell polarity (see **Chapter 1, YAP1-dependent signaling**). Regulation of YAP1 by any of these pathways should be taken into account as it may be a combinatorial effect that drives YAP1 activation as well as deactivation[172].

Cell-to-cell variability in YAP1 activity after the 4-cell state

After the 4-cell stage, YAP1 is deactivated within a subset of cells (**Chapter 3, Fig. 4a** and **Extended Data Fig. 7a, b**). In contrast to isolated cells where the full surface is exposed to the extracellular matrix, within growing cysts adherence junctions between cells are restored and cells start to compact. Compaction forces onto adherence junctions may lead to active shuttling of YAP1 out of the nucleus[182] and nuclear pore closing[186]. Local differences in cell crowding caused by asynchronous cell divisions or stochastic variegation in the Matrigel may change the ability of individual cells to attach to the matrix, affect the balance between extracellular matrix and adherence junction attachment, or change applied compression forces onto individual adherent junctions. These small cell-to-cell differences may be sufficient to deactivate YAP1 in certain cells and amplify activation of YAP1 in others **(Fig. 12)**. Corroborating evidences that local differences in the Matrix may play a role comes from experiments in finely controlled designed matrices where a homogenous stiff matrix leads to gradual downregulation of YAP1, likely through compaction, as cysts proliferate[172,253]. Symmetry can only be broken when the Matrix softens over time, presumably again leading to local differences[172,253].
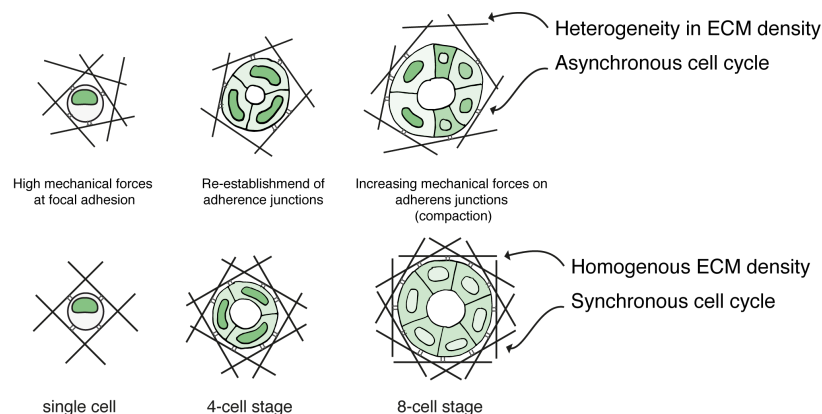
Fig. 12 | Cell-to-cell variability in YAP1 activity. (Top row) Cartoon shows how local differences in cell density caused by asynchronous cell divisions and/or density differences in the extracellular matrix could result in YAP1 variability after the 4-cell stage. **(Bottom row)** In homogeneous and stiff designer matrices, YAP1 is initially activated but becomes subsequently homogenous downregulated[253].

Furthermore, it will be important to characterize whether asynchrony in cell cycle precedes YAP1 variability or is a consequence of it. Besides leading to local asymmetries in crowding, the cell cycle state of each cells can affect the activity of YAP1[258].

In conclusion, the first steps of organoid development where single cells dedifferentiation into a common multipotent intermediate state are marked by an upregulation of the YAP1 protein and YAP1 activation by nuclear shuttling. The YAP1 driven regenerative program

involves cross-talk of multiple signaling pathways including Wnt and EGF signaling and results in loss of adult cell identity, multipotency and a high proliferative capacity. Whereas this section focused on the first steps of organoid development leading to a homogenous cysts and subsequent generation of YAP1 cellular heterogeneity in its activation, the next section will carry forward the question about which signaling pathways and gene networks underlie intestinal organoid development to the event of symmetry breaking. In particular, I will focus on the role of the described YAP1 cell-to-cell variabilities, how they can be quantified and how they contribute to symmetry breaking.

What drives symmetry breaking?

We show that cell-to-cell variability in YAP1 activation induces a Notch-Delta lateral inhibition event between the 8-16 cell stage (**Chapter 3, Fig. 5d**). Cells that retain high levels of nuclear YAP1 activate DLL1 and subsequently become Paneth cells (**Chapter 3, Fig. 5d, e**). Currently, it is not clear how YAP1 activity is translated into a Notch-Delta event. In our system, high levels of YAP1 activity correlate with high expression of Notch ligands (**Chapter 3, Fig. 5b, c, d**). In keratinocytes, YAP1 binding to distant enhancers activates the expression of Delta-like ligands[259]. Similar, in neural crest progenitors, YAP1 induces expression of the Notch ligand JAG1[259]. To probe whether YAP1 binds DLL1 enhancers or promoter regions in intestinal organoids, I suggest YAP1 ChIP-seq time course experiment.

Is symmetry breaking driven by deterministic causes?

Generating asymmetries in lateral inhibition as well as in other genetic fate switches is typically attributed to stochastic events (intrinsic noise) within individual cells, which are amplified to determine the cellular fate choice in a binary fashion[260] (see **Chapter 1, Intrinsic noise and deterministic cell-to-cell variability in symmetry breaking**). However, this modeling framework fails to explain how the onset of these event is accurately timed and how robust patterns can emerge[260]. Moreover, at least for binary fate switches, this renders symmetry breaking not as a true emergent property of a population of cells but is governed by a stochastic event within an isolated cell[260]. In contrast, our observations argue for a model in which symmetry is broken at the population level. We hypothesize that within a growing population of cells where the microenvironment changes dynamically, each cell constantly senses and translate the current status into YAP1 activity and therefore the propensity to break symmetry. Thus, coupling cell-fate decision making to tissue-scale changes. While this is just a hypothesis, it could explain how symmetry breaking is timely coupled to the re-establishment of tissue integrity, sensed for example by reaching a certain threshold of population density after injury.

Multifactorial contributions may underlie the Notch-Delta activation

Is YAP1 variability sufficient to trigger Notch-Delta lateral inhibition?

Although the role of YAP1 is intriguing, its cellular variability may not be the only factor contributing to symmetry breaking. Not every cell with high YAP1 activity between the 8-16 cell stage is DLL1+ (**Chapter 3, Fig 5d**). This could be a temporal aspect, where fixation preceded the deactivation of YAP1 or the activation of DLL1. Assuming that there is a certain threshold of expressed DLL1 receptor on the membrane, which has to be reached to block expression of DLL1 in the adjacent cell, it may require a certain time of higher YAP1 activity in one cell compared to the neighboring cell until this balance is tipped. To understand the temporal aspect of YAP1 variability, live-imaging will be essential. To my knowledge, no functional YAP1 reporter exists for intestinal organoids. However, by CRISPR-CAS9 mediated tagging of YAP1 with GFP and TEAD1 with mCherry, YAP1 and its main interaction partner TEAD1 have been simultaneous tracked in breast epithelial cell lines[252]. One could use a similar tagging strategy for YAP1 within a DLL1 reporter mice[99], as a tool to follow YAP1 and DLL1 dynamics in the same cell.

Single cell perturbations to introduce YAP1 cell-to-cell variability

We show with global perturbations that YAP1 variability is required to break symmetry and that symmetry breaking is mediated via the Notch pathway (**Chapter 3, Fig. 4g, h, Fig. 5g, Extended Data Fig. 7h** and **Extended Data Fig. 10c, d-f**). However, to probe whether YAP1 variability alone is also sufficient to induce symmetry breaking, individual cells in homogenous cysts at the ~ 4 cell stage have to be perturbed and the consequences of this perturbation followed in real-time. Optogenetic approaches can be developed to cell-specifically translocate YAP1 either indirectly[261] or potentially, as shown for other proteins, by directly controlling protein export[262]. Optogenetics can be implemented on the light sheet microscope used for organoid imaging. Alternatively, as shown for SOX21 heterogeneity in mouse blastomeres[34], siRNAs against YAP1 could be injected into 2-cell stage organoids. However, injections are low throughput and, caused by the small size of intestinal cells and the reduced cell accessibility within Matrigel, technically challenging. Complementary, heterogeneity in a high-throughput fashion could be introduced by using reporter lines where YAP1 can be knocked out conditionally with CreERT2[263]. Here, low Tamoxifen concentration could be used to only stochastically knock-out some cells within growing cysts.

Multifactorial contributions to trigger lateral inhibition

Alternative, variability in YAP1 activity alone may not suffice to break symmetry but a combinatorial effect may be required to trigger lateral inhibition. Cellular states and spatial heterogeneity of cell packing not only affect YAP1 activity but have wide spread consequences on individual cells (see **Chapter 1, Deterministic cell-to-cell variability**) including altered signaling activities[64] and distinct cell-cell contact areas. Indeed, different cell contact areas affect Notch signaling directly[264,265]. Noteworthy, we also observed pairs of neighboring DLL1+ cells, presumably due to a division event which may link lateral inhibition to cell division (own observation). Besides, HES1 is expressed in an oscillatory manner in various cell lines[266]. Oscillation of HES1 could give certain cells a higher propensity to undergo lateral inhibition which may then be stabilized by YAP1 activity. To determine whether HES1 oscillates during intestinal organoid development, HES1-GFP reporter lines can be tested[267,268]. Moreover, fixed samples can be used to correlate the nuclear states of HES1 with nuclear YAP1. This analysis will give insight whether differences in levels of HES1 exist, potentially preceding YAP1 variability, and whether putative cells with lower nuclear HES1 levels are more likely to become DLL1+ in YAP1 high cells.

Three-dimensional segmentation to analyze population context

To investigate how cell geometry, cellular microenvironment and cellular states influence YAP1 activity and Notch-Delta lateral inhibition, these attributes need to be measured simultaneously within the same cell in a given organoid. For this, further development of the multiplexing and image analysis pipeline presented in this work are required. Currently, analysis is mostly conducted on two-dimensional projections of the tissue level. To allow population context measurements and single cell quantification, three-dimensional single cell segmentation and feature extraction need to be implemented. In contrast to attaching layers of cells where analysis of the population context is well established this type of analysis is currently limited in three dimensional structures. Mainly because of two technical limitations: 1) Most tissues are not transparent which causes light scattering and limits imaging depth within the tissues[269]; 2) segmentation and analysis tools are optimized for single plane images and not volumetric image stacks. Preliminary results prove promising that with sample stabilization[219] and clearing[218], imaging quality for organoids can be improved substantially (**Fig. 13a**). Moreover, novel convolutional neural network based three-dimensional segmentation algorithm allow to segment nuclei with high quality in three dimensions[270] (**Fig. 13a, b**).
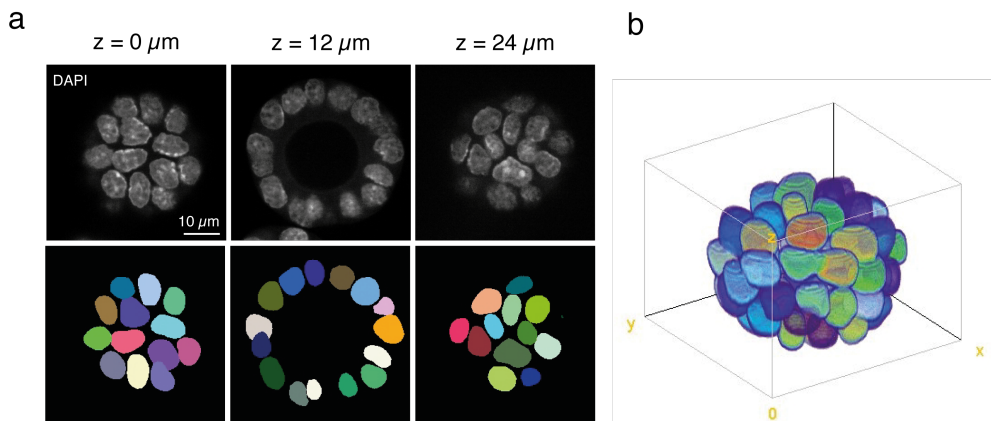
Fig. 13 | Three-dimensional segmentation of cleared organoids. **a) Raw images and segmentation masks. (Top row)** For the same organoid different z-planes stained with a nuclear marker (DAPI) are shown. **(Bottom row).** Corresponding segmentation masks to the DAPI images. Nuclei are segmented on the volume not plane wise. **b) Three-dimensional representation of the segmentation shown in a.** Different colors correspond to individual nuclei. Images acquired on a Yokogawa (CellVoyager 7000S), with an enhanced CSU-W1 spinning disk (Microlens enhanced dual Nipkow disk confocal scanner), a 60x water immersion (NA = 1.2) Olympus objective, and a Neo sCMOS camera (Andor, 2,560 × 2,160 pixels) with 2x2 binning. Organoids prepared as described in the appendix section, sample stabilization based on Ref. [219] clearing based on Ref. [218]. Three-dimensional segmentation algorithm based on Ref. [270]. Segmentation implemented by Markus Rempfler from the Friedrich Miescher institute for biomedical research faculty for advanced imaging.

Undoubtedly, there are more technical hurdles to overcome to multiplex single cells in three-dimensions such as non-linear signal decay over z, morphological alterations and sample movements caused by elution as well as challenges to obtain cell segmentations in addition to nuclei segmentations. Nonetheless, these preliminary results are a first step to quantitatively correlate YAP1 activity with cell shape, cellular state and population context.

Predictive modeling of YAP1 activity and symmetry breaking

Such measurements can then be used to build predictive models. Bayesian network learning has been shown to successfully infer causal interactions between microenvironment, cellular state and virus infection[63] and multi linear regression can predict population context dependent transcript abundance[42]. Similar approaches are conceivable to infer causal upstream factors of YAP1 activity and DLL1 specification (which could for example be the cell shape, local density or cell cycle position) and furthermore may allow to predict YAP1 states and DLL1+ cells.

Subsequently, to understand the interconnections and dynamics resulting in symmetry breaking computational models need to be applied. Modelling frameworks such as agent based modeling can recapitulate dynamics of complex biological systems[271]. Various modeling approaches have been developed to model organoid cultures in general[272] and intestinal organoids in particular[273,274]. These models prove promising to recapitulate aspects of self-organization of intestinal organoids but would greatly benefit from high dimensional

quantitative data and single cell perturbation approaches. Ultimately, the aim of such efforts is to determine to which degree YAP1 activity and subsequent symmetry breaking are predictable, identify potential upstream regulators of these processes and gain understanding in dynamics leading to these outcomes.

In summary, more experimental evidences are required to understand causal factors underlying the variability in YAP1 activity and how these variabilities translate into a Notch-Delta event. Nevertheless, the well-established regulation of YAP1 by structural features of the microenvironment argues that symmetry breaking in intestinal organoids is not a random unpredictable process but rather that (measurable) factors of the tissue context control the behavior of individual cells. Nonetheless, symmetry breaking may involve the coincidence of multiple dynamic event.

Symmetry breaking, Paneth cells and the emergence of other cell types

We show that DLL1+ cells (which mark secretory progenitors [99]) subsequently become Paneth cells (**Chapter 3, Fig. 5e and Extended Data Fig. 10b**). This constitutes the first symmetry breaking event in intestinal organoids. Within this work we do, however, not address what mechanism underlies this maturation into Paneth cells. Likely only a subset of DLL1+ cells mature into Paneth cells (**Chapter 3, Fig 5e**), whereas the other cells will become other secretory cell types. Indeed, single cell sequencing data (**Extended Data Fig. 9c**) show that besides Paneth cells other secretory cells including goblet cells, enteroendocrine and Tuft cell re-emerge. Moreover, also intestinal stem cells and enterocytes are reconstituted (**Fig. 14**). Remarkably enough all within the first three days of organoid development.
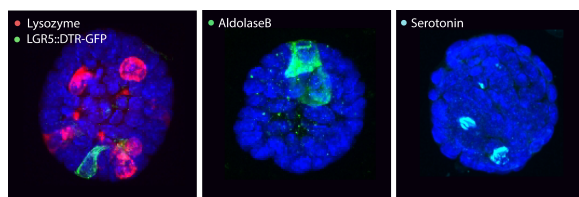
Fig. 14 | Reconstitution of adult cell types. Representative images (maximum intensity projections) showing the appearance of markers for Paneth cells (Lysozyme), intestinal stem cells (LGR5::DTR-GFP), enterocytes (AldolaseB) and enteroendocrine cells (Serotonin) on the protein level. Organoids are fixed at day 3. Experimental conditions as described in the appendix section.

Differentiation of each of these cell types requires distinct signaling inputs (see **Chapter 1: Signaling pathways controlling the intestinal epithelium**). During homeostasis, as progenitors migrate away from the crypt they experience changing concentration gradients of Wnt, BMP and other signaling molecules shown to promote their differentiation and maturation (**Fig. 15a**). Nevertheless, the same cell types are reconstituted within a homogenous WNT3A environment during early stages of organoid development (**Fig. 15b**).
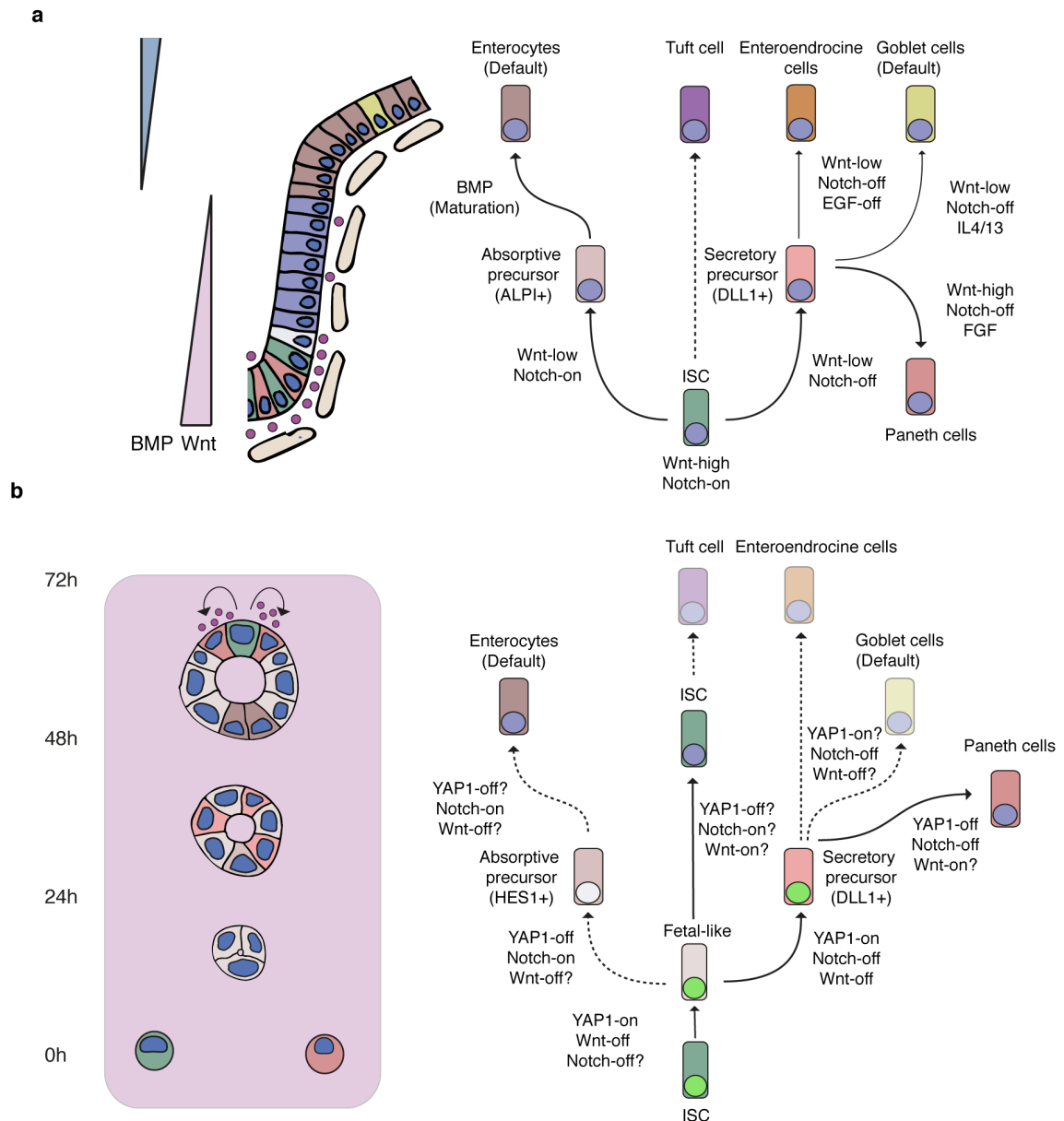
Fig. 15 | Cell differentiating hierarchy in the small intestine and intestinal organoids. a) During homeostasis, intestinal stem cells continuously produce fast proliferating transient amplifying precursor cells. These cells give rise to various differentiated cell types while migrating away from the crypt signaling environment. Maturation of each cell type requires distinct signaling inputs. **b)** During organoid development, different cell types revert into a fetal-like multipotent state from which all cell types of the small intestine can be reconstituted. Cell type specification occurs under a homogenous WNT3A environment. Faded colors indicate cell types for which the exact time of specification is not known. Dotted lines indicate cell types for which the required signaling inputs are not known. Putative signaling requirements are based on literature[108] and experimental observations (**Chapter 3**).

When these cell fates are specified and how the different signaling environments required for these specifications are established is still not well understood. Interestingly, in the embryo maturation of LGR5+ cells is initiated by a switch from non-canonical to canonical Wnt signaling[124]. Thus, after passing through a fetal-like cyst state and establishment of Notch-

Delta lateral inhibition an additional switch toward canonical Wnt signaling in a subset of cells may partly underlie cell maturation in organoid development. Again, controlled by YAP1 dynamics where deactivation could release inhibition of canonical Wnt signaling to promote the reestablishment of LGR5+ cells from fetal progenitors[124] as well as Paneth cell differentiation[154,155] from DLL1+ progenitors. Corroborating results for theses speculations come from the observation that DLL1+ cells lose nuclear YAP1 while still in WNT3A-CM (**Chapter 3, Fig. 5f** and **Extended Data Fig. 10a).** Besides, asynchronous oscillations of the cell cycle and potentially HES1 could contribute to distinct cell differentiation[275].

Cell-to-cell variabilities reveal distinct signaling activities

Although these models are currently pure speculation, they serve as an example of how temporal signaling cross-talk within individual cells could explain distinct self-organized responsiveness in homogenous conditions. Different activity states of signaling and genetic networks within individual cells of an organoid appear as cellular heterogeneity in fixed samples. Indeed, in addition to YAP1 other key factors involved in cell type specification including the transcription factors HES1, SOX9 and the cell cycle position show cell-to-cell variability during the first three days of organoid development (**Fig. 16**). Whether they are a downstream consequence of YAP1 variability or if they occur independently of YAP1 is yet to be determined.
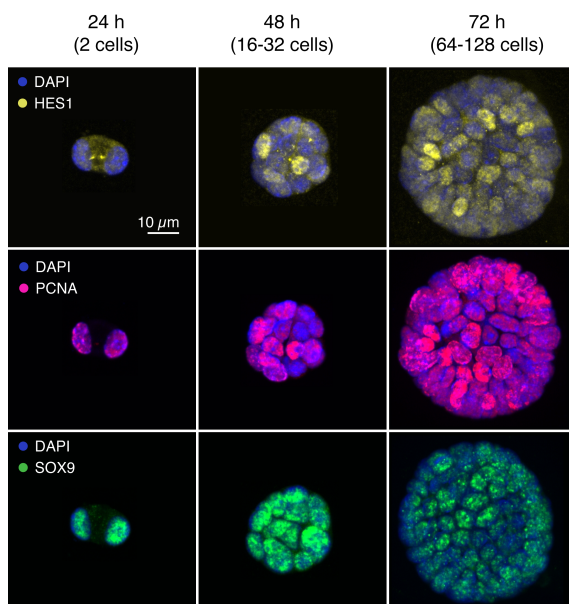
Fig. 16 | Cell-to-cell variabilities in intestinal organoid development. For each time point, representative images (maximum intensity projection) show different markers stained within the same organoid over multiple imaging rounds. After 48 hours, HES1 (a Notch target), the proliferation marker PCNA (which is elevated in G1/S phase of the cell cycle) and SOX9 (a marker implicated in Paneth cell specification) show cellular heterogeneity in protein expression.

It will be important to characterize the sources of these variabilities and there extend at different times preceding to, around and after the first symmetry breaking event. Correlation of signaling and transcriptional activity within individual cells with known expression pattern for cell type specification will aid as a first step to deepen our understanding on how different

cell types emerge. Thus, allowing the identification of key interactions required to specify distinct cell types and device perturbation strategies to probe causality.

Further improvements in multiplexing (see above under **Three-dimensional segmentation to analyze population context**) or alternative image-based transcriptome and proteome analysis (as discussed in **Chapter 2**) can be implemented to move toward this goal. Although technically challenging, by barcoding individual organoids, single cell sequencing may allow the comparison of transcripts of individual cells within an organoid in an unbiased transcriptome wide fashion[276]. Alternatively, single cell sequencing could be done at different cell stages (2, 4, 8, 16, 32-cell stages). These early stages potentially can be separated by size gating and FACS sorting. Complementarily, multiplexed smFISH measurement or *in-situ* sequencing can be extremely powerful approaches to reveal multiple cellular heterogeneities while preserving spatial information.

Reconstitution of the niche

More broadly, it will be fascinating to disentangle how crypt reconstitution progresses after the specification of Paneth cells. For example, are Paneth cells the first and only symmetry breaking event in a truly self-organizational sense (where order emerges from homogenous conditions without guidance from a positional cue) after which subsequent steps are instructed by step wise refinement of prior asymmetries guided by a Paneth cell mediated WNT3 gradient? In other words, to link back to the frameworks introduced in the introduction, can intestinal organoid development be described by a self-organized Turing-like mechanism to generate the first asymmetries which are then refined by cell fate patterning akin to positional information? Clearly, after the removal of Wnt from the medium (after day 3), secreted WNT3 gradients act as strong morphogens instructing local proliferation and likely are decoded into cellular decisions and morphological changes[104] required to drive crypt formation. Nonetheless, most cell types occur before removal of WNT3A. How does the occurrence of Paneth cells links to these later events? What is the minimal number of Paneth cells required to build a sufficient Wnt gradient? How do differentiated cells coordinate migration and rearrange to build the crypt? These and many more open questions remain and answering them will likely reveal even more principles of self-organization in intestinal organoid formation.

Future perspectives and conclusion

Many biological processes only unfold after cells can attach to an extracellular matrix and interact in three-dimensions. Compared to two-dimensional cell cultures, studying these processes comes however with increased complexity and technical requirements. Organoids are a great tool to bridge the gap between two-dimensional cell cultures and living animals. Thus, allowing investigating aspects of development, regeneration and homeostasis not accessible before. These insights hold the promise of being translated into improved and novel human therapies. For example, by developing strategies to boost regeneration[173] or by generating organoids to apply them to cell replacement or whole-organ transplantation[277,278].

While current efforts to improve protocols so that organoids resemble more their *in vivo* counterparts[279-281] and the development of bioengineering methods to make organoids more reproducible[79] are important, I would argue that faster progress in this direction would greatly benefit from a better insight of what the model system in use truly recapitulates. Moreover, to efficiently devise strategies to support regeneration and prevent malignant growth, it will be crucial to understand the mechanisms endowing single cells with the capacity to reconstruct various damaged tissues in different contexts[237]. Symmetry breaking is a fundamental requirement to reestablish homeostasis[282] and aberrant symmetry breaking can have severe consequences for a self-organizing system. Thus, it will be indispensable to deepen our understanding about symmetry breaking events driving regeneration on a cellular and tissue level [237].

YAP1-dependent signaling holds great promise in this regard. It will be essential to gain insights on how YAP1 senses and regulates tissue integrity during regeneration. How cellular heterogeneities in YAP1 activation are created and propagated to contribute to cellular decision making in organoids remains an open question. The prospect that cells actively sense and integrate cellular as well as tissue dynamics to create deterministic cell-to-cell variabilities which ultimately leads to symmetry breaking and that this could one day become predictable is to me fascinating. It is truly captivating to try to elucidate the nature of determining upstream factors, the extend of variabilities also in other molecules and how much biological information they contain.

Moreover, further improvements in multivariate imaging technologies combined with modeling approaches will allow studying how dynamic integrations between individual cells give rise to many more emergent properties besides symmetry breaking in population of cells. Thus, unravelling basic patterns and mechanisms of self-organization.

On the practical side, knowledge about deterministic factors underlying symmetry breaking will allow the adaptation of culture conditions so that symmetry is broken more homogenously. Thus, approaching the problem of low reproducibility in organoid culture system. For example, by using controllable designer matrices instead of Matrigel[253], by spatially restricted light induced softening of the surrounding matrix or by spatiotemporal controlled release of Notch ligands[283].

Besides, it will be exciting to probe how universal the observed mechanisms underlying organoid regeneration are. Do different types of injury elicit similar mechanisms for intestinal repair? Indeed, exposure to interferon-γ triggers a similar fetal-like reversion as observed in intestinal organoids *in vivo*[227]. Thus, indicating that multiple types of triggering signaling are able to cause a similar regenerative response. Whether they all converge to YAP1 to drive identical self-organizing pattern will be exciting to study. Likewise, by comparing human and mouse derived organoids, it will be fascinating to see to which degree regenerative responses are conserved from mouse to human and to what degree they mimic developmental programs.

In conclusion, within this thesis we study the self-organizing potential of single intestinal cells. We show that plasticity of stem-cell and non-stem populations leads to cellular dedifferentiation into a common feta-like homogenous cysts from which morphogenesis and patterning akin to the small intestine emerges. We demonstrate that organoid development resembles regeneration *in vivo* and is driven by YAP1 activity. Our results reinforce the evidence that YAP1 acts as a sensor for cellular and tissue integrity and give novel insights on how transient and variable YAP1 activation couples Notch-Delta mediated cell-fate decision to three-dimension tissue level changes. This work illustrates how cutting-edge imaging approaches such as 4i multiplexing and light-sheet microscopy combined with sequencing enable the study of emergent collective behaviors of interacting cells. It shows the power of intestinal organoids to study basic research question and gives first insights on how asymmetric structures can emerge from homogenous conditions.

Acknowledgments

First and foremost, I would like to thank Prisca for the opportunity to do my PhD in her lab and for being an outstanding mentor during this time. Early on, I became intrigued by how interactions between individual cells can shape the behavior of a population of cells. Prisca not only shares this enthusiasm passionately but also gave me the possibility to work on this project covering this fascinating aspect of biology. Prisca guided me through my PhD, was always open to discuss experiments and sometimes wildly speculative hypothesis and gave me the freedom to pursue the aspects of this project which I liked most.

Further, I would like to thank my thesis committee members Darren Gilmour, Luca Giorgetti and Susan Gasser for great discussions, excellent ideas and great support. Also, I would like to thank Marc Buehler for chairing my PhD defense.

A big thanks to all members of the Liberali lab. The atmosphere in the lab is really outstanding, marked by friendship, mutual helpfulness and acceptance. I immensely enjoyed all the discussion we had in the office or during lunch about science but also about miscellaneous and complete unexpected topics which came up continuously. In particular, I would like to thank Andrea and Denise with whom I shared my main project. Andrea for being a huge help during my first month in the lab and Denise for a really great, extremely fruitful and friendly collaboration. Further, I would like to thank Ilya for all the time he has spent to improve the infrastructure of the lab to bring it to the outstanding level it is.

A special thank also to Ludivine, for proofreading my thesis and being a great help with experimental work in the lab. Furthermore, I would like to thank Markus and Dario for their great help with programming and imaging analysis in general and their contribution to the imaging pipeline in particular.

Furthermore, I would like to say thanks to the outstanding facilities at FMI, especially to Hubertus from the FACS facility, Laurent from FAIM and Enrico from IT. Without the support and the remarkable infrastructures these facilities provide at the FMI, this ambitious and technically demanding project would not have been possible.

Finally, I would like to thank my family. My parents for their endless support. Without their help, neither studying nor a PhD would have been possible. Noemi, thanks for always being there for me, for dealing with my sometimes stressed and moody disposition and for making my life just more enjoyable.

Acknowledgments

Abbreviations

AGR2	Anterior gradient 2
ALPI	Alkaline phosphatase
AMPK	AMP-activated protein kinase
APC	Adenomatosis polyposis coli
ASC	Adult stem cell
ATAQ-seq	Assay for Transposase-Accessible Chromatin using sequencing
ATOH1	Atonal homolog 1
AXIN2	Axis inhibition protein 2
BMI1	B cell-specific Moloney murine leukemia virus integration site 1
BMP1/4	Bone Morphogenetic Protein 1/4
CAS9	CRISPR associated protein 9
CBC	Crypt base columnar
CD4/4	Cluster of differentiation 4/8
CDX	Caudal homebox
CHIP-seq	Chromatin immunoprecipitation followed by sequencing
CKIα	Casein kinase Iα
CM	Conditioned media
CRISPR	Clustered regularly interspaced short palindromic repeats
CTGF	Connective tissue growth factor
CYR61	Cysteine-rich angiogenic inducer 61
DAPI	4',6-diamidino-2-phenylindole
DKK1	Dickkopf 1
DLL1/4	Delta-like protein 1/4
DNA	Deoxyribonucleic acid
DTR	Diphtheria toxin receptor
DVL	Disheveled
ECM	Extracellular matrix
EGF	Epidermal growth factor
EGFR	Epidermal growth factor receptor
EHS	Engelbreth-Holm-Swarm
EREG	Epiregulin
ERK1	Extracellular signal-regulated kinases
ESC	Embryonic stem cell
FACS	Fluorescence-activated cell sorting
FAIM	Facility for advanced imaging and microcopy
FAK	Focal adhesion kinase
FGF	Fibroblast growth factor
FMI	Friedrich Miescher Institute
FOSL1	FOS Like 1
FZD	Frizzled
GFP	Green fluorescent protein

GSK3	Glycogen synthase kinase 3
H2B	Histone 2B
HES	Hairy and enhancer of split 1
HOPX	Homeodomain-only protein homeobox
IF	Immunofluorescence
IGFBP4	Insulin Like Growth Factor Binding Protein 4
iPSC	Induced pluripotent stem cell
ISC	Intestinal stem cell
JAG1	Jagged 1
KLF4	Krüppel-like factor 4
KO	Knockout
KRAS	Kirsten rat sarcoma viral oncogene
LATS1/2	Large tumor suppressor homolog 1 / 2
LEF	Lymphoid enhancer-binding factor
LGR4/5	Leucine-rich repeat-containing G-protein coupled receptor 4/5
LINC	Linker of Nucleoskeleton and Cytoskeleton
LRIG1	Leucine-rich repeats and immunoglobulin-like domains 1
LRP5/6	Low-density lipoprotein receptor-related protein 5/6
MAP4K	Mitogen-activated protein kinase kinase kinase kinase
MAPK	Mitogen-activated protein kinase
MCF10A	Michigan Cancer Foundation 10 A
MOB	Mps one binder
MOB1A	MOB kinase activator 1
MOB2A	MOB kinase activator 2
MST1/2	mammalian STE20-like protein kinase 1/2
MYC	Myelocytoma
NA	Numerical aperture
NF2	Neurofibromatosis type 2
NURD	Nucleosome Remodeling Deacetylase
OCT4	Octamer-binding transcription factor 4
PAK	p21-activated kinase
PCNA	Proliferating cell nuclear antigen
PCP	Planar Cell Polarity
PDK1	Phosphoinositide-dependent kinase-1
PDX1	Pancreatic and duodenal homeobox 1)
PDZ	PSD-95/Dlg-A/ZO-1
PI3K	Phosphoinositide 3-kinase
PKB	Protein kinase B
PSC	Pluripotent stem cell
RA	Retinoic acid
RAC1	Ras-related C3 botulinum toxin substrate 1
RBPJ	Recombination Signal Binding Protein for Immunoglobulin Kappa J Region
RNF43	Ring Finger Protein 43

ROCK	Rho- associated, coiled-coil containing protein kinase
ROR	Receptor tyrosine kinase-like orphan receptor
RSPO	Roof plate specific spondin
RUNX2	Runt-related transcription factor 2
SAV1	Salvador homologue 1
SDS	Dextran Sodium Sulfate
SHH	Sonic hedgehog
SMAD	Sma genes mothers against decapentaplegic
SNF	Sucrose Non-Fermenting
SOX2/9/21	Sry-related HMG box
SRC	Sarcoma gen
SWI	Mating-type switching
TAO1	Thousand-and-one amino acids 1
TAZ	Transcriptional co-activator with PDZ-binding motif
TCF4	T-cell factor 4
TEAD1	TEA domain family member 1
TERT	Telomerase reverse transcriptase
TGF	Transforming growth factor
TNF	Tumor necrosis factor
WNT	Wingless-type mouse mammary tumor virus (MMTV) integration site
WNT3/5A	Wingless and Int-1 3/3a
YAP1	Yes-associated protein 1
ZNRF3	Zinc and ring finger 3
ZO1	Zonula occludens-1

References

1   Xavier da Silveira Dos Santos, A. & Liberali, P. From single cells to tissue self-organization. *FEBS J* **286**, 1495-1513, doi:10.1111/febs.14694 (2019).
2   Turner, D. A., Baillie-Johnson, P. & Martinez Arias, A. Organoids and the genetically encoded self-assembly of embryonic stem cells. *Bioessays* **38**, 181-191, doi:10.1002/bies.201500111 (2016).
3   O'Brien, L. E., Zegers, M. M. & Mostov, K. E. Opinion: Building epithelial architecture: insights from three-dimensional culture models. *Nat Rev Mol Cell Biol* **3**, 531-537, doi:10.1038/nrm859 (2002).
4   Bryant, D. M. & Mostov, K. E. From cells to organs: building polarized tissue. *Nat Rev Mol Cell Biol* **9**, 887-901, doi:10.1038/nrm2523 (2008).
5   Sasai, Y. Cytosystems dynamics in self-organization of tissue architecture. *Nature* **493**, 318-326, doi:10.1038/nature11859 (2013).
6   Gilmour, D., Rembold, M. & Leptin, M. From morphogen to morphogenesis and back. *Nature* **541**, 311-320, doi:10.1038/nature21348 (2017).
7   Lawrence, P. A. Morphogens: how big is the big picture? *Nat Cell Biol* **3**, E151-154, doi:10.1038/35083096 (2001).
8   Rogers, K. W. & Schier, A. F. Morphogen gradients: from generation to interpretation. *Annu Rev Cell Dev Biol* **27**, 377-407, doi:10.1146/annurev-cellbio-092910-154148 (2011).
9   Wolpert, L. Positional information and the spatial pattern of cellular differentiation. *J Theor Biol* **25**, 1-47, doi:10.1016/s0022-5193(69)80016-0 (1969).
10   Kicheva, A., Cohen, M. & Briscoe, J. Developmental pattern formation: insights from physics and biology. *Science* **338**, 210-212, doi:10.1126/science.1225182 (2012).
11   Schweisguth, F. & Corson, F. Self-Organization in Pattern Formation. *Dev Cell* **49**, 659-677, doi:10.1016/j.devcel.2019.05.019 (2019).
12   Turing, A. M. The chemical basis of morphogenesis. 1953. *Bull Math Biol* **52**, 153-197; discussion 119-152 (1990).
13   Gierer, A. & Meinhardt, H. A theory of biological pattern formation. *Kybernetik* **12**, 30-39 (1972).
14   Green, J. B. & Sharpe, J. Positional information and reaction-diffusion: two big ideas in developmental biology combine. *Development* **142**, 1203-1211, doi:10.1242/dev.114991 (2015).
15   Kondo, S. & Miura, T. Reaction-diffusion model as a framework for understanding biological pattern formation. *Science* **329**, 1616-1620, doi:10.1126/science.1179047 (2010).
16   Werner, S., Vu, H. T. & Rink, J. C. Self-organization in development, regeneration and organoids. *Curr Opin Cell Biol* **44**, 102-109, doi:10.1016/j.ceb.2016.09.002 (2017).
17   Karsenti, E. Self-organization in cell biology: a brief history. *Nat Rev Mol Cell Biol* **9**, 255-262, doi:10.1038/nrm2357 (2008).
18   Halatek, J., Brauns, F. & Frey, E. Self-organization principles of intracellular pattern formation. *Philos Trans R Soc Lond B Biol Sci* **373**, doi:10.1098/rstb.2017.0107 (2018).
19   Tsiairis, C. D. & Aulehla, A. Self-Organization of Embryonic Genetic Oscillators into Spatiotemporal Wave Patterns. *Cell* **164**, 656-667, doi:10.1016/j.cell.2016.01.028 (2016).
20   Gierer, A. *et al.* Regeneration of hydra from reaggregated cells. *Nat New Biol* **239**, 98-101, doi:10.1038/newbio239098a0 (1972).
21   Li, R. & Bowerman, B. Symmetry breaking in biology. *Cold Spring Harb Perspect Biol* **2**, a003475, doi:10.1101/cshperspect.a003475 (2010).
22   Wang, F. The signaling mechanisms underlying cell polarity and chemotaxis. *Cold Spring Harb Perspect Biol* **1**, a002980, doi:10.1101/cshperspect.a002980 (2009).
23   Yamashita, Y. M., Yuan, H., Cheng, J. & Hunt, A. J. Polarity in stem cell division: asymmetric stem cell division in tissue homeostasis. *Cold Spring Harb Perspect Biol* **2**, a001313, doi:10.1101/cshperspect.a001313 (2010).
24   Munro, E. & Bowerman, B. Cellular symmetry breaking during Caenorhabditis elegans development. *Cold Spring Harb Perspect Biol* **1**, a003400, doi:10.1101/cshperspect.a003400 (2009).
25   Chen, Q., Shi, J., Tao, Y. & Zernicka-Goetz, M. Tracing the origin of heterogeneity and symmetry breaking in the early mammalian embryo. *Nat Commun* **9**, 1819, doi:10.1038/s41467-018-04155-2 (2018).
26   Sato, T. & Clevers, H. Growing self-organizing mini-guts from a single intestinal stem cell: mechanism and applications. *Science* **340**, 1190-1194, doi:10.1126/science.1234852 (2013).
27   Alagha, A. & Zaikin, A. Asymmetry in erythroid-myeloid differentiation switch and the role of timing in a binary cell-fate decision. *Front Immunol* **4**, 426, doi:10.3389/fimmu.2013.00426 (2013).
28   Andreu, P. *et al.* Crypt-restricted proliferation and commitment to the Paneth cell lineage following Apc loss in the mouse intestine. *Development* **132**, 1443-1451, doi:10.1242/dev.01700 (2005).
29   Bessonnard, S. *et al.* Gata6, Nanog and Erk signaling control cell fate in the inner cell mass through a tristable regulatory network. *Development* **141**, 3637-3648, doi:10.1242/dev.109678 (2014).
30   Graf, T. & Stadtfeld, M. Heterogeneity of embryonic and adult stem cells. *Cell Stem Cell* **3**, 480-483, doi:10.1016/j.stem.2008.10.007 (2008).
31   Dietrich, J. E. & Hiiragi, T. Stochastic processes during mouse blastocyst patterning. *Cells Tissues Organs* **188**, 46-51, doi:10.1159/000118783 (2008).
32   Dietrich, J. E. & Hiiragi, T. Stochastic patterning in the mouse pre-implantation embryo. *Development* **134**, 4219-4231, doi:10.1242/dev.003798 (2007).
33   Chambers, I. *et al.* Nanog safeguards pluripotency and mediates germline development. *Nature* **450**, 1230-1234, doi:10.1038/nature06403 (2007).
34   Goolam, M. *et al.* Heterogeneity in Oct4 and Sox2 Targets Biases Cell Fate in 4-Cell Mouse Embryos. *Cell* **165**, 61-74, doi:10.1016/j.cell.2016.01.047 (2016).
35   Snijder, B. & Pelkmans, L. Origins of regulated cell-to-cell variability. *Nat Rev Mol Cell Biol* **12**, 119-125, doi:10.1038/nrm3044 (2011).
36   Eldar, A. & Elowitz, M. B. Functional roles for noise in genetic circuits. *Nature* **467**, 167-173, doi:10.1038/nature09326 (2010).
37   Raj, A. & van Oudenaarden, A. Nature, nurture, or chance: stochastic gene expression and its consequences. *Cell* **135**, 216-226, doi:10.1016/j.cell.2008.09.050 (2008).

38   Altschuler, S. J., Angenent, S. B., Wang, Y. & Wu, L. F. On the spontaneous emergence of cell polarity. *Nature* **454**, 886-889, doi:10.1038/nature07119 (2008).
39   Arias, A. M. & Hayward, P. Filtering transcriptional noise during development: concepts and mechanisms. *Nat Rev Genet* **7**, 34-44, doi:10.1038/nrg1750 (2006).
40   Stoeger, T., Battich, N. & Pelkmans, L. Passive Noise Filtering by Cellular Compartmentalization. *Cell* **164**, 1151-1161, doi:10.1016/j.cell.2016.02.005 (2016).
41   Bahar Halpern, K. *et al.* Nuclear Retention of mRNA in Mammalian Tissues. *Cell Rep* **13**, 2653-2662, doi:10.1016/j.celrep.2015.11.036 (2015).
42   Battich, N., Stoeger, T. & Pelkmans, L. Control of Transcript Variability in Single Mammalian Cells. *Cell* **163**, 1596-1610, doi:10.1016/j.cell.2015.11.018 (2015).
43   Munoz Descalzo, S. & Martinez Arias, A. The structure of Wntch signalling and the resolution of transition states in development. *Semin Cell Dev Biol* **23**, 443-449, doi:10.1016/j.semcdb.2012.01.012 (2012).
44   Lestas, I., Vinnicombe, G. & Paulsson, J. Fundamental limits on the suppression of molecular fluctuations. *Nature* **467**, 174-178, doi:10.1038/nature09333 (2010).
45   Thattai, M. & van Oudenaarden, A. Intrinsic noise in gene regulatory networks. *Proc Natl Acad Sci U S A* **98**, 8614-8619, doi:10.1073/pnas.151588598 (2001).
46   Zeng, L. *et al.* Decision making at a subcellular level determines the outcome of bacteriophage infection. *Cell* **141**, 682-691, doi:10.1016/j.cell.2010.03.034 (2010).
47   St-Pierre, F. & Endy, D. Determination of cell fate selection during phage lambda infection. *Proc Natl Acad Sci U S A* **105**, 20705-20710, doi:10.1073/pnas.0808831105 (2008).
48   Volfson, D. *et al.* Origins of extrinsic variability in eukaryotic gene expression. *Nature* **439**, 861-864, doi:10.1038/nature04281 (2006).
49   Foreman, R. & Wollman, R. Mammalian gene expression variability is explained by underlying cell state. *bioRxiv*, 626424, doi:10.1101/626424 (2019).
50   Raser, J. M. & O'Shea, E. K. Noise in gene expression: origins, consequences, and control. *Science* **309**, 2010-2013, doi:10.1126/science.1105891 (2005).
51   Shahrezaei, V., Ollivier, J. F. & Swain, P. S. Colored extrinsic fluctuations and stochastic gene expression. *Mol Syst Biol* **4**, 196, doi:10.1038/msb.2008.31 (2008).
52   Champion, L., Linder, M. I. & Kutay, U. Cellular Reorganization during Mitotic Entry. *Trends Cell Biol* **27**, 26-41, doi:10.1016/j.tcb.2016.07.004 (2017).
53   Gardel, M. L., Schneider, I. C., Aratyn-Schaus, Y. & Waterman, C. M. Mechanical integration of actin and adhesion dynamics in cell migration. *Annu Rev Cell Dev Biol* **26**, 315-333, doi:10.1146/annurev.cellbio.011209.122036 (2010).
54   Cota, C. D. & Davidson, B. Mitotic Membrane Turnover Coordinates Differential Induction of the Heart Progenitor Lineage. *Dev Cell* **34**, 505-519, doi:10.1016/j.devcel.2015.07.001 (2015).
55   Luxenburg, C., Pasolli, H. A., Williams, S. E. & Fuchs, E. Developmental roles for Srf, cortical cytoskeleton and cell shape in epidermal spindle orientation. *Nat Cell Biol* **13**, 203-214, doi:10.1038/ncb2163 (2011).
56   Kim, W. *et al.* Hippo signaling is intrinsically regulated during cell cycle progression by APC/C(Cdh1). *Proc Natl Acad Sci U S A* **116**, 9423-9432, doi:10.1073/pnas.1821370116 (2019).
57   Liu, P. *et al.* Cell-cycle-regulated activation of Akt kinase by phosphorylation at its carboxyl terminus. *Nature* **508**, 541-545, doi:10.1038/nature13079 (2014).
58   Gut, G., Tadmor, M. D., Pe'er, D., Pelkmans, L. & Liberali, P. Trajectories of cell-cycle progression from fixed cell populations. *Nat Methods* **12**, 951-954, doi:10.1038/nmeth.3545 (2015).
59   Davidson, G. *et al.* Cell cycle control of wnt receptor activation. *Dev Cell* **17**, 788-799, doi:10.1016/j.devcel.2009.11.006 (2009).
60   Dupont, S. *et al.* Role of YAP/TAZ in mechanotransduction. *Nature* **474**, 179-183, doi:10.1038/nature10137 (2011).
61   Engler, A. J., Sen, S., Sweeney, H. L. & Discher, D. E. Matrix elasticity directs stem cell lineage specification. *Cell* **126**, 677-689, doi:10.1016/j.cell.2006.06.044 (2006).
62   Cha, K. J. *et al.* Cell density-dependent differential proliferation of neural stem cells on omnidirectional nanopore-arrayed surface. *Sci Rep* **7**, 13077, doi:10.1038/s41598-017-13372-6 (2017).
63   Snijder, B. *et al.* Population context determines cell-to-cell variability in endocytosis and virus infection. *Nature* **461**, 520-523, doi:10.1038/nature08282 (2009).
64   Frechin, M. *et al.* Cell-intrinsic adaptation of lipid composition to local crowding drives social behaviour. *Nature* **523**, 88-91, doi:10.1038/nature14429 (2015).
65   Gut, G., Herrmann, M. D. & Pelkmans, L. Multiplexed protein maps link subcellular organization to cellular states. *Science* **361**, doi:10.1126/science.aar7042 (2018).
66   Chang, H. H., Hemberg, M., Barahona, M., Ingber, D. E. & Huang, S. Transcriptome-wide noise controls lineage choice in mammalian progenitor cells. *Nature* **453**, 544-547, doi:10.1038/nature06965 (2008).
67   Hanna, J. *et al.* Direct cell reprogramming is a stochastic process amenable to acceleration. *Nature* **462**, 595-601, doi:10.1038/nature08592 (2009).
68   Yamanaka, S. Elite and stochastic models for induced pluripotent stem cell generation. *Nature* **460**, 49-52, doi:10.1038/nature08180 (2009).
69   Singh, A. M., Hamazaki, T., Hankowski, K. E. & Terada, N. A heterogeneous expression pattern for Nanog in embryonic stem cells. *Stem Cells* **25**, 2534-2542, doi:10.1634/stemcells.2007-0126 (2007).
70   Mamidi, A. *et al.* Mechanosignalling via integrins directs fate decisions of pancreatic progenitors. *Nature* **564**, 114-118, doi:10.1038/s41586-018-0762-2 (2018).
71   Connelly, J. T. *et al.* Actin and serum response factor transduce physical cues from the microenvironment to regulate epidermal stem cell fate decisions. *Nat Cell Biol* **12**, 711-718, doi:10.1038/ncb2074 (2010).
72   Wedlich-Soldner, R. & Betz, T. Self-organization: the fundament of cell biology. *Philos Trans R Soc Lond B Biol Sci* **373**, doi:10.1098/rstb.2017.0103 (2018).
73   Lei, M. *et al.* Self-organization process in newborn skin organoid formation inspires strategy to restore hair regeneration of adult cells. *Proc Natl Acad Sci U S A* **114**, E7101-E7110, doi:10.1073/pnas.1700475114 (2017).
74   Pelkmans, L. Cell Biology. Using cell-to-cell variability--a new era in molecular biology. *Science* **336**, 425-426, doi:10.1126/science.1222161 (2012).
75   Fujimori, T., Nakajima, A., Shimada, N. & Sawai, S. Tissue self-organization based on collective cell migration by contact activation of locomotion and chemotaxis. *Proc Natl Acad Sci U S A*, doi:10.1073/pnas.1815063116 (2019).

76   Durdu, S. *et al.* Luminal signalling links cell communication to tissue architecture during organogenesis. *Nature* **515**, 120-124, doi:10.1038/nature13852 (2014).

77   Trush, O. *et al.* N-Cadherin Orchestrates Self-Organization of Neurons within a Columnar Unit in the Drosophila Medulla. *J Neurosci* **39**, 5861-5880, doi:10.1523/JNEUROSCI.3107-18.2019 (2019).

78   Sasai, Y., Eiraku, M. & Suga, H. In vitro organogenesis in three dimensions: self-organising stem cells. *Development* **139**, 4111-4121, doi:10.1242/dev.079590 (2012).

79   Huch, M., Knoblich, J. A., Lutof, M. P. & Martinez-Arias, A. The hope and the hype of organoid research. *Development* **144**, 938-941, doi:10.1242/dev.150201 (2017).

80   Warmflash, A., Sorre, B., Etoc, F., Siggia, E. D. & Brivanlou, A. H. A method to recapitulate early embryonic spatial patterning in human embryonic stem cells. *Nat Methods* **11**, 847-854, doi:10.1038/nmeth.3016 (2014).

81   McCauley, H. A. & Wells, J. M. Pluripotent stem cell-derived organoids: using principles of developmental biology to grow human tissues in a dish. *Development* **144**, 958-962, doi:10.1242/dev.140731 (2017).

82   Takebe, T. & Wells, J. M. Organoids by design. *Science* **364**, 956-959, doi:10.1126/science.aaw7567 (2019).

83   Eiraku, M. *et al.* Self-organizing optic-cup morphogenesis in three-dimensional culture. *Nature* **472**, 51-56, doi:10.1038/nature09941 (2011).

84   Sato, T. *et al.* Single Lgr5 stem cells build crypt-villus structures in vitro without a mesenchymal niche. *Nature* **459**, 262-265, doi:10.1038/nature07935 (2009).

85   Lancaster, M. A. & Knoblich, J. A. Organogenesis in a dish: modeling development and disease using organoid technologies. *Science* **345**, 1247125, doi:10.1126/science.1247125 (2014).

86   Barker, N. *et al.* Lgr5(+ve) stem cells drive self-renewal in the stomach and build long-lived gastric units in vitro. *Cell Stem Cell* **6**, 25-36, doi:10.1016/j.stem.2009.11.013 (2010).

87   Huch, M. *et al.* Unlimited in vitro expansion of adult bi-potent pancreas progenitors through the Lgr5/R-spondin axis. *EMBO J* **32**, 2708-2721, doi:10.1038/emboj.2013.204 (2013).

88   Huch, M. *et al.* In vitro expansion of single Lgr5+ liver stem cells induced by Wnt-driven regeneration. *Nature* **494**, 247-250, doi:10.1038/nature11826 (2013).

89   Clevers, H. Modeling Development and Disease with Organoids. *Cell* **165**, 1586-1597, doi:10.1016/j.cell.2016.05.082 (2016).

90   Simunovic, M. & Brivanlou, A. H. Embryoids, organoids and gastruloids: new approaches to understanding embryogenesis. *Development* **144**, 976-985, doi:10.1242/dev.143529 (2017).

91   Simian, M. & Bissell, M. J. Organoids: A historical perspective of thinking in three dimensions. *J Cell Biol* **216**, 31-40, doi:10.1083/jcb.201610056 (2017).

92   Bissell, M. J., Hall, H. G. & Parry, G. How does the extracellular matrix direct gene expression? *J Theor Biol* **99**, 31-68, doi:10.1016/0022-5193(82)90388-5 (1982).

93   Hall, H. G., Farson, D. A. & Bissell, M. J. Lumen formation by epithelial cell lines in response to collagen overlay: a morphogenetic model in culture. *Proc Natl Acad Sci U S A* **79**, 4672-4676, doi:10.1073/pnas.79.15.4672 (1982).

94   McCracken, K. W. *et al.* Modelling human development and disease in pluripotent stem-cell-derived gastric organoids. *Nature* **516**, 400-404, doi:10.1038/nature13863 (2014).

95   Spence, J. R. *et al.* Directed differentiation of human pluripotent stem cells into intestinal tissue in vitro. *Nature* **470**, 105-109, doi:10.1038/nature09691 (2011).

96   Navis, M. *et al.* Mouse fetal intestinal organoids: new model to study epithelial maturation from suckling to weaning. *EMBO Rep* **20**, doi:10.15252/embr.201846221 (2019).

97   Sato, T. *et al.* Paneth cells constitute the niche for Lgr5 stem cells in intestinal crypts. *Nature* **469**, 415-418, doi:10.1038/nature09637 (2011).

98   Yin, X. *et al.* Niche-independent high-purity cultures of Lgr5+ intestinal stem cells and their progeny. *Nat Methods* **11**, 106-112, doi:10.1038/nmeth.2737 (2014).

99   van Es, J. H. *et al.* Dll1+ secretory progenitor cells revert to stem cells upon crypt damage. *Nat Cell Biol* **14**, 1099-1104, doi:10.1038/ncb2581 (2012).

100   Tetteh, P. W. *et al.* Replacement of Lost Lgr5-Positive Stem Cells through Plasticity of Their Enterocyte-Lineage Daughters. *Cell Stem Cell* **18**, 203-213, doi:10.1016/j.stem.2016.01.001 (2016).

101   Fordham, R. P. *et al.* Transplantation of expanded fetal intestinal progenitors contributes to colon regeneration after injury. *Cell Stem Cell* **13**, 734-744, doi:10.1016/j.stem.2013.09.015 (2013).

102   Mustata, R. C. *et al.* Identification of Lgr5-independent spheroid-generating progenitors of the mouse fetal intestinal epithelium. *Cell Rep* **5**, 421-432, doi:10.1016/j.celrep.2013.09.005 (2013).

103   Yu, S. *et al.* Paneth Cell Multipotency Induced by Notch Activation following Injury. *Cell Stem Cell* **23**, 46-59 e45, doi:10.1016/j.stem.2018.05.002 (2018).

104   Farin, H. F. *et al.* Visualization of a short-range Wnt gradient in the intestinal stem-cell niche. *Nature* **530**, 340-343, doi:10.1038/nature16937 (2016).

105   Farin, H. F., Van Es, J. H. & Clevers, H. Redundant sources of Wnt regulate intestinal stem cells and promote formation of Paneth cells. *Gastroenterology* **143**, 1518-1529 e1517, doi:10.1053/j.gastro.2012.08.031 (2012).

106   van Es, J. H. *et al.* Wnt signalling induces maturation of Paneth cells in intestinal crypts. *Nat Cell Biol* **7**, 381-386, doi:10.1038/ncb1240 (2005).

107   Groschwitz, K. R. & Hogan, S. P. Intestinal barrier function: molecular regulation and disease pathogenesis. *J Allergy Clin Immunol* **124**, 3-20; quiz 21-22, doi:10.1016/j.jaci.2009.05.038 (2009).

108   Gehart, H. & Clevers, H. Tales from the crypt: new insights into intestinal stem cells. *Nat Rev Gastroenterol Hepatol* **16**, 19-34, doi:10.1038/s41575-018-0081-y (2019).

109   Barker, N. *et al.* Crypt stem cells as the cells-of-origin of intestinal cancer. *Nature* **457**, 608-611, doi:10.1038/nature07602 (2009).

110   Schepers, A. G., Vries, R., van den Born, M., van de Wetering, M. & Clevers, H. Lgr5 intestinal stem cells have high telomerase activity and randomly segregate their chromosomes. *EMBO J* **30**, 1104-1109, doi:10.1038/emboj.2011.26 (2011).

111   Snippert, H. J. *et al.* Intestinal crypt homeostasis results from neutral competition between symmetrically dividing Lgr5 stem cells. *Cell* **143**, 134-144, doi:10.1016/j.cell.2010.09.016 (2010).

112   Barker, N. Adult intestinal stem cells: critical drivers of epithelial homeostasis and regeneration. *Nat Rev Mol Cell Biol* **15**, 19-33, doi:10.1038/nrm3721 (2014).

113   Darwich, A. S., Aslam, U., Ashcroft, D. M. & Rostami-Hodjegan, A. Meta-analysis of the turnover of intestinal epithelia in preclinical animal species and humans. *Drug Metab Dispos* **42**, 2016-2022, doi:10.1124/dmd.114.058404 (2014).

114   van der Flier, L. G. & Clevers, H. Stem cells, self-renewal, and differentiation in the intestinal epithelium. *Annu Rev Physiol* **71**, 241-260, doi:10.1146/annurev.physiol.010908.163145 (2009).

115   Ireland, H., Houghton, C., Howard, L. & Winton, D. J. Cellular inheritance of a Cre-activated reporter gene to determine Paneth cell longevity in the murine small intestine. *Dev Dyn* **233**, 1332-1336, doi:10.1002/dvdy.20446 (2005).

116   Clevers, H. C. & Bevins, C. L. Paneth cells: maestros of the small intestinal crypts. *Annu Rev Physiol* **75**, 289-311, doi:10.1146/annurev-physiol-030212-183744 (2013).

117   Gassler, N. Paneth cells in intestinal physiology and pathophysiology. *World J Gastrointest Pathophysiol* **8**, 150-160, doi:10.4291/wjgp.v8.i4.150 (2017).

118   Allaire, J. M. *et al.* The Intestinal Epithelium: Central Coordinator of Mucosal Immunity: (Trends in Immunology 39, 677-696, 2018). *Trends Immunol* **40**, 174, doi:10.1016/j.it.2018.12.008 (2019).

119   Wang, S. L. *et al.* Impact of Paneth Cell Autophagy on Inflammatory Bowel Disease. *Front Immunol* **9**, 693, doi:10.3389/fimmu.2018.00693 (2018).

120   Moor, A. E. *et al.* Spatial Reconstruction of Single Enterocytes Uncovers Broad Zonation along the Intestinal Villus Axis. *Cell* **175**, 1156-1167 e1115, doi:10.1016/j.cell.2018.08.063 (2018).

121   Wells, J. M. & Spence, J. R. How to make an intestine. *Development* **141**, 752-760, doi:10.1242/dev.097386 (2014).

122   Guiu, J. & Jensen, K. B. From Definitive Endoderm to Gut-a Process of Growth and Maturation. *Stem Cells Dev* **24**, 1972-1983, doi:10.1089/scd.2015.0017 (2015).

123   Walton, K. D. *et al.* Villification in the mouse: Bmp signals control intestinal villus patterning. *Development* **143**, 427-436, doi:10.1242/dev.130112 (2016).

124   Nigmatullina, L. *et al.* Id2 controls specification of Lgr5(+) intestinal stem cell progenitors during gut development. *EMBO J* **36**, 869-885, doi:10.15252/embj.201694959 (2017).

125   Guiu, J. *et al.* Tracing the origin of adult intestinal stem cells. *Nature* **570**, 107-111, doi:10.1038/s41586-019-1212-5 (2019).

126   Bry, L. *et al.* Paneth cell differentiation in the developing intestine of normal and transgenic mice. *Proc Natl Acad Sci U S A* **91**, 10335-10339, doi:10.1073/pnas.91.22.10335 (1994).

127   Beumer, J. & Clevers, H. Regulation and plasticity of intestinal stem cells during homeostasis and regeneration. *Development* **143**, 3639-3649, doi:10.1242/dev.133132 (2016).

128   Lindemans, C. A. *et al.* Interleukin-22 promotes intestinal-stem-cell-mediated epithelial regeneration. *Nature* **528**, 560-564, doi:10.1038/nature16460 (2015).

129   Richmond, C. A. *et al.* Dormant Intestinal Stem Cells Are Regulated by PTEN and Nutritional Status. *Cell Rep* **13**, 2403-2411, doi:10.1016/j.celrep.2015.11.035 (2015).

130   Tao, S. *et al.* Wnt activity and basal niche position sensitize intestinal stem and progenitor cells to DNA damage. *EMBO J* **36**, 2920-2921, doi:10.15252/embj.201797813 (2017).

131   Metcalfe, C., Kljavin, N. M., Ybarra, R. & de Sauvage, F. J. Lgr5+ stem cells are indispensable for radiation-induced intestinal regeneration. *Cell Stem Cell* **14**, 149-159, doi:10.1016/j.stem.2013.11.008 (2014).

132   Li, L. & Clevers, H. Coexistence of quiescent and active adult stem cells in mammals. *Science* **327**, 542-545, doi:10.1126/science.1180794 (2010).

133   Montgomery, R. K. *et al.* Mouse telomerase reverse transcriptase (mTert) expression marks slowly cycling intestinal stem cells. *Proc Natl Acad Sci U S A* **108**, 179-184, doi:10.1073/pnas.1013004108 (2011).

134   Munoz, J. *et al.* The Lgr5 intestinal stem cell signature: robust expression of proposed quiescent '+4' cell markers. *EMBO J* **31**, 3079-3091, doi:10.1038/emboj.2012.166 (2012).

135   Grun, D. *et al.* Single-cell messenger RNA sequencing reveals rare intestinal cell types. *Nature* **525**, 251-255, doi:10.1038/nature14966 (2015).

136   Buczacki, S. J. *et al.* Intestinal label-retaining cells are secretory precursors expressing Lgr5. *Nature* **495**, 65-69, doi:10.1038/nature11965 (2013).

137   Jadhav, U. *et al.* Dynamic Reorganization of Chromatin Accessibility Signatures during Dedifferentiation of Secretory Precursors into Lgr5+ Intestinal Stem Cells. *Cell Stem Cell* **21**, 65-77 e65, doi:10.1016/j.stem.2017.05.001 (2017).

138   Ayyaz, A. *et al.* Single-cell transcriptomes of the regenerating intestine reveal a revival stem cell. *Nature* **569**, 121-125, doi:10.1038/s41586-019-1154-y (2019).

139   Li, V. S. W. Yap in regeneration and symmetry breaking. *Nat Cell Biol* **21**, 665-667, doi:10.1038/s41556-019-0334-1 (2019).

140   Van Camp, J. K., Beckers, S., Zegers, D. & Van Hul, W. Wnt signaling and the control of human stem cell fate. *Stem Cell Rev Rep* **10**, 207-229, doi:10.1007/s12015-013-9486-8 (2014).

141   Niehrs, C. The complex world of WNT receptor signalling. *Nat Rev Mol Cell Biol* **13**, 767-779, doi:10.1038/nrm3470 (2012).

142   Steinhart, Z. & Angers, S. Wnt signaling in development and tissue homeostasis. *Development* **145**, doi:10.1242/dev.146589 (2018).

143   Roose, J. *et al.* The Xenopus Wnt effector XTcf-3 interacts with Groucho-related transcriptional repressors. *Nature* **395**, 608-612, doi:10.1038/26989 (1998).

144   Angers, S. & Moon, R. T. Proximal events in Wnt signal transduction. *Nat Rev Mol Cell Biol* **10**, 468-477, doi:10.1038/nrm2717 (2009).

145   Komiya, Y. & Habas, R. Wnt signal transduction pathways. *Organogenesis* **4**, 68-75, doi:10.4161/org.4.2.5851 (2008).

146   Qian, D. *et al.* Wnt5a functions in planar cell polarity regulation in mice. *Dev Biol* **306**, 121-133, doi:10.1016/j.ydbio.2007.03.011 (2007).

147   Valenta, T. *et al.* Wnt Ligands Secreted by Subepithelial Mesenchymal Cells Are Essential for the Survival of Intestinal Stem Cells and Gut Homeostasis. *Cell Rep* **15**, 911-918, doi:10.1016/j.celrep.2016.03.088 (2016).

148   Stzepourginski, I. *et al.* CD34+ mesenchymal cells are a major component of the intestinal stem cells niche at homeostasis and after injury. *Proc Natl Acad Sci U S A* **114**, E506-E513, doi:10.1073/pnas.1620059114 (2017).

149   Korinek, V. *et al.* Depletion of epithelial stem-cell compartments in the small intestine of mice lacking Tcf-4. *Nat Genet* **19**, 379-383, doi:10.1038/1270 (1998).

150   van Es, J. H. *et al.* A critical role for the Wnt effector Tcf4 in adult intestinal homeostatic self-renewal. *Mol Cell Biol* **32**, 1918-1927, doi:10.1128/MCB.06288-11 (2012).

151   Pinto, D., Gregorieff, A., Begthel, H. & Clevers, H. Canonical Wnt signals are essential for homeostasis of the intestinal epithelium. *Genes Dev* **17**, 1709-1713, doi:10.1101/gad.267103 (2003).

152   de Lau, W. *et al.* Lgr5 homologues associate with Wnt receptors and mediate R-spondin signalling. *Nature* **476**, 293-297, doi:10.1038/nature10337 (2011).

153   Yan, K. S. *et al.* Non-equivalence of Wnt and R-spondin ligands during Lgr5(+) intestinal stem-cell self-renewal. *Nature* **545**, 238-242, doi:10.1038/nature22313 (2017).

154   Bastide, P. *et al.* Sox9 regulates cell proliferation and is required for Paneth cell differentiation in the intestinal epithelium. *J Cell Biol* **178**, 635-648, doi:10.1083/jcb.200704152 (2007).

155   Mori-Akiyama, Y. *et al.* SOX9 is required for the differentiation of paneth cells in the intestinal epithelium. *Gastroenterology* **133**, 539-546, doi:10.1053/j.gastro.2007.05.020 (2007).

156   Bray, S. J. Notch signalling in context. *Nat Rev Mol Cell Biol* **17**, 722-735, doi:10.1038/nrm.2016.94 (2016).

157   Sancho, R., Cremona, C. A. & Behrens, A. Stem cell and progenitor fate in the mammalian intestine: Notch and lateral inhibition in homeostasis and disease. *EMBO Rep* **16**, 571-581, doi:10.15252/embr.201540188 (2015).

158   Lewis, J. Notch signalling and the control of cell fate choices in vertebrates. *Semin Cell Dev Biol* **9**, 583-589, doi:10.1006/scdb.1998.0266 (1998).

159   Wilkinson, H. A., Fitzgerald, K. & Greenwald, I. Reciprocal changes in expression of the receptor lin-12 and its ligand lag-2 prior to commitment in a C. elegans cell fate decision. *Cell* **79**, 1187-1198, doi:10.1016/0092-8674(94)90010-8 (1994).

160   Corson, F., Couturier, L., Rouault, H., Mazouni, K. & Schweisguth, F. Self-organized Notch dynamics generate stereotyped sensory organ patterns in Drosophila. *Science* **356**, doi:10.1126/science.aai7407 (2017).

161   Basch, M. L. *et al.* Fine-tuning of Notch signaling sets the boundary of the organ of Corti and establishes sensory cell fates. *Elife* **5**, doi:10.7554/eLife.19921 (2016).

162   van Es, J. H. *et al.* Notch/gamma-secretase inhibition turns proliferative cells in intestinal crypts and adenomas into goblet cells. *Nature* **435**, 959-963, doi:10.1038/nature03659 (2005).

163   Pellegrinet, L. *et al.* Dll1- and dll4-mediated notch signaling are required for homeostasis of intestinal stem cells. *Gastroenterology* **140**, 1230-1240 e1231-1237, doi:10.1053/j.gastro.2011.01.005 (2011).

164   Yang, Q., Bermingham, N. A., Finegold, M. J. & Zoghbi, H. Y. Requirement of Math1 for secretory cell lineage commitment in the mouse intestine. *Science* **294**, 2155-2158, doi:10.1126/science.1065718 (2001).

165   Snippert, H. J., Schepers, A. G., van Es, J. H., Simons, B. D. & Clevers, H. Biased competition between Lgr5 intestinal stem cells driven by oncogenic mutation induces clonal expansion. *EMBO Rep* **15**, 62-69, doi:10.1002/embr.201337799 (2014).

166   Wong, V. W. *et al.* Lrig1 controls intestinal stem-cell homeostasis by negative regulation of ErbB signalling. *Nat Cell Biol* **14**, 401-408, doi:10.1038/ncb2464 (2012).

167   Kabiri, Z. *et al.* Wnt signaling suppresses MAPK-driven proliferation of intestinal stem cells. *J Clin Invest* **128**, 3806-3812, doi:10.1172/JCI99325 (2018).

168   Basak, O. *et al.* Induced Quiescence of Lgr5+ Stem Cells in Intestinal Organoids Enables Differentiation of Hormone-Producing Enteroendocrine Cells. *Cell Stem Cell* **20**, 177-190 e174, doi:10.1016/j.stem.2016.11.001 (2017).

169   He, X. C. *et al.* BMP signaling inhibits intestinal stem cell self-renewal through suppression of Wnt-beta-catenin signaling. *Nat Genet* **36**, 1117-1121, doi:10.1038/ng1430 (2004).

170   Haramis, A. P. *et al.* De novo crypt formation and juvenile polyposis on BMP inhibition in mouse intestine. *Science* **303**, 1684-1686, doi:10.1126/science.1093587 (2004).

171   Kosinski, C. *et al.* Gene expression patterns of human colon tops and basal crypts and BMP antagonists as intestinal stem cell niche factors. *Proc Natl Acad Sci U S A* **104**, 15418-15423, doi:10.1073/pnas.0707210104 (2007).

172   Totaro, A., Panciera, T. & Piccolo, S. YAP/TAZ upstream signals and downstream responses. *Nat Cell Biol* **20**, 888-899, doi:10.1038/s41556-018-0142-z (2018).

173   Moya, I. M. & Halder, G. Hippo-YAP/TAZ signalling in organ regeneration and regenerative medicine. *Nat Rev Mol Cell Biol* **20**, 211-226, doi:10.1038/s41580-018-0086-y (2019).

174   Lin, C. H. *et al.* Microenvironment rigidity modulates responses to the HER2 receptor tyrosine kinase inhibitor lapatinib via YAP and TAZ transcription factors. *Mol Biol Cell* **26**, 3946-3953, doi:10.1091/mbc.E15-07-0456 (2015).

175   Dobrokhotov, O., Samsonov, M., Sokabe, M. & Hirata, H. Mechanoregulation and pathology of YAP/TAZ via Hippo and non-Hippo mechanisms. *Clin Transl Med* **7**, 23, doi:10.1186/s40169-018-0202-9 (2018).

176   Zhao, B. *et al.* Inactivation of YAP oncoprotein by the Hippo pathway is involved in cell contact inhibition and tissue growth control. *Genes Dev* **21**, 2747-2761, doi:10.1101/gad.1602907 (2007).

177   Zhao, B., Li, L., Tumaneng, K., Wang, C. Y. & Guan, K. L. A coordinated phosphorylation by Lats and CK1 regulates YAP stability through SCF(beta-TRCP). *Genes Dev* **24**, 72-85, doi:10.1101/gad.1843810 (2010).

178   Yu, F. X. *et al.* Regulation of the Hippo-YAP pathway by G-protein-coupled receptor signaling. *Cell* **150**, 780-791, doi:10.1016/j.cell.2012.06.037 (2012).

179   Mohseni, M. *et al.* A genetic screen identifies an LKB1-MARK signalling axis controlling the Hippo-YAP pathway. *Nat Cell Biol* **16**, 108-117, doi:10.1038/ncb2884 (2014).

180   Varelas, X. *et al.* The Crumbs complex couples cell density sensing to Hippo-dependent control of the TGF-beta-SMAD pathway. *Dev Cell* **19**, 831-844, doi:10.1016/j.devcel.2010.11.012 (2010).

181   Yin, F. *et al.* Spatial organization of Hippo signaling at the plasma membrane mediated by the tumor suppressor Merlin/NF2. *Cell* **154**, 1342-1355, doi:10.1016/j.cell.2013.08.025 (2013).

182   Furukawa, K. T., Yamashita, K., Sakurai, N. & Ohno, S. The Epithelial Circumferential Actin Belt Regulates YAP/TAZ through Nucleocytoplasmic Shuttling of Merlin. *Cell Rep* **20**, 1435-1447, doi:10.1016/j.celrep.2017.07.032 (2017).

183   Aragona, M. *et al.* A mechanical checkpoint controls multicellular growth through YAP/TAZ regulation by actin-processing factors. *Cell* **154**, 1047-1059, doi:10.1016/j.cell.2013.07.042 (2013).

184   Sero, J. E. & Bakal, C. Multiparametric Analysis of Cell Shape Demonstrates that beta-PIX Directly Couples YAP Activation to Extracellular Matrix Adhesion. *Cell Syst* **4**, 84-96 e86, doi:10.1016/j.cels.2016.11.015 (2017).

185   Sabra, H. *et al.* beta1 integrin-dependent Rac/group I PAK signaling mediates YAP activation of Yes-associated protein 1 (YAP1) via NF2/merlin. *J Biol Chem* **292**, 19179-19197, doi:10.1074/jbc.M117.808063 (2017).

186   Elosegui-Artola, A. *et al.* Force Triggers YAP Nuclear Entry by Regulating Transport across Nuclear Pores. *Cell* **171**, 1397-1410 e1314, doi:10.1016/j.cell.2017.10.008 (2017).

187   Shiu, J. Y., Aires, L., Lin, Z. & Vogel, V. Nanopillar force measurements reveal actin-cap-mediated YAP mechanotransduction. *Nat Cell Biol* **20**, 262-271, doi:10.1038/s41556-017-0030-y (2018).

188   Hong, A. W., Meng, Z. & Guan, K. L. The Hippo pathway in intestinal regeneration and disease. *Nat Rev Gastroenterol Hepatol* **13**, 324-337, doi:10.1038/nrgastro.2016.59 (2016).

189   Johnson, R. & Halder, G. The two faces of Hippo: targeting the Hippo pathway for regenerative medicine and cancer treatment. *Nat Rev Drug Discov* **13**, 63-79, doi:10.1038/nrd4161 (2014).

190   Barry, E. R. *et al.* Restriction of intestinal stem cell expansion and the regenerative response by YAP. *Nature* **493**, 106-110, doi:10.1038/nature11693 (2013).

191   Camargo, F. D. *et al.* YAP1 increases organ size and expands undifferentiated progenitor cells. *Curr Biol* **17**, 2054-2060, doi:10.1016/j.cub.2007.10.039 (2007).

192   Cai, J. *et al.* The Hippo signaling pathway restricts the oncogenic potential of an intestinal regeneration program. *Genes Dev* **24**, 2383-2388, doi:10.1101/gad.1978810 (2010).

193   Imajo, M., Ebisuya, M. & Nishida, E. Dual role of YAP and TAZ in renewal of the intestinal epithelium. *Nat Cell Biol* **17**, 7-19, doi:10.1038/ncb3084 (2015).

194   Zhou, D. *et al.* Mst1 and Mst2 protein kinases restrain intestinal stem cell proliferation and colonic tumorigenesis by inhibition of Yes-associated protein (Yap) overabundance. *Proc Natl Acad Sci U S A* **108**, E1312-1320, doi:10.1073/pnas.1110428108 (2011).

195   Gregorieff, A., Liu, Y., Inanlou, M. R., Khomchuk, Y. & Wrana, J. L. Yap-dependent reprogramming of Lgr5(+) stem cells drives intestinal regeneration and cancer. *Nature* **526**, 715-718, doi:10.1038/nature15382 (2015).

196   Yui, S. *et al.* YAP/TAZ-Dependent Reprogramming of Colonic Epithelium Links ECM Remodeling to Tissue Regeneration. *Cell Stem Cell* **22**, 35-49 e37, doi:10.1016/j.stem.2017.11.001 (2018).

197   Ritsma, L. *et al.* Intestinal crypt homeostasis revealed at single-stem-cell level by in vivo live imaging. *Nature* **507**, 362-365, doi:10.1038/nature12972 (2014).

198   Gehart, H. *et al.* Identification of Enteroendocrine Regulators by Real-Time Single-Cell Differentiation Mapping. *Cell* **176**, 1158-1173 e1116, doi:10.1016/j.cell.2018.12.029 (2019).

199   Gerdes, M. J. *et al.* Highly multiplexed single-cell analysis of formalin-fixed, paraffin-embedded cancer tissue. *Proc Natl Acad Sci U S A* **110**, 11982-11987, doi:10.1073/pnas.1300136110 (2013).

200   Herring, C. A. *et al.* Unsupervised Trajectory Analysis of Single-Cell RNA-Seq and Imaging Data Reveals Alternative Tuft Cell Origins in the Gut. *Cell Syst* **6**, 37-51 e39, doi:10.1016/j.cels.2017.10.012 (2018).

201   Goldman, S. L. *et al.* The Impact of Heterogeneity on Single-Cell Sequencing. *Front Genet* **10**, 8, doi:10.3389/fgene.2019.00008 (2019).

202   Hadjantonakis, A. K. & Arias, A. M. Single-Cell Approaches: Pandora's Box of Developmental Mechanisms. *Dev Cell* **38**, 574-578, doi:10.1016/j.devcel.2016.09.012 (2016).

203   Kiselev, V. Y. *et al.* SC3: consensus clustering of single-cell RNA-seq data. *Nat Methods* **14**, 483-486, doi:10.1038/nmeth.4236 (2017).

204   Tritschler, S. *et al.* Concepts and limitations for learning developmental trajectories from single cell genomics. *Development* **146**, doi:10.1242/dev.170506 (2019).

205   Bendall, S. C. *et al.* Single-cell trajectory detection uncovers progression and regulatory coordination in human B cell development. *Cell* **157**, 714-725, doi:10.1016/j.cell.2014.04.005 (2014).

206   Setty, M. *et al.* Wishbone identifies bifurcating developmental trajectories from single-cell data. *Nat Biotechnol* **34**, 637-645, doi:10.1038/nbt.3569 (2016).

207   Haghverdi, L., Buttner, M., Wolf, F. A., Buettner, F. & Theis, F. J. Diffusion pseudotime robustly reconstructs lineage branching. *Nat Methods* **13**, 845-848, doi:10.1038/nmeth.3971 (2016).

208   Farrell, J. A. *et al.* Single-cell reconstruction of developmental trajectories during zebrafish embryogenesis. *Science* **360**, doi:10.1126/science.aar3131 (2018).

209   Plass, M. *et al.* Cell type atlas and lineage tree of a whole complex animal by single-cell transcriptomics. *Science* **360**, doi:10.1126/science.aaq1723 (2018).

210   Trapnell, C. *et al.* The dynamics and regulators of cell fate decisions are revealed by pseudotemporal ordering of single cells. *Nat Biotechnol* **32**, 381-386, doi:10.1038/nbt.2859 (2014).

211   Rios, A. C. & Clevers, H. Imaging organoids: a bright future ahead. *Nat Methods* **15**, 24-26, doi:10.1038/nmeth.4537 (2018).

212   Yates, F. E. *Self-organizing systems: The emergence of order.* (Springer Science & Business Media, 2012).

213   Borten, M. A., Bajikar, S. S., Sasaki, N., Clevers, H. & Janes, K. A. Automated brightfield morphometry of 3D organoid populations by OrganoSeg. *Sci Rep* **8**, 5319, doi:10.1038/s41598-017-18815-8 (2018).

214   Mayr, U., Serra, D. & Liberali, P. Exploring single cells in space and time during tissue development, homeostasis and regeneration. *Development* **146**, doi:10.1242/dev.176727 (2019).

215   Garvey, C. M. *et al.* A high-content image-based method for quantitatively studying context-dependent cell population dynamics. *Sci Rep* **6**, 29752, doi:10.1038/srep29752 (2016).

216   Phan, N. *et al.* A simple high-throughput approach identifies actionable drug sensitivities in patient-derived tumor organoids. *Commun Biol* **2**, 78, doi:10.1038/s42003-019-0305-x (2019).

217   Dekkers, J. F. *et al.* Characterizing responses to CFTR-modulating drugs using rectal organoids derived from subjects with cystic fibrosis. *Sci Transl Med* **8**, 344ra384, doi:10.1126/scitranslmed.aad8278 (2016).

218   Murray, E. *et al.* Simple, Scalable Proteomic Imaging for High-Dimensional Profiling of Intact Systems. *Cell* **163**, 1500-1514, doi:10.1016/j.cell.2015.11.025 (2015).

219   Park, Y. G. *et al.* Protection of tissue physicochemical properties using polyfunctional crosslinkers. *Nat Biotechnol*, doi:10.1038/nbt.4281 (2018).

220   Chung, K. *et al.* Structural and molecular interrogation of intact biological systems. *Nature* **497**, 332-337, doi:10.1038/nature12107 (2013).

221   Saka, S. K. *et al.* Immuno-SABER enables highly multiplexed and amplified protein imaging in tissues. *Nat Biotechnol* **37**, 1080-1090, doi:10.1038/s41587-019-0207-y (2019).

222   Goltsev, Y. *et al.* Deep Profiling of Mouse Splenic Architecture with CODEX Multiplexed Imaging. *Cell* **174**, 968-981 e915, doi:10.1016/j.cell.2018.07.010 (2018).

223   Lonnberg, T. *et al.* Single-cell RNA-seq and computational analysis using temporal mixture modelling resolves Th1/Tfh fate bifurcation in malaria. *Sci Immunol* **2**, doi:10.1126/sciimmunol.aal2192 (2017).

224   Schiebinger, G. *et al.* Optimal-Transport Analysis of Single-Cell Gene Expression Identifies Developmental Trajectories in Reprogramming. *Cell* **176**, 1517, doi:10.1016/j.cell.2019.02.026 (2019).
225   Setty, M. *et al.* Characterization of cell fate probabilities in single-cell data with Palantir. *Nat Biotechnol* **37**, 451-460, doi:10.1038/s41587-019-0068-4 (2019).
226   Yan, K. S. *et al.* Intestinal Enteroendocrine Lineage Cells Possess Homeostatic and Injury-Inducible Stem Cell Activity. *Cell Stem Cell* **21**, 78-90 e76, doi:10.1016/j.stem.2017.06.014 (2017).
227   Nusse, Y. M. *et al.* Parasitic helminths induce fetal-like reversion in the intestinal stem cell niche. *Nature* **559**, 109-113, doi:10.1038/s41586-018-0257-1 (2018).
228   Holmes, C. & Stanford, W. L. Concise review: stem cell antigen-1: expression, function, and enigma. *Stem Cells* **25**, 1339-1347, doi:10.1634/stemcells.2006-0644 (2007).
229   Zhang, F. *et al.* Clusterin facilitates stress-induced lipidation of LC3 and autophagosome biogenesis to enhance cancer cell survival. *Nat Commun* **5**, 5775, doi:10.1038/ncomms6775 (2014).
230   Park, J. J., Lim, K. H. & Baek, K. H. Annexin-1 regulated by HAUSP is essential for UV-induced damage response. *Cell Death Dis* **6**, e1654, doi:10.1038/cddis.2015.32 (2015).
231   Buczacki, S. Fate plasticity in the intestine: The devil is in the detail. *World J Gastroenterol* **25**, 3116-3122, doi:10.3748/wjg.v25.i25.3116 (2019).
232   Potten, C. S., Martin, K. & Kirkwood, T. B. Ageing of murine small intestinal stem cells. *Novartis Found Symp* **235**, 66-79; discussion 79-84, 101-104 (2001).
233   Neumuller, R. A. & Knoblich, J. A. Dividing cellular asymmetry: asymmetric cell division and its implications for stem cells and cancer. *Genes Dev* **23**, 2675-2699, doi:10.1101/gad.1850809 (2009).
234   Kim, T. H. *et al.* Broadly permissive intestinal chromatin underlies lateral inhibition and cell plasticity. *Nature* **506**, 511-515, doi:10.1038/nature12903 (2014).
235   Yan, K. S. *et al.* The intestinal stem cell markers Bmi1 and Lgr5 identify two functionally distinct populations. *Proc Natl Acad Sci U S A* **109**, 466-471, doi:10.1073/pnas.1118857109 (2012).
236   Asfaha, S. *et al.* Krt19(+)/Lgr5(-) Cells Are Radioresistant Cancer-Initiating Stem Cells in the Colon and Intestine. *Cell Stem Cell* **16**, 627-638, doi:10.1016/j.stem.2015.04.013 (2015).
237   de Sousa, E. M. F. & de Sauvage, F. J. Cellular Plasticity in Intestinal Homeostasis and Disease. *Cell Stem Cell* **24**, 54-64, doi:10.1016/j.stem.2018.11.019 (2019).
238   Tian, H. *et al.* A reserve stem cell population in small intestine renders Lgr5-positive cells dispensable. *Nature* **478**, 255-259, doi:10.1038/nature10408 (2011).
239   Hosen, N. *et al.* Bmi-1-green fluorescent protein-knock-in mice reveal the dynamic regulation of bmi-1 expression in normal and leukemic hematopoietic cells. *Stem Cells* **25**, 1635-1644, doi:10.1634/stemcells.2006-0229 (2007).
240   Jones, J. C. *et al.* Cellular Plasticity of Defa4(Cre)-Expressing Paneth Cells in Response to Notch Activation and Intestinal Injury. *Cell Mol Gastroenterol Hepatol* **7**, 533-554, doi:10.1016/j.jcmgh.2018.11.004 (2019).
241   Hua, G. *et al.* Crypt base columnar stem cells in small intestines of mice are radioresistant. *Gastroenterology* **143**, 1266-1276, doi:10.1053/j.gastro.2012.07.106 (2012).
242   Kuijk, E. *et al.* Early divergence of mutational processes in human fetal tissues. *Sci Adv* **5**, eaaw1271, doi:10.1126/sciadv.aaw1271 (2019).
243   Panciera, T. *et al.* Induction of Expandable Tissue-Specific Stem/Progenitor Cells through Transient Expression of YAP/TAZ. *Cell Stem Cell* **19**, 725-737, doi:10.1016/j.stem.2016.08.009 (2016).
244   Monroe, T. O. *et al.* YAP Partially Reprograms Chromatin Accessibility to Directly Induce Adult Cardiogenesis In Vivo. *Dev Cell* **48**, 765-779 e767, doi:10.1016/j.devcel.2019.01.017 (2019).
245   Hicks-Berthet, J. & Varelas, X. Integrin-FAK-CDC42-PP1A signaling gnaws at YAP/TAZ activity to control incisor stem cells. *Bioessays* **39**, doi:10.1002/bies.201700116 (2017).
246   Schmitt, M., Metzger, M., Gradl, D., Davidson, G. & Orian-Rousseau, V. CD44 functions in Wnt signaling by regulating LRP6 localization and activation. *Cell Death Differ* **22**, 677-689, doi:10.1038/cdd.2014.156 (2015).
247   Schuijers, J. *et al.* Ascl2 acts as an R-spondin/Wnt-responsive switch to control stemness in intestinal crypts. *Cell Stem Cell* **16**, 158-170, doi:10.1016/j.stem.2014.12.006 (2015).
248   Blache, P. *et al.* SOX9 is an intestine crypt transcription factor, is regulated by the Wnt pathway, and represses the CDX2 and MUC2 genes. *J Cell Biol* **166**, 37-47, doi:10.1083/jcb.200311021 (2004).
249   Azzolin, L. *et al.* YAP/TAZ incorporation in the beta-catenin destruction complex orchestrates the Wnt response. *Cell* **158**, 157-170, doi:10.1016/j.cell.2014.06.013 (2014).
250   Park, H. W. *et al.* Alternative Wnt Signaling Activates YAP/TAZ. *Cell* **162**, 780-794, doi:10.1016/j.cell.2015.07.013 (2015).
251   Panciera, T., Azzolin, L., Cordenonsi, M. & Piccolo, S. Mechanobiology of YAP and TAZ in physiology and disease. *Nat Rev Mol Cell Biol* **18**, 758-770, doi:10.1038/nrm.2017.87 (2017).
252   Franklin, J. M., Ghosh, R. P., Shi, Q. & Liphardt, J. T. Concerted localization resets precede YAP-dependent transcription. *bioRxiv*, 539049, doi:10.1101/539049 (2019).
253   Gjorevski, N. *et al.* Designer matrices for intestinal stem cell and organoid culture. *Nature* **539**, 560-564, doi:10.1038/nature20168 (2016).
254   Kim, H. B. *et al.* Prostaglandin E2 Activates YAP and a Positive-Signaling Loop to Promote Colon Regeneration After Colitis but Also Carcinogenesis in Mice. *Gastroenterology* **152**, 616-630, doi:10.1053/j.gastro.2016.11.005 (2017).
255   Bertocchi, C. *et al.* Nanoscale architecture of cadherin-based cell adhesions. *Nat Cell Biol* **19**, 28-37, doi:10.1038/ncb3456 (2017).
256   Hirata, H., Samsonov, M. & Sokabe, M. Actomyosin contractility provokes contact inhibition in E-cadherin-ligated keratinocytes. *Sci Rep* **7**, 46326, doi:10.1038/srep46326 (2017).
257   Elbediwy, A. *et al.* Integrin signalling regulates YAP and TAZ to control skin homeostasis. *Development* **143**, 1674-1687, doi:10.1242/dev.133728 (2016).
258   Zhang, L. *et al.* KIBRA regulates aurora kinase activity and is required for precise chromosome alignment during mitosis. *J Biol Chem* **287**, 34069-34077, doi:10.1074/jbc.M112.385518 (2012).
259   Totaro, A., Castellan, M., Di Biagio, D. & Piccolo, S. Crosstalk between YAP/TAZ and Notch Signaling. *Trends Cell Biol* **28**, 560-573, doi:10.1016/j.tcb.2018.03.001 (2018).
260   Stanoev, A., Schröter, C. & Koseska, A. Robustness and timing of cellular differentiation through population-based symmetry breaking. *bioRxiv*, 578898, doi:10.1101/578898 (2019).

261   Valon, L., Marin-Llaurado, A., Wyatt, T., Charras, G. & Trepat, X. Optogenetic control of cellular forces and mechanotransduction. *Nat Commun* **8**, 14396, doi:10.1038/ncomms14396 (2017).
262   Niopek, D., Wehler, P., Roensch, J., Eils, R. & Di Ventura, B. Optogenetic control of nuclear protein export. *Nat Commun* **7**, 10624, doi:10.1038/ncomms10624 (2016).
263   Zhang, N. *et al.* The Merlin/NF2 tumor suppressor functions through the YAP oncoprotein to regulate tissue homeostasis in mammals. *Dev Cell* **19**, 27-38, doi:10.1016/j.devcel.2010.06.015 (2010).
264   Shaya, O. *et al.* Cell-Cell Contact Area Affects Notch Signaling and Notch-Dependent Patterning. *Dev Cell* **40**, 505-511 e506, doi:10.1016/j.devcel.2017.02.009 (2017).
265   Guisoni, N., Martinez-Corral, R., Garcia-Ojalvo, J. & de Navascues, J. Diversity of fate outcomes in cell pairs under lateral inhibition. *Development* **144**, 1177-1186, doi:10.1242/dev.137950 (2017).
266   Hirata, H. *et al.* Oscillatory expression of the bHLH factor Hes1 regulated by a negative feedback loop. *Science* **298**, 840-843, doi:10.1126/science.1074560 (2002).
267   Fre, S. *et al.* Notch lineages and activity in intestinal stem cells determined by a new set of knock-in mice. *PLoS One* **6**, e25785, doi:10.1371/journal.pone.0025785 (2011).
268   Ohtsuka, T. *et al.* Visualization of embryonic neural stem cells using Hes promoters in transgenic mice. *Mol Cell Neurosci* **31**, 109-122, doi:10.1016/j.mcn.2005.09.006 (2006).
269   Richardson, D. S. & Lichtman, J. W. Clarifying Tissue Clearing. *Cell* **162**, 246-257, doi:10.1016/j.cell.2015.06.067 (2015).
270   Weigert, M., Schmidt, U., Haase, R., Sugawara, K. & Myers, G. Star-convex Polyhedra for 3D Object Detection and Segmentation in Microscopy. *eprint arXiv:1908.03636*, arXiv:1908.03636 (2019).
271   Holcombe, M. *et al.* Modelling complex biological systems using an agent-based approach. *Integr Biol (Camb)* **4**, 53-64, doi:10.1039/c1ib00042j (2012).
272   Montes-Olivas, S., Marucci, L. & Homer, M. Mathematical Models of Organoid Cultures. *Front Genet* **10**, 873, doi:10.3389/fgene.2019.00873 (2019).
273   Thalheim, T. *et al.* Linking stem cell function and growth pattern of intestinal organoids. *Dev Biol* **433**, 254-261, doi:10.1016/j.ydbio.2017.10.013 (2018).
274   Yan, H., Konstorum, A. & Lowengrub, J. S. Three-Dimensional Spatiotemporal Modeling of Colon Cancer Organoids Reveals that Multimodal Control of Stem Cell Self-Renewal is a Critical Determinant of Size and Shape in Early Stages of Tumor Growth. *Bull Math Biol* **80**, 1404-1433, doi:10.1007/s11538-017-0294-1 (2018).
275   Li, H. J., Kapoor, A., Giel-Moloney, M., Rindi, G. & Leiter, A. B. Notch signaling differentially regulates the cell fate of early endocrine precursor cells and their maturing descendants in the mouse pancreas and intestine. *Dev Biol* **371**, 156-169, doi:10.1016/j.ydbio.2012.08.023 (2012).
276   Stoeckius, M. *et al.* Cell Hashing with barcoded antibodies enables multiplexing and doublet detection for single cell genomics. *Genome Biol* **19**, 224, doi:10.1186/s13059-018-1603-1 (2018).
277   Assawachananont, J. *et al.* Transplantation of embryonic and induced pluripotent stem cell-derived 3D retinal sheets into retinal degenerative mice. *Stem Cell Reports* **2**, 662-674, doi:10.1016/j.stemcr.2014.03.011 (2014).
278   Naganuma, H. & Nishinakamura, R. From organoids to transplantable artificial kidneys. *Transpl Int* **32**, 563-570, doi:10.1111/tri.13404 (2019).
279   Takebe, T. *et al.* Vascularized and Complex Organ Buds from Diverse Tissues via Mesenchymal Cell-Driven Condensation. *Cell Stem Cell* **16**, 556-565, doi:10.1016/j.stem.2015.03.004 (2015).
280   Mansour, A. A. *et al.* An in vivo model of functional and vascularized human brain organoids. *Nat Biotechnol* **36**, 432-441, doi:10.1038/nbt.4127 (2018).
281   Homan, K. A. *et al.* Flow-enhanced vascularization and maturation of kidney organoids in vitro. *Nat Methods* **16**, 255-262, doi:10.1038/s41592-019-0325-y (2019).
282   Terzic, J., Grivennikov, S., Karin, E. & Karin, M. Inflammation and colon cancer. *Gastroenterology* **138**, 2101-2114 e2105, doi:10.1053/j.gastro.2010.01.058 (2010).
283   Brassard, J. A. & Lutolf, M. P. Engineering Stem Cell Self-organization to Build Better Organoids. *Cell Stem Cell* **24**, 860-876, doi:10.1016/j.stem.2019.05.005 (2019).

Appendix

Supplementary information to Chapter 3: Self-organization and symmetry breaking in intestinal organoid development

Self-organization and symmetry breaking in intestinal organoid development

Denise Serra[1,2,6], Urs Mayr[1,2,6], Andrea Boni[1,5,6], Ilya Lukonin[1,2], Markus Rempfler[1], Ludivine Challet Meylan[1], Michael B. Stadler[1,3], Petr Strnad[1,5], Panagiotis Papasaikas[1,3], Dario Vischi[1], Annick Waldt[4], Guglielmo Roma[4] & Prisca Liberali[1,2]*

[1]Friedrich Miescher Institute for Biomedical Research (FMI), Basel, Switzerland. [2]University of Basel, Basel, Switzerland. [3]Swiss Institute of Bioinformatics, Basel, Switzerland. [4]Novartis Institutes for BioMedical Research, Novartis Pharma AG, Basel, Switzerland. [5]Present address: Viventis Microscopy Sàrl, EPFL Innovation Park, Lausanne, Switzerland. [6]These authors contributed equally: Denise Serra, Urs Mayr, Andrea Boni. *e-mail: prisca.liberali@fmi.ch

Methods

Organoid lines

All animal experiments were approved by the Basel Cantonal Veterinary Authorities and conducted in accordance with the Guide for Care and Use of Laboratory Animals. Male and female outbred mice between 7 and 15 weeks old were used for all experiments. Mouse lines used: C57BL/6 wild type (Charles River Laboratories), Lgr5–EGFP–Ires–CreERT2 (kind gift from Momo Bentires-Alj, University Hospital in Basel), Lgr5::DTR-EGFP (Genentech, de Sauvage laboratory), H2B-mCherry C57BL/6 x C3H F1 females heterozygous for H2B-mCherry (kind gift from T. Hiragi lab, EMBL), Lats1$^{\Delta/\Delta}$; Lats2$^{\Delta/\Delta}$ (LATS DKO, kind gift from Jeff Wrana, Department of Molecular Genetics, University of Toronto, Canada)[28], Yap1$^{tm1.1Dupa}$/J (Yap1^{flox})[48] from The Jackson Laboratory. For Lgr5-GFP/mem9-mCherry organoids, Lgr5–EGFP–Ires–CreERT2 organoids were infected with rLV.EF1.mCherry-Mem-9 lentiviral particles (Clontech, Takara Bio USA). For H2b-mCherry/mem9-GFP organoids, H2b-mCherry organoids were infected with LV.EF1.AcGFP1-Mem-9 lentivirus particle (Clontech, Takara Bio USA). For doxycycline inducible hYap1 overexpression organoids, C57BL/6 wild type organoids were infected with in-house produced FUW-tetO-wtYAP viral particles (Addgene plasmid # 84009) together with rLV.EF1.Tet3G-9 viral particles (Clontech, Takara Bio USA). For TCF-GFP organoids C57BL/6 wild type organoids were infected with TOP-GFP (Addgene plasmid #35489). For Yap1 KO, Yap1$^{tm1.1Dupa}$/J (Yap1^{flox}) organoids were infected with CRE (Puro) EF1a lentivirus in PBS (GeneTarget cat # LVP-520 PBS) or as control with pEGIP (Addgene plasmid #26777) at 0 hours.

Organoid culture

Organoids were generated from isolated crypts of the murine small intestine as previously described[49]. In brief, the section of the initial part of the small intestine was opened lengthwise, cleaned with cold PBS and, after removal of villi by scraping with a cold glass slide, sliced into small fragments roughly 2 mm in length. The tissue was then incubated in 2.5 mM EDTA/PBS at 4 °C for 30 min with shaking. Supernatant was removed and pieces of intestine were re-suspended in DMEM/F12 with 0.1% BSA. The tissue was then shaken vigorously. To collect the first fraction, the suspension was passed through a 70 μm strainer.

The remaining tissue pieces were collected from the strainer and fresh DMEM/F12 with 0.1% BSA was added, followed by vigorous shaking. The crypt fraction was again collected by passing through a 70 µm strainer. In total, 4 fractions were collected. Each fraction was centrifuged at 300g for 5 min at 4 °C. Supernatant was removed and the pellet was re-suspended into Matrigel with medium (1:1 ratio) and plated into 24 well plates. Organoids were kept in IntestiCult Organoid Growth Medium (STEMCELL Technologies) with 100 µg/ml Penicillin-Streptomycin for amplification and maintenance.

Time course experiments of fixed organoid samples

Organoids were collected 5-7 days after passaging and digested with TrypLE (Thermo Fisher Scientific) for 20 min at 37 °C. Dissociated cells were passed through a cell strainer with a pore size of 30 µm (Sysmex). For all experiments, single alive cells were sorted by FACS (Becton Dickinson FACSAria cell sort or Becton Dickinson Influx cell sorter). Forward scatter and side scatter properties were used to remove cell doublets and dead cells. To obtain Lgr5+ or Lgr5- starting populations, cells were gated as shown in (**Extended Data Fig. 1b**). Sorted cells were collected in ENR medium composed of advanced DMEM/F-12 with 15 mM HEPES (STEM CELL Technologies) supplemented with 100 µg/ml Penicillin-Streptomycin, 1×Glutamax (Thermo Fisher Scientific), 1×B27 (Thermo Fisher Scientific), 1xN2 (Thermo Fisher Scientific), 1mM N-acetylcysteine (Sigma), 500ng/ml R-Spondin (kind gift from Novartis), 100 ng/ml Noggin (PeproTech) and 100 ng/ml murine EGF (R&D Systems). Collected cells were mixed with Matrigel (Corning) in a medium to Matrigel ratio of 1:1. In each well of a 96 well plate, 5µl droplets with 3000 cells were seeded (except for Lgr5 time course experiments where 1300 and 3500 cells were seeded for Lgr5+ and Lgr5-respectively). After 20 min of solidification at 37 °C, 100 µl of medium was overlaid. From day 0 to day 1, ENR was supplemented with 20% Wnt3a-conditioned medium (Wnt3a-CM), 10 µM Y-27632 (ROCK inhibitor, STEMCELL Technologies) and 3 µM of CHIR99021 (GSK3B inhibitor, STEMCELL Technologies, cat # 72054). From day 1 to 3 ENR was supplemented with 20% Wnt3a-CM and 10 µM Y-27632. From day 3 to 5, only ENR was added to the cells. Wnt3a-CM was produced in-house by Wnt3a L-cells (kind gift from Novartis)

Compound treatments

Single cells derived from C57BL/6 wild type organoids were plated in a 96-well plate and exposed to 5 µM Verteporfin (SIGMA-ALDRICH, cat # SML0534) or DMSO (SIGMA-

ALDRICH, cat # D8418) diluted in ENR medium at different time points (0, 24, 48, or 72 hours). Organoids were fixed at different time points for analysis. Doxycycline inducible hYap1 overexpression organoids were treated with 0.05 µg/ml Doxycycline hyclate (SIGMA-ALDRICH, cat # D9891) or ddH$_2$O diluted in ENR medium right after single cell sorting and organoids were fixed at 72 or 96 hours. Lats1/2 double DKO organoids were exposed to 1 µg/ml 4-Hydroxytamoxifen (SIGMA-ALDRICH, cat # H6278) or DMSO one day before single cell isolation and fixed at different time points. Single cells derived from organoids C57BL/6 wild type were treated with 10 µM DAPT (Stemgent cat # 04-0041) or DMSO diluted in ENR medium, from single cell isolation until fixation at 96 hours, or treated at 120 hours and fixed at 144 hours. Single cells derived from organoids C57BL/6 wild type were treated with Ly411575 0.5 µM (kind gift from Novartis) or MK-0752 (kind gift from Novartis) 0.5 µM or DMSO in addition to the ENR medium, from 0 hours until fixation at 120 hours. Single cells Lgr5::DTR-EGFP positive and Lgr5::DTR-EGFP negative derived from organoids Lgr5::DTR-EGFP were treated with CHIR99021 5 µM (GSK3B inhibitor, STEMCELL Technologies cat # 72054) or IWP-2 2 µM (Porcupine Inhibitor, STEMCELL Technologies cat # 72124) or DMSO 5 µM or DMSO 2 µM diluted in ENR medium, from single cell isolation until organoids fixation at different time points. Single cells derived from organoids C57BL/6 wild type were treated with Ereg 0.5 µg/ml (R&D System cat # 1068-EP-050) or PBS in addition to the ENR medium, from 0 hours until fixation at different time points.

Re-plating experiment
Single cells (C57BL/6 wild type) were isolated from budding organoids at 120 hours and from spheres at 72 hours, that on average have more Yap1 activity. Same number of cells per condition were plated in different wells of 96-well plates and cultured for 24 hours.

Fixed sample preparation and imaging
Organoids are embedded in a Matrigel droplet. Due to the nature of the droplet, individual organoids are located at different heights in the Matrigel drop. To allow imaging of all organoids within a similar z-range, each 96-well plate was centrifuged at 3000 rpm for 10 min in a pre-cooled centrifuge at 10 °C prior to fixation. Organoids were fixed in 4% PFA (Electron Microscopy Sciences) in PBS for 45 min at room temperature. Day 0 plates were fixed 3h after seeding. For time course and compound experiments, organoids were permeabilized with 0.5% Triton X-100 (Sigma-Aldrich) for 1 h and blocked with 3% Donkey

Serum (Sigma-Aldrich) in PBS with 0.1% Triton X-100 for 1 h. Primary and secondary antibodies were diluted in blocking buffer and applied as indicated in **Table S2**. Cell nuclei were stained with 20 µg/ml DAPI (4',6-Diamidino-2-Phenylindole, Invitrogen) in PBS for 15 min. Cells were stained with 1 µg/ml of Alexa Fluor® 647 carboxylic acid succinimidyl ester (CellTrace, Invitrogen) in carbonate buffer (1.95 ml of 0.5 M $NaHCO_3$, 50 µl of 0.5 M Na_2CO_3, both from Sigma-Aldrich, in 8 ml of water for 10 ml of buffer).

High-throughput imaging was done with an automated spinning disk microscope from Yokogawa (CellVoyager 7000S), with an enhanced CSU-W1 spinning disk (Microlens-enhanced dual Nipkow disk confocal scanner), a 40x (NA = 0.95) Olympus objective, and a Neo sCMOS camera (Andor, 2,560 × 2,160 pixels). For imaging, an intelligent imaging approach was used in the Yokogawa CV7000 (Search First module of Wako software). For each well, one field was acquired with 2x resolution in order to cover the complete well. This overview fields were then used to segment individual organoids on the fly with a custom written ImageJ macro which outputs coordinates of individual organoid positions. These coordinated were then subsequently imaged with high resolution (40x, NA = 0.95). For each site, z-planes spanning a range up to 60 µm were acquired. For time course and compound experiment 5µm z-steps were used. For multiplexing 2 µm or 3 µm z-steps were used.

<u>Multiplexed imaging</u>

To allow multiple rounds of antibody staining and imaging for the same organoids, the 4i multiplexing protocol was applied to 3D organoid cultures. In brief, plates were permeabilized with -20 °C Methanol (Sigma-Aldrich) for 30 min at -20°C followed by blocking with 3% donkey serum in PBS for 1 h at room temperature. For each round of imaging, organoids were stained with 20 µg/ml DAPI in PBS for 15 min. Additionally for the first round, cell were stained with 1 µg/ml of Alexa Fluor® 647 carboxylic acid succinimidyl ester. For each round of staining, primary and secondary antibodies were diluted in 3% donkey serum with added 200 mM NH_4Cl and applied as indicated in **Table S2**. Plates were imaged in imaging buffer (700mM *N*-Acetyl-Cysteine, Sigma-Aldrich, in ddH_2O, pH adjusted to 7.4). After each round of imaging, antibodies were eluted for 3 times 10 minutes with elution buffer (0.5 M *L*-Glycine, 5 M Urea, 5 M Guanidinium chloride, 70 mM TCEP-HCl, all in ddH_2O with pH adjusted to pH2.5, all chemicals from Sigma-Aldrich). Plates were re-blocked after each round of imaging for 1 h at room temperature and antibodies of the next round were applied. For the multiplexed Lgr5 time course the following staining were used: Round 1 (DAPI, anti-GFP, anti-Lysozyme and CellTrace), Round 2 (DAPI and anti-PCNA),

Round 3 (DAPI and anti-Aldolase B). For the multiplexed Yap1 time course the following staining were used: Round 1 (DAPI, anti-Yap1, anti-Dll1 and CellTrace), Round 2 (DAPI and anti-Hes1)

Organoid clearing

To optically clear organoids after immunofluorescence staining, organoids were incubated for 20 min in a refractive index(RI)-matching solution[50] (9.2 ml 60% iodixanol solution, Sigma-Aldrich D1556, 4 g N-methyl-D-glucamine, Sigma Aldrich M2004, 5 g diatrizoic acid, Sigma Aldrich D9268, dissolved in 6.3 ml of ddH_2O). Per well of a 96-well plate, 200 µl of RI-matching solution were added. After 20 min of sample incubation the organoids were imaged in the IR-matching solution.

Image analysis and organoid feature extraction

Organoid segmentation in MIPs. For each acquired confocal z-stack field, maximum intensity projections (MIP) were generated. All MIP fields of a well were stitched together to obtain MIP well overviews for each channel. The high resolution well overviews were used for organoid segmentation and feature extraction. Each individual organoid was automatically segmented based on CellTrace signal. For small round organoids up to 84h after fixation we applied a watershed algorithm on a binary mask generated by Otsu thresholding. For bigger organoids observed 84h post fixation, a watershed algorithm was applied on prediction maps generated by a fully convolutional neural network (FCN). This network follows a U-Net architecture[51] with ResNeXt building blocks[52] and two output channels: The first predicts whether a pixel belongs to the foreground (i.e. an organoid) or not, whereas the second predicts whether a pixel is at the interface of two distinct organoids, thus acting as a mechanism for separating individual organoids with non-convex shape in the watershed.

Features MIP. For each segmented organoid, features describing shape (22 features) and features quantifying intensities for each acquired channel and staining round were extracted (11 features for each individual staining for each imaging round).

To quantify low abundance signal on MIP masks, each organoid mask was partitioned into superpixels. These superpixels were calculated with the SLIC (Simple Linear Iterative Clustering) method initialized uniformly with regions of approximately the size of a single

cell (2000 pixel). For each organoid, we calculated mean signal strength for each superpixel and ranked all of them in descending order. Subsequently, the mean over the top-k superpixel means was calculated in order to obtain a measure that is robust to local noise due to the spatial aggregation over the superpixels but sensitive enough to quantify signal that is only observed in subregions of the entire organoid. For our experiments, we found k=10 to be an informative threshold.

Enterocyst classification

A binary SVM classifier was trained to group organoids into budding organoids and enterocysts based on shape as well as intensity features.

Organoid linkage over imaging rounds. In each subsequent round of multiplexing, the position of the same organoid can slightly move or organoids can be lost due to segmentation errors. To re-identify the same organoid over multiple rounds, a custom linkage algorithm was developed. In short, for each segmented organoid in a round, the outline polygon is extracted and stored in a spatial index, based on the *R*Tree algorithm*. We then fix the first available imaging round as *reference round* and search for intersections with polygons of other rounds. We call such intersections a *link* between a segmentation of the reference round seg_{ref} and the segmentation of the target round seg_{target}. To consider shifts between imaging rounds, we expand each polygon by 100 pixels. In a refining step, we assign a *similarity score* to each intersection and keep only the closest, in terms of rounds, and most similar links. The similarity score is defined as the area of the intersection divided by the area of the union of seg_{ref} and seg_{target} multiplied by a distance term. The distance term is defined as 1 if the *L1 distance* between seg_{ref} and seg_{target} is 0 and exponential decreases as the L1 distance increases. *Union* and *intersection* are operations from the set theory.

$$similarity\ score = \frac{area(intersection(seg_{ref}, seg_{target}))}{area(union(seg_{ref}, seg_{target}))} \cdot exp^{(-0.001 \cdot L_1(seg_{ref}, seg_{target}))}$$

In a last step, we traverse all links, starting from each polygon of the reference round and group all connected segmentations as an *organoid object*.

3D segmentation and analysis. Given the organoid segmentation from processing the MIP as described in the previous section, the corresponding confocal stack was cropped to its mask region for each individual organoid. Two segmentation models were deployed on these stacks, one for 3D organoid segmentation and one for individual nuclei.

In-focus planes. The ratio of in-plane maximum intensity to the maximum intensity in the stack was used as metric for the plane being in-focus, being close to 1 in the regions of high intensity and decaying to 0 towards the background/empty planes. A logistic regression was fitted to transform this metric into a probability measure.

3D Organoid segmentation. 3D organoid segmentations were generated by applying an FCN to the CellTrace channel of the individual crops. The FCN is applied slice-by-slice and generates probability maps of pixels belonging to the foreground. The probabilities in planes that are not classified as "in-focus" are set to zero in order to make the segmentation more robust. Pixels that originate from outside the original MIP mask (e.g. from an adjacent organoid that is partially within the crop) are also masked out.

3D Features. A set of 20 features was calculated on each segmented 3D stack, including volume, lumen and area estimates, major/minor axis lengths, elevation angle as well as statistics on the in-focus planes.

Single cell segmentation. Following the scheme used for the organoid segmentation, a FCN was designed to segment individual nuclei in the DAPI channel of the cropped stacks. This FCN outputs both a foreground probability map, as well as a separator probability that peaks at the interface of two distinct nuclei. These two prediction maps are then combined by a watershed algorithm to yield a segmentation of individual nuclei. In order to obtain an estimate for the cytosol, the mask obtained from the organoid segmentation is partitioned such that pixels in its foreground are assigned to the closest nucleus. Pixels segmented as nucleus are removed from the cytosol. The method is applied on a slice-by-slice basis. The output is used for estimating cell count per organoid and quantifying marker intensities.

Estimating cell count. For each stack, individual nuclei are counted in every slide and summed up. The final estimate is then corrected by an experiment specific correction factor, accounting for the fact that we expect each nucleus being imaged in multiple planes. This

avoids having another linking step that tries to determine whether two nuclei in subsequent planes are from the same physical object or not. The experiment specific correction factor is estimated based on hand annotated nuclei counts. Before counting, a nuclei size filter was applied to remove miss-segmentations.

Trajectory of organoid development

For trajectory inference Wishbone, an algorithm originally developed to infer branching trajectories within a multivariate feature space of mass cytometry or single cell RNA sequencing data was used. Wishbone allows to infer a trajectory of organoid development based on their features and to identify the branch points between budding organoids and enterocyst. To use wishbone with imaging data, the original python Wishbone package was slightly adapted. A new imaging data type as well as additional possibilities to normalize data were added. Trajectory inference comprised the following steps: (1) A z-score based filtering was applied to remove segmentation outliers and imaging artefacts from the dataset, resulting in a dataset of 9798 Lgr5+ organoids and 13623 Lgr5- organoids (2) Data were power transformed followed by zero-mean, unit-variance normalization (3) Pseudotime ordering is inferred from molecular events and is dependent on the features selected to describe them. For initial diffusion map computation, the full pooled dataset with 23421 organoids and 66 features was used as input (full feature set, including morphological features, intensity features for DAPI, Lysozyme, PCNA and AldolaseB). Diffusion maps were then computed on the 10 first PCA components of the input dataset after removal of highly redundant features with Pearson correlation > abs(0.95) (**Extended Data Fig. 2f**) (4) To refine the separation between budding organoids and enterocyst around branch point and to minimize a stretch or compression in pseudotime compared to real time, we included an additional feature refinement step. To select a subset of features which optimally separate between budding organoids and enterocyst along time, we plotted for each of the features trends over time for budding organoid and enterocysts individually and selected features which allowed best to separate between groups. By this step we refined the final feature set used for diffusion map computation to 14 features (**Extended Data Fig. 2a b**). Any step of feature selection can introduce biases but we confirmed that the time progression and bifurcation are also present using the full feature set (**Extended Data Fig. 2f**). After calculation of diffusion

maps the pooled Lgr5+ and Lgr5- dataset was divided into Lgr5+ and Lgr5- groups. For each group individual, the three top diffusion components were used to infer a Wishbone trajectory. To find a continuous branching trajectory, Wishbone relies on the definition of a starting cell and a selected set of waypoints which help to refine the trajectory. For the starting cell, a random 1 cell stage cell was selected. 200 waypoints were set manually based on 3D diffusion plots to represent regions along the entire trajectory and its branches equally. To plot marker expression along trajectory, the trajectory was divided into 120 bins. Nuclei numbers were calculated for a subset of the full trajectory as described under *Estimating cell count*.

Dynamic time warping for trajectory

Dynamic time warping: An inferred trajectory is able to capture continuous progression of organoids along their development with pseudo temporal ordering. Pseudo-time ordering is inferred from features describing molecular events which can have a huge dynamic range between different organoid stages and can result in a pseudotime progression which does not necessarily represent development of the system in real time. To approximate the relation between real time and pseudotime we used dynamic time warping to map trajectory data against real time data extracted from light sheet imaging. DTW algorithms compute the local stretch or compression between one-time axis of one time series (query) against the time axis of a reference time series. The query sequence is warped non-linearly to find the optimal mapping onto the reference[53]. Since budding organoids represent the majority of organoids after branching (~80 percent of the data) only budding organoids (n=6) from light sheet data were used to calculate the warping. Based on the extracted light sheet imaging data, an average path of area progression every hour from hour 0 to hour 120 was calculated. The mean area progression extracted from the light sheet was then matched against the area progression from the pseudotime trajectory (averaged into 120 bins). The fastdtw package in python was used to map each point of the budding organoid branch (query branches) to the corresponding point of the light sheet data. This mapping between real time points and pseudotime points allows then to infer relations between real time and pseudotime (**Extended data figure 4h**).

RNA-seq mapping: To allow comparison between pseudotime trajectories of protein abundance and mRNA levels from fixed time points, RNAseq real time data were mapped onto the corresponding position on a pseudotime axis based on the inferred relations between

real time and pseudotime (i.e the real-time axis was compressed and stretched in accordance with the compression and stretching observed in the pseudotime trajectory)

Organoid mapping on trajectory

To analyze Yap1 protein abundance along pseudotime, organoids with staining for Yap1 protein abundance (Yap1 organoids) were mapped on the trajectory inferred from the Lgr5 dataset based on their area and type (budding organoids or enterocyst). Yap1 organoids where classified into budding organoids or entercysts using an svm classifier. This information was then used to assign each organoid to either the budding organoid or the enterocyst branch of the trajectory. To define the position on the respective branch, the organoid area was used to place each Yap1 organoid into the trajectory bin with the closest mean area. Yap1 intensity in each bin was then averaged and smoothed with a moving average filter.

Light sheet microscope setup and imaging

The custom light sheet microscope system (**Extended Data Figure 4**) is composed of two illumination branches (excitation beams shown in blue) and one imaging branch (emitted light shown in green). Excitation laser beams (LuxXPlus 488-60, OBIS 561-50 and LuxXPlus 630-150) are combined inside a laser combiner (SOLE-6 Light Engine, Omicron-Laserage Laserprodukte) and laser beams are collimated (0.7 mm beam diameter) at the end of optical fiber (kineFLEX; Qioptiq). Neutral density filters (NE10B, NE20B, NE30B, NE40B; Thorlabs), mounted in a filter wheel (96A357, Ludl Eletronics Product), are placed after the fiber to further attenuate laser intensity. The laser beam is first split into three laser branches by using three consecutive beam splitter cube (BS010, Thorlabs); in one laser branch the beam size remains unchanged while the in the other two laser branches beams are expanded by beam expanders (GBE02-A and GBE05-A, Thorlabs). In this way, the three laser branches result in light-sheet thicknesses (FWHM) of 1.1 μm, 2.2 μm and 3.3 μm at the sample. Each laser branch is split by a beam splitter cube (BS010, Thorlabs) into the two illumination objectives. The following arrangement is replicated in front of each illumination objective. Switching between the different laser branches and thus beam diameters is done by using a pair of right angle prisms (MRA35-E02, Thorlabs) mounted with a custom made support on a rotary stages (SR2812-S, SmarAct) that redirect only one laser branch beam through an aperture towards a scan unit. The scan unit comprises two galvanometric scanners (6210HM40B, Camtech) and a scan lens (ACA254-075-A, Thorlabs) mounted on a linear

stage (SLC2490-S, SmarAct). The light sheet is generated by scanning the laser beam with the second galvanometric scanner. Light sheet is de-magnified onto the sample by a 10X 0.3 NA water immersion objective lens (CFI Plan Fluor 10XW, Nikon) and a tube lens (f = 200 mm; Nikon). A 25X 1.1 NA objective (CFI75 Apo 25XW; Nikon) is used to collect the emitted fluorescence. The emitted light is then directed by a prism mirror (87-393; Edmund) towards a tube lens (f = 200 mm; Nikon) and image is acquired by an sCMOS camera (Zyla 4.1, Andor). A motorized filter wheel (96A357; Ludl Electronic Products) which contains the emission filters (488 LP Edge Basic Longpass Filter - F76-490; 561 LP Edge Basic Longpass Filter- F76-561; HC Dualband Emitter R 488/568 - F72-EY2, Semrock, AHF) is mounted before the camera. Because illumination and detection objectives are water dipping lens they are fixed on customized aluminum blocks and sealed in a custom made water reservoir made of polyaceral that can be filled with water so that the front lenses of all objectives are completely covered.

Sample mounting. A custom designed imaging chamber made of polyamide (PA2200) is 3D printed using selective laser sintering (RapidObject). A 25 μm thin membrane made of FEP (Katco) is placed into a groove of the imaging chamber and glued with biocompatible silicone glue (Silpuran 4200; Wacker) applied to the bottom of the chamber and left to cure overnight similar to what described in Strnad et al. 2016[54]. The internal surface of the membrane is plasma treated and then washed with ethanol once and rinsed three times with water before being UV sterilized for 20min. The imaging chamber is placed on a holder attached to a three-axis positioning system made of three perpendicularly arranged linear positioners (SLC-24; SmarAct) mounted using custom aluminum adapters. The sample part of the microscope is enclosed in an environmentally controlled incubator (37 °C, 5% CO_2, Life Imaging Service).

Organoids Imaging. H2b-mCherry / mem9-GFP organoids were collected and digested with TrypLE (Thermo Fisher Scientific) for 20 min at 37 °C. Alive double positive (mCherry/GFP) cells were sorted by FACS and collected in medium containing advanced DMEM/F-12 with 15 mM HEPES (STEM CELL Technologies) supplemented with 100 μg/ml Penicillin-Streptomycin, 1×Glutamax (Thermo Fisher Scientific), 1×B27 (Thermo Fisher Scientific), 1xN2 (Thermo Fisher Scientific), 1mM N-acetylcysteine (Sigma), 500ng/ml R-Spondin (kind gift from Novartis), 100 ng/ml Noggin (PeproTech) and 100 ng/ml murine EGF (R&D Systems). 2500 cells were then embedded in 5ul drop of

Matrigel/medium in 60/40 ratio. Drops were placed in the imaging chamber and incubated for 20 min before being covered with 1ml of medium. For the first three days, medium was supplemented with 20% Wnt3a-CM and 10 μM Y-27632 (ROCK inhibitor, STEMCELL Technologies). For the first day, in addition, 3μM of CHIR99021 (STEMCELL Technologies) were supplemented. After 2 hours incubation in a cell culture incubator the imaging chamber was transferred to the microscope kept at 37C and 5% CO_2. Different single cells were selected as starting positions and imaged every 10 min for up to 5 days. A volume of 150 -200μm was acquired with a Z spacing of 2μm between slices. Medium was exchanged manually under the microscopy every day.

Light sheet data analysis. For area and volume calculation of light sheet data we proceeded as follow. Initially raw data were cropped around the minimum organoids bounding box in order to reduce storage space. Data were two time down sampled to speed up processing and new Z planes are interpolated to achieve X,Y,Z isotropic voxel size. Each single plane intensity image is then converted to binary image based on an intensity threshold. Organoid volume, major axis and area are computed from the segmented regions.

To quantify Lgr5-GFP intensity during organoid development (**Video S4**) single cells in the bud or in the body of the organoid were randomly selected manually and intensity was measured at different days of development.

Dll1+ and Paneth cell overlap.

Number of Dll1+ cells and Paneth cells at different cell stages were quantified manually based on anti-Dll11 and anti-Lysozyme antibody staining's in cropped organoid z-stack images.

Yap1 cell state classification

Nuclear and cytosol mask were obtained as described under *Single cell segmentation.* A nuclei size filter was applied to remove miss-segmentations. Both nucleus and cytosol mask are used to calculate intensity statistics for the marker of interest.

Yap1-on/off states. For each nucleus, we first calculate the mean nuclear Yap1 intensity and then, normalize it by the corresponding plane-wise Yap1 intensity mean μ and standard deviation σ according to $I' = (I - \mu)/\sigma$. The plane-wise mean μ and standard deviation σ for this are calculated on the combined nucleus and cytoplasm masks (i.e. the foreground

covering all cells) of the corresponding plane. The resulting normalized nuclear Yap1 signal I' is then used to discriminate the different states. Nuclei with normalized nuclear Yap1 intensity greater than 0.1 were defined as *Yap1-on*, while those with normalized nuclear Yap1 intensity less than -0.1 were defined as *Yap1-off*. Nuclei with values falling into the range [-0.1, 0.1] were considered as *ambiguous* and excluded from further analysis.

By counting the nuclei in Yap1-on and Yap1-off states within an organoid, we calculate the relative frequency $p(k)$ of each state k within the organoid and in turn, its' Yap1-state entropy S as $S = \sum_{k \in \{\text{on,off}\}} p(k) \log_2 p(k)$.

Yap1 quantification in Dll1+ cells. To quantify signal intensity of the membrane protein Dll1, the intensity statistics were only computed on the border of the cytosol mask (to the outside of the cell) in a range of 5 px. The resulting total Dll1 intensity for each cell is then normalized by the mean μ and standard deviation σ of the total Dll1 intensity over all cells of the dataset according to $I' = (I - \mu)/\sigma$. Cells with normalized total Dll1 intensity values greater than 0.5 were defined as *Dll1 positive*, those with values below -0.1 as *Dll1-negative*. Again, cells in the range [-0.1, 0.5] are considered *ambiguous* and excluded from further analysis. Cell stages with less than one hundred partially Dll1 active organoids were not considered for Dll1-positive analysis.

Time-course WT Bulk RNA purification

RNA was isolated using Single Cell RNA Purification Kit (Norgen Biotek Corporation, Cat #51800) pooling 30 wells of 96-well plates (C57BL/6 wild type). RNA purification was performed in triplicate and for each day of organoid development (0 hours – 120 hours). Three different organoid lines C57BL/6 wild type have been used. A step of DNAse treatment was included (RNase-Free DNase I Kit, Cat #25710) for two replicates of samples (0 h – 120 h).

RNA sequencing libraries were prepared using the TruSeq Illumina mRNA Library Prep and sequenced with the Illumina HiSeq2500 platform. Reads were mapped to the UCSC mouse genome mm10 using STAR (version 2.5.2b, [55]) with parameters --outFilterType BySJout --outFilterMultimapNmax 20 --outMultimapperOrder Random --alignSJoverhangMin 8 --alignSJDBoverhangMin 1 --outFilterMismatchNmax 999 --alignIntronMin 20 --alignIntronMax 1000000 --alignMatesGapMax 1000000 --outSAMmultNmax 1. Genes expression level were quantified with the QuasR Bioconductor package[56], using gene

annotations from the TxDb.Mmusculus.UCSC.mm10.knownGene Bioconductor package. Log2(CountsPerMillion) (log2(cpm)) of uniquely mapped genes were used to describe similarities and differences among the samples by Principal Component Analysis (PCA) (**Extended Data Fig. 6a**).

Differentially expressed genes were determined with the package edgeR (version 3.20.5,[57]) by fitting a three-factor model (timepoint + mouse + dnase treatment) to the counts of genes that were detected in 2 or more samples with at least one read per million reads. For visualization of gene expression profiles averages of mean-centered log2(cpm) were mapped into pseudotime trajectory, applying the time warping shift described above to the fixed time points of Rna purification. For calculation of between gene correlations, averages of mean-centered log2(cpm) were used. The gene correlation matrix was then hierarchically clustered using Euclidian distances between correlation profiles. To display clusters profiles, clusters averages and quantiles were calculated. Cluster enrichment analysis was performed with DAVID Bioinformatics Resources 6.8.

Transcription Factor Binding Site Analysis was done applying an elastic net regression model (package glmnet, [58]) to the differential gene expression 24 hours versus 0 hours as follows: First, promoter regions were defined as a windows of 1500 bp centered on the transcript start site, only retaining a single region per gene. Transcription factor binding sites (TFBS) for 519 vertebrate motifs from the JASPAR2016 Bioconductor package (version 1.6) were predicted by converting the positional frequency matrices to log2-odds matrices (using a pseudocount of 1.0 per position and base and a uniform base frequencies as background), and then scanning the promoter regions with a cut-off score of 10.0 or the maximal motif score if less than 10. For each promoter region, the fraction G+C bases (f_{GC}) and the CpG observed over expected ratio (oe_{CpG}), defined as fraction of CG dinucleotides divided by the product of the fractions of C and G mononucleotides, were calculated and used in the linear model as regressors in addition to the predicted numbers of TFBS to control for sequence composition. The elastic net model was fit using alpha of 0.2 and lambda of 0.0588 identified based on a 10-fold cross-validation grid search over combinations of alpha and lambda values. The fitted model coefficients (beta values) represent the magnitude of contributions of each transcription factor to the differential gene expression between the two time-points. For visualization, only transcription factors with positive beta values (TFBS in the promoter is predicted to increase the transcription of the target gene from 0 hours to 24 hours) and positive log2FoldChange (log2FC) between 24 hours and 0 hours were considered.

To assess whether gene expression changes between 24 hours and 0 hours in the bulk RNA sequencing data resemble the observed expression changes in a intestine regenerative response, Pearson correlation coefficients between log2FC(24 hours-0 hours) and log2FC(Yap1 KD-Yap1 OE) expression changes were calculated.

Single cell RNA-Sequencing

Single cells were isolated from organoids at 72 hours and organoids at 120 hours (C57BL/6 wild type) and passed through a cell strainer with a pore size of 30 μm. Cellular suspensions were loaded on a 10x Genomics Chromium Single Cell instrument to generate single cell GEMs. Single cell RNA-Seq libraries were prepared using GemCode Single Cell 3' Gel Bead and Library Kit according to CG00052_SingleCell3'ReagentKitv2UserGuide_RevB. GEM-RT was performed in a Bio-Rad PTC-200 Thermal Cycler with semi-skirted 96-Well Plate (Eppendorf P/N 0030 128.605): 53 °C for 45 minutes, 85 °C for 5 minutes; held at 4 °C. After RT, GEMs were broken and the single strand cDNA was cleaned up with DynaBeads® MyOneTM Silane Beads (Life Technologies P/N 37002D). cDNA was amplified using a Bio-Rad PTC-200 Thermal cycler with 0.2ml 8-strip non-Flex PCR tubes, with flat Caps (STARLAB P/N I1402-3700): 98 °C for 3 min; cycled 12x: 98 °C for 15 s, 67 °C for 20 s, and 72 °C for 1 min; 72 °C for 1 min; held at 4 °C. Amplified cDNA product was cleaned up with the SPRIselect Reagent Kit (0.6X SPRI). Indexed sequencing libraries were constructed using the reagents in the Chromium Single Cell 3' library kit V2 (10x Genomics P/N-120237), following these steps: 1) Fragmentation, End Repair and A-Tailing; 2) Post Fragmentation, End Repair & A-Tailing Double Sided Size Selection with SPRIselect Reagent Kit (0.6X SPRI and 0.8X SPRI); 3) adaptor ligation; 4) post-ligation cleanups with SPRIselect (0.8X SPRI); 5) sample index PCR using the Chromium Multiplex kit (10x Genomics P/N-120262); 6) Post Sample Index Double Sided Size Selection- with SPRIselect Reagent Kit (0.6X SPRI and 0.8X SPRI). The barcode sequencing libraries were quantified using a Qubit 2.0 with a Qubit TM dsDNA HS Assay Kit (Invitrogen P/N Q32854) and the quality of the libraries were performed on a 2100 Bioanalyzer from Agilent using an Agilent High Sensitivity DNA kit (Agilent P/N 5067-4626). Sequencing libraries were loaded at 10pM on an Illumina HiSeq2500 with 2 × 50 paired-end kits using the following read length: 26 cycles Read1, 8 cycles i7 Index and 98 cycles Read2. The CellRanger suite (1.3.0) was used to generate the aggregated gene expression matrix from the BCL files generated by the sequencer based on the mm10 Cell Ranger mouse genome annotation files.

Single-cell expression profiles (raw UMI counts) were analysed using Griph (**see below**), which yields a graph encoding cell to cell relationships along with a 2D embedding. The graph represents cells as nodes and similar cells are connected by weighted edges. This graph was also used to identify the k-nearest-neighbours of each cell for smoothing of expression values in visualizations as indicated. The 2D embedding generated using the LargeVis module from Griph (see below) places similar cells close to each other in two dimensions.

In order to control for variable cell size and quality, marker gene expression in individual cells were normalized as follows: For a given set of marker genes, the log2 scaled UMI counts were first smoothed by calculating the average over 10-nearest-neighbor cells and then summed up (e_{obs}). Then, 200 control gene sets, containing equal numbers of genes as the marker genes and having a similar average expression distribution over all cells were randomly sampled. The mean of the expression of these control gene sets was calculated (e_{exp}) and used to generate a normalized marker gene expression score as ns = ($e_{obs} - e_{exp}$) for mapping to colors. For all the 72 hours cells and for 72 hours cells not expressing Paneth, Goblet, Enteroendocrine, Enterocyte or Stem cell markers, Spearman correlation coefficients between the normalized expression scores of Yap1 target genes (**Table S1**) and Notch receiving cell marker genes (*Dll1, Dll4, Jag1, Jag2, Atoh1*) were calculated.

For the identification of genes that are co-expressed with Yap1 target genes, raw UMI counts for variable genes used by griph (see below) from 72 hours organoid cells were normalized using "computeSumFactors" from the scran package version 1.10.1[59] and "normalize" from the scater package version 1.10.0[60]. The average Yap1 target gene expression was calculated for each cell as the mean log2 normalized UMI over variable Yap1 target genes (n=135), and cells with high expression of Yap1 targets were selected as the cells with a value greater than 0.8 (75 cells). Spearman correlation coefficients and p values were then calculated, separately in these cells and in all other cells, between the average Yap1 target gene expression and the log2 normalized UMI counts in other variable gene (n=8,025) using the R function cor.test. Finally, raw p values were corrected for multiple testing by calculating false discovery rates using the R function p.adjust with method="fdr". Annotation enrichment of genes that are co-expressed with Yap1 target genes or anti-correlated with Yap1 target genes expression was performed with DAVID Bioinformatics Resources 6.8.

Single Cell Clustering and Visualization Using Griph

The objective of any single cell clustering and projection technique is to obtain a high-quality embedding of the cell gene-count data that, ideally, both adequately captures the biological

variance and at the same time is robust to extraneous technical noise. Griph (**G**raph **I**nference of **P**opulation **H**eterogeneity) is a graph-based clustering and visualization framework that:

- Uses as features a small set of data-derived cell prototypes that encapsulate the biological variability inherent to the dataset at hand and ensures that cells are embedded in a subspace with an appropriate level of granularity.

- Is robust in the presence of severe signal distortions typically present in single cell-datasets.

- Can accurately identify cell types while being lean on memory usage and operating at near-linear time complexity by employing state-of-the-art techniques in graph structure estimation and partitioning along with recent advances in efficient graph representation, querying and projection. This extends the potential applicability of our algorithm to datasets with millions of cells.

- Naturally controls for known sources of unwanted variance by enforcing topological constraints on node connectivity.

Pre-processing of data before input to Griph

By default Griph operates on raw read counts and employs a strategy for feature selection (see section 1b.). As such, there is no need to employ pre-processing steps for library normalization or gene filtering. There is, however, no policy for cell filtering and therefore exclusion of low-quality cells (e.g based on library size and/or number of mitochondrial reads) is recommended before employing Griph.

Algorithmic details

The algorithm proceeds in two steps:

1. In an initialization step a graph is constructed and clustering is performed on a representative subset of cells.
2. In the second step the cluster centroids estimated during initialization serve as reference bases for efficiently constructing a full graph of the data and for estimating clusters across the complete set of cell libraries

1. Graph reconstruction and cluster identification of cluster on a sampled cell population

1a. Cell sampling

Random sampling on imbalanced datasets in terms of cell type frequencies can result in omission of rare cell types along with overrepresentation of the cells that belong to the most

common classes. In order to sample effectively the space of cell types we employ a filtering approach:

The average similarity of a cell to the remaining cell population is partly a function of the frequency of that cell type's library. In addition, average similarity of cells is an increasing function of the cell library size. We observed that a simple linear model adequately captures the dependence of average cell similarity, as this is captured by Spearman's rho, to the library size. We thus use this fit in order to exclude a preset fraction of cells f that have an average similarity higher that what is expected based on their library size.

1b. Selection of informative genes

Prior to algorithm initialization genes with 0 counts or negligible variance (coefficient of variation, $CV < 0.001$) across all libraries are removed. Selection of informative genes is based on estimation of their dispersion on the sampled subset of cells. We used the semi-parametric approach followed in [61]. Briefly, genes are split in bins according to their mean expression across the whole dataset. The median and median absolute deviation of the genes' coefficient of variation are then calculated for each bin.

Finally, a robust Z-score is calculated for each gene i belonging to a gene expression bin bi as:

$$Z_i = \frac{CV_i - Median(CV_{bi})}{M.A.D(CV_{bi})}$$

Selection of the top n overdispersed genes is then simply based on the sorted vector of the calculated robust Z-scores.

1c. Kernel construction

A squared similarity matrix of the sampled cells is constructed using a composite kernel from four similarity metrics:

1. 1-Canberra distance on log transformed gene counts.
2. Pearson's correlation coefficient on log transformed count.
3. Spearman's correlation coefficient on the raw gene counts.
4. 1-Hellinger distance on the raw gene counts.

Each of these metrics captures different aspects of the gene count distributions and offer complementary views of cell-to-cell similarity.

The four metrics are combined in a single similarity index between two cells c_i, c_j using the kernel function:

$$K(c_i, c_j) = cosd(R_i^2, R_j^2)$$

where *cosd* is the cosine distance and R_i, R_j are the mean-centered rank vectors of the four metrics of the two cells against the remaining cells.

1d. Graph-structure estimation and batch correction using the graphical lasso.

At this point we cast the problem of cluster identification as a graph community detection task. Note that the similarity matrix estimated above is symmetric and non-negative and can therefore be used as the input for graphical model selection methods that are typically applied in undirected graphical models (UGMs). We use the QUIC implementation [62] of the graphical lasso algorithm (glasso) for regularized inverse covariance matrix estimation [63] in order to obtain a sparse graph structure. The glasso algorithm enforces an L1 type regularization to its estimate of the inverse covariance matrix using the objective function:

$$\log\det\Theta - \text{tr}(S\Theta) - \|\Theta\|_1 * R$$

where Θ is an estimate Σ^{-1} for the inverse covariance matrix, S is the empirical covariance matrix of the data, $\|\Theta\|_1$ is the $L1$ norm of Σ^{-1}, and R is a regularization parameter. Non-zero entries of the Σ^{-1} directly correspond to the edges in the reconstructed graph. Edges are finally weighted by the corresponding entries of S.

Importantly, glasso can accommodate variable-specific regularization terms. In that case R is a $p \ x \ p$ regularization matrix and $*$ indicates component-wise multiplication. This reformulation allows us to inject prior information on variable relationships to the optimization function. We take advantage of this formulation to encode batch levels; same-batch variables are penalized with a higher regularization parameter alleviating the graph from batch-originating topologies. In the extreme, case edges between same batch variables can be completely disallowed and can only become part of the same graph module through intermediary connections that indicate batch-independent relationships. Thus, batch-encoding using topological constraints provides a flexible, natural way for batch correction avoiding corruption and/or overcorrection of the input data.

1e. Edge reweighting using structural similarity of nodes.

Noise distortions in the input data can give rise to spurious structures in the graph topology. Typical examples are long vertex chains resulting from library-size gradients or hub-like structures produced by high-library-quality cells. In order to moderate such effects, we introduce an edge reweighting step using personalized pagerank (PPR), a measure of structural similarity between nodes that captures both local and global properties of the graph topology [64]. PPR quantifies the probability of a random walk landing on a terminal vertex t when starting from a source vertex s:

$$PPR_s[t] = \mathbb{P}[X_L = t]$$

where X_L is the landing vertex of a random walk of length $L \sim Geometric(\alpha)$.
Edge weights are then updated using a symmetrized version of PPR:

$$W_{ij}{}^* = W_{ij} \cdot \frac{(PPR_j[i] + PPR_i[j])}{2}$$

PPR reweighting reduces the effects of noise distortions allowing information to flow through the graph, effectively flattening the edge-weight distribution.

1f. Graph sparsification

In order to increase efficiency of steps whose complexity depends on graph sparsity (mainly PPR calculation and community detection, see complexity analysis table) the graph is further sparsified after each steps 1d. and 1e. We use two complementary graph sparsification policies:

- mutual k-nearest neighbor-based pruning where an edge is retained if it is among the top k neighbors of both adjacent vertices.
- Top k-nearest neighbors fraction-based pruning where an edge is retained if its weight is within the top f fraction of edge weights of the vertex.

1g. Cluster identification using community detection.

Identification of clusters is performed using the multilevel Louvain algorithm for community detection [65] on the reweighted graph.

2. Efficient graph re-construction and clustering for the complete cell dataset

In the second step of the algorithm we utilize the centroids of the *c* clusters identified in the sampling step as reference bases to calculate the full kernel matrix for the full cell population *p*. Kernel matrix calculation is performed as above, that is:

$$K(c_i, c_j) = cosd(R_i{}^2, R_j{}^2)$$

where now R_i, R_{ij} are vectors of length *c*.

Note that the complexity of calculating *R* for all cells with *n* features (genes) is *O(c p n)* (as opposed to O(*p² n*)), linear to the numbers of cells, effectively reducing calculation time.

However, calculation of the full matrix *K* for graph construction would still require *O(p²c)* calculations. We sidestep explicit calculation of *K* using the LargeVis approach for construction of an approximate *k*-nearest neighbor graph [66]. LargeVis combines random projection trees with neighbor exploring techniques to efficiently obtain a highly accurate *k*-nearest neighbor graph. LargeVis queries can operate on cosine distance space allowing its direct application to this task. The complexity of LargeVis graph construction is *O(p)* thus preserving linear complexity of graph reconstruction to the number of cells.

The graph is further sparsified at this step as described above (section 1f).

Finally, cluster identification on the full reconstructed graph proceeds as above using the multilevel louvain algorithm for community detection.

Graph Visualization

The weighted adjacency matrix *A* of the full graph is used directly or after conversion to a distance matrix (*1-A*) as the input for three different methods of graph visualization:

- LargeVis [66] provides a scalable and effective method for graph visualization.
- *t*-Distributed Stochastic Neighbor Embedding (tSNE) [67].
- A graph projection based on the Fructherman Reingold algorithm for force-directed graph drawing [68].

Implementation

- The code for selection of informative genes was adapted from the authors implementation available at: https://github.com/10XGenomics/single-cell-3prime-paper.

- For graph manipulation and projection, personalized pagerank calculation and community detection we used the igraph R package implementations . igraph is available at http://igraph.org/
- The LargeVis code for k-nearest neighbor graph construction and visualization was ported to Griph from the R implementation available at: https://github.com/elbamos/largeVis
- The Rtsne R package used for tSNE projections is available at https://cran.r-project.org/web/packages/tsne/

<u>Griph robustness analysis and comparison to other methods</u>

In order to compare the lower dimensional embedding produced by griph, and also to analyze the sensitivity to the method for variable gene selection, 4 different embedding approaches (griph/LargeVis, PCA, PCA combined with t-SNE or diffusion maps) were systematically applied to 5 different sets of variable genes (selected using griph to retain 10%, 25% or 50% of genes per bin, by Michaelis-Menten fitting of the gene dropout rates as implemented in M3Drop, or by the mean-variance fitting procedure described in [69].